Solving Cosmological Tensions with Neutrino Physics

A thesis

submitted for the degree of

Doctor of Philosophy

in

The Department of Physics,

Pondicherry University,

Puducherry - 605 014, India

by

Ravi kumar sharma

Indian Institute of Astrophysics,

Bangalore - 560 034, India

November 2023

Solving Cosmological Tensions with Neutrino Physics

Ravi kumar sharma
Indian Institute of Astrophysics

Indian Institute of Astrophysics
Bangalore - 560 034, India

Title of the thesis	:	**Solving Cosmological Tensions with Neutrino Physics**
Name of the author	:	**Ravi kumar sharma**
Address	:	Indian Institute of Astrophysics II Block, Koramangala Bangalore - 560 034, India
Email	:	ravi.sharma@iiap.res.in
Name of the supervisor	:	**Prof. Subinoy Das**
Address	:	Indian Institute of Astrophysics II Block, Koramangala Bangalore - 560 034, India
Email	:	subinoy@iiap.res.in

Declaration of Authorship

I hereby declare that the matter contained in this thesis is the result of the investigations carried out by me at the Indian Institute of Astrophysics, Bangalore, under the supervision of Prof. Subinoy Das. This work has not been submitted for the award of any other degree, diploma, associateship, fellowship, etc. of any other university or institute.

Signed: _____

Date: _____

Certificate

This is to certify that the thesis titled **'Solving Cosmological Tensions with Neutrino Physics'** submitted to Pondicherry University by Mr. Ravi Kumar sharma for the award of the degree of Doctor of Philosophy is based on the results of the investigations carried out by her under my supervision and guidance, at the Indian Institute of Astrophysics. This thesis has not been submitted for the award of any other degree, diploma, associateship, fellowship, etc. of any other university or institute.

Signed: _____

Date: _____

List of Publications

1. Subinoy Das, Anshuman Maharana, Vivian Poulin, and **Sharma*, Ravi Kumar.** Nonthermal neutrino-like hot dark matter in light of the S8 tension. Phys. Rev. D, 105(10):103503, 2022

2. Antareep Gogoi, **Sharma, Ravi Kumar,** Prolay Chanda, and Subinoy Das. Early Mass-varying Neutrino Dark Energy: Nugget Formation and Hubble Anomaly. Astrophys. J., 915(2):132, 2021

3. Arka Banerjee, Subinoy Das, Anshuman Maharana, and **Sharma*, Ravi kumar.** Signatures of Light Massive Relics on nonlinear structure formation. Mon. Not. Roy. Astron. Soc., 516(2):2038–2049, 2022

4. **Sharma, Ravi Kumar,** Kanhaiya Lal Pandey, and Subinoy Das. Implications of an Extended Dark Energy Model with Massive Neutrinos. Astrophys. J., 934(2):113, 2022

5. Arka Banerjee, Subinoy Das, Anshuman Maharana, Ethan O. Nadler, and **Sharma*, Ravi kumar** Non-thermal warm dark matter limits from small-scale structure. (arxiv:2305.15736), Phys.Rev.D 108 (2023) 4, 043518

6. **Sharma*, Ravi kumar,** Subinoy Das, and Vivian Poulin. Early Dark Energy beyond slow-roll: implications for the cosmic tension. (Under Review, PRD) (arxiv:2309.00401)

Presentations

1. *Poster Presented*: On "Nonthermal neutrino-like hot dark matter in light of the S8 tension" at The 28th International Workshops on Weak Interactions and Neutrinos(WIN 2021, 7-12 June) Online

2. *Poster Presented*: On "Nonthermal neutrino-like hot dark matter in light of the S8 tension" at The 24th International Conference on Particle Physics and Cosmology (COSMO'21) 2-6 August) Online

3. *Contributed Talk* On "Nonthermal neutrino-like hot dark matter in light of the S8 tension" at Gravity: Current challenges in black hole physics and cosmology, Japan (20 June-1 July 2022) Online

4. *Contributed Talk* On "Signatures of Light Massive Relics on nonlinear structure formation" at Young Astronomers' Meet 2022 ARIES Nainital (9-13 Nov 2022) In person

5. *Contributed Talk* On "Signatures of Light Massive Relics on nonlinear structure formation" at The 16th International Workshop on the Dark Side of the Universe, Sydney Australia, 5-9 Dec 2022. In-person

6. *Contributed Talk* On "Signatures of Light Massive Relics on nonlinear structure formation" at 32nd Meeting of Indian Association for General Relativity and Gravitation (IAGRG), Dec 19-21, 2022. In-person

7. *Contributed Talk* On "Signatures of Light Massive Relics on nonlinear structure formation" at Less Travelled Path to the Dark Universe ICTS, Bangalore 13- 24 March 2023 In-person

Acknowledgements

I am sincerely grateful to all the individuals who have contributed to my journey, both directly and indirectly. First of all, I extend my deepest gratitude to my supervisor, Prof. Subinoy Das, whose guidance made my Ph.D. journey enjoyable, easy and truly wonderful. He has been always there to help me and give me valuable input. I am very thankful to my esteemed collaborators. Prof. Anshuman Maharana, a luminary in theoretical physics, imparted invaluable insights that profoundly influenced my thinking. I also greatly thank to Prof. Vivian Poulin, whose dedication honed my skills in data analysis. He has been a wonderful and polite person whom I can always approach. Additionally, Prof. Arka Banerjee's instruction in N-body simulation laid a strong foundation for my research. I am particularly grateful for the collaborative visit hosted by Prof. Arka Banerjee at IISER Pune, which proved to be immensely productive. I extend heartfelt thanks to Dr. Kanhaiya Lal Pandey and Dr. Ethan Nadler, with whom I shared a fruitful collaboration. To my colleagues, friends, seniors, and juniors, who engaged in stimulating scientific discussions, I express my appreciation. I acknowledge with gratitude the teachers who taught me during my B.Sc. and M.Sc. studies. My thanks extend to the Board of Graduate Studies, IIA Dean, and IIA Director for their support. I am thankful for the resources provided by IIA computing facilities, the IIA library, and Bhaskara. Lastly, I want to express my deep appreciation to my family for their constant support and motivation.

Dedicated to
My family

Abstract

The ΛCDM model is the most successful model of cosmology to fit most of the cosmological observations, yet a few discrepancies exist. There is a 4σ to 5σ mismatch in determining the Universe's current expansion rate from CMB observations using ΛCDM Model and the direct estimates. There is a milder tension in measuring the growth of structures from CMB and several weak lensing surveys. The solution of these tensions might hint towards new physics in the Universe. In this thesis, we explore the possibilities of the answer coming from the neutrino sector. We showed that 'S_8' Tension might be due to the existence of non-thermal sterile (neutrino-like) particles produced from moduli decay. These non-thermal sterile neutrinos contribute fractionally to overall dark matter density, suppressing matter power spectra at small scales. The cosmological effect of such neutrino-like species can be parameterized by its effective mass $m_{\rm sp}^{\rm eff}$ and relativistic degree of freedom$\Delta N_{\rm eff}$. The tension can be reduced below 2σ from Planck data only, but it does not favor a non-zero $\{m_{\rm sp}^{\rm eff}, \Delta N_{\rm eff}\}$. With the inclusion of the measurement of S_8 from KIDS1000+BOSS+2dfLenS, the S_8-tension would hint at the presence of nonthermal neutrinos with parameters ($m_{\rm sp}^{\rm eff} \simeq 0.67^{+0.26}_{-0.48}$ eV,$\Delta N_{\rm eff} \simeq 0.06 \pm 0.05$). Furthermore, inclusion of Pantheon and BOSS BAO/$f\sigma_8$ data gives ($m_{\rm sp}^{\rm eff} \simeq 0.48^{+0.17}_{-0.36}$,$\Delta N_{\rm eff} \simeq 0.046^{+0.004}_{-0.031}$). Once these two parameters are matched, present linear cosmological observations can't differentiate between the two models. Using this equivalence, We transferred our non-thermal model parameters to other hidden sector hot dark matter models, such as the Dodelson-Widrow and thermal models with a temperature different than the standard sector. These might have interesting implications from a particle physics point of view. The scales affected by these Light but massive relics (LiMRs) are nonlinear. Also, linear cosmological observables cannot differentiate between two non-thermal models. In the next part, we initiate a systemic study of the effects of LiMRs on smaller (non-linear) scales employing N-body

simulations. We mainly focused on the nonthermal LiMRs produced from moduli decay. However, the approaches proposed here are easily generalizable to a wide range of LiMR models — for instance, we took the Dodelson-Widrow model. In broad terms, we find that small-scale signatures of LiMRs are different from the ΛCDM model, even if the σ_8 value matches between the models. We demonstrated that in future surveys, weak lensing observations around massive clusters, between $\sim [0.1, 10]\,\mathrm{h}^{-1}\mathrm{Mpc}$, will have enough signal-to-noise ratio to differentiate between LiMR models and ΛCDM model, which are fitting both CMB data and large (linear) scale structure data at late times. Furthermore, we find that the LiMR models, which were indistinguishable using linear cosmological observations, may be distinguished by using these nonlinear probes. Therefore, combined large- and small-scale analyses of CMB and late-time structure formation data are the most effective ways to evaluate and restrict LiMR models.

We also consider the possibility that if the produced particles are kev range and account for the entire dark matter budget in the Universe. We derived constraints from small-scale structures. We show that linear power spectra (and transfer functions) corresponding to non-thermal WDM produced from moduli decay can be mapped to effective thermal-relic warm dark matter models. This production mechanism is, therefore, subject to warm dark matter constraints from small-scale structures as probed by the abundances of the ultra-faint dwarf galaxies and strong gravitational lensing flux ratio statistics. We use the correspondence to thermal-relic models to derive a lower bound on the non-thermal particle mass of 107 keV at 95$\%$ confidence. Next, we studied the Hubble tension, which might hint towards the modification in the early Universe. Early dark energy(EDE) is one of the most favored candidates to address the Hubble tension. We show that neutrinos might interact with the scalar field in the early Universe and act as early dark energy. This interaction naturally takes place around matter radiation equality (depending on neutrino mass) and solves the problem of fine-tuning, which the conventional EDE models suffer. Further, We explore the possibility that Early Dark Energy (EDE) is dynamical and study its effect on cosmological observables. We find that the present data have a mild preference for

non-cc early dark energy ($w_i = -0.78$) using Planck+BAO+Pantheon+SH_0ES data sets, leading to $\Delta\chi^2_{\rm min}$ improvement of -2.5 at the expense of one more parameter. However, w_i is weakly constrained, with $w_i < -0.56$ at 1σ. We argue that allowing for $w_i \neq -1$ can decrease the σ_8 parameter. Yet, in practice, the decrease is only $\sim 0.4\sigma$, and σ_8 is still larger than weak lensing measurements. We conclude that while promising, a dynamical EDE cannot simultaneously resolve both H_0 and σ_8 tensions. In the last chapter of the thesis, we study an extended dark energy model (comprising four free parameters governing the dark energy equation of state) in light of cosmological tensions. We found that present cosmological observations can not constrain all four parameters simultaneously. We also report that the model favors a non-zero value for the neutrino mass parameter at the most at $\sim 1\sigma$ level ($\Sigma m_\nu = 0.1847^{+0.0698}_{-0.165}$ eV) with Planck+ BAO+SN1a+MB+S8. This model also brings down the Hubble tension to $\sim 2.5\sigma$ level and the S_8 tension to $\sim 1.5\sigma$ level. The present value of the equation of state for dark energy is better constrained in this model and consistent of cosmological constant.

Contents

List of Figures

List of Tables

Chapter 1

Introduction

After photons, the abundance of neutrinos is the most in our universe. Despite this, their fundamental properties remain a mystery. We're uncertain about their origin, exact mass, and whether they engage in hidden interactions with unknown particles. It's also unclear if they have any connection with the mysterious dark sector or if there might be more than the known three generations of neutrinos. Regarding energy density, cosmic neutrinos are less dominant than baryonic matter, dark matter, and vacuum (dark) energy. However, this wasn't the case in the earlier epochs of the universe. During this period, the earlier universe was dominated by radiation; neutrinos constituted a significant portion of this radiation, thus playing an important role in governing the dynamics and evolution of the universe.

From the early stages of Big Bang nucleosynthesis to the late time structure formation, neutrinos have played a significant part in the field of cosmology. These neutrinos illustrate the complex interplay between particle physics and the study of the cosmos. Cosmology mainly focuses on three critical properties of neutrinos: their density, the number of different types, and their masses.

Through experiments on neutrino oscillations, we've established that neutrinos have mass. However, the mechanism behind how neutrinos acquire this mass remains unclear. Moreover, these experiments provide information about the difference in masses but not the absolute mass. The total mass of neutrinos is still a puzzle. Cosmology provides a powerful tool for determining this total mass because massive neutrinos significantly influence the formation of cosmic structures. Depending on their mass, neutrinos can be either relativistic or non-relativistic. Non-relativistic neutrinos interact weakly, are electrically neutral, and are strong candidates for dark matter. However, standard neutrinos may only contribute a tiny portion of the Universe's dark matter budget due to constraints on their mass and known high temperatures. On the other hand, massive sterile neutrinos could potentially account for a substantial portion of dark matter. However, several questions remain about them, including how they were generated (via decay or mixing) and whether they reached thermal equilibrium. Additionally, their interactions are not yet fully understood. In my thesis, I aim to employ observations in cosmology to address some of the inquiries mentioned above.

This chapter will introduce basic cosmology and neutrino physics, which will be handy for understanding and interpreting the results in upcoming chapters.

1.1 Basic Cosmology

The Universe is homogeneous and isotropic on large sizes, a concept known as the "cosmological principle." This principle, in conjunction with Einstein's General Theory of Relativity Einstein (1916), forms the foundation of the standard cosmological model.

Einstein's field equation is expressed as:

$$G_{\mu\nu} \equiv R_{\mu\nu} - \frac{1}{2}Rg_{\mu\nu} = 8\pi G T_{\mu\nu} \tag{1.1}$$

The stress-energy tensor, which represents the universe's components, is located on the right side of the equation. On the left side of this equation, we have terms describing the geometric features of spacetime. This equation expresses that the universe's energy-stress tensor determines the curvature of spacetime.

A universe that is both homogeneous and isotropic on a vast scale is described by the Friedmann-Lemaître-Robertson-Walker (FLRW) metric Walker (1937); Robertson (1935); Lemaître (1931); Friedmann (1924) as follows:

$$ds^2 = dt^2 - a^2(t)\left[\frac{dr^2}{1-kr^2} + r^2(d\theta^2 + \sin^2\theta d\phi^2)\right] \tag{1.2}$$

In this metric, t represents time, whereas r, θ, and ϕ denote the usual spherical coordinates. The parameter (a(t)) indicates the universe's expansion (scale factor), and the parameter (k) describes the overall geometry of the cosmos (curvature constant).

1.1.1 Friedmann Equations

In cosmology, two crucial Friedmann equations explain the behavior of an expanding universe. These equations can be extracted from Einstein's field equations and offer essential insights into the universe's dynamics Einstein (1916); Carroll (2019).

The first equation, extracted from Einstein's 00 component, is:

$$\frac{\dot{a}^2 + kc^2}{a^2} = \frac{8\pi G\rho + \Lambda c^2}{3}$$

Note that a is the universe's scale factor, denoting its size at a given time. $\dot{a}$ represents the rate of expansion or contraction. k indicates the universe's curvature (0 for flat, 1 for closed, -1 for open). Λ is the cosmological constant, and G is the gravitational constant.

The second equation, extracted from the trace of Einstein's field equations, is:

$$\frac{\ddot{a}}{a} = -\frac{4\pi G}{3}\left(\rho + \frac{3p}{c^2}\right) + \frac{\Lambda c^2}{3}$$

Here, $\ddot{a}$ relates to the acceleration (deceleration) of the universe to ρ is the density and, more importantly, to p the pressure exerted by cosmic components. To simplify, introducing Λ:

$$\rho \to \rho - \frac{\Lambda c^2}{8\pi G}$$

$$p \to p + \frac{\Lambda c^4}{8\pi G}$$

Resulting in streamlined equations:

$$H^2 = \left(\frac{\dot{a}}{a}\right)^2 = \frac{8\pi G}{3}\rho - \frac{kc^2}{a^2}$$

$$\dot{H} + H^2 = \frac{\ddot{a}}{a} = -\frac{4\pi G}{3}\left(\rho + \frac{3p}{c^2}\right)$$

For density parameter comparisons:

$$\rho_c = \frac{3H^2}{8\pi G}$$

Leading to Ω_{tot}:

$$\Omega_{tot} \equiv \frac{\rho}{\rho_c} = \frac{8\pi G\rho}{3H^2}$$

Where Ω_{tot} signifies: $\Omega_{tot} = 1$ implies a flat universe. $\Omega_{tot} < 1$ indicates an open universe. $\Omega_{tot} > 1$ suggests a closed universe. $H \equiv \frac{\dot{a}}{a}$ is the Hubble parameter that refers to how fast the universe is expanding. The quantity $\rho_{\mathrm{c}} = \frac{3\mathrm{H}^2}{8\pi\mathrm{G}}$ is critical density of the universe.

Another vital equation is the continuity equation obtained from the conservation of energy-momentum ($\nabla_\mu T^{\mu\nu} = 0$) reads the follows

$$\dot{\rho} + 3\mathrm{H}(\rho + \mathrm{p}) = 0$$

The equation of state(EoS) is an entity that relates the density of the fluid to the pressure of that fluid; let's say for any fluid, EoS is w, then

$$p = w\rho$$

using this relation solution of the continuity equation and Friedman equation becomes as :

$$a(t) = \begin{cases} t^{\frac{2}{3(w+1)}}, & w \neq -1 \\ \exp(H_0 t), & w = -1 \end{cases} \tag{1.3}$$

Describing how the universe's size changes over time, and:

$$\rho(a) \propto \begin{cases} a^{-3(w+1)}, & w \neq -1 \\ constant., & w = -1 \end{cases} \tag{1.4}$$

Demonstrating how mass density evolves with the universe's expansion, showcasing the influence of different components(or EoS). Let's briefly show the solutions for the main components of the universe.

- **Radiation** For radiation the the equation of state is $w = \frac{1}{3}$, so its relations 1.3 ,1.4 becomes as $a \propto \sqrt{t}$ and $\rho \propto \frac{1}{a^4}$, It should be noted that the radiation density in the early universe includes photons as well as relativistic neutrinos. Its density scales as a^{-4} because the volume of the universe scales as a^{-3} as the universe expands, and its wavelength also stretches as $1/a$.
- **Matter** Matter mainly comprises the universe's baryons and cold dark matter. The equation of state of matter component is $w = 0$. So relations 1.3 ,1.4 reduces to $a \propto t^{\frac{2}{3}}$ and $\rho \propto \frac{1}{a^3}$.
- **Dark Energy** For dark energy, in a cosmological constant (vacuum energy) scenario, EoS is $w = -1$, Dark energy has a constant density and $a \propto \exp(H_0 t)$, e.g., the universe goes through exponential expansion. However, any fluid with EoS $w < -\frac{1}{3}$ can be a candidate for dark energy. In that case, the relations 1.3 and 1.4 holds as it is.

The Friedmann equations and associated parameters offer a robust framework for comprehending the universe's evolution and destiny. Rooted in Einstein's general relativity, they provide crucial insights into cosmic behavior, from expansion to composition and ultimate fate.

Horizons and Distances in Cosmology

This section will define some length scales and distances. These distances are commonly used in cosmology and are also relevant to our discussions. The scale factor

'a' indicates how much the universe has expanded. To simplify our discussions, we introduce the redshift parameter z, defined as:

$$\frac{a}{a_0} = \frac{1}{1+z}$$

At present time, z = 0, and at the beginning, z $\to \infty$. The redshift is a measure of how light from a source at redshift z gets stretched by the universe's expansion. It relates the observed (λ) and emitted (λ_0) wavelengths as:

$$z = \frac{\lambda - \lambda_0}{\lambda_0}$$

Next, we introduce the comoving distance χ:

$$\chi = \int c\frac{dt'}{a(t')}$$

This quantity remains constant despite the universe's expansion. The maximum distance that a photon could have traveled from the beginning to time 't', is also known as the particle horizon. Anything beyond this horizon cannot affect us today. It's defined as:

$$\chi_H = \int_0^{t_0} \frac{dt'}{a(t')}$$

This is simply the comoving time multiplied by the speed of light. The distance traveled by tightly coupled photons and baryons before decoupling is defined as the sound horizon, as follows:

$$\mathrm{r_s(t)} = \int_0^{\mathrm{t_{dec}}} \frac{\mathrm{c_s(t')dt'}}{\mathrm{a(t')}}$$

The photon baryon plasma fluid's sound speed is defined here as $\mathrm{c_s} = \frac{1}{\sqrt{3(1+\mathrm{R})}}$ in units of the speed of light, where $\mathrm{R} = \frac{\mathrm{p_b}+\rho_\mathrm{b}}{\mathrm{p}_\gamma+\rho_\gamma}$. The angular diameter distance is the distance photons traveled to us since decoupling:

$$\mathrm{d_A} = \int_{\mathrm{t_{dec}}}^{\mathrm{t_0}} \frac{\mathrm{cdt'}}{\mathrm{a(t')}}$$

The luminosity distance is crucial for measuring distances using the intrinsic brightness of objects. It's calculated from the luminosity (L) and observed flux (F) as:

$$\mathrm{d_L} = \sqrt{\frac{\mathrm{L}}{4\pi\mathrm{F}}}$$

For objects with known intrinsic brightness, like cepheids and supernovas, this helps measure large distances and the universe's expansion rate. It relates to the angular diameter distance through redshift as:

$$\mathrm{d_L} = (1+\mathrm{z})^2\mathrm{d_A}$$

.

1.2 Overview of the thermal history of the Universe

The Universe has evolved over billions of years and went through important epochs and events. This summary offers an informative glimpse into the significant events that have shaped the cosmos into its current form. We outline the corresponding temperatures, timeframes, and redshifts.

- **Baryogenesis, Electroweak, and QCD Phase Transition**: Early on, baryogenesis led to excess matter over antimatter in the Universe Riotto (1998); Sakharov (1967); Trodden (1999). Although various models exist, none are experimentally confirmed. It likely occurred before the electroweak phase transition Higgs (1964); Englert and Brout (1964); Guralnik *et al.* (1964), around $T \geq 125$ GeV ($z \approx 10^{15}$), when the Higgs field gained a non-vanishing value, resulting in breaking electroweak symmetry and imparting

mass to particles at about 10^{-11} seconds old. At roughly $T \approx 100$ MeV ($z \approx 10^{12}$), the QCD phase transition occurred Gross and Wilczek (1973), forming hadrons and mesons, reducing system complexity. This event unfolded around 10^{-5} seconds after the Big Bang.

- **Neutrino Decoupling**: Neutrinos weakly interacted with the surrounding plasma. However, at around $T \approx 1$ MeV (or $z \approx 5 \times 10^9$), the interaction rate of neutrinos fell below the universe's expansion rate, causing neutrinos to decouple from the remaining plasma Mangano *et al.* (2005); Hannestad and Madsen (1995). Further details will be discussed in section 1.3.

- **Electron-Positron Annihilation**: At high enough temperatures,electron-positron annihilation or pair-production process ($e^+ + e^- \rightarrow \gamma\gamma$) were active. Just after neutrino decoupled, the Universe's temperature dropped below the rest mass of electrons, approximately $T \approx 0.5$ MeV (or $z \approx 3 \times 10^9$), photons did not have enough energy to produce the electron-positron pair, which could only occur in the forward direction. So, the entropy of positrons and electrons was deposited to photons, resulting in the heating of photons. More details will be covered in section 1.3.

- **Big Bang Nucleosynthesis (BBN)**: When the age of the Universe was just about 3 minutes, the temperature of approximately $T \approx 100$ keV (or $z \approx 4 \times 10^8$), neutrons and protons fused to form light atomic nuclei. This is known as Big Bang Nucleosynthesis (BBN) Tytler *et al.* (2000); Fields and Sarkar (2006).

- **Matter-Radiation Equality**: The energy density of radiation in the Universe redshifted more rapidly than the energy density of matter. Eventually, both densities became equal, marking the era of matter-radiation equality. This event occurred at a redshift of $z_{\rm eq} \approx 3400$ and a temperature of approximately $T \approx 0.75$ eV, and the age of the Universe was approximately 60,000 years.

- **Recombination, Photon Decoupling, and Drag Epoch**: As the universe cools down further, photons in plasma don't have a threshold to ionize the neutral hydrogen. At this epoch, electrons and protons recombine to form neutral hydrogen. This recombination happens around a temperature of roughly $T \approx 0.3$ eV (or $z \approx 1100$). Subsequently, at a temperature of about $T \approx 0.25$ eV (or $z_{\text{dec}} \approx 1090$), the scattering rate of photons and free electrons ($e^- + \gamma \rightarrow e^- + \gamma$) became less than the rate of the expansion of the universe, the photons decouple from the remaining plasma and move freely. These photons were detected in the form of the "Cosmic Microwave Background"Penzias and Wilson (1965). After photons had decoupled, due to the small baryon ratio compared to photons, baryons feel drag due to photons. The temperature at the drag epoch was around $T \approx 0.20$ eV (or $z_{\text{drag}} \approx 1060$) when the Universe was roughly 400,000 years old.

- **Dark Ages and Cosmic Dawn**: From the time of the CMB epoch to the formation of the first luminous structures (first galaxies, first stars) in the universe, the Universe remained transparent to radiation, constituting a phase known as the "dark ages"Miralda-Escude (2003); Natarajan and Yoshida (2014). This term is used because no luminous structures existed during this period. The emergence of the first stars and first galaxies heralded the era known as the cosmic dawn.

- **Reionization**: Following the formation of the initial luminous structures (such as the first galaxies and first stars) in the Universe, photons from these structures began ionizing the intergalactic medium's neutral hydrogen again. This event is termed reionization Barkana and Loeb (2001); Zaroubi (2013). Reionization began when the Universe's temperature was roughly 5 meV ($z \approx 15$), and the Universe's age was approximately 200 million years.

- **Matter-Dark Energy Equality**: As the matter-energy density diminished over time, there came an epoch where it equaled the dark energy density of the Universe. This occurred at a redshift of $z_\Lambda \approx 0.3$ ($T \approx 0.75$ eV) when

the Universe was about 9 billion years old. After this, the Universe has dark energy domination.

- **Today**: Presently, the Universe's temperature is roughly $T \approx 0.24$ meV, with a redshift of $z = 0.0$". The current Universe is dominated by dark energy (nearly 70%), and matter is the second most dominant component. It is expanding at an accelerating rate.

1.3 Neutrino thermal history

In the earlier epochs in the Universe, the temperature was so high that the neutrinos were in thermal equilibrium through weak interaction with plasma. Following the fermi-dirac distribution

$$f(E, T_\nu) = \frac{1}{\exp(E/T_\nu) + 1}$$

during this time, the neutrinos also maintain the same temperature as the rest of Plasma $T_\nu = T_\gamma = T$. The number density of neutrinos is given as

$$n_\nu = \frac{g}{(2\pi)^3} \int f(E, T_\nu) d^3p$$

Similarly, the energy density of neutrinos

$$\rho_\nu = \frac{g}{(2\pi)^3} \int E f(E, T_\nu) d^3p$$

The weak interaction rate of the neutrinos is given as $\Gamma_\nu \sim G_F T^5$, and The rate of expansion of the cosmos during the radiation-dominated epoch is $H(T) \sim \sqrt{g_*} \frac{T^2}{m_{pl}}$ with g_* being the relativistic degrees of freedom and m_{pl} being Planck mass. The

Universe cools as it expands, and the interaction rate of neutrinos with surrounding plasma decreases. The neutrinos decouple from the surrounding plasma as the interaction rate falls below the universe's expansion rate. Just after the neutrino decoupled, the positrons-electrons turn non-relativistic and annihilate into photons (the reverse process stops); they deposit their entropy into photons through this process. As a result, photons heated up. However, most neutrinos already decoupled by this time, So they appeared colder than the photon temperature.

The entropy density $s = \frac{\rho+P}{T}$. For coupled electron-positron and photon fluid, its $s_{e^{\pm},\gamma} = \frac{2\pi^2}{45} T^3 g_s(T)$ scales as a^{-3}. This scaling holds for the total entropy, including all species in equilibrium. This fact can be used to calculate neutrino background temperature using electron-positron annihilation. The ratio of neutrino temperature to photon temperature is given by

$$\frac{T_\nu}{T_\gamma} = \left(\frac{4}{11}\right)^{\frac{1}{3}}$$

Now we can calculate the total number density of neutrinos per species is

$$\mathrm{n}_\nu = \left(\frac{3}{4}\right)\left(\frac{4}{11}\right)\mathrm{n}_\gamma$$

The factor $\frac{3}{4}$ is derived from the difference in statistics between Bose-Einstein and Fermi-Dirac. The relativistic neutrinos' energy density per species is determined by

$$\rho_\nu = \left(\frac{7}{8}\right)\left(\frac{4}{11}\right)^{\frac{4}{3}}\rho_\gamma$$

where ρ_γ energy density of photons. Again, the factor $\frac{7}{8}$ comes from the fact that neutrinos are fermions while photons are bosons.

The contribution of neutrinos to overall radiation density can be described using a quantity known as the effective number of relic neutrinos, $\mathrm{N_{eff}}$, using the following

equation:

$$\rho_{\rm R} = [1 + \left(\frac{7}{8}\right)\left(\frac{4}{11}\right)^{\frac{4}{3}} {\rm N_{eff}}]\rho_\gamma$$

This relation is valid as long as all the neutrinos are relativistic ($m_\nu \ll T_{\nu,0}$). If neutrinos are non-relativistic ($m_\nu \gg T_{\nu,0}$) their energy density is given as $\rho_\nu = m_\nu n_\nu$, this relation reduces to

$$\Omega_\nu h^2 = \frac{m_\nu}{93.14{\rm eV}}$$

Even after neutrinos have turned non-relativistic, they still free-stream with very high velocity. When the mass of neutrinos $m_\nu =< p >$, the neutrinos turn non-relativistic, also knowing that $< p >= 3.15 T_\nu(z) = 3.15 \left(\frac{4}{11}\right)^{4/3} T_\gamma(1+z)$, we get the desired redshift as a function of neutrino mass

$$1 + z_{nr} \simeq 1900 \frac{m_\nu}{eV}$$

The average free streaming velocity of neutrinos is given as

$$< v_{\rm fs} >= 158(1+z)\frac{\rm eV}{m_\nu}\,{\rm km/s}$$

let's say for a standard neutrino of mass $m_\nu = 0.1$eV, the average velocity at present is order of 10^3km/s. Whereas the velocity dispersion of the MilkyWay-like galaxies is the order of 10^2km/s. That's why we can say that standard neutrinos are not the ideal candidate for galactic dark matter. We can associate a free streaming length with such velocity that is given as

$$\lambda_{\rm fs}(z) = a\frac{2\pi}{k_{\rm fs}(z)} = 2\pi\sqrt{\frac{2}{3}}\frac{v_s(z)}{H(z)}$$

where $k_{\rm fs}$ is comoving free streaming scale. This characteristic length scale is significant while discussing the impact of neutrinos in structure formation. This will specify the length scale below this, which will be affected by neutrino-free

streaming (opposing to the clustering of matter); however, the scale larger than this will not be affected (neutrinos will cluster the same as the Cold dark matter). For more details, please see Wong (2011); Lesgourgues and Pastor (2006).

1.4 Neutrino flavors and their oscillations

Nowadays, we have strong proof that flavor neutrinos change their type Pontecorvo (1957a, 1967). This comes from experiments with different kinds of neutrinos from the sun Orebi Gann (2015); Davis *et al.* (1968), atmosphere Kajita (2012, 2016), reactors Adams *et al.* (2013), and accelerators. This discovery is important because it means neutrinos have some weight, leading to new physics ideas. Many well-respected reviews explain these changes in neutrinos and why they're essential. The unitary mixing matrix describes the connection between different types of neutrinos and those with known weights. It has three angles and one phase important for understanding this phenomenon.

If we represent mass eigenstates as ν_k (where $k = 1, 2, 3$), and flavor states as ν_α (where $\alpha = e, \nu, \mu$), their mixing can be shown as:

$$\nu_k = \sum U_{\alpha k} \nu_\alpha$$

where Unitary matrix $U_{\alpha k}$ is known as Pontecorvo–Maki–Nakagawa–Sakata matrix Pontecorvo (1957b); Maki *et al.* (1962). This is given as

$$\begin{pmatrix} c_{13}c_{12} & s_{12}c_{13} & s_{13}e^{-i\delta_p} \\ -s_{12}c_{23} - s_{23}c_{12}s_{13}e^{i\delta_P} & c_{12}c_{23} - s_{12}s_{23}s_{13}e^{i\delta_p} & s_{23}c_{13} \\ s_{12}s_{23} - c_{12}c_{23}s_{13}e^{i\delta_p} & -c_{12}s_{23} - s_{12}c_{23}s_{13}e^{i\delta_p} & c_{13}c_{23} \end{pmatrix}.$$

Here,$ij = 12, 23$ or 13,$s_{ij} = \sin\theta_{ij}$ and $c_{ij} = \cos\theta_{ij}$ also δ_p represents a phase.

The evolution of massive neutrino states over time follows the behavior of plane waves:

$$|\nu_k(t)\rangle = e^{-iE_k t + ip_k x} |\nu_k\rangle$$

This translates into:

$$|\nu_\alpha(t)\rangle = \sum \left(\sum U^*_{\alpha k} e^{-iE_k t + ip_k x} U_{\beta k} \right) |\nu_\beta\rangle$$

The transition amplitude from $\alpha \longrightarrow \beta$ flavor can be expressed as:

$$A_{\nu_\alpha \longrightarrow \nu_\beta (L,T)} = \langle \nu_\beta | \nu_\alpha(t) \rangle = \sum_k U^*_{\alpha k} U_{\beta k} e^{-iE_k T + ip_k L}$$

The transition probability is the square of the amplitude de Gouvea (2004):

$$P_{\nu_\alpha - \nu_\beta}(L,T) = |\, \langle \nu_\beta | \nu_\alpha(t) \rangle \,|^2 = |\sum_k U^*_{\alpha k} U_{\beta k} e^{-i\frac{m_k^2}{2E}L}|^2$$

Alternatively:

$$P_{\nu_\alpha - \nu_\beta}(L,T) = \sum_k |U^*_{\alpha k}|^2 |U_{\beta k}|^2 + 2Re \sum_{k,j} U^*_{\alpha k} U_{\beta j} U_{\alpha k} U^*_{\beta j} e^{-i\frac{\Delta m^2_{jk} L}{2E}}$$

The phase of oscillations depends on the ratio $\frac{L}{E}$, where L is the distance from

source-to-detector and E is the neutrino energy. Within the Standard Model, the probability remains Lorentz invariant, indicating that the ratio $\frac{L}{E}$ is also Lorentz invariant. This has prompted experiments like the ICE Cube experiment to investigate potential violations of Lorentz symmetry in neutrino oscillations.

Oscillation experiments can't determine the absolute neutrino masses. However, they can measure the differences in mass, denoted as $\Delta m^2_{21} > 0$ and $|\Delta m^2_{31}|$. These differences lead to two possible hierarchies determined by the sign of Δm^2_{31}. For Normal Hierarchy (NH) $\Delta m^2_{31} > 0$ e.g. $(\mathrm{m}_1 < \mathrm{m}_2 \ll \mathrm{m}_3)$ and for Inverted Hierarchy (IH) $\Delta m^2_{31} < 0$ e.g. $(\mathrm{m}_3 \ll \mathrm{m}_1 < \mathrm{m}_2)$. When the lightest neutrino mass, say m_l (i.e., m_1 for NH, m_3 for IH), is small, the mass states have a hierarchical structure. For masses significantly greater than the difference between neutrinos, all neutrinos effectively have the same mass, resulting in a degenerate scenario.

Recent results from global fits to neutrino oscillation experiments yield the following mass differences Esteban *et al.* (2020) (1σ confidence limits).

$$\Delta \mathrm{m}^2_{21} \equiv \mathrm{m}^2_2 - \mathrm{m}^2_1 = 7.42^{+0.21}_{-0.20} \times 10^{-5}\mathrm{eV}$$

$$\Delta \mathrm{m}^2_{31} \equiv \mathrm{m}^2_3 - \mathrm{m}^2_1 = 2.517^{+0.026}_{-0.028} \times 10^{-3}\mathrm{eV} \quad \textbf{(NH)}$$

$$\Delta \mathrm{m}^2_{32} \equiv \mathrm{m}^2_3 - \mathrm{m}^2_2 = -2.498^{+0.028}_{-0.025} \times 10^{-3}\mathrm{eV} \quad \textbf{(IH)}$$

The specific relationship between each neutrino mass and the sum of neutrino masses can be calculated numerically. if the sum of neutrino mass ($\sum \mathrm{m}_\nu = \mathrm{m}_1 + \mathrm{m}_2 + \mathrm{m}_3$), is given by For Normal Hierarchy (NH)

$$\sum \mathrm{m}_\nu = \mathrm{m}_\mathrm{l} + \sqrt{\mathrm{m}^2_\mathrm{l} + \Delta \mathrm{m}^2_{21}} + \sqrt{\mathrm{m}^2_\mathrm{l} + \Delta \mathrm{m}^2_{31}}$$

For Inverse Hierarchy (IH)

$$\sum \mathrm{m}_\nu = \mathrm{m}_\mathrm{l} + \sqrt{\mathrm{m}_\mathrm{l}^2 - \Delta\mathrm{m}_{32}^2} + \sqrt{\mathrm{m}_\mathrm{l}^2 - \Delta\mathrm{m}_{32}^2 - \Delta\mathrm{m}_{21}^2}$$

To get the minimum possible total mass of neutrinos ($\sum m_\nu$), we put the lightest mass of neutrinos to be zero. However, the upper bound on neutrino mass can not be set by oscillation experiments. Through cosmological inferences 1.7, we get the upper bound on neutrino mass.

1.5 Cosmological Observations

1.5.1 Cosmic Microwave Background (CMB)

In the early epochs, the universe was hotter and denser. It's been cooling as it expands, a process called adiabatic cooling. The universe was mainly ionized during this time, with photons and baryons (protons and electrons) tightly coupled through electromagnetic interactions.

The photons are in equilibrium through the process $e^- + p^+ \rightarrow H + \gamma$. As the universe cools down further, photons in plasma don't have a threshold to ionize the neutral hydrogen. At this epoch, electrons and protons recombine to form neutral hydrogen. This recombination happens around a temperature of roughly $T \approx 0.3$ eV (or $z \approx 1100$).

Subsequently, as the electron density decreased, the scattering rate of photons and free electrons ($e^- + \gamma \rightarrow e^- + \gamma$) became less than the universe's expansion rate, and the photons decoupled from the surrounding plasma. After photons

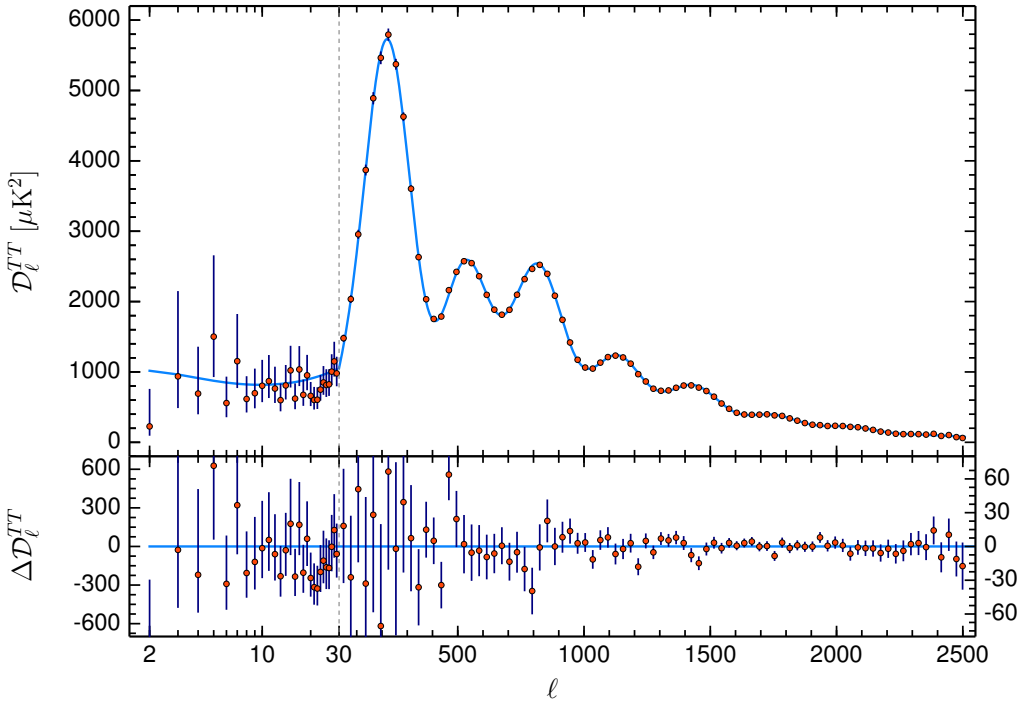

FIGURE 1.1: The CMB temperature anisotropy spectrum from Planck 2018. Here y-axis is $D_l^{TT} == \frac{l(l+1)C_l}{2\pi}$ and the x-axis is angular scale 'l'. The Upper panel comprises the vanilla λCDM (light blue) theoretical power spectra (Planck-18 best-fit values). In the lower panel, Residuals concerning this model are shown. This figure is taken from Aghanim *et al.* (2020b)

had decoupled, due to the small baryon ratio compared to photons, baryons feel drag due to photons. This is called the drag epoch. After that, the photons travel nearly without interacting with the present epoch. This radiation, at a temperature of 2.728K, was first detected several decades ago by COBESmoot *et al.* (1992), WMAP Kogut *et al.* (2003) and is known as the Cosmic Microwave Background Radiation (CMBR). The CMB is not the same in all directions; it is anisotropic. There are small fluctuations in the temperature across the sky of the order of 10^{-5}.

These fluctuations are mapped onto a spherical surface. It's advantageous to represent them using spherical harmonics Y_ℓ^m (in contrast to Fourier decomposition in flat space). Specifically, for temperature fluctuations, we have:

$$\frac{\delta T}{T}(\theta,\phi) = \sum_{\ell=0}^{\infty}\sum_{m=-\ell}^{\ell} a_{\ell m} Y_{\ell}^{m}(\theta,\phi)$$

Here, θ and ϕ refer to angular measurements in the spherical coordinate system, and $d\Omega$ represents the solid angle. The fluctuation statistics are characterized at the basic level by a two-point correlator:

$$\langle a_{X\ell m} a^{*}_{Y\ell' m'} \rangle = \delta_{\ell\ell'}\delta_{mm'} C_{XY\ell}$$

In this, X and Y represent temperature and the polarizations in E and B modes. It's worth noting that $C_{XY\ell}$ lacks dependence on the index m due to statistical uniformity and isotropy. Figure 1.1 illustrates the temperature power spectra.

1.5.2 Baryon Acoustic Oscillations (BAO)

Before the recombination, electromagnetic interaction tightly coupled photons to electrons and baryons in the plasma. This tightly coupled fluid exhibits oscillation because of attractive gravity force and plasma pressure. These oscillations continue till the time of photon decoupling. The baryons got free from photons after the drag epoch (z_d). The baryon acoustic oscillations (BAO) provide a characteristic scale that can act as a standard ruler. These oscillations can be observed in galaxy power spectra or galaxy correlation functions.

This scale can be used to measure the angular diameter distance,

$$d_A(z) = \frac{c}{(1+z)} \int_0^z \frac{1}{H(z')}\, dz'$$

and expansion rate $H(z)$ of the universe using clustering along the line of sight. Adjustments in cosmological parameters can alter the clustering scale of the galaxies, which is related to the sound horizon $r_d = \int_{z_d}^{\infty} c_s(z)/H(z)\, dz$, where c_s is the sound speed of photon baryon plasma and z_d is the redshift of drag epoch. Effectively, BAO measurements actually constrain the combination $r_d \times H(z)$ or $d_A(z)/r_d$.

Another important observable in redshift surveys is $f\sigma_8$, which is defined as a combination of growth rate $f(a)$ and the RMS (root-mean-squared) normalization of the matter power spectra σ_8,

$$f\sigma_8(a) = a\frac{\delta'_m(a)}{\delta_m(1)}\sigma_{8,0}$$

1.5.3 Supernovae Type Ia Data

Supernovae are the brightest objects in the sky. Type 1a supernovas are considered the standard candles. The theoretical model and observations are compared with the measured luminosities. If the apparent magnitude of SNe is m and M is the absolute magnitude of the supernova, then

$$M = m - 5\,\log_{10}\left(\frac{d_L}{10}\right)$$

where $d_L = c\,(1+z)\int_0^z \frac{1}{H(z')}\, dz'$ is their luminosity distance in parsecs. This depends on the model of the Universe through $H(z)$.

1.6 Standard Model of Cosmology

The ΛCDM model is the most successful model to fit the various cosmological observations (including the above) and astrophysical observations to date. As the name suggests, Λ stands for the cosmological constant or the vacuum energy($\mathrm{w_{de}} = -1$), the dominating component, and CDM stands for the Cold Dark Matter is the second most dominant component of the Universe. The main assumptions of this model are as follows: The Generality holds on all scales of the universe. It is the homogeneous and isotropic universe that is expanding and defined by the FLRW metric. The geometry of the universe is flat. A single-field inflation model sets the initial conditions for the perturbations. This model usually consists of 6 baseline parameters as follows.

Physical dark matter density ($\omega_{\mathrm{cdm}} \equiv \Omega_{\mathrm{cdm}}\mathrm{h}^2$), **Physical baryon density** ($\omega_{\mathrm{b}} \equiv \Omega_{\mathrm{b}}\mathrm{h}^2$) **Sound Horizon size** (θ_s) **Amplitude of primordial power spectra** (A_s): **Scalar spectral index or Tilt Parameter** n_s **Optical depth of reionization** τ

In addition to these six parameters, it contains some derived parameters. Like the expansion rate of the universe today H_0, Dark energy density (Ω_{DE}), total matter density (Ω_M) etc. The Vanilla ΛCDM model assumes a flat universe ($\Omega_k = 0$) and does not consider massive neutrinos ($\sum m_\nu$), $\mathrm{N_{eff}}$ (relativistic degree of freedom) is fixed to 3.044 corresponding to 3 massless neutrinos. It can be slight extension of ΛCDM model including few extra variable parameters such as Ω_k $\sum m_\nu$, $\mathrm{N_{eff}}$. The data sets discussed in section 1.5 clearly constrains the six baseline parameters. The value of ΛCDM model parameters using Planck 2018 CMB Measurements Aghanim *et al.* (2020b) are as follows:

$$(100 \times \theta_s = 1.04092 \pm 0.00031, \omega_{cdm} = 0.12 \pm 0.0012, \omega_b = 0.02237 \pm 0.00015)$$

$(\tau = 0.0544 \pm 0.0073, n_s = 0.9649 \pm 0.0042, \ln(10^{10} A_s) = 3.044 \pm 0.014)$.

1.7 Effect of Massive Neutrinos on Cosmological Observations

Three parameters can parameterize the impact of massive neutrinos on linear cosmological observations Acero and Lesgourgues (2009a) as follows:

- $\Delta N_{\rm eff}$: The contribution that it makes to the universe's relativistic energy density, which is parameterized by $\Delta N_{\rm eff}$.

$$\Delta N_{\rm eff} \equiv \frac{\rho_s^{\rm rel}}{\rho_\nu} = \frac{1}{\pi^2}\left[\int dp\ p^3 \hat{f}(p)\right] / \left[\frac{7}{8}\frac{\pi^2}{15} T_\nu^{\rm id\,4}\right] \tag{1.5}$$

  with $T_\nu^{\rm id} \equiv (4/11)^{1/3} T_\gamma$

- $M_s^{\rm eff}$ The contribution that it makes to the universe's current energy density, which is parameterized by

$$\frac{M_s^{eff}}{94.05{\rm eV}} \equiv \omega_s \equiv \Omega_s h^2 = \frac{1}{\pi^2}\left[m_{\rm sp}\int dp\ p^2 \hat{f}(p)\right] \times \left[\frac{h^2}{\rho_c^0}\right] \tag{1.6}$$

- The typical free streaming velocity

$$< V_{fs} >= 5.5 \times 10^{-6} \frac{\Delta N_{\rm eff}}{\omega_s} \tag{1.7}$$

  Out of these three, only two are independent. So from here onwards, we will use $M_s^{\rm eff}$, $N_{\rm eff}$ as phenomenological parameters to study the effect of neutrino-like particles.

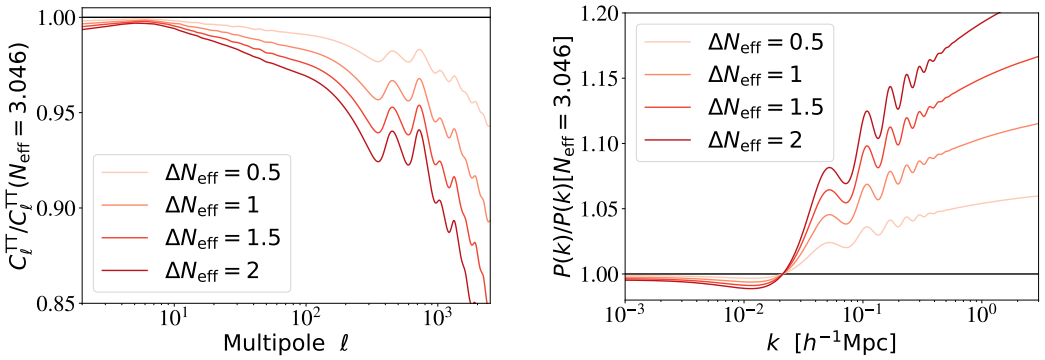

FIGURE 1.2: Left panel: Ratio of CMB TT power spectra for $\Delta N_{eff} = 0.5, 1.0, 1.5, 2.0$ with respect to $N_{eff} = 3.046$. Right panel: Ratio of matter power spectra for $\Delta N_{eff} = 0.5, 1.0, 1.5, 2.0$ with respect to $N_{eff} = 3.046$. Note that these plots are produced using code CLASS for fixed (z_{eq}, z_Λ). In order to fix the equalities, we vary the dark energy and total matter density in the same ratio as the increased radiation density due to an increase in N_{eff}.

1.7.1 Impact of ΔN_{eff} on CMB and matter power spectra

If we fix other density parameters and only increase N_{eff}, the epoch of matter-radiation equality (z_{eq}) delays, i.e., a shorter epoch with faster expansion between decoupling and z_{eq} which leads to a decrease in CMB acoustic peaks. However, this effect is not explained only for N_{eff} as several other parameters can produce it. To see the true effect of Neff, let us fix the matter radiation equality and matter -Λ equality by increasing (Ω_R, Ω_M and Ω_Λ by the same amount). Other parameters like ω_b and τ are kept fixed. The effect of increasing N_{eff} is demonstrated in the left side of figure 1.2, where N_{eff} is increasing from 0.5 to 2; we see there is a decrease in peaks of Cl^{TT} at high 'l' and a slight change in peak location. The main background effect is due to increased silk damping (diffusion damping), and a slight change in the decoupling epoch is a perturbation effect.

The impact of N_{eff} on matter power spectra when we (z_{eq},z_Λ) are kept fixed is demonstrated in the right side of figure 1.2. There is an increase in power at smaller scales, and this is because to fix z_{eq}, a higher N_{eff} means a higher dark matter density (ω_{cdm}), which leads to more clumping of dark matter and hence more power.

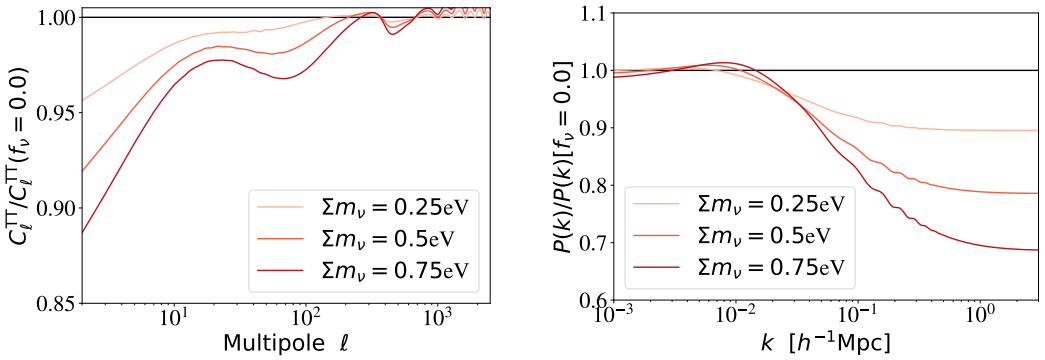

FIGURE 1.3: Left panel: Ratio of CMB TT power spectra for $\sum \mathrm{m}_\nu = 0.25, 0.50, 0.75\,\mathrm{eV}$ with respect to $\sum \mathrm{m}_\nu = 0.0$. Right panel: Ratio of matter power spectra for $\sum \mathrm{m}_\nu = 0.25, 0.50, 0.75\,\mathrm{eV}$ with respect to $\sum \mathrm{m}_\nu = 0.0$. Note that these plots are produced using code CLASS for fixed $(\omega_b, \omega_c, \tau)$.

1.7.2 Impact of $\mathrm{M}_\mathrm{s}^\mathrm{eff}$ on CMB and matter power spectra

The massive neutrino, which is non-relativistic after the photon decoupling epoch (CMB), contributes now to the universe's non-relativistic energy budget i.e., $\omega_\mathrm{M} = \omega_\mathrm{b} + \omega_\mathrm{cdm} + \omega_\nu$. So they can change angular diameter distance to CMB $d_A(z_{rec})$ and may alter matter to Λ equality.The main impact of neutrino mass m_ν on CMB is through the Integrated Sachs-Wolf (ISW) effect. This is demonstrated in the left side of figure 1.3. The effect is milder, and CMB alone cannot determine the m_ν.

The main impact of neutrino mass on matter power spectra arises from their free streaming. Because even if neutrinos become non-relativistic, they have very high-velocity dispersion. Because of this velocity, they can not be clustered and oppose dark matter clustering. All this happens at below-free streaming scales, scales larger than free streaming scales, and these massive neutrino clusters like CDM. If neutrino fraction $f_\nu = \frac{\omega_\nu}{\omega_m}$, the growth of is reduced by a factor (1-2f_ν) due to neutrinos. The back-reaction on CDM is responsible for suppression by a factor of (1-6f_ν) on the growth. So overall, the matter growth is reduced by the factor of (1-8f_ν). This is demonstrated in the right side of figure 1.3. The fact that matter growth is suppressed by neutrinos at small scales is used to determine their mass

from large-scale structures.

1.8 Current Cosmological Tensions

The standard model of the universe has been the most successful model to describe all cosmological observations, yet a few discrepancies exist. These mismatches, also called tensions (or anomalies), are mainly in parameters predicted from CMB using ΛCDM and its direct measurement using astrophysical observations (independent from cosmological models). Two of the most discussed anomalies are in determining the Hubble parameter and the growth of structures.

1.8.1 Hubble Tension

The Cosmic Microwave Background (CMB) doesn't directly provide the universe's current expansion rate. Instead, it precisely measures the angular size of the sound horizon during recombination. This angular sound horizon size, denoted as θ_s, is determined by the ratio of the size of the sound horizon at recombination ($\mathrm{r_s(z*)} = \int_{\mathrm{z*}}^{\infty} \frac{\mathrm{c_s dz}}{\mathrm{H(z)}}$) and the comoving angular diameter distance from recombination ($\mathrm{D_A(z*)} = \int_{\mathrm{z*}}^{\infty} \frac{\mathrm{cdz}}{\mathrm{H(z)}}$). In simple terms, $\theta_\mathrm{s} = \frac{\mathrm{r_s(z*)}}{\mathrm{D_A(z*)}}$. These parameters are defined in the ΛCDM model and depend explicitly on certain parameters like (ω_b, ω_cdm, $\mathrm{c_s}$, ω_r), which can be determined by studying their effects on CMB power spectra. The angular diameter distance relies on the universe's current expansion rate, allowing us to deduce H_0 from the CMB. The latest measurements from Planck for the CMB yield a Hubble parameter value of $\mathrm{H_0} = 67.36 \pm 0.54 \mathrm{km/s/Mpc}$ using the ΛCDM model. Additionally, early-time data, such as BBN and BAO data, align with this lower value inferred from the CMB. Conversely, H_0 can also be determined from direct observations of the brightest celestial objects like cepheids

and type1a supernovae. These objects have a known intrinsic luminosity and are known as standard candles. By using spectroscopy and the Doppler effect, we can measure their velocity. We can determine their distance through the distance ladder method, considering them as standard candles and the fact that their observed brightness will depend on distance. After establishing a relation between redshift and distance, we can infer the H_0. Using this approach, the SH0ES (Supernovae H0 for the equation of state) group determined a Hubble parameter value of $\mathrm{H_0} = 73.2 \pm 1.3\mathrm{km/s/Mpc}$. Some other direct/local determinations also align with this higher value of the Hubble parameter. More discussion and references to this tension are made in the concerned chapters.

1.8.2 S8 tension

Likewise, there is a relatively milder discrepancy in the determination of local growth interpreted by σ_8 as

$$\sigma_8^2 = \frac{1}{2\pi^2} \int \mathrm{W}^2_{8\,\mathrm{Mpc/h}} \mathrm{P(k)k^2dk}$$

If the total matter budget of the Universe is Ω_M then generally the referred parameter is S_8 instead σ_8 defined as: $S_8 = \sigma_8 \sqrt{\frac{\Omega_M}{0.3}}$ The Cosmic Microwave Background observations by Planck 2018 considering the ΛCDM universe gives the value of this parameter to be $S_8 = 0.832 \pm 0.013$ Aghanim *et al.* (2020b). Other ways to determine the concerned parameter include cluster abundance and weak lensing. The weak gravitational lensing observations of galaxies by the CFHTLenS collaboration reveal that the ΛCDM model anticipates a S_8 value exceeding the direct measurement at a 2σ confidence level. This discrepancy has garnered more attention with diverse datasets, such as the KiDS/Viking data Heymans *et al.* (2020) and DES data. Recently, the amalgamation of SDSS and KiDS/Viking

data has established a 3σ tension, indicating $S_8 = 0.766^{+0.02}_{-0.014}$. More discussion and references to this tension are made in the concerned chapters.

1.9 Outlines

In the Introduction chapter, we have presented the fundamental cosmology and neutrino physics concepts. Chapter 2 discusses the methodology used in the thesis to obtain the results, mainly the Bayesian technique for parameter estimation from linear cosmological observations and Nbody simulation for obtaining constraints from nonlinear scales. The following five chapters are the main research works. Each chapter contains its introduction, methodology, results, and conclusion sections. In the last chapter, we summarize the findings of the thesis. There is also essential material in the appendix, sometimes referred to in the main text.

Chapter 2

Numerical and statistical methods

2.1 Bayesian Inference

2.1.1 Notion about probability

Probabilities are intrinsically linked to event frequencies, constituting the basis of Frequentist statistics.

$$P = \frac{n}{N}$$

Here, 'n' signifies successful outcomes, while 'N' represents the overall count of trials.

However, Bayesian statistics expands the concept of probability to encompass degrees of confidence in a statement. In Bayesian statistics, probabilities fundamentally capture the extent of our knowledge concerning an event. Some references in this regards Trotta (2008); Verde (2007); Heavens (2009).

Several foundational probability principles exist, a few of which are outlined below. Consider 'x' as a random variable associated with a specific event, with its corresponding probability distribution denoted as $P(x)$.

$$P(x) \geq 0$$

This criterion underscores that an event's probability is consistently equal to or greater than zero.

$$\int_a^b P(x)dx = 1$$

This requirement is known as the normalization condition, indicating that the integral of the probability distribution over a defined range [a, b] equals unity.

Combined probability of two events

$$P(x_1 \cup x_2) = P(x_1) + P(x_2) - P(x_1 \cap x_2)$$

for two events which do not depend on each other$P(x_1 \cap x_2) = 0$

$$P(x_1 \cup x_2) = P(x_1) + P(x_2)$$

If an event occurs(x_1), assuming the happening of another event (x_2), then the probability of both x_1 and x_2 occurring is equivalent to the probability of x_1

multiplied by the probability of x_2 given that x_1 has already taken place.

$$P(x_1 \cap x_2) = P(x_1)P(x_1|x_2)$$

2.1.1.1 Bayes theorem

we now know,

$$P(x_1 \cap x_2) = P(x_2 \cap x_1)$$

we can deduce that

$$P(x_2|x_1) = \frac{P(x_1|x_2)P(x_2)}{P(x_1)}$$

Data and models exist in the same domain within Bayesian analysis, erasing any formal distinction between measured quantities and parameters. For a given model, M, consider x_1 as a set of data and x_2 as a set of parameters, then we have:

$$P(\theta|d, M) = \frac{P(d|\theta, M)P(\theta|M)}{P(d|M)}$$

This equation is recognized as Bayes' theorem. On the left-hand side, the quantity is referred to as the posterior probability for parameter θ. On the right-hand side, $P(d|\theta) = L(\theta)$ represents the likelihood, while $P(\theta)$ signifies the prior probability distribution. The component below $P(d)$ is a normalization factor.

Interpretation: Bayes' theorem establishes a connection between the posterior probability of θ (indicating our updated knowledge about the parameter after observing the data) and the likelihood, alongside the prior (depicting what we understood about the parameter before encountering the data). Essentially, it serves as a broad principle to transition our understanding of a quantity (in this

case, θ) from its prior state to the subsequent posterior state.

2.1.2 Posterior Likelihoods and Priors

The likelihood pertains to the probability of the event or data provided a specified value of some parameters. It gauges how well a statistical model conforms to a dataset using particular parameter values.

As fresh data becomes available, bayesian inference operates by progressively refining our understanding of a parameter (or hypothesis). The posterior derived from a previous round of observations is adopted as the prior for subsequent iterations. This process does demand an initiation point, which necessitates specifying an initial prior—this initial prior is not prescribed by the theory itself but must be provided by the user. This prior should accurately reflect the user's knowledge about the quantity of interest. The posterior probability distribution will ultimately converge to a distinct (objective) outcome, even if disparate researchers begin with different priors. A conventional (though not without implications) option involves adopting a uniform prior (also termed a "flat prior") for θ.

2.1.3 Monte Carlo Methods

The MCMC technique is a methodology used to ascertain the posterior distribution of the parameter we are interested in. Specifically, this algorithm employs Monte Carlo simulations by leveraging the Markov property and then selectively accepts these simulations at a designated rate to derive the posterior distribution. MCMC comprises three key components: Monte-Carlo simulations, Markov chains, and Acceptance-Rejection sampling.

Monte Carlo simulations are employed to model intricate systems by generating random numbers.

Markov chains essentially embody the dynamic transition of a random variable between different states over time. The Markov property governs these chains. A sequence $S_1, S_2, \ldots$ of elements from a particular set constitutes a Markov Chain when the probability of S_{n+1} given $S_1, S_2, \ldots, S_n$ relies solely on S_n, not on the previous elements such as S_{n-1}, S_{n-2}, etc. A Markov Chain represents a chain or sequence where subsequent steps can be computed exclusively from the current state. A noteworthy characteristic of a Markov Chain is its tendency to converge to a stationary state where successive chain members serve as samples from the target distribution. This convergence occurs towards the posterior $P(\theta|d, M)$. This phenomenon allows us to estimate various standard parameters (mean, variance, etc.) from this distribution.

The target density is estimated through an assembly of the Dirac-delta function:

$$p(X|d, M) \simeq \frac{1}{N} \sum_{N=1}^{N} \delta(X - X_i)$$

Here, 'N' denotes the number of points per chain. Consequently, the mean of the posterior is calculated as:

$$< X >= \int X \, dX P(X|d, M) \simeq \frac{1}{N} \sum_{N=1}^{N} X_i$$

The approximate equality, denoted by $\simeq$, is valid due to the intrinsic nature of the samples X_i, which are inherently drawn from the posterior distribution.

Furthermore, any integral estimations encompassing quantities like mean, variance, etc., can be calculated as follows:

$$< f(X) > \simeq \frac{1}{N} \sum_{N=1}^{N} f(X_i)$$

2.1.3.1 Metropolis-Hastings algorithm

Generating a fresh point X_{i+1} from the current point X_i is an essential aspect of the Markov Chain process. However, as anticipated, establishing criteria becomes imperative for determining the acceptance or rejection of this new point based on its suitability within our model. Even when this new step represents a less favorable outcome than the previous one, it might still be deemed acceptable. This approach acknowledges that confining acceptance solely to steps with higher probabilities might lead to convergence towards a local maximum in the parameter space, thus missing out on comprehensively mapping the entirety of the space. The Metropolis-Hastings algorithm Metropolis *et al.* (2004); Hastings (1970) encapsulates these considerations within its methodology and is recognized as the simplest algorithm of this kind.

Within the Metropolis-Hastings algorithm, the journey commences with a randomly chosen starting point X_i associated with a posterior probability p_i. The subsequent step entails the proposition of a candidate X_n, which is drawn from a proposal distribution $q(X_i, X_n)$. This distribution serves as a generator for new random steps, capturing the inherent randomness of the Markov Chain process while navigating the parameter space. Then, the acceptance probability of the new candidate is given by

$$p(acceptance) = min[1, \frac{p_n q(X_c, X_i)}{p_i q(X_i, X_n)}]$$

complete algorithm steps are as follows

a. Randomly select a starting condition X_i within the parameter space, and then calculate the posterior distribution.

b. Create a new point by sampling from a given range within the parameter space and subsequently determine the posterior distribution associated with this point.

c. if $p(X_n) > p(X_i)$ then definitely accept the point. d.if$p(X_n) < (X_i)$ then let $\alpha = \frac{p(X_n)}{p(X_i)}$ and generate a number u in [0,1]. if $\alpha > u$ accept the point X_n if $\alpha < u$ return to previous point

e. Repeat steps (b) to (d) until the chain has large enough points.

2.1.3.2 Criteria of Convergence

Evidently, a criterion is imperative to ascertain the convergence of our chains. We must ascertain that the points within the chain do not gravitate towards a local maxima or a false convergent point. In this regard, our algorithm necessitates an inherent capacity to address this potential challenge.

One straightforward approach to gauge whether our chain is converging towards a global extremum (or not!) is by initiating multiple chains, each commencing with diverse initial parameter proposals of interest. This method, while informal, offers a practical way to assess convergence and mitigate the risk of being trapped in local maxima.

Gelman Rubin convergence: Consider M chains starting from substantially distinct starting points, each chain with N points. If X_i^m denotes a point within the parameter space corresponding to position 'i' and belongs to chain 'j,' the following calculations are required:

Calculate the mean of each chain:

$$< \mu_m >= \frac{1}{N} \sum_{i=1}^{N} X_i^m$$

Determine the mean of all chains (average of means corresponding to each chain):

$$< \mu >= \frac{1}{NM} \sum_{i=1}^{N} \sum_{j=1}^{M} \mu_i^m$$

Compute the average variance for each chain:

$$W = \frac{1}{M(N-1)} \sum_{i=1}^{N} \sum_{j=1}^{M} (X_i^m - \mu_m)^2$$

Calculate the chain-to-chain variance 'B':

$$B = \frac{1}{M-1} \sum_{i=1}^{M} (\mu_m - \mu)^2$$

When our chains converge, the values of W and B/N should align. In fact, convergence is deemed to have occurred when the following quantity approaches unity:

$$R = \frac{\frac{N-1}{N} W + \frac{M+1}{M} B}{W}$$

A common convergence criterion is met when $|R - 1| < 0.03$, indicating that the ratio of the two estimates is within this range Gell-Mann *et al.* (1979).

2.2 Nonlinear Simulations

When the distribution of particles in the Universe is uniform, or deviations from uniformity are very small, the linear approximations are valid, and one can solve Boltzmann equations directly. However, when the perturbations start to grow, and density perturbations cross the value $\delta \approx 1$, modes don't grow independently but rather mix. That's why N-body simulations are used to study structure evolution in such scenarios. Usually, in these methods, We divide the initial phase space into small sub-volume elements with a certain mass and treat them as particles. Then, generally integrate the equation of motions. The following sections will discuss various methodologies involved in N-body simulations.

2.2.1 Particle Method

The easiest method to calculate the position and velocity of each particle. One has to integrate the 3N equation of motion. In this method, particles are assumed to have a specific size ϵ (for Plummer softening). The force on j^{th} particle due to i^{th} particle is

$$F_{ij} = Gm^2 \frac{\boldsymbol{x_i} - \boldsymbol{x_j}}{(\epsilon^2 + (\boldsymbol{x_i} - \boldsymbol{x_j})^2)^{3/2}}$$

For total force on N^{th} particle, One must calculate the force for the rest of the N-1 particles. This direct integration approach is flexible and very accurate but has a high computational cost. for N particle calculations are $O(N^2)$.

2.2.1.1 Particle-Mesh algorithms

A PM (Particle-Mesh) code employs a uniformly spaced three-dimensional grid to solve the Poisson equation Klypin and Holtzman (1997); Klypin *et al.* (1999);

Klypin and Shandarin (1983); Hockney and Eastwood (1981). It usually involves three main steps. The first step is the particle density assignments to mesh using an interpolation scheme. The next step is solving the Poisson equation on the mesh and finally interpolating it back to particles.

Density Assignment: In the context of density assignment in Particle Mesh (PM) Codes, particles are assumed to have a certain size, shape, mass, and internal density. There are various schemes of interpolation, such as Triangular Shaped Cloud (TSC), Cloud In Cell (CIC), and Nearest Grid Points (NGP). An appropriate scheme is selected based on the computational efficiency and accuracy balance. Among these options, the CIC scheme has gained prominence and is commonly used in Particle Mesh (PM) codes. Let's briefly explain the CIC interpolation method.

Let's introduce the concept of a one-dimensional particle shape, denoted as $S(x)$, representing the density function in mass at a distance x from the particle within a cell of size Δx (Hockney and Eastwood (1981)). In the CIC scheme, particles are envisioned as cubes in three dimensions, possessing uniform density and a size corresponding to one grid cell.

The mathematical representation of $S(x)$ is given by:

$$S(x) = \frac{1}{\Delta x} \begin{cases} 1 - \frac{x}{\Delta x}, & \text{if } |x| \leq \Delta x \\ 0, & \text{else} \end{cases} \tag{2.1}$$

The shape function averaged over this cell ijk to determine the mass assigned to this cell :

$$W(x_n - x_{ijk}) = \int_{x_{ijk}-\frac{\Delta x}{2}}^{x_{ijk}+\frac{\Delta x}{2}} dx' S(x - x_n)$$

$$W(r_n - r_{ijk}) = W(x_n - x_{ijk}) W(y_n - y_{ijk}) W(z_n - z_{ijk})$$

The density corresponding to cell ijk is then.

$$\rho_{ijk} = \sum_{n=1}^{N_n} m_p W(r_n - r_{ijk})$$

Solving Poisson Equation: Once we have calculated the density of the mesh, we want to solve the Poisson equation to get the potential.

$$\nabla^2 \phi = 4\pi G \rho$$

firstly do FFT of $\rho(i,j,k)$ to get $\rho(\tilde{\boldsymbol{k}})$, Now we multiply the Green functions $G(\tilde{k})$ and harmonics $\rho(\tilde{\boldsymbol{k}})$ to obtain amplitudes of Fourier harmonics of the gravitational potential ϕ:

$$\phi(\tilde{k}) = 4\pi G \boldsymbol{G}(\tilde{\boldsymbol{k}}) \rho(\tilde{\boldsymbol{k}}) \tag{2.2}$$

To obtain the green function, we discretized the Poisson equation,

$$\nabla^2 \phi = \frac{\partial^2 \phi}{\partial x^2} + \frac{\partial^2 \phi}{\partial y^2} + \frac{\partial^2 \phi}{\partial z^2}$$

$$\frac{\partial^2 \phi}{\partial x^2} = \frac{1}{\Delta x^2}[\phi(i+1,j,k) - 2 * \phi(i,j,k) + \phi(i-1,j,k)] = \frac{3}{2a}\Omega_0(\rho(i,j,k) - 1)$$

The green function for this is

$$G(\mathbf{k}) = -\frac{3\Omega_0}{8a}\left[\sin^2\left(\frac{k_x}{2}\right) + \sin^2\left(\frac{k_y}{2}\right) + \sin^2\left(\frac{k_z}{2}\right)\right]^{-1}$$

where $k_x = \frac{2\pi l}{L}$, $k_y = \frac{2\pi m}{L}$, $k_z = \frac{2\pi n}{L}$
for component (l,m,n).

2.2.1.2 Tree Algorithms

The TREE method divides the simulation volume into small cubic cells. The force due to particles at large distances is calculated assuming a group of particles as a single particle of a specific size instead of calculating force from individual particles Bagla (2002); Barnes and Hut (1986); Xu (1995). The TREE codes usually consist of four steps as follows:

Grouping (Octree Algorithm): The simulation volume is subdivided into small cubic cells. If the number of particles within a cell surpasses a specific threshold N_{T}, the cell is partitioned into eight smaller cells. The cell remains unsplit if $N_{\mathrm{particles}} \leq N_{\mathrm{T}}$. Usually, the threshold is set to $\mathrm{N_T} = 1$. The cell with a minimum threshold is called a leaf.

Multipole Expansion Key physical properties, such as the mass (M_i) and center of mass ($\mathbf{X}_i$) of each cell, are stored for efficient force calculations. The multipole expansion involves expressing the gravitational potential (Φ) due to a cell using the Taylor expansion. The monopole term is just the total mass ($\sum_i m_i$), and the dipole term vanishes if the expansion is taken to the center of mass. Then there are higher-order terms like quadrupole, octapole, etc. However, there is no strict rule on which order we should terminate.

Cell Opening Condition If we chose a size 'l' cell located at distance d. The force due to this cell is calculated only if the angle subtended by the cell $\theta \leq \frac{l}{d}$ is less than a certain threshold. The angle is more than the threshold angle, and We go to children's cells to calculate the force. The criteria for cell subdivision are

determined based on the spatial distribution of particles and the desired accuracy. This might involve assessing the mass distribution within a cell relative to its size.

Spiltting Force: The total force ($\mathbf{F}_i$) exerted on each particle (P_i) is divided into two parts. A Particle-Mesh approach is used to determine long-range force, which requires solving Poisson's equation for gravitational potential in Fourier space. The short-range force is estimated using the TREE method through multipole expansion and interactions with nearby cells, often computed via a Taylor expansion or other approximation methods.

$\phi_{\mathrm{k}} = \phi_{\mathrm{k}}^{\mathrm{PM}} + \phi_{\mathrm{k}}^{\mathrm{Tree}}$ where

$$\phi_{\mathrm{k}}^{\mathrm{PM}} = \phi_{\mathrm{k}} \exp\left(-\mathrm{k}^2 \mathrm{r}_{\mathrm{s}}^2\right)$$

$$\phi_{\mathrm{k}}^{\mathrm{Tree}} = \phi_{\mathrm{k}}(1 - \exp\left(-\mathrm{k}^2 \mathrm{r}_{\mathrm{s}}^2\right))$$

r_s is the scale to determine the force split. It is usually a few times larger than the PM cell size.

2.2.2 Updating the position and velocities

After completing the force computation on each particle, we use the leapfrog approach to integrate the equation of motion and update the particle's position and velocity. The Kick-Drift-Kick (KDK) and Drift-Kick-Drift (DKD) methods are commonly used to integrate equations of motion. These methods are crucial in accurately advancing particle positions and velocities over discrete time steps (Δt). The fundamental principle underlying these methods is to mitigate the issue of velocity changes during position updates.

The Leapfrog method is a widely used algorithm for this purpose. It involves two sequential steps: the Kick, where velocities are updated, and the Drift, where positions are updated. Mathematically, these steps can be expressed as follows:

Kick Step:

$$\mathbf{v}(t + \frac{\Delta t}{2}) = \mathbf{v}(t) + \frac{\mathbf{F}(t)}{m} \cdot \frac{\Delta t}{2}$$

Drift Step:

$$\mathbf{x}(t + \Delta t) = \mathbf{x}(t) + \mathbf{v}(t + \frac{\Delta t}{2}) \cdot \Delta t$$

The challenge arises from the fact that during the Drift step, the particle's velocity changes due to the forces acting on it. To address this, the position update for the full-time step (Δt) is performed using velocities updated for half of the time step ($\frac{\Delta t}{2}$). This preserves accuracy in the integration.

There are two prevalent variants of this method: KDK and DKD. In the KDK method, the sequence of steps is Kick-Drift-Kick. This method is frequently employed in simulations involving multiple interacting bodies (n-body simulations).

For the KDK method, the equations are as follows:

First Kick:

$$\mathbf{v}(t + \frac{\Delta t}{2}) = \mathbf{v}(t) + \frac{\mathbf{F}(t)}{m} \cdot \frac{\Delta t}{2}$$

Drift:

$$\mathbf{x}(t + \Delta t) = \mathbf{x}(t) + \mathbf{v}(t + \frac{\Delta t}{2}) \cdot \Delta t$$

Second Kick:

$$\mathbf{v}(t + \Delta t) = \mathbf{v}(t + \frac{\Delta t}{2}) + \frac{\mathbf{F}(t + \Delta t)}{m} \cdot \frac{\Delta t}{2}$$

The KDK and DKD methods provide accurate and stable integration schemes,

with their choice dependent on the system's specific characteristics being simulated.

2.2.3 Initial Conditions

Initial conditions for N-body simulations are set by linear theory such that it satisfies all the aspects. The initial positions and initial velocity of particles are assigned using Zeldovich approximations Zel'Dovich (1970); Carroll *et al.* (1992). The Zeldovich approximation uses linear matter power spectra and linear growth rates. We employ the Boltzmann solver CLASS code to generate the linear matter power spectra and use them as input of the code N-GenIC, which generates the initial conditions. Note that the CDM component has only gravitational peculiar velocities (minimal). On the other hand, the neutrino components have enormous intrinsic thermal velocities. Generating initial velocities of neutrino components needs attention. Our method to deal with the neutrino component is discussed in 4.2.

Halo finder: After we get the particles' evolved positions and velocity, we aim to identify the Halos. There has been a continuous upgrade in halofinding algorithms. We make use of the code ROCKSTAR to identify the halos.

Chapter 3

Nonthermal neutrino-like sterile particles and S8 tension[1]

3.1 Introduction

The Λ Cold Dark Matter model has proven remarkably effective in explaining various cosmological and astrophysical observations with high precision, even though its major ingredients - Cold Dark Matter and Dark Energy - remain mysterious. However, in recent times, several inconsistencies have appeared between the predicted values of certain cosmological parameters within the vanilla ΛCDM model, estimated using Cosmic Microwave - Background (CMB) Planck 2018 data, Baryon Acoustic Oscillations (BAO), and the luminosity distances to Type Ia Supernovae (SNIa), and their directly measured values.

[1]This chapter is based on publication Das *et al.* (2022)

One of the long-standing discrepancies in determining the level of matter fluctuations often parameterized as $S_8 \equiv \sigma_8\sqrt{(\frac{\Omega_m}{0.3})}$, here σ_8 denotes the root-mean-squared (RMS) of matter density fluctuations on 8 Mpc/h scale, and Ω_m denotes the overall matter budget. According to the most recent estimation based on CMB data by Planck 2018 using ΛCDM model, $S_8 = 0.832 \pm 0.013$ Aghanim *et al.* (2018b).

Initially, the weak lensing observations of galaxies suggested that the vanilla ΛCDM model anticipates a value of S_8 higher than its direct measurements by the CFHTLenS collaboration at a significance order of 2σ Heymans *et al.* (2013); MacCrann *et al.* (2015). Furthermore, the KiDS/Viking data have reinforced this mismatch Hildebrandt *et al.* (2020); Joudaki *et al.* (2020), but appears less pronounced with the Dark Energy Survey (DES) data Abbott *et al.* (2018a). Nevertheless, a re-evaluation of the DES data, when combined with KiDS/Viking data, led to an estimation of S_8 that deviates from Planck at a significance order of 3σ, with $S_8 = 0.755^{+0.019}_{-0.021}$ Joudaki *et al.* (2020). In a more recent study, the analysis of KiDS1000/Viking and SDSS data has confirmed $S_8 = 0.766^{+0.02}_{-0.014}$ Heymans *et al.* (2020).

Furthermore, it is now recognized that this tension arises from a lower amplitude of matter clustering, σ_8. This is primarily due to the robust constraints placed on Ω_M, even in extensions beyond the ΛCDM, from BAO observations and supernovae luminosity distance observations. This has significant implications for model development: addressing the S_8 tension necessitates a reduction in the growth of matter perturbations on small scales around $k \sim 0.1 - 1\ h/\text{Mpc}$, a feat readily accomplished in a wide class of models often associated with new Dark Matter characteristics Kumar and Nunes (2016); Haridasu and Viel (2020); Murgia *et al.* (2016); Poulin *et al.* (2016); Archidiacono *et al.* (2019); Di Valentino *et al.* (2020); Clark *et al.* (2020); Becker *et al.* (2021); Enqvist *et al.* (2015); Vattis *et al.* (2019); Pandey *et al.* (2020); Abellan *et al.* (2020); Abellán *et al.* (2021b), or new neutrino

properties Poulin *et al.* (2018); Kreisch *et al.* (2019).

This study investigates the potential explanation for the 'S_8-tension' by considering the presence of a non-thermal neutrino-like hot dark matter constituent. This non-thermal component consists of hidden sector particles or light sterile neutrinos, adding to only a small proportion of the universe's total dark matter (DM) budget. It suppresses the growth of matter fluctuations on small scales and, hence, the matter power spectrum. It's important to note that simply introducing thermal standard neutrinos even with a non-vanishing mass (m_ν) or neutrino-like radiation $\Delta N_{\rm eff}$ does not resolve the S_8 issue (due to its higher temperature and constraints on their mass) Aghanim *et al.* (2018b); Poulin *et al.* (2018). However, we expect nonthermal neutrinos might have implications for S_8 tension because of the mass bounds loosening.

In this context, we study the implications of the non-thermal momentum distribution for the hot dark matter constituent (or neutrinos with a temperature differing from our visible sector) in relation to the S_8 discrepancy. Our focus is on the momentum distribution of sterile particles that resemble neutrinos generated through decay as the universe transitions from early matter domination to radiation domination. We name this model "$\nu_{\rm NT}\Lambda$CDM".

From a theoretical standpoint, it has been studied that the early universe underwent a matter-dominated era just before the radiation-dominated phase Kane *et al.* (2015); Kofman *et al.* (1997); Allahverdi *et al.* (2010). This early matter-dominated era (EMDE) consists of the inflaton or cold moduli decay into lighter particles, and the universe goes into a radiation-dominated era. Alternatively, EMDE may arise from dark sector physics Berlin *et al.* (2016); Tenkanen and Vaskonen (2016). According to string theory and supergravity theories, this happens as a result of moduli-vacuum misalignment Coughlan *et al.* (1983); de Carlos *et al.* (1993); Banks *et al.* (1994). For comprehensive arguments on the universality

of these models and calculations in specific scenarios, see, for example, Refs. Randall and Thomas (1995); Cicoli *et al.* (2016); Acharya *et al.* (2019).

It has been demonstrated that decay products acquire a characteristic momentum distribution Scherrer and Turner (1988); Miller *et al.* (2019b); Hasenkamp and Kersten (2013b); Bhattacharya *et al.* (2020), linked to decay occurring in a universe evolving from matter-dominated to radiation-dominated phases. The kinematics are used to establish the form of the momentum distribution function. For this, certain assumptions are followed: the particles originate from the $1 \rightarrow 2$ decay of an unstable particle (which dominated the universe) and possess a much smaller mass than the decaying particle. Additionally, the particles are assumed to be inert, allowing them to free stream subsequently. When the product particles undergo thermalization, most of the information regarding the kinematics of this decay process is lost. However, in a scenario involving several hidden sectors, it can be expected that some of the decay products do not thermalize because of extremely weak interaction. Our scenario falls into a class where an inflaton or moduli field decays into non-thermal sterile particles. There may also be some other particles, like Feebly Interacting Massive Particles (FIMPs), which can generate non-thermal or partially thermal neutrinos Boyarsky *et al.* (2021). Nonthermal dark radiation would impact both the CMB Hou *et al.* (2013) and large-scale structures uniquely and can be investigated through precise cosmological data.

The investigations of the consequences of sterile particles with such momentum distribution for modern precise cosmological observations was recently initiated[2] in Bhattacharya *et al.* (2020). Given that the impact of such massive sterile neutrino-like particles on the matter power spectra and CMB power spectra is well-documented (see, e.g., Acero and Lesgourgues (2009b); Lesgourgues and Pastor (2006); Lesgourgues (2011) for details), it was expected that a significant power suppression at smaller scales in the matter power spectra could occur as a result

[2]For earlier work on inert particles from decays, see for example Scherrer and Turner (1988); Hasenkamp and Kersten (2013b); Conlon and Marsh (2013b); Miller *et al.* (2019b)

of the nonthermal momentum distribution of product particles from decay. Such suppression in power has consequences for the S_8 discrepancy.

In this study, we conduct an extensive Markov Chain Monte Carlo (MCMC) analysis using the latest data from Planck, BOSS (including Baryon Acoustic Oscillations and redshift space distortions $f\sigma_8$), and Pantheon. We explore scenarios both with and without incorporating a prior on parameter S_8 obtained from the KiDS1000/Viking+BOSS+2dFLens data[3].

Our findings indicate that the model $\nu_{\rm NT}\Lambda$CDM alleviates the tension between direct S_8 measurements and Planck. However, this resolution is somewhat diminished when the analysis includes Pantheon and BOSS data. To gain a deeper insight into the characteristics of the model responsible for resolving the discrepancy, we compare our non-thermal model with the standard model involving massive neutrinos and additional relativistic degrees of freedom. We observe that, for a nearly identical effect on the CMB power spectra, the nonthermal sterile neutrino model leads to a much stronger suppression in the total matter power spectra at late times, resulting in a more substantial reduction in σ_8. While the effect of the $\nu_{\rm NT}\Lambda$CDM model is barely noticeable on the luminosity distances and BAO scales, it does influence the predictions for $f\sigma_8$. Therefore, the model faces further constraints from redshift space distortions data (from BOSS). Upcoming observations of the matter power spectrum, as well as $f\sigma_8$ at later times, will serve as critical tests for this scenario Benisty (2021).

Although our MCMC analysis specifically addresses sterile particles with the described momentum distributions, its implications extend to a broad class of models. As established in prior work (see e.g. Acero and Lesgourgues (2009b); Cuoco

[3]For related analyses with a focus on short baseline neutrino experiments, see e.g. Roy Choudhury and Hannestad (2020); Roy Choudhury and Choubey (2019b). In this context, we assume that the momentum distribution of such sterile particles follows the patterns motivated by neutrino physics, i.e., either thermal or the Dodelson-Widrow distribution Dodelson and Widrow (1994a).

et al. (2005)), the cosmological consequences of a hot dark component can be effectively summarized by two parameters: a) its contribution to the present-day energy density, often parameterized as the effective mass $m_{\rm eff}$; and b) its contribution of the relativistic component to the energy density at the time of CMB decoupling, parameterized in terms of $\Delta N_{\rm eff}$[4]. The above parameters can be calculated through the first couple of moments of the momentum distribution and the desired particle's mass. A variety of models with identical values of $m_{\rm eff}$ and $\Delta N_{\rm eff}$ will exhibit the same phenomenological effects, even if their origin and shape of the momentum distribution function differ. We leverage these properties to imply our analysis results for our model parameters to phenomenological parameters. Consequently, our findings hold direct relevance for other well-discussed nonthermal momentum distributions in literature, for example a thermal distribution with a distinct temperature from that of the visible standard sectorFeng *et al.* (2008); Das *et al.* (2018); Das and Sigurdson (2012); Berlin *et al.* (2019), the Dodelson-Widrow distribution Dodelson and Widrow (1994a), or distributions akin to the Dodelson-Widrow distribution as discussed in Refs. Gelmini *et al.* (2004, 2008).

3.2 Non-thermal Hot Dark Matter

3.2.1 The Model

The characteristics of a dark matter constituent species are contingent on their masses, interactions, and momentum distributions. For species that undergo thermalization, the process leads to a momentum distribution following the Bose-Einstein or the Fermi-Dirac form. Conversely, the momentum distribution of non-thermal components is inferred through their production mechanism. Hence, it is

[4]In the models under discussion, this is equivalent to $\Delta N_{\rm eff}$ at the time of neutrino decoupling.

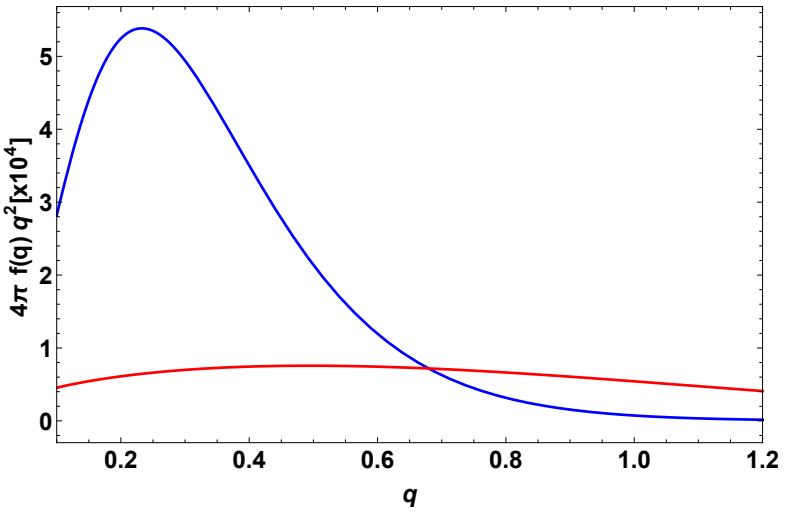

FIGURE 3.1: The momentum distribution in units of $T_{\rm ncdm,0}$ for nonthermal Hot dark matter species (orange) compared with a thermal distribution (blue). The parameters set in nonthermal model as $\tau = 10^8/m_\varphi$,$m_\varphi = 10^{-6}M_{\rm pl}$. Both plots correspond to the same $\Delta N_{\rm eff} = 0.15$.

crucial to identify the natural production mechanism for such species, obtain the related momentum distribution, and understand their cosmological implications.

Here, we provide an overview of how we got the momentum distribution for the production mechanism we are considering. Although our discussion will be short, we urge the readers to review Ref. Bhattacharya *et al.* (2020) for more details and cited references. In the earlier stages, the universe's overall energy density mostly comprises heavy (cold) particles belonging to a species φ of mass m_φ and τ is their decay width. We will specifically focus on the scenario where φ serves as the inflaton, with inflation occurring at the GUT era and then inflaton decaying due to a non-renormalizable interaction at that same scale. Consequently, we have $\tau \sim 10^8/m_\varphi$ and $m_\varphi \sim 10^{-6}M_{\rm pl}$, $B_{\rm sp}$ is the branching fraction of decay of φ particles to the daughter sterile particles. These produced sterile particles are assumed not to undergo thermalization. We also believe that the rest of the decay products thermalize because this sector includes the Standard Model. This category is referred to as the Standard Model sector. All decay products are considered relativistic at the time of generation. When almost all of the φ particles decay, the universe transitions from a matter-dominated state to a radiation-dominated

universe. During the transition period, the universe's evolution is governed by the following equations:

$$\dot{\rho}_{\rm mat} + 3H\rho_{\rm mat} = -\frac{\rho_{\rm mat}}{\tau}, \tag{3.1}$$

$$\dot{\rho}_{\rm rad} + 4H\rho_{\rm rad} = +\frac{\rho_{\rm mat}}{\tau}, \tag{3.2}$$

and

$$H = \left(\frac{\dot{a}}{a}\right) = \sqrt{\frac{\rho_{\rm mat} + \rho_{\rm rad}}{3M_{\rm pl}^2}}. \tag{3.3}$$

Here, $\rho_{\rm mat}$ represents the matter-energy density, and $\rho_{\rm rad}$ represents radiation, the energy density. Note that radiation density includes both the Standard Model sector and sterile particles (because they were relativistic at production time). It is convenient to use the dimensionless variables:

$$\theta = \tfrac{t}{\tau}, \quad \hat{s}(\theta) = a(\tau\theta),$$
$$e_{\rm mat}(\theta) = \tfrac{\tau^2\rho_{\rm mat}(\tau\theta)}{M_{\rm pl}^2} \quad \text{and} \quad e_{\rm rad}(\theta) = \tfrac{\tau^2\rho_{\rm rad}(\tau\theta)}{M_{\rm pl}^2}. \tag{3.4}$$

As soon as nearly all φ particles decay, the universe can be considered to comprise a thermal bath (containing the Standard sector particles) and sterile particles, and standard equations govern evolution. Practically, at an 'initial time' ($t = \theta = 0$), we begin with a matter-dominated universe and the universe evolves using equations (3.1), (3.2), and (3.3) up to a dimensionless fiducial time θ^* (we choose $\theta^* = 15$ in practice), which is sufficiently large so that most of φ particles decay till that time. The findings of this procedure are the initial conditions for conventional cosmic evolution. For the initial energy densities, we set $e_{\rm rad}(0) = 0$ and $e_{\rm mat}(0) = \frac{4}{3}\alpha$ and with $\alpha \gg 1$ (for our analysis, we took $\alpha = 10^4$, the factor 4/3 is chosen for simplicity). This tells that we begin with an entirely matter-dominated universe with the initial Hubble parameter ($H_{\rm in}$) fulfilling $H_{\rm in}\tau \gg 1$. This fact ensures that our results will not depend on different choices of initial conditions.

To determine the momentum distribution of such sterile neutrinos, We use the fact that the comoving number density of the sterile particles decreases as $N(t) = N(0)e^{-t/\tau}$ as a result of decay. The branching ratio to sterile particles is $B_{\rm sp}$. The particles will free-stream after they have been produced. This nonthermal momentum distribution of sterile particles has been incorporated in the publicly accessible code CLASS. This was obtained in Bhattacharya *et al.* (2020) as:

$$f(\vec{q}) = \frac{32}{\pi \hat{E}^3} \left(\frac{N(0) B_{\rm sp}}{\hat{s}^3(\theta^*)} \right) \frac{e^{-\hat{s}^{-1}(y)}}{|\vec{q}|^3 \hat{H}(\hat{s}^{-1}(y))}, \tag{3.5}$$

where $y = \frac{|\vec{q}|}{4} \hat{s}(\theta^*)$, and the argument of the function $\vec{q}$ is constrained so that

$$\frac{4}{\hat{s}(\theta^*)} < |\vec{q}| < 4. \tag{3.6}$$

Here,$N(0)$ is the initial number density of the φ particles, $\hat{E} = m_\varphi/2$, $\hat{s}(\theta^*)$ is the value scale factor at the reference dimensionless time θ^*, $\hat{s}^{-1}$ represents the inverse function of the scale factor in units of dimensionless time. Meanwhile, $\hat{H} = \frac{\hat{s}'(\theta)}{\hat{s}(\theta)}$ signifies the dimensionless Hubble constant. The momentum vector $\vec{q}$ in equation 3.5 is expressed in units relative to the typical momentum magnitude of sterile particles today, denoted as $T_{\rm ncdm,0}$.

In a previous study by Bhattacharya *et al.* (2020), it was determined that

$$T_{\rm ncdm,0} = 0.418 \left(\frac{m_\varphi^2 \tau}{M_{\rm pl}} \right)^{1/2} \frac{T_{\rm cmb}}{(1 - B_{\rm sp})^{1/4}} \equiv \zeta T_{\rm cmb} \tag{3.7}$$

The distribution function in equation 3.5 is measured in units of $T^3_{\rm ncdm,0}$. Therefore, when you consider the function $f(\vec{q})d^3q$, it provides the number density of

particles whose dimensionless momentum falls within the range $(q_i, q_i + dq_i)$, with the number density measured in units of $T^3_{\rm ncdm,0}$.

Mapping onto General Parameters

Our model consists of four additional microscopic parameters: m_φ (mass of decaying particle) and τ (decay width), $B_{\rm sp}$ (indicating the branching fraction for decay into the sterile particle), and $m_{\rm sp}$ (denoting the mass of the daughter particle), in addition to those of ΛCDM. The selection of the first two parameters ($m_\varphi \sim 10^{-6} M_{\rm pl}$ and $\tau \sim 10^8/m_\varphi$) is influenced by considering φ as the driving force behind inflation at the GUT scale and its subsequent decay through GUT scale interactions.

On the contrary, the remaining parameters $B_{\rm sp}$ and $m_{\rm sp}$ will be exchanged for effective parameters more directly tied to observables. Indeed, the tangible impacts of the new sterile particle/species on the cosmological perturbation and background evolution can be fully characterized by three parameters: $\Delta N_{\rm eff}$ (representing the effective number of relativistic neutrinos at the time of neutrino decoupling), $w_{\rm sp} \equiv \Omega_{\rm sp} h^2$ (where $\Omega_{\rm sp}$ signifies the fractional contribution of the particle to today's energy density, and h is the reduced Hubble parameter, often expressed in terms of the effective mass of the particle $m^{\rm eff}_{\rm sp}. = w_{\rm sp} \times 94.05{\rm eV}$), and $\lambda_{\rm FS}$ (the free-streaming length associated with the species). The free-streaming length is determined once the first two quantities are known, effectively resulting in two parameters Acero and Lesgourgues (2009b). From a physical standpoint, the two key parameters for diminishing σ_8 are $\omega_{\rm sp}$, which sets the depth of the power suppression, and $\lambda_{\rm FS}$, which establishes the scale above which modes are suppressed. Nevertheless, for their more straightforward connection with micro-physics, in this context, we consider $\Delta N_{\rm eff}$ and $m^{\rm eff}_{\rm sp}$ as two independent quantities, defined as

$$\Delta N_{\rm eff} \equiv \frac{\rho_s^{\rm rel}}{\rho_\nu} = \frac{1}{\pi^2}\left[\int dp\ p^3 \hat{f}(p)\right] / \left[\frac{7}{8}\frac{\pi^2}{15} T_\nu^{\rm id\,4}\right] \tag{3.8}$$

with $T_\nu^{\rm id} \equiv (4/11)^{1/3} T_\gamma$ and

$$\frac{m_{\rm sp}^{\rm eff}}{94.05{\rm eV}} \equiv \omega_s \equiv \Omega_s h^2 = \frac{1}{\pi^2}\left[m_{\rm sp}\int dp\ p^2 \hat{f}(p)\right] \times \left[\frac{h^2}{\rho_c^0}\right] \tag{3.9}$$

where $\hat{f}(p)$ signifies the distribution function as a function of the magnitude of the physical momentum in the conventions of Acero and Lesgourgues (2009b). In these conventions, an additional species of neutrinos at temperature T_s has $\hat{f}(p) = \frac{1}{e^{p/T_s}+1}$. For our non-thermal distribution, $\hat{f}(p) = 4\pi^3 f(\frac{p}{T_{\rm ncdm,0}}\hat{\mathbf{e}})$, where the function f is as defined in Eq. 3.5 and $\hat{\mathbf{e}}$ is an arbitrary unit vector. ρ_c^0 is the critical density today, and h is the reduced Hubble parameter.

In our model, the effective parameters $m_{\rm eff}$ and $\Delta N_{\rm eff}$ in terms of the microscopic parameters are given by 3.5:

$$\Delta N_{\rm eff} = \frac{43}{7}\frac{B_{\rm sp}}{1-B_{\rm sp}}\left(\frac{g_*(T(t_\nu))}{g_*(T(t^*))}\right)^{1/3} \tag{3.10}$$

and

$$m_{\rm sp}^{\rm eff} = \frac{62.1 m_{\rm sp}}{g_*^{1/4}(T(t^*))}\frac{B_{\rm sp}}{(1-B_{\rm sp})^{3/4}}\left(\frac{M_{\rm pl}}{\tau m_\varphi^2}\right)^{1/2}, \tag{3.11}$$

where $g_*(T(t_\nu))$ and $g_*(T(t^*))$ are the effective number of degrees of freedom at the time of neutrino decoupling and the end of the reheating epoch (we will take the latter to be equal to 100). We will thus explore over $m_{\rm sp}$ and $B_{\rm sp}$ (maintaining $m_\varphi = 10^{-6} M_{\rm pl}$ and $\tau \sim 10^8/m_\varphi$ constant), and see Eqs. 3.10 and 3.11 to establish relationships with phenomenological parameters.

On the relationship between observables and effective parameters

The fact that the two parameters $\Delta N_{\rm eff}$ and $m_{\rm eff}$ determine the physical observables is well known, as mentioned already Acero and Lesgourgues (2009b). In fact, this is also used by the Planck collaboration for their analysis; see, e.g., figure 37, section 7.5.2 of Aghanim *et al.* (2020b). In this section, we analyze this expectation in our setting for completeness. In the model discussed in the main text $m_\varphi = 10^{-6} M_{\rm pl}$ and $\tau = 10^8/m_\varphi$ (we will refer to this as model X). Here, we consider $m_\varphi = 10^{-8} M_{\rm pl}$ and $\tau = 10^9/m_\varphi$ (we will refer to this as model Y).

Note that equations (3.10) and (3.11) imply that if $B^Y_{\rm sp} = B^X_{\rm sp}$ and $m^Y_{\rm sp} = m^X_{\rm sp}/\sqrt{10}$, models X and Y will have equal values of $\Delta N_{\rm eff}$ and $m_{\rm eff}$. We compare the CMB and matter power spectra today for equal values of m_{sp} and B_{sp} in figure 3.2. As expected, we find that the CLASS inputs of models X and Y are in very good agreement (better than 10^{-5}). Therefore, our constraints are robust to the specific choice of these parameters.

parameter	model X1	model Y1	model X2	model Y2	model X3	model Y3
m_φ	$10^{-6} M_{\rm pl}$	$10^{-8} M_{\rm pl}$	$10^{-6} M_{\rm pl}$	$10^{-8} M_{\rm pl}$	$10^{-6} M_{\rm pl}$	$10^{-8} M_{\rm pl}$
τ	$10^8/m_\varphi$	$10^9/M_\varphi$	$10^8/m_\varphi$	$10^9/m_\varphi$	$10^8/m_\varphi$	$10^9/m_\varphi$
$m_{\rm sp}$ (in eV)	38.62194	$\frac{38.62194}{\sqrt{10}}$	38.62194	$\frac{38.62194}{\sqrt{10}}$	28.62194	$\frac{28.62194}{\sqrt{10}}$
$B_{\rm sp}$	0.0118	0.0118	0.0218	0.0218	0.0218	0.0218

TABLE 3.1: Table shows the parameters of three pairs of model(X1,Y1),(X2,Y2) and (X3,Y3). Both the models of each pair have different values of τ and m_ϕ but same $(\Delta {\rm N_{eff}}, {\rm m^{eff}_{sp}})$

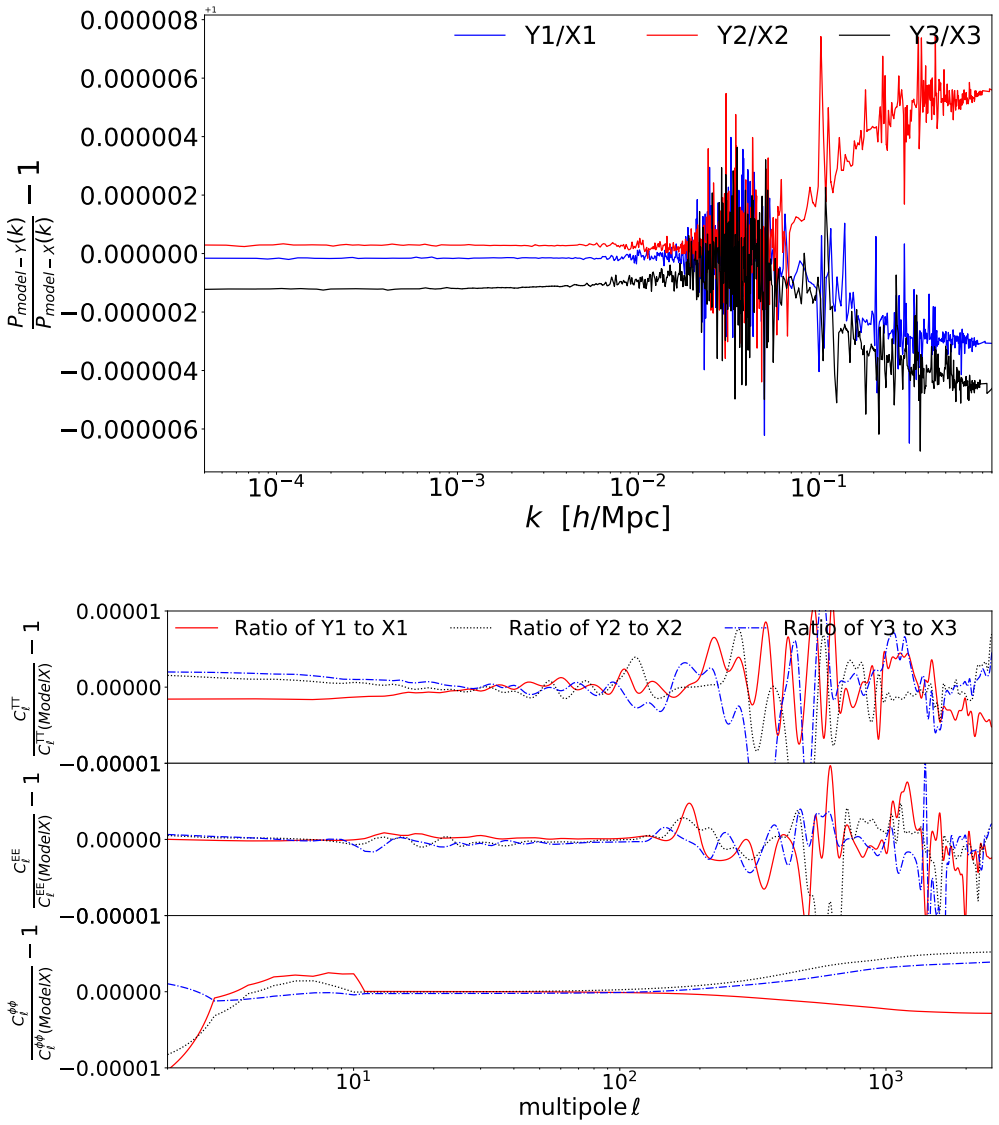

FIGURE 3.2: Residuals of Matter power spectra and CMB TT EE and $\phi\phi$ power spectra for various models (see legend). Here the models (X1,Y1),(X2, Y2) and (X3, Y3) correspond to the models described in table 3.1.

3.3 Data and methodology

3.3.1 Data

- The Planck 2018 observations encompass a range of measurements, including the low-ℓ Cosmic Microwave Background (CMB) TT, EE power spectra, and the high-ℓ TT, TE, EE power spectra. These observations also involve reconstructing the gravitational lensing potential, as detailed in Planck Collaboration and Aghanim (2020).

- Baryon Acoustic Oscillation (BAO) measurements originate from diverse sources. Specifically, data from the 6-degree Field Galaxy Survey (6dFGS) at a redshift of $z = 0.106$ Beutler *et al.* (2011), the Sloan Digital Sky Survey Data Release 7 (SDSS DR7) at $z = 0.15$ Ross *et al.* (2015), and the Baryon Oscillation Spectroscopic Survey Data Release 12 (BOSS DR12) at multiple redshifts ($z = 0.38, 0.51, 0.61$) Alam *et al.* (2017a) have been employed. Additionally, the combined limits from the extended Baryon Oscillation Spectroscopic Survey Data Release 14 (eBOSS DR14), involving Ly-α auto-correlation at $z = 2.34$ and cross-correlation at $z = 2.35$, have been integrated de Sainte Agathe *et al.* (2019), Blomqvist *et al.* (2019).

- The growth function $f\sigma_8(z)$ (FS) was determined by CMASS and BOSS DR12 (LOWZ galaxy samples) at redshifts ($z = 0.38, 0.51, 0.61$) Alam *et al.* (2017a).

- The Pantheon catalog of Type Ia supernovae covers a range of redshifts ($0.01 < z < 2.3$) Scolnic *et al.* (2018b).

- Weak lensing data from KIDS1000+BOSS+2dfLenS was condensed into a split-normal likelihood for the parameter S_8, yielding a value of $0.766^{+0.02}_{-0.014}$ Heymans *et al.* (2020).

Model	ΛCDM		νΛCDM		$\nu_{\rm NT}$ΛCDM	
Parameter	Planck	Planck + S_8	Planck	Planck + S_8	Planck	Planck + S_8
$100\ \omega_b$	$2.24(2.24)^{+0.014}_{-0.015}$	$2.252(2.256)^{+0.014}_{-0.015}$	$2.244^{+0.016}_{-0.018}$	$2.257(2.259) \pm 0.017$	$2.241(2.247)^{+0.015}_{-0.016}$	$2.247(2.247)^{+0.014}_{-0.015}$
$\omega_{\rm cdm}$	$0.1198(0.1195)^{+0.0013}_{-0.0012}$	$0.1182(0.1177) \pm 0.0011$	$0.1217^{+0.0015}_{-0.002}$	$0.1198(0.1182)^{+0.0013}_{-0.0018}$	$0.118(0.1198)^{+0.0041}_{-0.0022}$	$0.1142(0.1110)^{+0.0049}_{-0.003}$
$100 * \theta_s$	$1.04190(1.04178)^{+0.00029}_{-0.0003}$	$1.04202(1.04217)^{+0.00029}_{-0.0003}$	$1.04166^{+0.00037}_{-0.00033}$	$1.04179(1.04191)^{+0.00035}_{-0.00032}$	$1.04180(1.04187) \pm 0.00032$	$1.04186(1.04190)^{+0.00031}_{-0.00029}$
n_s	$0.9661(0.9663)^{+0.0041}_{-0.0043}$	$0.9695(0.971)^{+0.0039}_{-0.0041}$	$0.9685^{+0.0049}_{-0.006}$	$0.9717(0.9732)^{+0.0048}_{-0.0056}$	$0.9652(0.9677)^{+0.0044}_{-0.0051}$	$0.9652(0.9661)^{+0.0047}_{-0.0045}$
$\ln(10^{10}A_s)$	$3.044(3.044) \pm 0.014$	$3.041(3.042)^{+0.014}_{-0.015}$	$3.052^{+0.015}_{-0.016}$	$3.048(3.050)^{+0.016}_{-0.017}$	$3.047(3.0480) \pm 0.015$	$3.046(3.044)^{+0.014}_{-0.016}$
$\tau_{\rm reio}$	$0.0541(0.0541)^{+0.0075}_{-0.0071}$	$0.0542(0.0556)^{+0.0074}_{-0.0078}$	$0.0558^{+0.0073}_{-0.0081}$	$0.0555(0.0590)^{+0.0077}_{-0.0082}$	$0.0545(0.0559)^{+0.0073}_{-0.0081}$	$0.0548(0.0536)^{+0.0069}_{-0.0079}$
m_ν [eV]	–	–	< 0.073	$< 0.1(0)$	–	–
$m_{\rm sp}^{\rm eff}$ [eV]	–	–	–	–	$< 1.02(0)$	$0.67(0.90)^{+0.26}_{-0.48}$
$\Delta N_{\rm eff}$	–	–	< 0.28	$< 0.24(0.03)$	$< 0.15(0.03)$	$0.0614(0.034)^{+0.0052}_{-0.047}$
S_8	$0.834(0.832) \pm 0.013$	$0.814(0.809)^{+0.01}_{-0.011}$	$0.834(0.838)^{+0.013}_{-0.013}$	$0.812(0.814) \pm 0.011$	$0.815(0.831)^{+0.022}_{-0.018}$	$0.789(0.791) \pm 0.016$
Ω_m	$0.3078(0.3068)^{+0.0074}_{-0.0076}$	$0.2981(0.2948)^{+0.0061}_{-0.0066}$	$0.3154(0.3084)^{+0.0094}_{-0.015}$	$0.3084(0.295)^{+0.0081}_{-0.018}$	$0.3138(0.305)^{+0.0084}_{-0.0097}$	$0.311(0.308)^{+0.008}_{-0.01}$
H_0 [km/s/Mpc]	$68(68.04) \pm 0.56$	$68.73(68.99)^{+0.49}_{-0.51}$	$67.83(67.95)^{+1.2}_{-1}$	$68.26(69.11)^{+1.5}_{-0.93}$	$67.72(68.34)^{+0.62}_{-0.65}$	$67.91(68.04)^{+0.67}_{-0.61}$
$\chi^2_{\rm min}$	2774.8	2783.4	2774.9	2782.0	2775.0	2778.60

TABLE 3.2: The cosmological parameters in format "mean (best-fit) $\pm 1\sigma$ error" for the ΛCDM and $\nu_{\rm NT}$ΛCDM model extracted from the analysis of Planck Aghanim *et al.* (2018a) as well as Planck+S_8 Heymans *et al.* (2020) data. The parameter $m_{\rm sp}^{\rm eff}$ is defined in Eq. 3.11 and Upper bounds are given at the 95% Confidence Limit.

Model	ΛCDM		νΛCDM		$\nu_{\rm NT}$ΛCDM	
Parameter	Planck+Ext	Planck+Ext+S_8	Planck+Ext	Planck+Ext+S_8	Planck+Ext	Planck+Ext+S_8
$100\ \omega_b$	$2.241(2.238)^{+0.013}_{-0.014}$	$2.248(2.258) \pm 0.013$	$2.249(2.248) \pm 0.015$	$2.257(2.250) \pm 0.015$	$2.245(2.245) \pm 0.014$	$2.250(2.253)^{+0.013}_{-0.014}$
$\omega_{\rm cdm}$	$0.1197(0.1204) \pm 0.0009$	$0.1187(0.1182)^{+0.0009}_{-0.0008}$	$0.121(0.1194)^{+0.0012}_{-0.0019}$	$0.1198(0.1186)^{+0.0011}_{-0.0017}$	$0.1181(0.1179)^{+0.0030}_{-0.0018}$	$0.1152(0.1101)^{+0.0036}_{-0.0023}$
$100 * \theta_s$	$1.04192(1.04204)^{+0.00028}_{-0.00029}$	$1.04197(1.04186)^{+0.0003}_{-0.00029}$	$1.04172(1.04194)^{+0.00034}_{-0.00031}$	$1.04179(1.04194)^{+0.00036}_{-0.00031}$	$1.04187(1.04193)^{+0.0003}_{-0.00029}$	$1.04193(1.04194)^{+0.00029}_{-0.00028}$
n_s	$0.9664(0.9660)^{+0.0038}_{-0.0037}$	$0.9683(0.9705)^{+0.0036}_{-0.0038}$	$0.9699(0.9693)^{+0.0044}_{-0.0049}$	$0.9721(0.9706)^{+0.0043}_{-0.0048}$	$0.9667(0.9664)^{+0.0039}_{-0.0041}$	$0.9669(0.9678)^{+0.0039}_{-0.004}$
$\ln(10^{10}A_s)$	$3.044(3.05)^{+0.014}_{-0.015}$	$3.038(3.045)^{+0.013}_{-0.015}$	$3.052(3.049)^{+0.014}_{-0.016}$	$3.046(3.035)^{+0.015}_{-0.016}$	$3.049(3.052)^{+0.014}_{-0.015}$	$3.046(3.054)^{+0.014}_{-0.015}$
$\tau_{\rm reio}$	$0.0542(0.0574)^{+0.0069}_{-0.0073}$	$0.0526(0.056)^{+0.0069}_{-0.0076}$	$0.0561(0.0569)^{+0.0066}_{-0.0081}$	$0.0548(0.0515)^{+0.0073}_{-0.0081}$	$0.0559(0.0576)^{+0.007}_{-0.0076}$	$0.0556(0.0586)^{+0.0068}_{-0.0076}$
m_ν [eV]	–	–	$< 0.040(0.005)$	$< 0.057(0.01)$	–	–
$m_{\rm sp}^{\rm eff}$ [eV]	–	–	–	–	$< 0.67(0.21)$	$0.48(0.92)^{+0.17}_{-0.36}$
$\Delta N_{\rm eff}$	–	–	$< 0.27(0.02)$	$< 0.26(0.006)$	$< 0.12(0.02)$	$0.0457(0.0336)^{+0.0038}_{-0.031}$
S_8	$0.832(0.842) \pm 0.011$	$0.818(0.815)^{+0.0091}_{-0.0094}$	$0.830(0.827) \pm 0.011$	$0.814(0.815)^{+0.01}_{-0.0097}$	$0.815(0.820)^{+0.017}_{-0.015}$	$0.795(0.787)^{+0.015}_{-0.013}$
Ω_m	$0.3067(0.31) \pm 0.0055$	$0.3007(0.2974)^{+0.0051}_{-0.0049}$	$0.3084(0.3042)^{+0.0059}_{-0.006}$	$0.3045(0.3037)^{+0.0061}_{-0.0072}$	$0.309(0.308)^{+0.0057}_{-0.0061}$	$0.306(0.304) \pm 0.006$
H_0 [km/s/Mpc]	$68.07(67.82)^{+0.41}_{-0.43}$	$68.52(68.78)^{+0.38}_{-0.4}$	$68.35(68.33)^{+0.56}_{-0.7}$	$68.58(68.28)^{+0.64}_{-0.73}$	$68.06(67.97)^{+0.44}_{-0.47}$	$68.22(68.37)^{+0.41}_{-0.43}$
$\chi^2_{\rm min}$	3810.4	3818.2	3809.5	3816.4	3809.7	3814.5

TABLE 3.3: Same as Tab.3.2, this including data BAO/FS+Pantheon.

3.3.2 Methodology

Our fundamental cosmological framework is defined by a specific amalgamation of six ΛCDM parameters denoted as $\{\omega_{\rm cdm}, \omega_b, 100 \times \theta_s, \ln(10^{10}A_s), n_s, \tau_{\rm reio}\}$. Additionally, we introduce two parameters related to the non-thermal HDM model, denoted as $\{B_{\rm sp}, m_{\rm sp}\}$. This model is called $\nu_{\rm NT}$ΛCDM. It is assumed that standard-model neutrinos possess zero mass.

To get a deeper insight into how the $\nu_{\rm NT}\Lambda$CDM model addresses the discrepancy represented by S_8, we will contrast it with two other models: the standard model (ΛCDM) considering only massless neutrinos; also the ΛCDM model considering additional relativistic degrees of freedom $\Delta N_{\rm eff}$ and variable neutrino masses m_ν. In the latter scenario, we assume neutrino masses to be degenerate and incorporate a freely moving $\Delta N_{\rm eff}$. Noteworthy is the fact that in this model, the $\Delta N_{\rm eff}$ component remains unaltered and does not acquire mass at later stages, which differs from what occurs in the non-thermal neutrino model. This discrepancy plays a pivotal role in distinguishing between the two models. This variant is termed $\nu\Lambda$CDM. Our Markov Chain Monte Carlo (MCMC) simulations are conducted using the Metropolis-Hasting algorithm, using the code "MontePython-v3" interfaced with our modified version of code "CLASS". All computed minimum χ^2 values are derived using the Python package iMinuit James and Roos (1975). To handle a substantial number of nuisance parameters, we employ a Choleski decomposition for improved efficacy Lewis *et al.* (2000). We also ascertain the convergence of the chains using the Gelman-Rubin convergence criterion, ensuring $R-1 \lesssim 0.05$ Gelman and Rubin (1992).

3.4 Results

We conduct two sets of runs: in the first set of runs, we compare the $\nu_{\rm NT}\Lambda$CDM with ΛCDM, $\nu\Lambda$CDM models against Planck data alone, as well as Planck combined with S_8. We incorporate BAO and Pantheon data sets into our analysis for the second set of runs.

Our primary findings are outlined in Tables 3.2 and 7.3, and visually presented in Figures 3.3 and 3.4. The results for the $\nu_{\rm NT}\Lambda$CDM model are expressed in terms

of $\Delta N_{\rm eff}$ and $m_{\rm sp}^{\rm eff}$ as defined in Equations 3.10 and 3.11. We provide the minimum χ^2 per experiment, as detailed in Appendix 6.6[5].

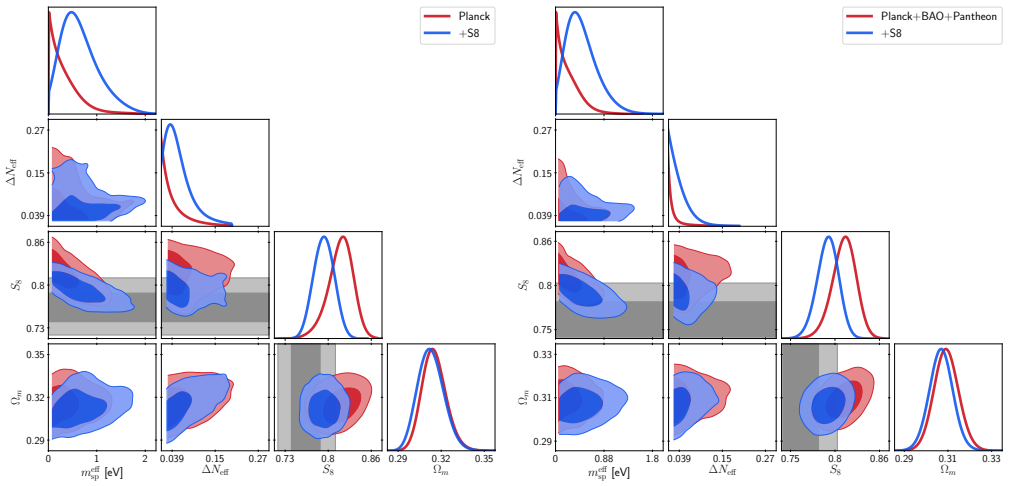

FIGURE 3.3: 2D posterior distributions of the parameters $\{\Delta N_{\rm eff}, m_{\rm sp}^{\rm eff}, S_8, \Omega_m\}$ reconstructed from analysis of Planck and Planck+S_8 data (left panel) as well as Planck+BAO+SN1a and Planck+BAO+SN1a+S_8 data (right panel).

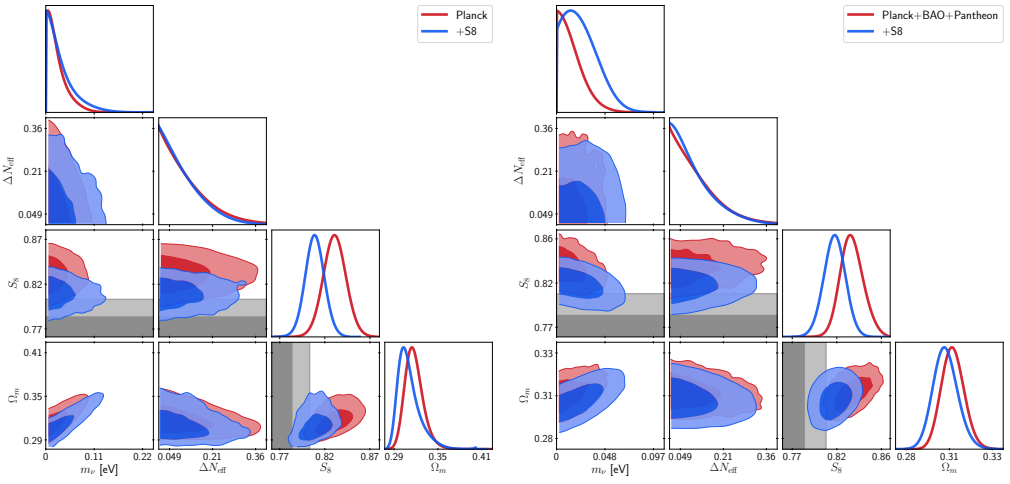

FIGURE 3.4: Same as above fig. 3.3 in the thermal standard neutrino case.

[5]It's worth noting that we assume both thermal and non-thermal neutrinos to have degenerate masses, whereas the ΛCDM model features two zero mass neutrinos and one with a mass of 0.06 eV (in accordance with Planck convention). This leads to negligible practical discrepancies, explaining why an exact recovery of the ΛCDM model's χ^2 is not achieved in massive neutrino cases. Similarly, the non-thermal model does not 'precisely' reduce to the thermal model in certain parameter regions. Consequently, slight discrepancies in χ^2 are anticipated and deemed statistically insignificant.

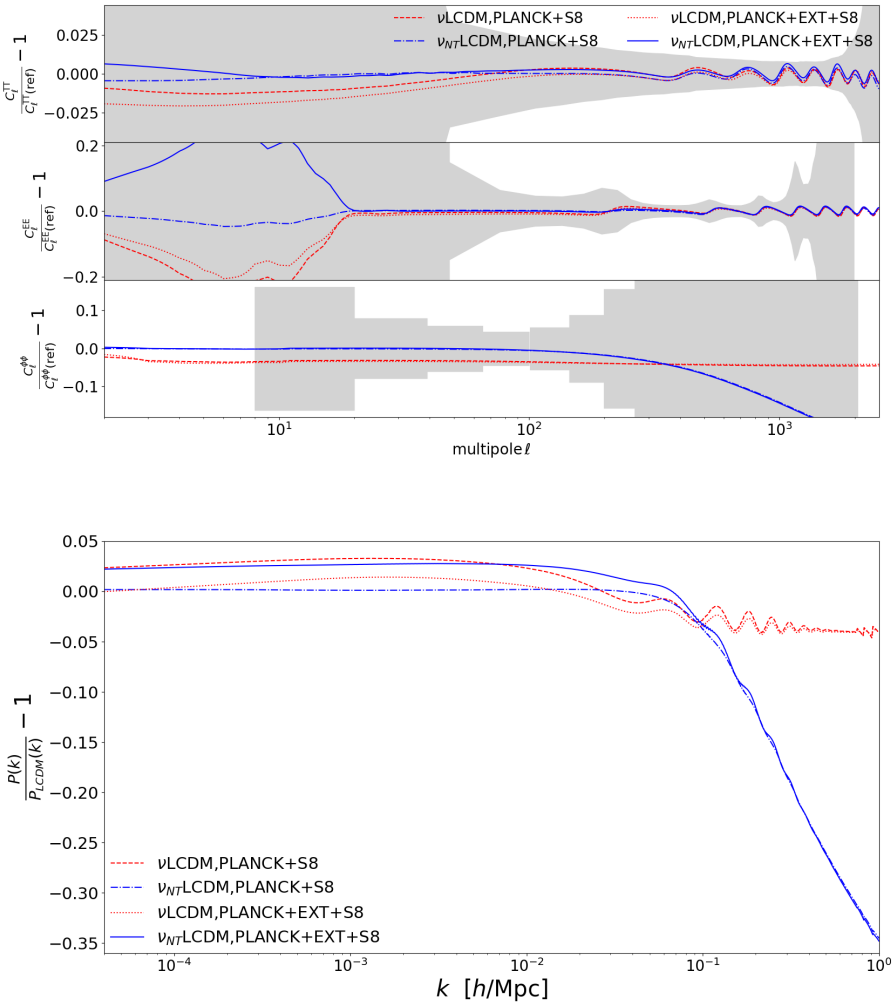

FIGURE 3.5: Residuals of the CMB TT, EE, $\phi\phi$ power spectra of (top panel) and matter power spectra (bottom panel). Residuals are here shown for best fit $\nu\Lambda$CDM and $\nu_{\rm NT}\Lambda$CDM models for two different datasets (see legends) with respect to standard ΛCDM. The 'Ext' data denotes to BAO/FS+SN1a. Note that shaded regions are 1σ error bars from Aghanim *et al.* (2018c).

3.4.1 Understanding the MCMC

3.4.1.1 Planck only

When we examine the $\nu_{\rm NT}\Lambda$CDM model against Planck data exclusively, we derive an upper limit[6] of $m_{\rm sp}^{\rm eff} < 1.02$ eV and $\Delta N_{\rm eff} < 0.15$. Similarly, in the $\nu\Lambda$CDM scenario, we obtain $m_\nu < 0.073$ eV and $\Delta N_{\rm eff} < 0.28$ (noting that this constraint applies to individual neutrino masses in the degenerate case). The minimum χ^2 value for Planck in both the $\nu\Lambda$CDM and $\nu_{\rm NT}\Lambda$CDM scenarios does not show improvement over that of ΛCDM. It is worth mentioning that the $\nu_{\rm NT}\Lambda$CDM model predicts a lower value of S_8 compared to other models. Specifically, we find $S_8(\nu\Lambda{\rm CDM}) = 0.831^{+0.012}_{-0.013}$ and $S_8(\Lambda{\rm CDM}) = 0.832 \pm 0.011$, in contrast to $S_8(\nu_{\rm NT}\Lambda{\rm CDM}) = 0.816^{+0.022}_{-0.016}$, representing a downward shift of $\gtrsim 1\sigma$. Consequently, the S_8 tension is mitigated from roughly $\sim 2.7\sigma$ to about $\sim 1.9\sigma$ in the non-thermal HDM model. Note that decrease of tension level comes through shift of posterior peak and increased uncertainties in S_8. It's worth noting that our constraints on $\Delta N_{\rm eff}$ in the non-thermal case are more stringent than those reported in Ref. Aghanim *et al.* (2018a) (with constraints being identical in the thermal case). So overall it results in a better fit to data. This discrepancy likely arises from the influence of running on physical parameters rather than just phenomenological parameters when exploring the parameter space.

With the inclusion of the prior on S_8, we observe a modest indication of non-zero values for $m_{\rm sp}^{\rm eff} = 0.67^{+0.26}_{-0.48}$ eV and $\Delta N_{\rm eff} = 0.0614^{+0.0052}_{-0.047}$ in the $\nu_{\rm NT}\Lambda$CDM model. In contrast, the constraints on the thermal neutrino mass simply relax to $m_\nu < 0.1$ eV. This leads to a deduced $S_8(\nu_{\rm NT}\Lambda{\rm CDM}) = 0.789 \pm 0.016$ and $S_8(\nu\Lambda{\rm CDM}) = 0.812 \pm 0.011$, as compared to the baseline $S_8(\Lambda{\rm CDM}) = 0.814^{+0.01}_{-0.011}$. As a result, the minimum χ^2 value in the combined analysis is lower in the non-thermal HDM

[6]Throughout, we present one-sided constraints at 95% confidence level (C.L.), and two-sided constraints at 68% C.L.

case, with $\Delta\chi^2_{\rm min}(\nu_{\rm NT}\Lambda{\rm CDM}) = \chi^2_{\rm min}(\Lambda{\rm CDM}) - \chi^2_{\rm min}(\nu_{\rm NT}\Lambda{\rm CDM}) = -4.8$, in comparison to the thermal neutrino case where $\Delta\chi^2_{\rm min}(\nu\Lambda{\rm CDM}) = \chi^2_{\rm min}(\Lambda{\rm CDM}) - \chi^2_{\rm min}(\nu\Lambda{\rm CDM}) = -1.4$. Should the S_8 tension intensify in the future, a more comprehensive Bayesian analysis comparing these models would be of interest. It is worth noting, however, that the total minimum χ^2 value is far less affected by the incorporation of the S_8 prior in the non-thermal case (+3.6) compared to the thermal case (+6.9). This is an encouraging sign, suggesting that the $\nu_{\rm NT}\Lambda$CDM model may potentially alleviate the tension between Planck and KIDS+BOSS. Nevertheless, it remains to be seen whether this holds true with additional data sets (and in the future, it should be validated against the full KiDS and BOSS likelihoods).

Before incorporating external data, we address the potential of non-thermal hot dark matter to reconcile the Hubble tension (as discussed in, for instance, Riess *et al.* (2020); Freedman *et al.* (2020); Di Valentino *et al.* (2021a) for an overview). Our findings indicate that, regardless of whether we incorporate the S_8 prior or not, the value of H_0 is scarcely influenced by the additional $\Delta N_{\rm eff}$ (in fact, it is even marginally shifted towards lower values of H_0 due to the well-established inverse relationship with $m^{\rm eff}_{\rm sp}$ Lesgourgues (2011)). As a result, we affirm that these models cannot account for the elevated H_0 measurement obtained from certain local probes.

3.4.1.2 Planck+BOSS+SN1a

Upon inclusion of the BAO/FS and SN1a data in our analysis, the constraints on both the thermal neutrino mass and the non-thermal hot dark matter mass become more stringent. In the $\nu_{\rm NT}\Lambda$CDM model, we obtain $m^{\rm eff}_{\rm sp} < 0.67$ eV and $\Delta N_{\rm eff} < 0.12$, while in the thermal case, we find $m_\nu < 0.04$ eV and $\Delta N_{\rm eff} < 0.27$. Nevertheless, the derived S_8 values, $S_8(\nu_{\rm NT}\Lambda{\rm CDM}) = 0.814^{+0.017}_{-0.014}$ and $S_8(\nu\Lambda{\rm CDM}) =$

0.83 ± 0.011, are marginally smaller compared to the Planck-only analysis. This is attributed to a slight reduction in the reconstructed value of $\omega_{\rm cdm}$ in the combined analysis with BAO/FS and SN1a data, regardless of the model.

Upon adding the prior on S_8 to the analysis, we again observe a modest indication of non-zero values for $m_{\rm eff} = 0.48^{+0.17}_{-0.36}$ eV and $\Delta N_{\rm eff} = 0.0457^{+0.0038}_{-0.031}$. However, the mean value has decreased by 0.5σ due to the inclusion of BAO/FS and SN1a data. This leads to a slightly higher reconstructed S_8 value, $S_8(\nu_{\rm NT}\Lambda{\rm CDM}) = 0.795^{+0.015}_{-0.013}$. A similar trend is observed in the thermal case, where the relaxation of the constraint to $m_\nu < 0.057$ eV is much milder than without BAO/FS and SN1a data, while the reconstructed $S_8(\nu\Lambda{\rm CDM}) = 0.814 \pm 0.01$ remains stable.

Examining the $\chi^2_{\rm min}$ values, we observe that the non-thermal case still provides a better fit, with $\Delta\chi^2_{\rm min}(\nu_{\rm NT}\Lambda{\rm CDM}) = -3.7$, compared to the thermal case with $\Delta\chi^2_{\rm min}(\nu\Lambda{\rm CDM}) = -1.8$. However, including the S_8 prior has increased the total $\chi^2_{\rm min}$ by +4.8 in the non-thermal case and +6.9 in the thermal case.

It is worth noting an interesting development: the tension level between Planck and KiDS increases from 1.9σ to 2.2σ once BAO data are included. In other words, these data exacerbate the tension. This contrasts the ΛCDM case, where the tension shifts from 2.9σ (without BAO) to 2.8σ (with BAO). Consequently, more accurate BAO/FS and SN1a data could present a substantial challenge to this model.

3.4.2 Understanding MCMC

To gain deeper insights into the outcomes of our MCMC analyses, we examine the residuals of the CMB TT, EE, lensing (top panel of figure 3.5), and matter (bottom panel of figure 3.5) power spectra in comparison to the ΛCDM model.

These results are based on the best-fit parameters obtained for the $\nu\Lambda$CDM and $\nu_{\rm NT}\Lambda$CDM models, considering both Planck+S8 and Planck+Ext+S8 data. Additionally, we display the transverse BAO (top panel), longitudinal BAO (middle panel), and growth factor (bottom panel) in Fig. 3.6.

A prominent observation is that, for a similar impact on the CMB power spectra, the corresponding suppression in the matter power spectrum is notably more pronounced in the $\nu_{\rm NT}\Lambda$CDM model compared to the $\nu\Lambda$CDM model. This discrepancy accounts for the $\nu_{\rm NT}\Lambda$CDM's superior performance in alleviating the S_8 tension.

Upon inspecting the BAO and $f\sigma_8$ predictions, the most significant disparity lies in the latter, which exhibits a substantial reduction at all redshifts in the $\nu_{\rm NT}\Lambda$CDM due to the aforementioned power suppression. This elucidates the slight degradation in χ^2 observed in the combined analysis with S_8. Furthermore, the inferred dark matter density $\omega_{\rm cdm}$ in the $\nu_{\rm NT}\Lambda$CDM experiences a downward shift of approximately $\sim 1\sigma$ (to compensate for the higher energy density stemming from the non-relativistic transition of the non-thermal neutrinos). This shift also contributes to a minor decrease in the fit to Planck data, albeit it is scarcely discernible in the CMB power spectra residuals.

This modest discrepancy in the matter density is also apparent in the small-k (large scales) branch of the matter power spectrum, which is particularly sensitive to Ω_m Lesgourgues *et al.* (2013). Although these distinctions do not definitively disqualify the $\nu_{\rm NT}\Lambda$CDM as a resolution to the S_8 tension, they offer an intriguing avenue for further probing the model with forthcoming data. This is especially relevant through precise measurements of the matter power spectrum, CMB lensing power spectrum, and growth factor $f\sigma_8$.

One potential method to enhance the results of the $\nu_{\rm NT}\Lambda$CDM model presented

here is to consider that the hot component arises from the decay of a metastable cold dark matter species in the late universe Abellan *et al.* (2020); Abellán *et al.* (2021b), rather than being present throughout all epochs. A satisfactory fit to all data can then be achieved when the mass ratio of the daughter to mother particle, ε, is approximately ~ 0.007, and the CDM lifetime $\tau \sim$ 55 Gyrs Abellán *et al.* (2021b).

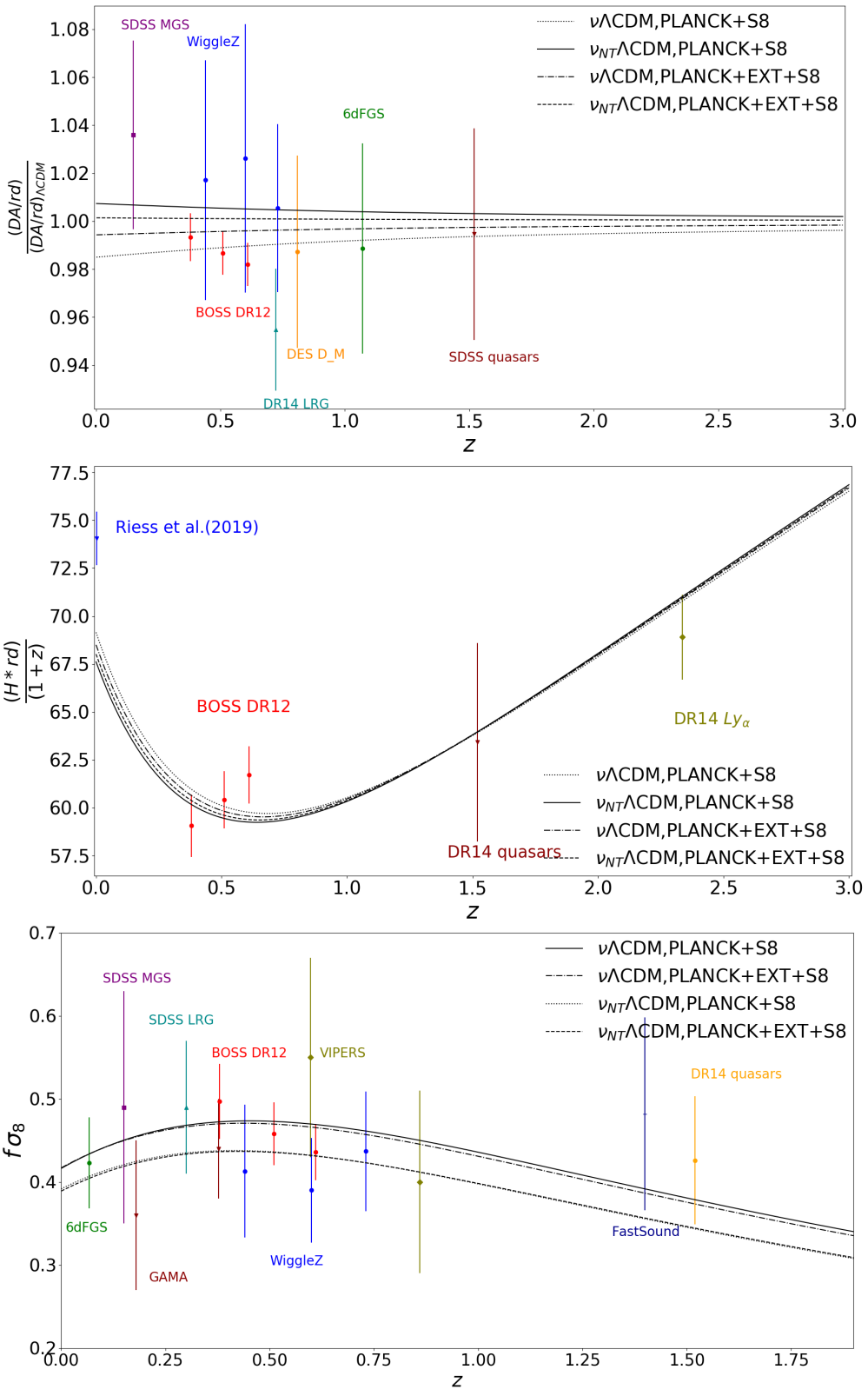

FIGURE 3.6: Transverse BAO (top panel), longitudinal BAO (middle panel) and growth factor (bottom panel) in the best fit $\nu\Lambda$CDM and $\nu_{\rm NT}\Lambda$CDM models for two different datasets (see legend). The 'Ext' data refers to BAO/FS+SN1a. The transverse BAO has been normalized to the ΛCDM prediction, as in Ref. Aghanim *et al.* (2020a).

Model	Non-thermal		Thermal		Dodelson Widrow	
Data set	$m_{\rm sp}$ [eV]	$B_{\rm sp}$	$m_{\rm sp}$ [eV]	$\frac{T_s}{T_\nu}$	$m_{\rm sp}$ [eV]	χ
Planck	0.05	0.01	0	0.40	0	0.03
Planck+S_8	38.62	0.012	11.36	0.43	26.43	0.03
Planck+Ext	18.98	0.01	04.59	0.36	12.85	0.02
Planck+Ext+S_8	39.81	0.01	11.75	0.43	27.49	0.03

TABLE 3.4: Best-fit values of the physical parameters in the non-thermal, thermal, and Dodelson-Widrow sterile neutrino models derived from our analyses.

3.4.3 Implication for other dark matter models

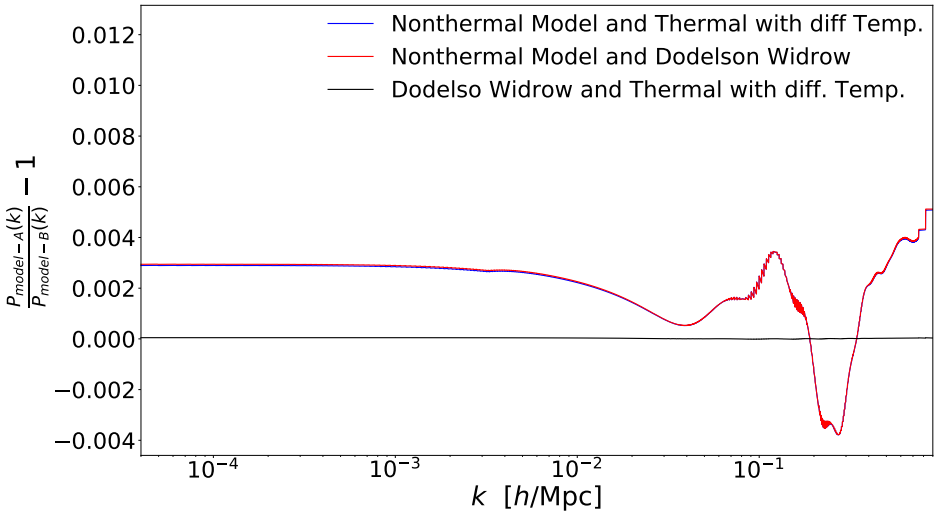

FIGURE 3.7: Residuals of linear matter power spectra for various nonthermal neutrino models. The residuals here are with respect to different models (see legend). Note that the residual plot of the nonthermal model to ΛCDM model is not shown because of the small differences, that lie upon each other.

As discussed in the introduction and detailed in section 3.2.1, it's important to note that any distribution sharing identical values for $\Delta N_{\rm eff}$ and $m_{\rm sp}^{\rm eff}$ as our model should also mitigate the σ_8 tension. Consequently, our findings can be leveraged to draw implications for the microscopic characteristics of models characterized by different momentum distributions than the ones we have employed. Here, we present such results for two specific models:

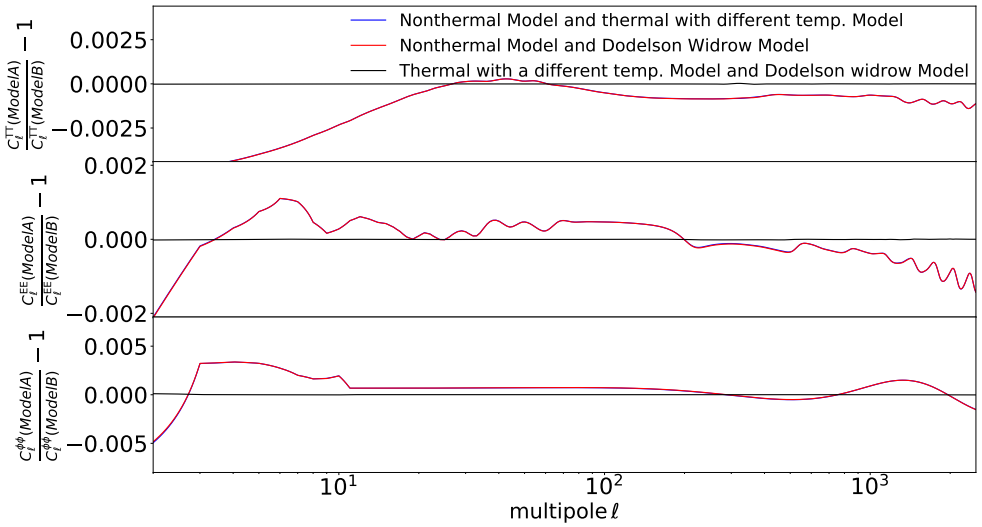

FIGURE 3.8: Residuals of CMB TT, EE, and $\phi\phi$ power spectra for a variety of nonthermal neutrino models. The residuals here are with respect to different models (see legend). Note that the residual plot of the nonthermal model to ΛCDM model is not shown because of the small differences, that lie upon each other.

a) Sterile particles at a distinct temperature from that of the Standard Model neutrinos. In this model, sterile neutrinos follow a thermal Fermi-Dirac Distribution, represented as:

$$\hat{f}(p) = \frac{1}{e^{p/T_s} + 1} \tag{3.12}$$

where T_s denotes the temperature of sterile particles. For a thermal sterile particle distribution with a Fermi-Dirac profile and a different temperature T_s, the quantities $\Delta N_{\rm eff}$ and ω_s are given by:

$$\Delta N_{\rm eff} = \left(\frac{T_s}{T_\nu^{\rm id}}\right)^4, \qquad \omega_s = \frac{m_{sp}}{94.05}\left(\frac{T_s}{T_\nu}\right)^3. \tag{3.13}$$

b) The Dodelson-Widrow distribution Dodelson and Widrow (1994a), defined as:

$$\hat{f}(p) = \frac{\chi}{1 + e^{p/T_\nu}}$$

In this distribution, T_ν represents the temperature of the neutrinos today, while χ is a parameter associated with the phenomenological parameters as described in

Acero and Lesgourgues (2009b). Specifically:

$$\Delta N_{\rm eff} = \chi, \qquad m_{\rm sp}^{\rm eff} = m_{\rm sp} \times \chi\,, \tag{3.14}$$

where $m_{\rm sp}$ represents the individual neutrino mass in this particular model. We present the model parameter values in Tab. 3.4, derived from translating our constraints on $\Delta N_{\rm eff}$ and $m_{\rm sp}^{\rm eff}$. Figures 3.7 and 3.8 showcase the discrepancies in the matter power spectra and CMB TT, TE, EE power spectra between our optimal non-thermal HDM model and these two counterparts. This conclusively establishes our assertion that once $\Delta N_{\rm eff}$ and $m_{\rm sp}^{\rm eff}$ are set, the observables become indistinguishable. We must note, however, that the residuals between the thermal neutrino model at different temperatures and our non-thermal HDM model are of a magnitude close to the sensitivity of forthcoming LSS experiments like EUCLID and LSST. As a result, this simple mapping might face limitations in the future.

We abstain from converting our reconstructed posterior on $\Delta N_{\rm eff}$ and $m_{\rm sp}^{\rm eff}$ into the model parameters to avoid potential biases from prior effects.

The values presented in Tab. 3.4 bear direct implications for the thermalized hidden sector, both from a particle physics Reece and Roxlo (2016) and cosmological standpoint Gariazzo *et al.* (2013); Cyr-Racine *et al.* (2014). Of particular interest is the pivotal parameter for constructing a thermal hidden sector model, namely the temperature ratio $\chi_s = \frac{T_s}{T_{vis}}$. Our analysis provides a competitive constraint on this parameter (though it is contingent on the specific model), which may carry significant ramifications for light sterile neutrino scenarios Gariazzo *et al.* (2013) or other models within the hidden sector particle physics framework Foot (2014); Franχ_b*ca et al.* (2013). If the thermally active hidden particle interacts with dark matter or other entities within the dark sector, our findings can offer constraints on the coupling and other particle physics parameters Brust *et al.* (2013).

It is intriguing to consider a potential connection between the hot dark matter under discussion and the longstanding (and debated) short baseline (SBL) anomalies Aguilar-Arevalo *et al.* (2001, 2013) (for recent reviews, see Maltoni; Dentler *et al.* (2018)). Specifically, within the "3+1" neutrino scenario, these anomalies could be explained by a sterile neutrino with $m_s \simeq \sqrt{\Delta m^2_{41}}$ 1eV and a mixing angle leading to $\Delta N_{\rm eff} \simeq 1$. However, our findings suggest that the sterile particles required to address the S_8 tension fall into a somewhat higher mass range, around $m_s \sim \mathcal{O}(10)$ eV (see Tab. 3.4), and exhibit an almost negligible $\Delta N_{\rm eff}$. Hence, our constraints, regardless of whether we include the S_8-prior or not, further affirm that a viable sterile neutrino solution to the SBL anomalies would necessitate an additional mechanism to curtail substantial $\Delta N_{\rm eff}$ production (for examples, see e.g. Hamann *et al.* (2011); Archidiacono *et al.* (2016); Chu *et al.* (2015); de Salas *et al.* (2015)). Nonetheless, it could be of interest to conduct an analysis incorporating results from short baseline neutrino oscillation experiments (e.g. with an additional prior, as in Ref. Gariazzo *et al.* (2013)). This is currently beyond the scope of our paper and is earmarked for future investigation.

Finally, we acknowledge that integrating data from experiments such as the Bicep2/Kek array Ade *et al.* (2016, 2018), SPT-3G Balkenhol *et al.* (2021), or ACT Aiola *et al.* (2020) could offer further constraints on the sterile neutrino parameters, thanks to their higher precision measurements of the CMB damping tail and lensing spectrum. We defer this to future studies but refer to Refs. Roy Choudhury and Choubey (2019a); Balkenhol *et al.* (2021) for examples (typically resulting in an increase in constraints by approximately $\sim 10\%$, without considering a prior on S_8).

3.5 Discussion and Conclusions

This paper has delved into the potential solution to the persistent 'S_8-tension'. We have considered the existence of a non-thermal HDM component contributing fractionally to the DM density in the universe. There is suppression in the matter power spectra at small scales due to this new component (a product of moduli decay). However, we argued that any similar model that contributes to the same $\Delta N_{\rm eff}$ and $m_{\rm sp}^{\rm eff}$ as our model (without having new physics elements additionally) would yield comparable effects on the cosmological observables; thus, our constraints can be generalized to a broader class of HDM models.

For our extensive MCMC analysis, we used the latest data from Planck, BOSS ($f\sigma_8$ and BAO), and Pantheon, both with prior and without prior on the value of S_8 obtained from KiDS/Viking+BOSS+2dFLens data. Our key findings are as follows:

- The $\nu_{\rm NT}\Lambda$CDM model demonstrates potential in alleviating the tension between Planck and S_8 measurements, albeit this resolution weakens when we include BOSS and Pantheon data.
- The $\nu_{\rm NT}\Lambda$CDM leads to a notably stronger suppression in the matter power spectrum at small scales compared to standard model thermal neutrinos for a similar impact on the CMB power spectrum, consequently resulting in a more significant reduction in σ_8.
- While the $\nu_{\rm NT}\Lambda$CDM model exerts minimal impact on the BAO scale and luminosity distance, it does affect $f\sigma_8$ predictions. This implies that the $\nu_{\rm NT}\Lambda$CDM model is mildly constrained by current BOSS (growth factor) measurements and the forthcoming data of the matter power spectra and $f\sigma_8$ at late-times will serve as further tests.

- We connected our model and generic phenomenological parameters that are generally constrained by the observational data. Thus we translated our constraints to the other similar nonthermal HDM models such as the Dodelson-Widrow models or a thermal sterile particle with a different temperature in the hidden sector. Our study provides competitive constraints on the hidden sector temperature of the thermal model and the scaling parameter of the Dodelson Widrow model, which may hold intriguing particle physics implications, particularly in the context of Short Baseline anomalies Aguilar-Arevalo *et al.* (2001, 2013); Maltoni; Dentler *et al.* (2018).

In conclusion, it would be intriguing to subject this model to a Lyman-α forest flux power spectrum analysis akin to recent works Wang *et al.* (2013); Murgia *et al.* (2017); Baur *et al.* (2017); Murgia *et al.* (2018); Archidiacono *et al.* (2019); Miller *et al.* (2019b); Palanque-Delabrouille *et al.* (2020); Enzi *et al.* (2020). This could potentially probe the model given its distinctive spectrum behavior at certain scales. Nevertheless, it's important to note that the non-thermal neutrino-like HDM constitutes only a small portion of the total DM budget of the universe, and the constraints may not straightforwardly apply to the model due to the suppression's halt at larger scales.

Moreover, the recent study related to the thermal warm dark matter and neutrinos has shown a mild tension (3σ) between Lyman-α and Planck data Palanque-Delabrouille *et al.* (2020). Given the σ_8 tension, it would be worthwhile to thoroughly examine whether a non-thermal hot dark matter model can contribute to resolving the "Lyman-α tension". Additionally, the forthcoming high-precision observational data for the matter-power spectra at small scales by surveys like Euclid Amendola *et al.* (2018), LSST Alonso *et al.* (2018), and DESI Aghamousa *et al.* (2016) can further scrutinize these models as potential resolutions to the S_8-tension.

χ^2 Tables referred in the main text

We report $\chi^2_{\rm min}$ per experiment in each analysis.

Data sets	ΛCDM			
Planck high$-\ell$ TT,TE,EE	2346.7	2350.8	2346	2349.1
Planck low$-\ell$ EE	396	396.1	396.8	396.2
Planck low$-\ell$ TT	23.2	22.5	23.4	22.6
Planck lensing	8.8	9.6	9.2	9.1
Pantheon set	–	–	1026.9	1026.7
BOSS DR12 (BAO/FS)	–	–	6.9	6.5
BOSS low$-z$	–	–	1.2	2.3
KiDS/BOSS/2dFGS	–	4.6	–	5.9
total	2774.8	2783.4	3810.4	3818.2

TABLE 3.5: Minimum of χ^2 for each data sets (also total) in the ΛCDM model.

Data sets	νΛCDM			
Planck high$-\ell$ TT,TE,EE	2345.98	2348.2	2346.9	2348.6
Planck low$-\ell$ EE	396.54	396.8	396.5	395.7
Planck low$-\ell$ TT	23.3	22.2	22.8	22.4
Planck lensing	9.03	8.9	8.8	9.3
Pantheon data	–	–	1026.8	1026.7
BOSS DR12(BAO/FS)	–	–	6.1	5.9
BOSS low$-z$	–	–	1.7	1.7
KiDS/BOSS/2dFGS	–	5.8	–	6.1
total	2774.9	2782.0	3809.5	3816.4

TABLE 3.6: Minimum of χ^2 for each data sets (also total) in the model with massive thermal neutrinos and additional relativistic degrees of freedom.

Experiment	$\nu_{\rm NT}\Lambda$CDM			
Planck high$-\ell$ TT,TE,EE	2346.7	2348.7	2 2346.4	2349.1
Planck low$-\ell$ EE	396.3	395.9	396.8	396.9
Planck low$-\ell$ TT	23.1	23.3	23.4	23.1
Planck lensing	8.8	9.2	8.8	9.1
Pantheon data	–	–	1026.8	1026.7
BOSS DR12(BAO/FS)	–	–	6.1	6.8
BOSS low$-z$	–	–	1.4	1.7
KiDS/BOSS/2dFGS	–	1.6	–	1.2
total	2775.0	2778.6	3809.7	3814.5

TABLE 3.7: Minimum of χ^2 for each experiment (also total) in the non-thermal sterile neutrino model.

Chapter 4

Nonlinear Signatures of Light massive relics[1]

4.1 Introduction

The pursuit of understanding the fundamental constituents of Dark Matter, or the mysterious dark sector that interacts weakly with the visible domain, continues to propel research at intersecting particle physics and cosmology. The Early efforts in constructing models of Dark Matter around the Weakly Interacting Massive Particle (WIMP) concept featuring a single cold, non-collisional component. However, diverse and well-grounded models have emerged in recent years, proposing a more complex dark sector.

Some of the models support the existence of massive yet light particles, constituting a minor portion of the dark sector and, consequently, the Universe's total energy content (e.g. Cheung and Yuan 2007; Feldman *et al.* 2007; Abel *et al.* 2008;

[1]This chapter is based on publication Banerjee *et al.* (2022)

Burgess *et al.* 2008; Arkani-Hamed and Weiner 2008; Essig *et al.* 2009; Arvanitaki *et al.* 2010; Beranek *et al.* 2013; Chacko *et al.* 2015; Arkani-Hamed *et al.* 2016). In certain extensions of neutrino sector theories beyond the standard model of particle physics, these lightly massive relics could easily possess mass within the eV range (Das and Weiner 2011; Abellán *et al.* 2021b; Bjaelde and Das 2010). Other concealed sector relics originating from various particle physics theories are also discussed in works such as Das and Sigurdson (2012); Ko *et al.* (2017); Bogorad and Toro (2021). This chapter refers to these entities as Light Massive Relics (LiMRs).

LiMRs can influence both the epoch of the CMB and the later epochs in the Universe. If these particles are not entirely non-relativistic during recombination, they mimic "dark radiation," so their impact can be detected through parameter $\Delta N_{\rm eff}$ (deviations in $N_{\rm eff}$ from standard scenarios). Even if at late times, LiMRs turn non-relativistic, their thermal velocities are so high compared to their gravitational peculiar velocities. Corresponding to such high velocities, often a characteristic free-streaming scale is associated. On the scales below the free-streaming scale, the growth in perturbations of the LiMR component is damped. If LiMRs constituents a significant fraction of dark matter, it suppresses the growth of matter perturbations at small scales. Recent studies have explored limitations on such models by combining observations from both the early Universe observational probes (e.g. CMB) and the later Universe observational probes (e.g., galaxy clustering and lensing), (as seen in Baumann *et al.* 2016; Banerjee *et al.* 2018a; DePorzio *et al.* 2021; Xu *et al.* 2021).

LiMRs can be thermal or non-thermal in nature, depending on their origin. Light sterile neutrinos with masses in the eV range are one of the candidates for LiMRs.

These sterile neutrinos are potentially linked to Short Baseline (SBL) anomalies.[2]. The CMB and Large-scale Structure (LSS) observations notably limit the simplest scenario where this new light sterile neutrino species remains inert and free-streaming. In such a minimal context, reconciling SBL anomalies while remaining consistent with CMB and LSS data becomes highly improbable. Consequently, several models have been proposed that extend beyond the basic non-interacting thermal LiMR concept, introducing hidden interactions Archidiacono *et al.* (2020) or alternative non-thermal or partially thermal distribution functions Archidiacono *et al.* (2013).

Meanwhile, recent investigations have uncovered a consistent 2σ-3σ discrepancy between the forecasts of later-stage clustering as projected by the optimal-fit model to the *Planck* CMB primary data (Planck Collaboration and Aghanim 2020) and the empirical measurements (e.g. Krolewski *et al.* 2021; DES Collaboration *et al.* 2021; Tröster *et al.* 2021; Hikage *et al.* 2019; Ivanov *et al.* 2020; D'Amico *et al.* 2020). This disparity is commonly contextualized in terms of variations in the σ_8 value, representing the amplitude of matter fluctuations on an $8h^{-1}$Mpc scale based on linear perturbation theory, or in relation to $S_8 = \sigma_8(\Omega_m/0.3)^{0.5}$. Although the outcomes of the *Planck* data and low-redshift observations do not inherently conflict from a statistical standpoint, the recurring trend among all low-redshift analyses revealing a lower σ_8 value lends intrigue to this matter. With LiMR models inherently introducing power damping on minor scales, they offer a tangible avenue for resolving the σ_8 discrepancy. Consequently, it becomes imperative to thoroughly explore LiMR phenomenology within the context of structure formation, encompassing both particle physics and cosmological viewpoints.

Despite extensive scrutiny of the effects of LiMRs on structure formation and the

[2]Recent findings from the MicroBooNE experiment Abratenko *et al.* (2021); Argüelles *et al.* (2021) challenge the sterile neutrino interpretation of the MiniBooNE anomaly as electron neutrino appearance from a muon neutrino beam. However, a recent analysis indicates a 2.2σ preference for an eV-scale sterile neutrino mass if the MicroBooNE data is considered as electron neutrino disappearance Denton (2021).

potential limitations imposed on LiMR models by survey data for large (linear) scales, the precise ramifications on nonlinear scales (below $\sim 10h^{-1}$Mpc), particularly concerning nonthermal LiMRs, have remained uncharted — for discussions regarding small-scale effects of thermal LiMRs, refer to Brandbyge and Hannestad (2017)[3]. A comprehensive investigation into these effects becomes essential, given the compelling theoretical grounds supporting LiMRs and the imminent observational pursuits targeting these scales. Furthermore, the σ_8 disparity is a direct empirical incentive to characterize the nonlinear effects of LiMR models. In light of this incongruity, it is vital to grasp the interplay between the influences of LiMRs and potential rescalings or adjustments in the tilt of the initial power spectrum within the ΛCDM framework. Both scenarios lead to modifications in the linear σ_8, thus highlighting the significance of their effects on smaller scales for distinguishing between models. Moreover, nonlinear scales possess the potential to differentiate between various LiMR models featuring distinct velocity distributions. In linear theory, the progression of perturbations is determined by the effective velocity dispersion, namely the second moment of the velocity distribution, rather than the overall distribution itself. This implies that different LiMR models could yield identical effects on larger scales, provided their velocity dispersions match, even if their actual distributions substantially differ. Conversely, on nonlinear scales, the clustering of the LiMR component can be highly sensitive to the intricacies of the velocity distribution, providing a means to discriminate between models.

Building upon these significant considerations, this study employs cosmological N-body simulations to trace LiMR cosmologies' nonlinear evolution meticulously. The approach involves a direct representation of both the LiMR component and the CDM+baryon component. The investigation delves into the impacts on specific cosmological observables of relevance to ongoing and upcoming photometric

[3]For cosmologies involving mixed dark matter with somewhat heavier relics, refer to works such as Parimbelli *et al.* (2021); Anderhalden *et al.* (2013); Boyarsky *et al.* (2009); **?**

surveys, including the DES[4] and the Legacy Survey of Space and Time (LSST) by VRO[5]. Our examination encompasses LiMRs characterized by explicitly nonthermal velocity distributions and those that can be matched to thermal distributions.

Given the extensive array of potential LiMR models, our analysis relies on a particular model for this inaugural exploration. Specifically, we adopt the model presented in Bhattacharya *et al.* (2021b); Das *et al.* (2022), a choice aligned with its relevance due to its implications in the context of the σ_8 tension Das *et al.* (2022). The study involves a comparative analysis, contrasting the predictions originating from the LiMR model against the Planck best-fit ΛCDM model. Furthermore, we juxtapose the nonlinear predictions stemming from the LiMR model with those of an ΛCDM universe wherein the linear power spectrum has been globally rescaled to align its σ_8 with that of the LiMR model. The methodologies developed here readily extend to various LiMRs featuring diverse velocity distributions as long as they exhibit minimal interactions. In section 4.4, we demonstrate the generalizability of our outcomes and discoveries to other LiMR models explored within the literature, such as LiMRs following a Dodelson-Widrow distribution (Dodelson and Widrow 1994b). We also outline the scenarios under which their predictions diverge.

4.1.1 Nonthermal Relics

LiMRs characterized by negligible interactions are fully defined by their distribution functions and mass. Within the linear theory, the physics primarily responds to the first two moments of these distribution functions (refer to Acero and Lesgourgues 2009a), culminating in observables contingent on two associated parameters. The foremost parameter is the effective mass ($m_{\rm eff}$), a gauge of the sterile

[4]https://www.darkenergysurvey.org/
[5]https://lsst.org/

particles' contribution to the present-day energy density, given by:

$$\frac{m_{\rm eff}}{94.05{\rm eV}} \equiv \left[m_{\rm sp}\int dp\ p^2 f(p)\right] \times \left[\frac{h^2}{\rho_c^0}\right], \tag{4.1}$$

where $m_{\rm sp}$ denotes the mass of sterile particle, and ρ_c^0 denotes the universe's current total energy density. The second parameter, $\Delta N_{\rm eff}$, quantifies the effective relativistic degrees of freedom during neutrino decoupling:

$$\Delta N_{\rm eff} \equiv \left[\int dp\ p^3 f(p)\right] / \left[\frac{7}{8}\frac{\pi^2}{15}{T_\nu}^4\right], \tag{4.2}$$

with $T_\nu \equiv (4/11)^{1/3} T_{\rm cmb}$, the present-day temperature of the cosmic neutrino background. The linearity of cosmological dynamics, dictated by a mere two parameters, implies that both the CMB and linear matter power spectra do not comprehensively probe specific LiMR models. Addressing this limitation, the objective of this chapter, as introduced earlier, involves scrutinizing nonlinear signatures.

Let's briefly revisit the LiMR distribution functions that hold relevance for our discussion.

Dodelson-Widrow Distribution: The Dodelson-Widrow momentum distribution is given by Dodelson and Widrow (1994b):

$$f(p) = \frac{\chi}{\exp({\rm p}/{\rm T}_\nu) + 1}\ ,$$

where χ is a model parameter, this distribution function can be equivalently expressed as a thermal distribution function with a temperature different from T_ν through parameter redefinition. It finds widespread use in the context of sterile

neutrino relics.

Gaussian Distribution: Non-equilibrium decays can yield distribution functions that approximate a Gaussian form (see, for instance Cuoco *et al.* 2005):

$$f(\vec{p}) = N\frac{T_\nu^3}{|\vec{p}|^2}\exp\left(-\left(\frac{(|\vec{p}|-p_0)^2}{2\sigma^2}\right)\right);$$
$$N = \left(4\pi\sqrt{2\pi\sigma^2}\right)^{-1}.$$

where p_0 and σ are model parameters.

Non-thermal Distribution from Decays: Non-thermal distribution of LiMRs can also stem from the decay of a heavy scalar (Hasenkamp and Kersten 2013a; Conlon and Marsh 2013a; Miller *et al.* 2019a; Bhattacharya *et al.* 2021b). In this scenario, the distribution function's exact form is somewhat intricate. Here, we provide a qualitative description of the production process and direct readers to the aforementioned references for precise distribution function details. At the universe's early stages, the energy density is dominated by cold particles of a species φ. φ subsequently decays into the Standard Model sector and a light sterile particle (the LiMR). Although the Standard Model sector attains thermal equilibrium, the sterile particles remain non-thermalized. The LiMR production rate hinges on the φ particle's decay rate and the branching ratio for the LiMR channel. The LiMRs' late-time momentum distribution results from redshifting them from their production time. The distribution function is characterized by the mass of the heavy particle (m_φ), its decay rate (τ), and the branching ratio for decay into LiMRs ($B_{\rm sp}$).

In the study conducted by Das *et al.* (2022), a detailed analysis using the MCMC method was undertaken to examine sterile Light Massive Relics (LiMRs) in light

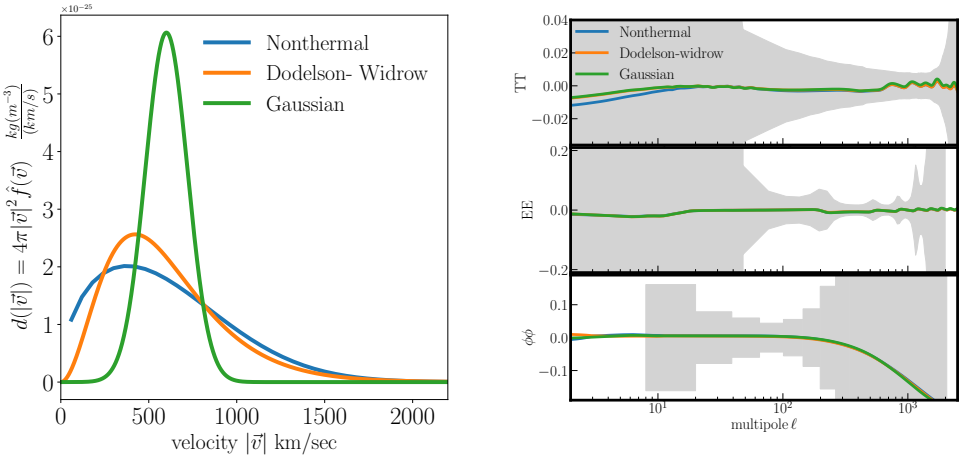

FIGURE 4.1: Left panel: Comparision of the velocity distribution corresponding to three nonthermal models, namely the Nonthermal distribution from decays (blue), Dodelson Widrow model (orange), and the Gaussian distribution (Green) at redshift z = 99. All the plots corresponds to $\Delta N_{\rm eff} = 0.034$ and $m_{\rm eff} = 0.90$eV. Right panel: The Residuals of CMB C_l^{TT}, C_l^{EE}, and $C_l^{\phi\phi}$ power spectra for all three models (see legend) to ΛCDM model using best-fit values of *Planck* data with a late-time S_8 prior. The grey shaded area is the Planck 2018 1σ uncertainties. $\Delta N_{\rm eff} = 0.034$ and $m_{\rm eff} = 0.90$eV in all three cases. All three models are indistinguishable from the baseline ΛCDM model given the *Planck* error bars.

of contemporary data from sources including *Planck* (Planck Collaboration and Aghanim 2020), BOSS (BAO and $f\sigma_8$) (Beutler *et al.* 2011; Ross *et al.* 2015; Alam *et al.* 2017a), and Pantheon data (Scolnic *et al.* 2018a). The investigation was carried out both with and without incorporating a prior linked to the value of S_8, as gauged by KiDS/Viking+BOSS+2dFLens data (Heymans *et al.* 2020). The study revealed that the tension between *Planck* and S_8 measurements could be alleviated through the presence of the nonthermal LiMR component. The optimal fit parameters derived from *Planck* data, incorporating an S_8 prior, were $\Delta N_{\rm eff} = 0.034$ and $m_{\rm eff} = 0.90$ eV. In terms of parameters pertinent to the late-time Universe, these constraints translate to $\Omega_{\rm LiMR} \approx 0.021$ at $z = 0$. These effective boundaries on $m_{\rm eff}$ and $\Delta N_{\rm eff}$ are convertible to parameters for the discussed models above[6]: for the Dodelson-Widrow Model, the deduced best-fit

[6]For both the Gaussian distribution and the nonthermal distribution from decays, specific values of $\Delta N_{\rm eff}$ and $m_{\rm eff}$ don't single out precise points in their parameter spaces but rather

values imply $\chi = 0.034$ and $m_s = 26.43$ eV. In the case of the Gaussian distribution, they suggest $p_0 = 0.01957T_\nu$, $\sigma = p_0/5$, and $m_{\rm sp} = 0.1644$ eV. Finally, for the nonthermal distribution from decays, the values are $m_\varphi = 10^{-6}M_{\rm pl}$, $\tau = 10^8/m_\varphi$, $B_{\rm sp} = 0.0118$, and $m_{\rm sp} = 38.62$ eV. The parameter matching implies that the three models exhibit indistinguishable behavior at the linear level. Visual representation of the residuals of the CMB C_l^{TT}, C_l^{EE}, and $C_l^{\phi\phi}$ for all three models compared to the baseline ΛCDM model, utilizing the best-fit values from *Planck* and S_8 data, is presented in Fig. 4.1. Notably, all residuals fall within the Planck 2018 1σ uncertainties, thus confirming the statistical indistinguishability of the models, as anticipated.

The pivotal input necessary for calculating the impact of Light Massive Relics (LiMRs) at the non-linear scale is the normalized velocity distribution ($\hat{f}(\vec{v})$) at the initialization redshift of $z = 99$, a customary practice in simulations, as elaborated upon in the subsequent section. This normalized distribution is conveniently derived from the momentum distribution functions of the LiMRs. In Fig. 4.1, we present the normalized velocity distributions for the three models under consideration. Notably, this velocity distribution pertains to the underlying background and does not encompass the peculiar velocities stemming from perturbations within the density field. The latter aspect is comprehensively addressed in the ensuing section.

To maintain the paper's coherence, our primary focus within the main text will revolve around the non-thermal distribution originating from decays, as discussed in (Bhattacharya *et al.* 2021b; Das *et al.* 2022). Specifically, the model's parameters will be adopted in accordance with the description provided above, signifying the best-fit parameters aligned with Planck data in conjunction with an S_8 prior. In section 4.4, we will document the outcomes pertaining to the other models and

specify subspaces. For these models, we will select particular points from these subspaces while reserving in-depth exploration of the entire parameter spaces for future endeavors.

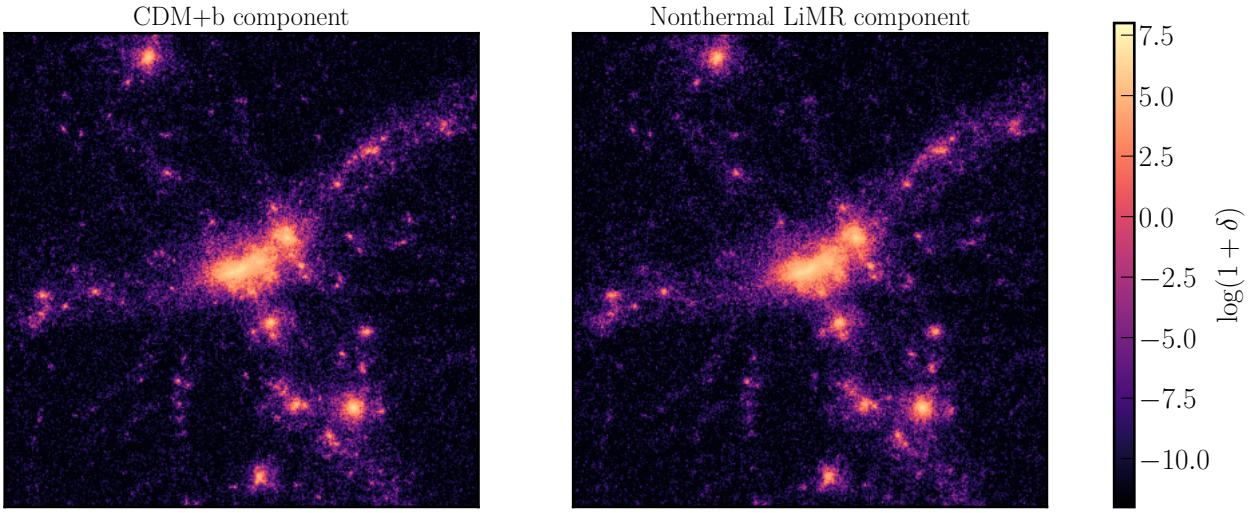

FIGURE 4.2: Projected density fields from a $(30h^{-1}\text{Mpc})^3$ simulation volume from the model with a LiMR component. The left panel shows the simulation's projected density field for the CDM+b component. The right panel shows the projected density field of the LiMR component. While the cosmic web structure is clear in both components, the LiMR structures are more smeared out(not directly visible to eyes). Note LiMRs parameters are chosen to best fit Planck 18 Das *et al.* (2022)

delve into the potential for distinguishing between these models by harnessing the information conveyed by non-linear signatures.

4.2 Methodology

To investigate the non-linear evolution of matter perturbations in LiMR models and compare the outcomes with those of the *Planck* best-fit Λ-CDM model at low redshifts, we employ N-body simulations. These simulations use a suitably adapted version of the publicly available cosmological N-body code GADGET2 (Springel 2005). For simulations involving the LiMR model, two types of particles are utilized: one type represents the mass-weighted average of the Cold Dark Matter (CDM) and baryon constituents, while the other stands for the LiMR component. The particle masses are determined based on the background abundances of these distinct components. It's important to note that standard neutrinos are

not explicitly modeled in the simulations employed in this study. Instead, they are incorporated into the background evolution, where a value of $M_\nu = 0.06$ eV is used. This approach is justifiable because this value typically induces an effect on the power spectrum of approximately 5%, which is considerably smaller than the effects arising from the LiMR model. Thus, we adopt the simplifying assumption of not actively simulating Standard Model (SM) neutrinos for the current investigation. The joint modeling of both these light components will be addressed in future research.

Generating initial conditions involves leveraging the linear power spectrum and growth rate of various components at $z = 99$ from the publicly accessible Boltzmann code CLASS (Blas *et al.* 2011). The requisite modifications to incorporate LiMRs, encompassing different velocity distributions, within CLASS have been verified and discussed in Das *et al.* (2022). These modified outputs are subsequently translated into the initial positions and velocities of particles in the N-body simulation utilizing the Zel'Dovich approximation (Zel'Dovich 1970), a procedure implemented through the NGenIC code[7]. To account for the fact that the N-body evolution does not incorporate the radiation component, unlike the CLASS outputs (see e.g. Zennaro *et al.* 2017, for an in-depth discussion), an overall rescaling of the $z = 99$ power spectrum is applied. This adjustment ensures that the simulations accurately capture the correct linear growth rate on large scales at $z = 0$.

In the context of the CDM simulation particles, their initial positions and velocities are solely determined by the $z = 99$ power spectrum and growth rate. However, an additional consideration arises for the simulation particles representing the LiMR component due to the substantial velocity distribution, elaborated upon in Section 4.1.1. Regarding SM neutrinos, there is a lot of literature available about various approaches for integrating the velocity distribution into cosmic N-body

[7]https://www.h-its.org/2014/11/05/ngenic-code/

simulations, as well as their benefits and limitations (see e.g. Ali-Haïmoud and Bird 2013; Brandbyge *et al.* 2008; Elbers *et al.* 2021; Viel *et al.* 2010; Banerjee and Dalal 2016; Banerjee *et al.* 2018b; Bayer *et al.* 2021, and references therein). To assign velocities to the LiMR particles in our work, we use a mechanism similar to that used in Viel *et al.* (2010). The technique is given shortly below: The Cumulative Distribution Function CDF(v) is computed starting with a theoretical velocity distribution $f(v)$. CDF(v), by definition, takes values between 0 and 1. Generate a random number x from a uniform distribution inside the interval $(0, 1)$ for each LiMR particle in the simulation. Subsequently, the velocity v^* satisfying $\mathrm{CDF}(v^*) = x$ is selected as the magnitude of the velocity attributed to the particle. Furthermore, a random direction within the simulation box is chosen, and this velocity is added as a 3-vector to the gravitational peculiar velocity derived from the linear $P(k)$ and growth factor. This procedure is iteratively applied for each LiMR particle in the simulation[8].

In this configuration, we conduct two distinct simulations: one involves the non-thermal LiMR component, while the other corresponds to the ΛCDM best-fit model, both within $(1\ \mathrm{h}^{-1}\mathrm{Gpc})^3$ volumes. Additionally, a separate ΛCDM simulation is carried out with the goal of matching the value of σ_8 at $z = 0$ to that of the nonthermal LiMR cosmology. To ensure a consistent basis for comparison, the same seed is utilized to generate pseudo-random numbers in the initial conditions module for the amplitude and phase of each mode. This ensures that all three simulations pertain to the same "realization" of their initial power spectrum, thus mitigating the influence of sample variance. Specifically, for the ΛCDM simulations, a particle count of 1024^3 is used to represent both the CDM and baryonic components, with a particle mass of $7.92 \times 10^{10} M_\odot/h$. Correspondingly, for simulations involving nonthermal LiMRs, an additional 1024^3 particles are allocated to represent this component, with particle masses of $7.51 \times 10^{10} M_\odot/h$ and

[8]While in principle, the velocity distribution of the LiMR could be influenced by the local potential (see e.g. Bird *et al.* 2018), at sufficiently high redshifts, where typical LiMR velocities dwarf gravitationally-induced peculiar velocities, the assumption of a position-independent velocity distribution is well-justified.

$5.51 \times 10^{10} M_{\odot}/h$ for the CDM+baryon and LiMR simulations, respectively. The force softening scale for both simulations is set at 25 h^{-1}kpc.

In Figure 4.2, we present the projected density fields from the simulation incorporating the LiMR component. This visualization showcases two distinct fields: the CDM+baryon component displayed on the left and the LiMR component on the right. Owing to the initial velocity distribution of the LiMR component, the resulting structures exhibit a "fuzzier" appearance characterized by less prominent peaks and voids, as compared to the CDM+baryon component. Dark matter halos are identified by employing the ROCKSTAR halo finder code (Behroozi *et al.* 2013), which identifies halo positions and masses using solely the GADGET Type 1 particles, representing the CDM+baryon component within the simulations. While this approximation may introduce some inaccuracies in terms of identifying halo centers and boundaries, it's a widely used approach within the context of massive neutrino literature (e.g., Liu *et al.* (2018); Villaescusa-Navarro *et al.* (2020)), regardless of the specific halo finder algorithm employed. Although the exact level of inaccuracy stemming from this approximation isn't quantified within the context of LiMR models in this work, it's noteworthy that since the CDM+baryon component clusters more intensely than the LiMR component, halos are predominantly governed by CDM+baryon matter, both in comparison to the overall universe and the background. In terms of proportion, the considered LiMR model constitutes approximately 7% of the total matter, signifying its subdominant role in the background. Consequently, within the virialized regions of halos, its influence is expected to be even more marginal. Throughout the remainder of this chapter, we employ the $M_{\rm vir}$ and $R_{\rm vir}$ values reported by ROCKSTAR to denote the mass and radius of halos.

4.3 Results

In this section, we present the outcomes derived from the N-body simulation and delve into the distinctions between the Planck best-fit ΛCDM model and the nonthermal LiMR model, focusing on three distinct "observables." As previously indicated, our attention in this section is directed solely towards the outcomes of simulations involving the nonthermal LiMR model (Bhattacharya *et al.* 2021b). A comprehensive comparison involving other LiMR models defined by their velocity distributions is available in section 4.4.

4.3.1 Power Spectrum

Our initial examination concerns the comparison of the nonlinear matter power spectrum at $z = 0$ between the ΛCDM simulation and the nonthermal LiMR simulation. For the nonthermal LiMR cosmology, multiple power spectra can be formulated. The total matter power spectrum, denoted as $P_{\rm m}(k)$, is expressed as follows:

$$P_{\rm m}(k) = f_{\rm cb}^2 P_{\rm cb}(k) + 2 f_{\rm cb} f_{\rm nt} P_{\rm cb,nt} + f_{\rm nt}^2 P_{\rm nt}\,, \tag{4.3}$$

where the subscript cb pertains to the CDM+baryon component, the subscript nt pertains to the nonthermal LiMR component, and:

$$f_{\rm cb} = \frac{\Omega_{\rm cb}}{\Omega_{\rm cb} + \Omega_{\rm nt}}\ ;\ f_{\rm nt} = \frac{\Omega_{\rm nt}}{\Omega_{\rm cb} + \Omega_{\rm nt}}\,. \tag{4.4}$$

In this specific model, $f_{\rm nt} = 0.068$ and $f_{\rm cb} = 0.932$. $P_{\rm cb}(k)$ signifies the auto power spectrum of the CDM+baryon component, $P_{\rm nt}$ represents the auto power spectrum of the nonthermal component, and $P_{\rm cb,nt}$ indicates the cross power spectrum between the two components. It's important to note that while observables such as weak and strong lensing, contingent on the total gravitational potential, are

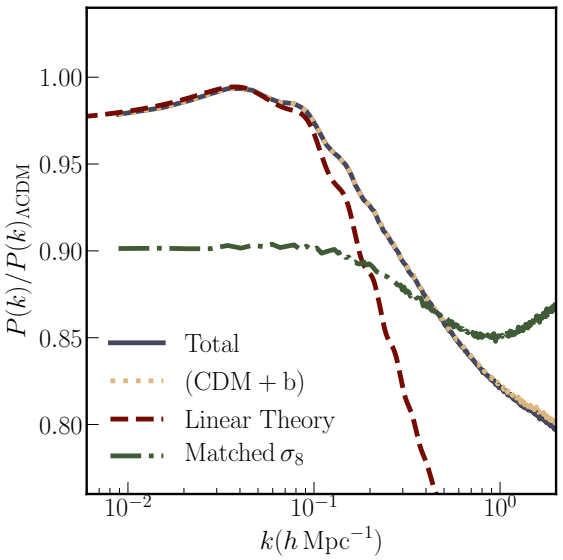

FIGURE 4.3: Ratio of matter-power spectrum of nonthermal LiMRs with respect to the ΛCDM model. Solid blue lines represent the total matter power spectra; the matter power spectra corresponding to only CDM+baryon components are shown in dashed yellow lines. The dashed maroon line also shows the linear prediction of total matter power spectra. The green dashed line corresponds to ΛCDM model for which the value of σ_8 is matched to the nonthermal model (by adjusting amplitude parameter (A_s)).

directly influenced by $P_{\rm m}$, the clustering of galaxies, determined by the peaks of overdensities in the CDM+baryon component, is directly impacted by $P_{\rm cb}$. The other two components, $P_{\rm nt,cb}$ and $P_{\rm nt}$, do not correspond directly to any cosmological observable. In a pure ΛCDM cosmology, $P_{\rm m}$ and $P_{\rm cb}$ coincide. However, in massive neutrino cosmologies, such as this one, the distinction can be significant (Villaescusa-Navarro *et al.* 2014; Banerjee and Dalal 2016; Banerjee *et al.* 2020b).

In Figure 4.3, we depict the ratio of various $P(k)$ to the $P(k)$ derived from the Planck best-fit ΛCDM simulation. The solid blue line symbolizes the ratio for the total $P_{\rm m}(k)$ from the nonthermal LiMR simulation, while the dotted yellow line illustrates the ratio for $P_{\rm cb}$. For reference, the linear theory forecast for the ratio of $P_{\rm m}(k)/P(k)_{\Lambda\rm CDM}$ is depicted with the dashed maroon line. Evidently, the damping of both $P_{\rm m}$ and $P_{\rm cb}$ on small scales is evident; however, the magnitude of damping is notably lower compared to the linear theory prediction. This aligns

with the findings from Brandbyge and Hannestad (2017) in the context of thermal LiMRs. Nonetheless, the observed damping of around 15% at $k \sim 1\,h\mathrm{Mpc}^{-1}$ remains substantially larger than the damping attributed to standard neutrinos with $M_\nu = 0.06\mathrm{eV}$. Importantly, contrary to the standard neutrino case where substantial damping typically begins at $k \sim 10^{-2}\,h\mathrm{Mpc}^{-1}$, the onset of damping in this scenario transpires at $k \sim 10^{-1}\,h\mathrm{Mpc}^{-1}$. The divergence in the damping scale, associated with the free-streaming scale of the LiMR, stems from the variance in velocity distribution between nonthermal LiMRs and standard neutrinos. The dot-dashed green line in Fig. 4.3 corresponds to the ΛCDM cosmology ratio, featuring a linear σ_8 matched to the nonthermal LiMR cosmology. As anticipated, the ratio remains scale-independent on larger scales yet significantly deviates in shape on smaller scales, distinct from the pattern observed in the nonthermal LiMR case. This distinct behavior sets it apart from standard massive neutrino cosmologies, where small-scale damping of $P(k)$ is generally degenerate between M_ν and σ_8 (Bayer *et al.* 2022).

In a photometric survey sensitive to both P_{cb}, via galaxy clustering, and P_{m}, through cosmic shear or galaxy-galaxy lensing, the signal of small-scale damping should be detectable provided sufficient sensitivity on those scales. Furthermore, the fact that a change in σ_8 doesn't confound this damping simplifies the task of either confirming or disproving this model using a combination of galaxy clustering and lensing. However, the precise estimation of constraints from these observables is deferred to subsequent research.

4.3.2 Halo Mass Function

The halo mass function (HMF), representing the number density of dark matter halos within specific mass intervals, is a sensitive probe of the power spectrum's shape and various cosmological parameters influencing it (e.g. Holder *et al.* 2001;

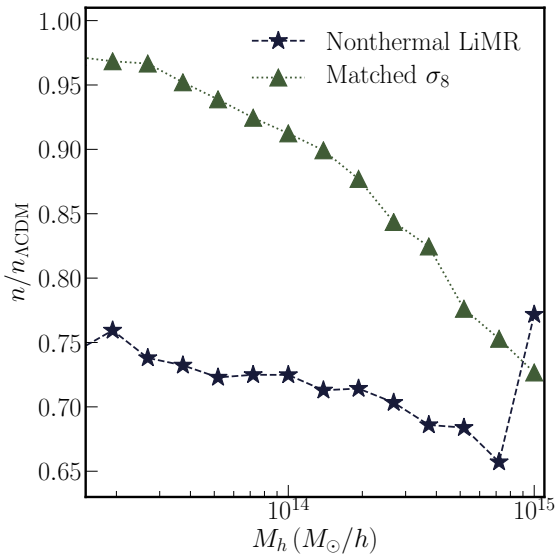

FIGURE 4.4: The blue (starred) points represent the ratio of the halo mass function in the nonthermal LiMR cosmology to the *Planck* best-fit ΛCDM cosmology. The green points (triangles) represent the same ratio for a ΛCDM cosmology with σ_8 matched to the nonthermal LiMR cosmology. While a simple change in σ_8 within the ΛCDM framework affects the high end of the HMF, with minimal effects on smaller objects, the LiMR cosmology produces fewer halos on all mass scales.

Weller *et al.* 2002; Tinker *et al.* 2008; McClintock *et al.* 2019). In cosmologies involving Warm Dark Matter (WDM), for instance, the presence of a damping scale in the power spectrum, resulting from the suppression of small-scale perturbations due to the thermal velocity of dark matter, often manifests as a cut-off scale in the HMF (e.g. Schneider *et al.* 2012)[9]. Observationally, the halo mass function can only be indirectly probed across diverse mass scales – from galaxy clusters residing within the most massive virialized halos ($\sim 10^{15} M_\odot/h$) (e.g. Burenin and Vikhlinin 2012; Mantz *et al.* 2015; Cataneo *et al.* 2015; Bocquet *et al.* 2019; Abbott *et al.* 2020; To *et al.* 2021), to dwarf galaxies inhabiting halos of approximately $10^8 M_\odot/h$ (e.g. Wang *et al.* 2021).

For HMF computations in simulations, we rely on the halo mass values provided

[9]For a discussion on numerical artifacts that make the cut-off challenging to identify, refer to Angulo *et al.* (2013)

by ROCKSTAR[10]. We categorize the halos into 15 logarithmic bins spaced evenly between $10^{13}M_{\odot}/h$ and $10^{15}M_{\odot}/h$. To highlight disparities in the HMF across different cosmologies, we depict the ratio of HMFs for various cosmologies normalized to the HMF from the *Planck* best-fit ΛCDM cosmology in Figure 4.4. Blue data points (stars) represent the ratio for the cosmology featuring the non-thermal LiMR component. The green data points (triangles) portray the ratio for the ΛCDM cosmology with σ_8 aligned to the LiMR cosmology. Notably, both cases significantly deviate from a ratio of 1. In the LiMR cosmology, the HMF experiences a reduction across the range of mass scales shown in Figure 4.4, with a slightly more pronounced decrease at higher mass scales. The scatter observed in the highest mass bin is likely a consequence of limited statistics. On the contrary, for the ΛCDM cosmology with matched σ_8 (akin to the LiMR cosmology), the ratio varies extensively with a mass scale, particularly impacting the high-mass range. Smaller halos around $10^{13}M_{\odot}/h$ show far less susceptibility. Therefore, akin to the power spectrum, precise HMF measurements hold the potential to differentiate between the *Planck* best-fit ΛCDM model and the LiMR model, which also aligns with *Planck* data. Furthermore, the HMF can discern between the implications of the LiMRs-inclusive cosmology and a straightforward scale-independent rescaling of the power spectrum within the ΛCDM model.

4.3.3 Mass-Concentration Relationship

The developmental trajectory of dark matter halos throughout cosmic history is encoded in several attributes of their density profiles. Among these, the mass-concentration relationship stands out – an average concentration of halos contingent on their virial mass (Navarro *et al.* 1996; Bullock *et al.* 2001). Concentration (c) is defined as the ratio of the virial radius of a halo ($r_{\rm vir}$) to its scale radius

[10]It's worth noting that ROCKSTAR conducts halo identification and mass estimation based solely on CDM-type particles in the simulation. In simulations containing the LiMR component, this definition may not be optimal.

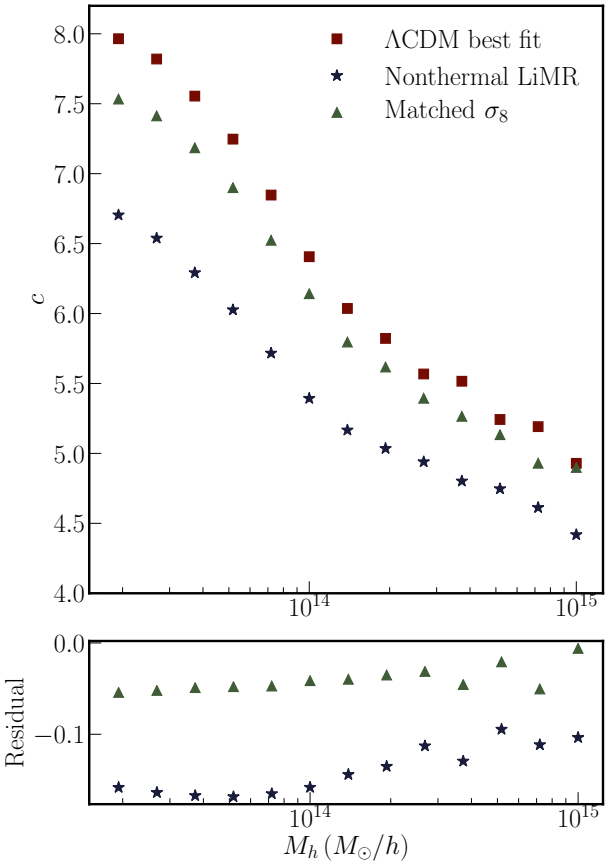

FIGURE 4.5: *Top panel:* Mean mass-concentration relation obtained for the three models. The maroon (square) points are for the *Planck* best-fit ΛCDM model, the blue (star) points are for the nonthermal LiMR model, while the green (triangle) points are for the ΛCDM model with σ_8 matched to the nonthermal LiMR model. *Bottom panel: Residual of the nonthermal LiMR model and the matched σ_8 model with respect to the Planck best-fit model in the upper panel.* The nonthermal LiMR model has a marked effect, lowering the mean concentration at fixed mass, and a simple change of σ_8 within the ΛCDM model is unable to replicate the same level of suppression.

(r_s), i.e. $c = r_{\rm vir}/r_s$. The scale radius itself is the radius where the logarithmic derivative of the halo's density profile, $\mathrm{d}\log\rho/\mathrm{d}\log r$, equals -2. Numerous observational endeavors have aimed to discern the mass-concentration relationship in the Universe, utilizing various methods. Gravitational lensing, encompassing strong and weak lensing, constitutes one such approach (see e.g., Comerford and Natarajan 2007; Mandelbaum *et al.* 2008; Covone *et al.* 2014; Umetsu *et al.* 2014, 2016; Du *et al.* 2015; Merten *et al.* 2015; Van Uitert *et al.* 2016). As wider-area

photometric surveys continue, gravitational lensing is poised to provide increasingly precise assessments of the mass-concentration relation.

In Warm Dark Matter (WDM) cosmologies, where the power spectrum experiences damping on minor scales due to the thermal motion of the primary dark matter component, the typical correlation between halo mass and concentration deviates from that exhibited in Cold Dark Matter (CDM) models (Schneider *et al.* 2012; Macciò *et al.* 2013; Ludlow *et al.* 2016). Conceptually, this occurs because damping delays the inception of nonlinear evolution on small scales, causing low-mass halos to form later than in CDM scenarios. Given that halo concentration correlates with the background universe's density during formation, postponed formation entails diminished background density and, consequently, lower concentrations. Unlike CDM scenarios where mean concentration increases with descending mass, WDM models yield a non-monotonic relationship. Concentration diminishes on both sides of a specific halo mass scale (dictated by the WDM particle mass). In the nonthermal LiMR model considered here, power damping on minor scales emerges due to a completely distinct mechanism from WDM models. In this case, it results from a subdominant yet non-negligible component clustering less than the CDM component. Consequently, we explore whether this model elicits a similar impact on the mass-concentration relationship. In WDM models featuring realistic masses, damping initiates at $k > 1h^{-1}$Mpc, exerting minimal influence on the mass-concentration relationship for larger halos, such as clusters and groups ($\gtrsim 10^{13}M_{\odot}/h$). In the nonthermal LiMR model, relative damping to the CDM model arises on notably larger scales, as depicted in Figure 4.3. This discrepancy potentially influences higher-mass halos.

To ascertain the mean association between mass and concentration, we leverage the halo mass data provided by ROCKSTAR. Our methodology involves categorizing halos into 20 logarithmically spaced bins spanning from $10^{13}M_{\odot}/h$ to $10^{15}M_{\odot}/h$. For each individual halo, we calculate its concentration (c) by employing the values

of $R_{\rm vir}$ and the scale radius R_s supplied by ROCKSTAR, utilizing the formula $c = R_{\rm vir}/R_s$. Subsequently, we compute the average concentration of halos within a specific mass bin. It's important to note that in the case of the lowest mass bin, each halo contains approximately $\sim$ 200 particles, which implies that the ROCKSTAR estimates for R_s may not be fully converged. However, this limitation is expected to affect all simulations in a fairly uniform manner. The outcomes stemming from various simulations are depicted in Figure 4.5.

The maroon (square) data points signify the mass-concentration relationship within the framework of the *Planck* best-fit ΛCDM model. Meanwhile, the blue (starred) data points represent the mass-concentration relationship of the nonthermal LiMR model, while the green (triangular) data points illustrate the relationship in the context of the ΛCDM model, with σ_8 adjusted to align with the nonthermal LiMR model. Notably, the nonthermal LiMR model, within the considered scales, does not exhibit the non-monotonic mass-concentration relationship that is evident in WDM models. Instead, it demonstrates an overarching reduction in mean concentration across the entire spectrum of mass scales. This reduction encompasses objects at the uppermost range of mass scale, specifically massive galaxy clusters. An intriguing observation is that modifying σ_8 within the ΛCDM framework, represented by the green data points, generates a notably smaller effect. Given that the mass-concentration relation is intricately tied to the complete evolutionary history simply aligning σ_8 at $z = 0$ is insufficient to capture the repercussions of the nonthermal LiMRs. Although the average relation retains its monotonous nature over the range of well-resolved halo mass scales in these simulations, further investigation into the behavior at lower mass scales is warranted, along with potential implications for smaller systems, including the satellite population of systems like the Milky Way. Addressing this would necessitate simulations with higher resolutions, a task we defer to future endeavors.

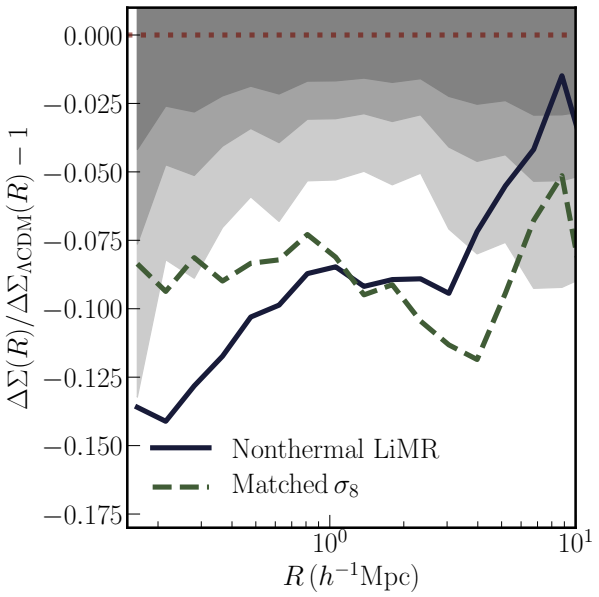

FIGURE 4.6: Residual of $\Delta\Sigma$, with respect to the ΛCDM Planck best-fit. The maroon (dotted) line represents 0 residual. The blue (solid) line represents the residual for the nonthermal LiMR model. The green (dashed) line represents the residual for a ΛCDM model with σ_8 matched to the nonthermal LiMR model. The lightest shaded region corresponds to error estimates from the measurements in Chang *et al.* (2018) in DES Y1 data, rescaled to the measurement of the signal in the *Planck* best fit ΛCDM model (see text for more details). The progressively darker shaded regions represent projections for error bars expected in DES Y3 and LSST (VRO), based on the increase in the fraction of the sky covered by those surveys compared to DES Y1.

4.3.3.1 Exploring Weak Lensing Measurements around Cluster-Mass Halos

Lastly, we delve into analyzing stacked weak lensing measurements surrounding halos with masses typically exceeding $10^{14}M_{\odot}/h$. In recent years, the precision and accuracy of such measurements have shown significant improvements (see e.g., Miyatake *et al.* 2016; Chang *et al.* 2018; Shin *et al.* 2021). These measurements offer a sensitive means of probing clustering within the range of scales $0.1h^{-1}\mathrm{Mpc} \lesssim r \lesssim 10h^{-1}\mathrm{Mpc}$. Given that the presence of the nonthermal component predominantly affects these smaller scales, cluster lensing emerges as a potent tool to either constrain or potentially disprove models involving such components.

The observed weak lensing signal is directly linked to the surplus surface mass density, expressed as:

$$\Delta\Sigma(R) = \Sigma(< R) - \Sigma(R)\,, \tag{4.5}$$

where R denotes the projected distance from the cluster's center. Our simulation-based computation of this metric entails selecting a specific direction within the simulation volume as the line-of-sight (LOS) direction. We extract all particles within a cylinder along the LoS direction for each halo, centered at the halo's location as identified by ROCKSTAR and with a height of $100h^{-1}$Mpc. The first term on the right-hand side of Eq. 4.5, which represents the mass enclosed within the cylinder up to radius R, is determined by tallying the enclosed mass and dividing it by the enclosed area. Meanwhile, the second term corresponds to the mass within the circular annulus around R. We calculate $\Delta\Sigma(R)$ within logarithmically spaced bins ranging from $0.15h^{-1}$Mpc to $15h^{-1}$Mpc. The process is repeated around the centers of the $20,000$ most massive halos in each simulation box, and the resulting measurements are averaged (stacked).

It is worth noting that the halo mass utilized here is derived from the ROCKSTAR catalog, which only considers Type 1 particles (representing the CDM and baryonic components) for halo identification and mass determination.

Figure 4.6 showcases the residuals of the $\Delta\Sigma(R)$ measurements compared to those obtained from the *Planck* best-fit ΛCDM simulation. The (dotted) maroon line indicates no deviation from the baseline model. The (solid) blue line depicts the residuals associated with the nonthermal LiMR model, while the (dashed) green line portrays the residuals stemming from the ΛCDM simulation, with linear σ_8 matched to the nonthermal LiMR model.

The lightest gray-shaded region denotes the relative 1σ error ranges derived from measurements on a cluster sample conducted by Chang *et al.* (2018), using the Dark Energy Survey (DES) Year 1 data. These measurements were performed

on a set of REDMAPPER clusters (Rykoff *et al.* 2016) within a richness range of $20 < \lambda < 100$ and a redshift span of $0.2 < z < 0.55$. To adapt the data error bars for meaningful interpretation within the simulation sample of this study, we adjust the data covariance matrix by squaring the ratio between the mean signal in the data and that obtained from the fiducial ΛCDM simulation. This adjustment maintains the covariance structure between different radial bins, encompassing the off-diagonal terms. Additionally, it's important to note that while the simulation measurements are at $z = 0$, the data spans a redshift range of $0.2 < z < 0.55$. Hence, we make the simplifying assumption that the error bars exhibit minimal redshift dependence. The progressively darker gray regions reflect the same errors adjusted to account for the extended sky coverage anticipated in DES Year 3 and LSST data from the VRO. However, these rescaled error bars do not factor in the enhanced coverage depth and the subsequent increase in the density of background lensed galaxies. Consequently, these shaded regions provide a rough guide to how the nonthermal LiMR model could be discerned from the best-fit ΛCDM model across various surveys. We observe that the nonthermal LiMR model generates notably distinct predictions, as indicated by the shaded gray regions, for the stacked weak lensing signal encircling the top $20,000$ most massive halos within the simulations. Referring to the DES Y1 data covariance matrix, recalibrated based on the simulation mean as previously explained, the $\Delta\chi^2$ between the *Planck* best-fit ΛCDM model and the nonthermal LiMR model amounts to 31.32 across 16 degrees of freedom. Translating to the anticipated DES Y3 error bars, the $\Delta\chi^2$ value increases to 93.64, while for the projected LSST (VRO) error bars, it skyrockets to 313.21. In the latter case, the resulting p-value stands below 1×10^{-5}, signifying that the nonthermal LiMR model and the baseline ΛCDM model can be discerned with an exceedingly high level of statistical significance. Although this assessment involves multiple approximations, we have aimed to maintain a conservative approach regarding the projected signal-to-noise enhancements in DES Y3 and LSST.

It's important to highlight that the distinction in the lensing signal is evident both within the 1-halo virialized region, roughly $\sim 1h^{-1}$Mpc, and extends to the largest scales we've measured, around $10h^{-1}$Mpc in the infall regime of these entities. This stands in contrast to another expansion of the ΛCDM model known as the Self-Interacting Dark Matter (SIDM) model, where the signal is impacted solely within the virial radius due to (elastic) interactions between dark matter particles (Banerjee *et al.* 2020a).

Additionally, it's noteworthy that alterations in σ_8 do not overlap with the presence of the nonthermal LiMR component, as evidenced by the disparity between the blue and yellow curves. This contrast between the two models is particularly pronounced on smaller scales, roughly $\lesssim 1h^{-1}$Mpc. This discrepancy on small scales holds significant relevance, given that a number of studies indicating the tension in σ_8, or equivalently $S_8 = \sigma_8(\Omega_m/0.3)^{0.5}$, between *Planck* primary anisotropies and low redshift clustering measurements (e.g. Ivanov *et al.* 2020; Tröster *et al.* 2021; Hikage *et al.* 2019; DES Collaboration *et al.* 2021; Krolewski *et al.* 2021; D'Amico *et al.* 2020), typically do not incorporate these smaller scales. Therefore, even if the nonthermal LiMR model is fine-tuned to address the σ_8 tension on intermediate, quasi-linear scales, the difference in predictions for the smaller scale, the nonlinear regime can be utilized to constrain or disprove the model. For further details, we direct readers to section 4.4, where we illustrate how the discussion above applies to other classes of LiMR models.

4.4 Effect of LiMR velocity distributions on nonlinear structure formation

In this section, we are examining how altering the velocity distribution of a specific particle model (referred to as LiMR) affects the characteristics of the model on

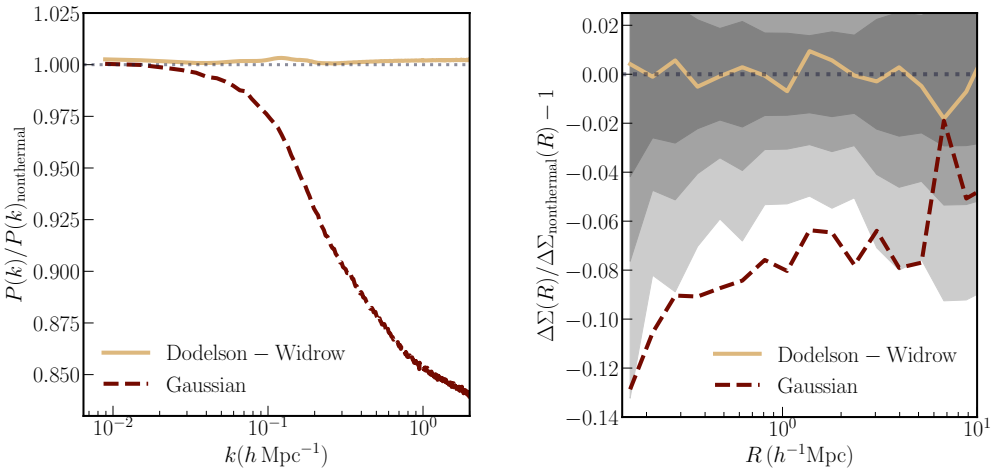

FIGURE 4.7: *Left panel:* Ratio of the total matter power spectrum at $z = 0$ for the Dodelson-Widrow model (solid yellow curve) and the Gaussian model (dashed maroon curve), to the total matter power from the nonthermal LiMR model discussed in Sec. 6.5. The dotted line is the expectation for no deviation from the fiducial nonthermal LiMR model. *Right panel:* Residual of $\Delta\Sigma$ to the nonthermal LiMR model discussed in the main text. Once again, the solid yellow line is the residual for the Dodelson-Widrow model, and the dashed maroon line is the residual for the Gaussian model. The dotted line represents zero deviation from the fiducial nonthermal LiMR model. Shaded regions represent expected data error bars from DES-Y1, DES-Y3 and VRO LSST (see Sec. 4.3.3.1 for details on how the error bars are computed). Even with future surveys, it will be difficult to distinguish the fiducial nonthermal LiMR model and a LiMR model with a Dodelson-Widrow distribution. However, if the velocity distribution is sufficiently different, as is the case for the Gaussian distribution, the differences in the observables are large enough to be detected. Note that, in contrast to Figs. 4.3 and 4.6, the fiducial model in this figure (both panels) is the nonthermal model from Das *et al.* (2022), rather than the *Planck* best-fit ΛCDM model.

small scales (less than 10 Mpc/h).

In this section, I will compare this nonthermal model with two other models: the Dodelson-Widrow model and the Gaussian model, which we discussed in Section 4.1.1. I perform N-body simulations, as explained in Section 4.2. The key differences between these models are the initial predictions from the "CLASS" model, a tool for linear theory predictions, and the velocity distributions at a specific redshift, which are depicted in Figure 4.1.

We analyze two aspects of these models. First, in the left panel of Figure 4.7, we illustrate how changing the LiMR velocity distribution impacts the overall matter power spectrum. The curves represent the power spectrum ratio in each LiMR model compared to the standard nonthermal LiMR model. The solid yellow line corresponds to the Dodelson-Widrow model, and the dashed maroon curve represents the Gaussian model. The dotted line indicates no deviation from the standard model.

In the right panel of Figure 4.7, we explore the effects of altering the LiMR velocity distribution on weak lensing measurements, particularly the excess surface density $\Delta\Sigma(R)$ around the 20,000 most massive halos in each simulation. We show the differences from the standard nonthermal LiMR model. Again, the yellow solid curve represents the Dodelson-Widrow model, and the dashed maroon curve represents the Gaussian model. The dotted line indicates no deviation from the standard model. The shaded grey areas represent expected fractional error margins for measurements similar to those of DES Y1 (lightest grey band), DES Y3, and LSST (darkest grey band).

It's crucial to note that the model parameters are tuned to ensure that the linear theory predictions for all three LiMR models are identical. However, we observe deviations on small, nonlinear scales, breaking the formal degeneracy. Nevertheless, the differences between the standard non-thermal model and the Dodelson-Widrow model remain small, and even with a powerful survey like LSST at VRO, distinguishing between the two models might not be possible. This implies that the results in Section 6.5 and the discussions in Section 7.5, derived from the specific nonthermal LiMR model in the original paper, can be extended to the broader class of Dodelson-Widrow models.

The Gaussian model's velocity distribution differs notably from the other models,

leading to distinct small-scale structural features. This model has lower particle occupancy at low velocities, as shown in Figure 4.1, compared to the other models. This low-velocity behavior significantly affects nonlinear clustering, as demonstrated in a previous study for massive neutrinos. Consequently, the LiMR component in the Gaussian model exhibits reduced clustering and a more substantial damping effect on the power spectrum on small scales, as evident from the comparison between the yellow and maroon curves in the left panel of Figure 4.7. In terms of weak lensing measurements (right panel of Figure 4.7), the Gaussian model stands out from the other two models for the same reasons. In fact, these differences are substantial enough that it might be feasible to distinguish the Gaussian model from the others with high statistical significance using future data.

4.5 Discussion and Summary

This chapter comprehensively investigates the nonlinear characteristics of a mixed dark matter cosmology combining Cold Dark Matter (CDM) and a nonthermal Light Relic (LiMR) component. The focus is on discerning effects and distinctions from the standard ΛCDM universes, with implications for observations in present and forthcoming photometric surveys. Our approach employs cosmological N-body simulations incorporating cold and LiMR components simultaneously. The primary model used in this initial study is that of Bhattacharya *et al.* (2021b); Das *et al.* (2022); additional explorations involving alternative distribution functions were conducted in the supplementary section. To summarize our findings:

- Initially, we investigate the influence on the power spectrum and identify a scale-dependent attenuation on small scales. The magnitude of this attenuation significantly deviates from what linear theory predicts, underscoring

the necessity for comprehensive N-body simulations to calibrate the impact of this model on small scales. Crucially, the attenuation pattern also differs from what would be obtained by simply rescaling the initial power spectrum within the ΛCDM model. This implies that characteristics on small scales can potentially differentiate between the two models, potentially resolving ambiguities that exist on larger scales.

- Subsequently, we scrutinize the effects on the mass function and the mass-concentration relationship of dark matter halos. In terms of the Halo Mass Function (HMF), the nonthermal LiMR model leads to a reduction in the HMF across all mass scales between $10^{13}M_{\odot}/h$ and $10^{1}5M_{\odot}/h$, with no substantial variation as a function of mass. In contrast, a modification in σ_8 through a scale-independent factor within ΛCDM has a much more pronounced impact on the high-mass end of the HMF compared to the low-mass end. Regarding the mass-concentration relation, we observe that the nonthermal LiMR model results in an overall decrease in the mean concentration relative to halo mass across the range of $10^{13}M_{\odot}/h < M_h < 10^{15}M_{\odot}/h$, while maintaining a roughly monotonic trend. Once again, this reduction cannot be replicated by merely adjusting the ΛCDM power spectrum to match the σ_8 of the nonthermal LiMR model.

- We examine the discernible effects of the nonthermal LiMR model on weak lensing measurements around the most massive galaxy clusters. Under specific simplifying assumptions, we demonstrate that the expected signal-to-noise ratio in these types of measurements, particularly in DES Y3 and LSST (VRO), should be substantial enough to differentiate between the nonthermal LiMR model and the best-fit ΛCDM model derived from *Planck* data, with a high level of statistical significance. To our knowledge, this represents the first simulation-based investigation into the effects of a category of LiMRs on cluster lensing, underscoring the feasibility of distinguishing these models from a standard ΛCDM universe using such measurements.

- Finally, in the supplementary section, we delve into the nonlinear characteristics of LiMR models that are entirely indistinguishable at the linear level. Notably, we identify disparities at the nonlinear level, which can serve as indicators of the LiMR velocity distribution functions. Encouragingly, as the velocity distributions of LiMRs are linked to their production mechanism, these disparities offer a potential window into early universe dynamics.

Therefore, the optimal approach for testing and constraining LiMR models involves a combined analysis of data from Cosmic Microwave Background (CMB) and late-time structure formation, encompassing both large and small scales.

We now focus on some intriguing aspects of our findings and avenues for future research. One notable point emphasized throughout Section 6.5 is that the effects of the LiMR model lie between those observed for massive neutrinos and those in Warm Dark Matter (WDM) cosmologies without aligning completely with either. The scale at which the power spectrum initiates damping, relative to the ΛCDM model, is approximately $10^{-1}h^{-1}$Mpc. In contrast, for massive neutrinos, this scale typically stands at $10^{-2}h^{-1}$Mpc, while for permissible WDM models, it exceeds $1h^{-1}$Mpc. Another point of divergence from massive neutrinos is that the behavior on small scales is not entirely synonymous with a change in σ_8. This bears significance for the proposed role of LiMRs in resolving the σ_8 discrepancy. Lastly, the LiMR influences the mass-concentration relationship of even the most massive halos, in contrast to viable WDM models, which exclusively impact the relationship for lower mass entities.

It is worth noting that the specific parameters of the LiMR model explored in this study yield a satisfactory fit to the primary *Planck* data. In other words, early Universe observations alone do not provide sufficiently robust constraints on LiMR models. In light of our findings, it becomes imperative to integrate early Universe data with late-time structure formation to obtain the most robust constraints on

these models. Moreover, incorporating small, nonlinear scales of structure formation into such analyses offers the added benefit of potentially distinguishing between different velocity distributions of the LiMRs despite their identical predictions for linear evolution on large scales.

LiMR models have been proposed as a potential resolution to the modest tension between early Universe and late-time clustering probes, parameterized in terms of σ_8. It should be noted that Standard Model neutrinos, by themselves, cannot account for the extent of this discrepancy. Clustering probes at low redshifts that point to a σ_8 tension (e.g. Hikage *et al.* 2019; D'Amico *et al.* 2020; Ivanov *et al.* 2020; Tröster *et al.* 2021; DES Collaboration *et al.* 2021; Krolewski *et al.* 2021), do not encompass small nonlinear scales in their analysis. Consequently, it is always possible to fine-tune the parameters of a specific LiMR model to yield a late-time σ_8 consistent with these studies. A comprehensive characterization of the nonlinear predictions of the models on small scales, as undertaken in this study, is therefore pivotal in rendering the models predictive and testable once more. The fact that we ascertain that the nonlinear effects of this specific LiMR model do not align with an overall rescaling of the initial power spectrum within the ΛCDM framework suggests that it is entirely conceivable to either rule out or constrain the model with present and future data. If the model is indeed ruled out, alternative solutions to the σ_8 tension will need to be pursued.

While our focus has centered on a subset of the signatures of LiMRs on small, nonlinear scales that bear relevance for large-scale photometric surveys, their impacts should also be evident in other observables. For instance, the small-scale damping in the power spectrum will influence Lyman-α forest measurements, thereby enabling these measurements to be translated into effective constraints on LiMR models, akin to what has been achieved for WDM (Viel *et al.* 2013; Iršič *et al.* 2017b), and Fuzzy Dark Matter (FDM) (Iršič *et al.* 2017a; Rogers and Peiris 2021) models. This damping also implies effects on the satellite population of the Milky

Way, which now stands as a source of some of the most stringent constraints on various dark matter models (see e.g. Nadler *et al.* 2019, 2021; Das and Nadler 2021). A thorough exploration of LiMR effects on these observables and potential constraints will be reserved for future investigations.

Chapter 5

Constraints on Nonthermal Warm dark matter from small scale structure [1]

5.1 Introduction

The ΛCDM model has effectively explained the accelerated expansion of the Universe and the evolution of large-scale perturbations. It also aligns well with various cosmological observations. These observations, including those from the Cosmic Microwave Background, galaxy clustering, weak lensing, and Lyman-α measurements, suggest that around 30 percent of the current Universe's energy density is attributed to matter Alam *et al.* (2017b); Aghanim *et al.* (2020b); Abbott *et al.* (2022). The majority of this matter is of a mysterious nature referred to as "dark matter." In the framework of the ΛCDM model, this dark matter is characterized as cold, implying its negligibly small free-streaming effects. Despite being the

[1] This chapter is based on publication Banerjee *et al.* (2023)

simplest model consistent with the data, the Cold Dark Matter (CDM) theory has been subject to investigations regarding potential tensions at small non-linear scales Bullock and Boylan-Kolchin (2017). Over time, issues like the "missing satellites" Moore *et al.* (1999); Klypin *et al.* (1999), "too big to fail" Boylan-Kolchin *et al.* (2011), and "core–cusp" Moore (1994); Flores and Primack (1994) have drawn significant attention. Additionally, more subtle evaluations of galaxy diversity have surfaced in recent years Sales *et al.* (2022).

Though many of these tensions can potentially be reconciled by considering baryonic physics, they have also triggered proposals for alternative dark matter physics beyond the CDM paradigm. One established model is warm dark matter (WDM), where dark matter particles exhibit free-streaming on macroscopic scales of $\mathcal{O}$(kpc) or more, causing small-scale suppression compared to CDM Bond and Szalay (1983); Bode *et al.* (2001). WDM particle candidates, including sterile neutrinos, are often modeled with production mechanisms leading to a thermal phase-space distribution Dodelson and Widrow (1994a), but these are significantly limited by small-scale structure constraints Abazajian and Koushiappas (2006). Recent exploration has also extended to production mechanisms with non-thermal distributions Shi and Fuller (1999); De Gouvêa *et al.* (2020), though such models also face stringent structure formation restrictions Nadler *et al.* (2021a); Zelko *et al.* (2022); An *et al.* (2023).

In this chapter, we investigate the consequences of WDM production through the decay of a massive scalar particle, influenced by moduli decay models Bhattacharya *et al.* (2021b); Das *et al.* (2022); Banerjee *et al.* (2022), where the neutrino-like hot dark matter arises from the decay of moduli in the early universe, contributing small fraction to the total dark matter content. This chapter focuses on a scenario where the entire dark matter relic density emerges in a warm state due to the decay of a moduli field. Remarkably, despite the non-thermal phase-space distribution, our model generates linear matter power spectra that closely resemble those of

thermally-produced WDM while establishing a unique connection to a thermal-relic mass. This connection enables us to establish constraints on the non-thermal particle mass through modern observations of small-scale structures.

The limits from the small-scale structure have been derived from observations of the satellite population of the Milky Way galaxy by the Dark Energy Survey Abbott *et al.* (2005) and Pan-STARRS1 Chambers *et al.* (2016). Specifically, the presence of satellite galaxies, especially the smallest "ultra-faint" dwarf galaxies in proximity, has been utilized to set a lower limit on the abundance of low-mass ($\gtrsim 10^8\ M_\odot$) subhalos around the Milky Way Nadler *et al.* (2020). This measurement subsequently constrains any dark matter scenario that suppresses subhalo abundance, resulting in a 95% confidence lower bound on the thermal-relic WDM (Th-WDM) particle mass of 6.5 keV Nadler *et al.* (2021a); Maamari *et al.* (2021); Das and Nadler (2020); Nguyen *et al.* (2021); Mau *et al.* (2022); An *et al.* (2023). Additionally, we incorporate strong gravitational lensing constraints, which have been used to establish limitations on WDM Gilman *et al.* (2020) and other dark matter physics Gilman *et al.* (2023); Laroche *et al.* (2022); Dike *et al.* (2023). Recent work Nadler *et al.* (2021b) combines WDM constraints from strong lensing and Milky Way satellite galaxies to set a 95% confidence lower BOUND on the Th-WDM mass of 9.7 keV, providing us with a stringent constraint on our non-thermal production mechanism.

It is crucial to note that the thermal-relic WDM limits we consider, both from Milky Way satellites alone and in combination with strong lensing, account for uncertainties in system properties and non-linear effects (e.g., galaxy formation physics in the case of satellites and tidal stripping in the case of lensing) that could impact observables. This ensures that the constraints we derive remain conservative. Moreover, due to the nearly identical transfer functions generated by our model and thermal-relic WDM, and the absence of additional non-linear physics, the constraints based on the mapping to existing WDM limits are robust.

5.2 Short overview of Production Mechanism and Phase-space Distribution

WDM scenarios are characterized by the initial phase-space distribution of the warm species, which is determined by the production mechanism. Our focus is on WDM produced through the decay of a massive scalar, following previous works Hasenkamp and Kersten (2013a); Conlon and Marsh (2013a); Miller *et al.* (2019a); Bhattacharya *et al.* (2021a). In this context, the energy density of the universe is dominated by a heavy, cold species φ at early times. This dominance could arise from perturbative reheating post-inflation or due to moduli domination. Subsequently, φ decays into the Standard Model sector and WDM particles. The decay mode to WDM particles is $1 \to 2$, leading to the production of two identical relativistic WDM particles. While the Standard Model sector attains thermal equilibrium, the WDM particles are considered sterile and thus do not thermalize. This scenario emerges naturally when considering sterile dark matter resulting from the decay of a heavy parent particle or in cases where sterile dark matter originates directly from the decay of the inflaton.

The rate of WDM production in this model is determined by the decay rate of φ and the branching ratio for the WDM channel. As φ decays, WDM particles are continuously generated, possessing momentum $m_\varphi/2$ at the time of production. The final momentum of a WDM particle is determined by redshifting its initial momentum. Because different WDM particles are produced at different times (though with identical initial momentum), this redshifting effect gives rise to a non-thermal momentum distribution, as depicted in Fig. 5.1.

The mass of the heavy particle governs the distribution function in our model, (m_φ), its decay rate, τ, and the branching fraction for the decay to WDM, $B_{\rm sp}$. Particularly, the momentum distribution of the WDM particles can be computed

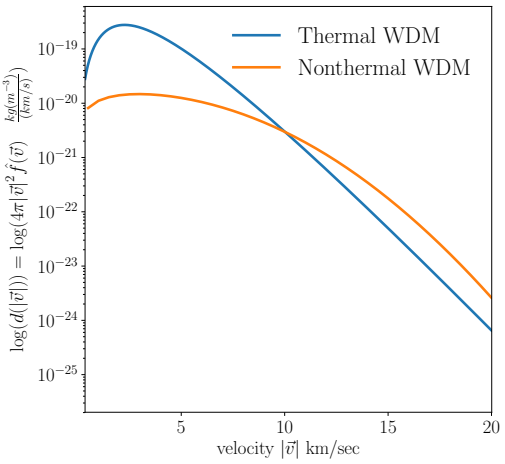

FIGURE 5.1: Comparision of Velocity distributions at redshift z=99 of two WDM models for same 5 keV mass (thermal-relic Warm dark matter (blue) and our non-thermal Warm dark matter model (orange)

.

by considering that, due to the decays, the co-moving number density of φ diminishes as $N(t) = N(0)e^{-t/\tau}$ with a branching fraction $B_{\rm sp}$ to the WDM particles. Once generated, the WDM particles freely stream. We employ the publicly available package `CLASS` Lesgourgues (2011); Lesgourgues and Tram (2011) to assess the influence of WDM, using Eq. 3.5 normalized by $T^3_{\rm ncdm,0}$.

A comparison between a typical momentum distribution in our model and that of thermal-relic WDM is shown in Fig. 5.1. For equivalent $\Delta N_{\rm eff}$ (the effective number of additional neutrino-like species) at Big Bang Nucleosynthesis (BBN), the non-thermal distribution peaks at higher momentum values and exhibits a broader profile compared to the thermal distribution. Notably, the small-scale structure constraints we derive later indicate that permissible WDM particle masses in our model are significantly lower than the universe's temperature during BBN.

Note that although naively $f(\vec{q})$ appears to rely on $N(0)$, the complete expression remains independent of $N(0)$ provided we assume the universe to be entirely matter-dominated at the initial time Bhattacharya *et al.* (2021a). Conversely,

altering the parameter $B_{\rm sp}$ results in an overall constant scaling of the distribution function. For any chosen WDM particle mass, the `CLASS` package scales the distribution function to maintain consistency with observational $\Omega_{\rm WDM}$ values. Consequently, our analysis effectively explores different $B_{\rm sp}$ values. The other parameters in the distribution function are m_φ and τ. Informed by the concept of high-scale inflation as the theory governing the early universe and the decay of the inflaton via perturbative Grand Unified Theory (GUT) scale interactions, we focus on $m_\varphi \sim \mathcal{O}(10^{-6} M_{\rm pl})$ and $\tau \sim \mathcal{O}(10^8/m_\varphi)$. In the Appendix, we demonstrate that our results remain largely unaffected by the specific values of these parameters.

5.3 Transfer function and Linear Matter Power Spectra

We employ a modified version of `CLASS`[2] Lesgourgues (2011); Lesgourgues and Tram (2011) to produce the linear matter power spectra for our non-thermal warm dark matter model. Our analysis uses the same values of cosmological parameters detailed in Ref. Das *et al.* (2022). For our WDM `CLASS` runs, we set $\omega_{\rm cdm} = 0$. We incorporate two non-CDM species, the first corresponding to standard massless neutrinos and the second representing the WDM species with $N_{\rm ncdm} = 2$ and $\omega_{\rm ncdm} = 0.12$. We keep the fiducial phase-space distribution parameters consistent with our non-thermal WDM production mechanism as outlined in Ref. Das *et al.* (2022), namely $B_{\rm sp} = 0.0118$, $m_\phi = 10^{-6} M_{pl}$, and $\tau = 10^8/m_\phi$. We establish in the Appendix that our outcomes remain robust against parameter variations; hence, our constraints remain independent of this selection.

The left section of Fig. 5.2 represents the ratio of the linear matter power spectra relative to CDM, referred to as the *transfer function*, for diverse non-thermal

[2] https://github.com/ravi398/WDM

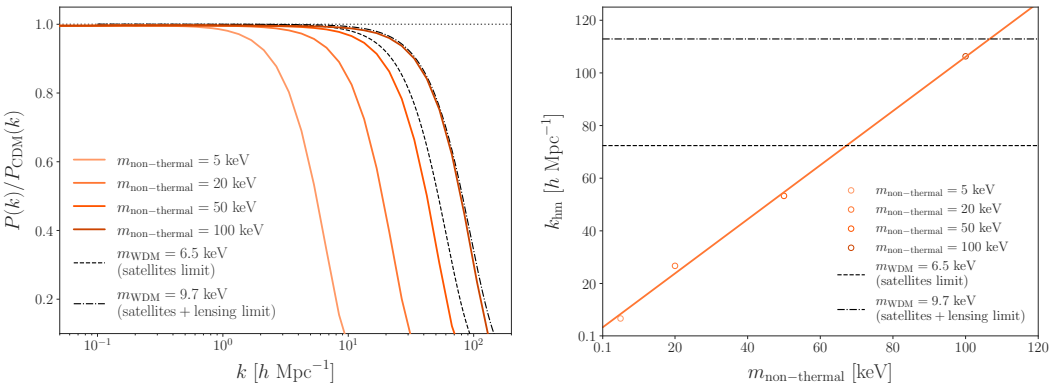

FIGURE 5.2: *Left panel*: The plot shows the ratio of matter power spectra of nonthermal model (orange) for WDM mass values (5 keV,20 keV,50 keV 100 keV) light to dark color with respect to ΛCDM model. The transfer functions for Th-WDM corresponding to masses 9.7 keV and 6.5 keV are plotted in dot-dashed and dashed lines, respectively. *Right panel*: relation between half mode wavenumber and mass of nonthermal WDM particles as shown in equation 5.5. The horizontal dashed (dot-dashed) lines indicate half-mode wavenumbers for 6.5 keV (9.7 keV) Th-WDM models, respectively.

particle masses. Specifically, we define

$$T^2(k) \equiv \frac{P(k)}{P_{\rm CDM}(k)}. \tag{5.1}$$

We juxtapose these transfer functions with the Th-WDM transfer function fit from Ref. Viel *et al.* (2005). Notably, the correlation between Th-WDM mass and the cutoff scale deduced from the Ref. Viel *et al.* (2005) fitting function becomes inaccurate for adequately cold models, encompassing those proximate to our 95% confidence restrictions. Nonetheless, the profile of the Ref. Viel *et al.* (2005) transfer function cutoff remains accurate Decant *et al.* (2022); Vogel and Abazajian (2022). Considering that the analyses we compare to also adopted the Ref. Viel *et al.* (2005) functional form, which we only use as a mechanism to map to effective thermal-relic models, this disparity does not influence our constraints.

Evidently, the transfer function cutoff in our non-thermal model closely resembles that in Th-WDM. This enables us to establish a mapping between these models, following a methodology akin to Refs. Nadler *et al.* (2019, 2021b). As depicted in

Fig. 5.2, we ascertain that (given our standard cosmological parameters) the half-mode scale $k_{\rm hm}$, determined by $T^2(k_{\rm hm}) \equiv 0.25$, correlates with the non-thermal particle mass as indicated by

$$k_{\rm hm} = \left(3.3 + \frac{m_{\rm non-thermal}}{1\ {\rm keV}}\right)\ h\ {\rm Mpc}^{-1}, \tag{5.2}$$

where $m_{\rm non-thermal}$ denotes our non-thermal particle mass.

As elaborated in Viel *et al.* (2005), the transfer function for Th-WDM can be expressed as

$$T(k) = \left[1 + (\alpha k)^{2\nu}\right]^{-5/\nu}, \tag{5.3}$$

with $\nu = 1.12$, and

$$\begin{aligned}\alpha =& 0.049 \left(\frac{m_{\rm WDM}}{1\ {\rm keV}}\right)^{-1.11} \left(\frac{\Omega_{\rm WDM}}{0.25}\right)^{0.11} \left(\frac{h}{0.7}\right)^{1.22} \\ & h^{-1}\ {\rm Mpc}.\end{aligned} \tag{5.4}$$

To derive the relationship between $k_{\rm hm}$ and $m_{\rm WDM}$, we sample values of $m_{\rm WDM} \in [3\ {\rm keV}, 12\ {\rm keV}]$, solve for their half-mode wavenumbers $k_{\rm hm}$ using Eq. 5.3, and fit the outcomes to obtain

$$k_{\rm hm} = 12.5 \left(-0.6 + \frac{m_{\rm WDM}}{1\ {\rm keV}}\right)\ h\ {\rm Mpc}^{-1}, \tag{5.5}$$

where $m_{\rm WDM}$ represents the Th-WDM mass. By comparing Eqs. 5.5 and 5.2, we infer the ensuing relationship between $m_{\rm WDM}$ and $m_{\rm non-thermal}$:

$$m_{\rm non-thermal} = 12.2 \left(-0.9 + \frac{m_{\rm WDM}}{1\ {\rm keV}}\right)\ {\rm keV}. \tag{5.6}$$

Based on comparing the corresponding transfer functions, we have validated this relationship across the entire spectrum of non-thermal masses we explore. Along

the initial cutoff, disparities between matched transfer functions typically remain at the sub-percent level; such deviations remain undetectable in the datasets from which we deduce our constraints. Consequently, Eq. 5.6 offers a robust avenue to translate prevailing Th-WDM constraints into constraints on our non-thermal model.

It is noteworthy that $m_{\rm non-thermal}$ significantly surpasses the corresponding $m_{\rm WDM}$ as per Eq. 5.6. This outcome mirrors the findings for hot dark matter in the considered non-thermal distribution Bhattacharya *et al.* (2021a). This follows because the non-thermal momentum distribution exhibits an extended tail toward higher velocities (as seen in Figure 5.1). Consequently, non-thermal WDM particles in our model demonstrate higher average velocities than Th-WDM particles, even when possessing the same mass at a given redshift.

Further insight into the relationship between $m_{\rm non-thermal}$ and $m_{\rm WDM}$ can be gleaned by computing the free-streaming length using

$$\lambda_{\rm fs} = \int_0^{a_{\rm eq}} \frac{\langle v(a)\rangle}{a^2 H(a)} {\rm d}a, \tag{5.7}$$

where the contributions from the relativistic and non-relativistic regimes are respectively given by

$$\lambda_{\rm fs} = 2ct_0 a_{nr} + I.$$

Here, the non-relativistic contribution I takes the form

$$I = \int_{a_{\rm nr}}^{a_{\rm eq}} \frac{\langle v(a)\rangle}{a^2 H(a)} {\rm d}a,$$

with the average velocity given by

$$\langle v(a)\rangle = \frac{\int_0^\infty v f(v) 4\pi v^2 {\rm d}v}{\int_0^\infty f(v) 4\pi v^2 {\rm d}v}.$$

For Th-WDM, these integrals can be analytically evaluated under the assumption

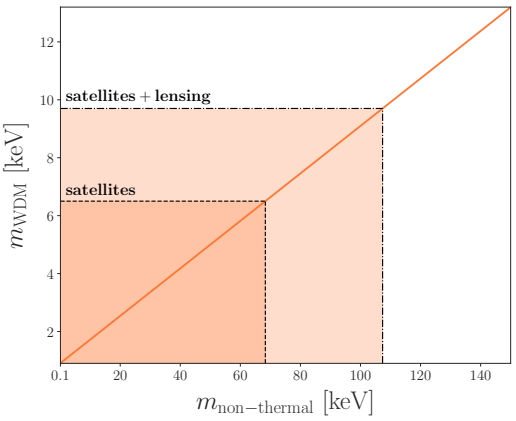

FIGURE 5.3: The relation between masses of nonthermal WDM model and Th-WDM model as shown by equation 5.6. The shaded regions show excluded limits at 95% by Milky Way population (dark) and Milky Way combined strong lensing (light).

that $H^2(a) = \Omega_m a^{-3} + \Omega_{\rm rad} a^{-3} + \Omega_\Lambda$, where Ω_i represent fractional energy densities and a is the scale factor. We numerically solve the integral equations for non-thermal WDM to compute the free-streaming scale as a function of $m_{\rm non-thermal}$. We have verified that the non-thermal and thermal-relic free-streaming scales match each other well along the relationship provided by Eq. 5.6.

5.4 Constraints from Thermal Relic WDM Mapping

We derive constraints on our non-thermal model based on Eq. 5.6. In particular, we use the 95% confidence lower limits on Th-WDM of 6.5 keV, derived from the satellite population Milky Way galaxy, and 9.7 keV, derived from its combination with strong lensing flux ratio statistics. These constraints are illustrated in Figure 5.3 and map to lower limits on the non-thermal WDM mass of 68 and 107 keV, respectively. Following our calculation above, the corresponding free-streaming lengths are $\lambda_{\rm fs} = 31$ kpc for $m_{\rm non-thermal} = 107$ keV and $\lambda_{\rm fs} = 29$ kpc for

$m_{\rm WDM} = 9.7$ keV. The latter value reasonably agrees with the fit in Ref. Schneider *et al.* (2012).

We emphasize that our non-thermal transfer functions are essentially identical to thermal-relic models, including for non-thermal masses at our 95% confidence limits (e.g., see the left panel of Figure 5.2). Furthermore, there is no new, non-linear physics introduced by our model: in both the non-thermal and Th-WDM cases, suppression of structure formation relative to CDM is set by the free-streaming scale, which is imprinted well before matter-radiation equality. Thus, we expect nonlinear observables that drive the small-scale structure limits we map to, such as the halo and subhalo mass functions and mass-concentration relations, to be practically identical to those in Th-WDM, which are well-studied.

We note that the precise mapping between our non-thermal transfer functions and Th-WDM at and below the cutoff scale justifies our use of combined Milky Way satellite and strong lensing limits. In particular, the lensing limits depend sensitively on halo concentrations (Gilman *et al.* 2020, 2022), which are in turn sensitive to power on scales even smaller than $k_{\rm hm}$.

5.5 Conclusions

We put constraints on nonthermal Warm Dark Matter (produced from moduli decay) from small-scale structures. Theoretically, this production mechanism is well motivated, and WDM particles obey nonthermal phase space distributions. Considering that this WDM accounts for the entire dark matter budget of the Universe, the linear matter power spectra are equivalent to corresponding thermal Warm dark matter relics. Using this equivalence, we established a relation between nonthermal WDM particles' mass and thermal WDM relics' mass. We get a lower

mass bound on the nonthermal WDM particles around 107 keV at 95% confidence through observations data from the satellite population of Milky Way and strong gravitational lensing. These are the first precise constraints on the nonthermal WDM model to date (also see Ref. Ballesteros *et al.* (2021)).

However, The precision of these data sets (Milky Way galaxy and string lensing) will increase in the future. Specifically, the combination of next-generation observational facilities, including the VRO Ivezić *et al.* (2019), and space telescopes, including the Nancy Grace Roman Space Telescope Spergel *et al.* (2015), is expected to probe most of the undiscovered Milky Way satellite galaxy population as well as faint dwarf galaxies throughout the Local Volume Drlica-Wagner *et al.* (2019); Gezari *et al.* (2022). The above-mentioned observational facilities will also significantly enhance the sample of strongly-lensed systems available for deep follow-up observations that is required to constrain dark matter Oguri and Marshall (2010); Weiner *et al.* (2020), and will also provide qualitatively new probe of low-mass halos Pardo and Doré (2021). Combinedly, these observations are supposed to constrain WDM masses up to ~ 20 keV Drlica-Wagner *et al.* (2019), which is equivalent to ~ 200 keV for non-thermal WDM particles masses produced via moduli decay.

In the above analysis, we considered that nonthermal WDM accounts for the entire dark matter budget of the universe. The next generation's constraints may change in the case of a smaller fraction of lower mass WDM. Also, we assumed the nonthermal WDM model parameters as phenomenological; however, it will be interesting to consider explicit realizations of this scenario that naturally yield mixed cold-plus-warm dark matter scenarios. In the string theory, two WDM production scenarios are particularly relevant: the decay of the inflaton to excitations at the bottom of a warped throat Frey *et al.* (2009), or a hidden sector with keV-scale condensation (e.g., see Ref. Halverson and Langacker (2018)). According to string theory, there can be mixed scenarios of warm and cold dark matter

the warm component coming from sterile particles of moduli decay and the cold component corresponding to a thermal relic that freezes out from the Standard Model sector (see Ref. Cicoli *et al.* (2023) for a recent review of various scenarios for dark matter in string theory). A detailed study of such mixed scenarios is left for future research.

Chapter 6

Early Dark Energy beyond Slow Roll and Cosmological Tensions [1]

6.1 Introduction

The most successful cosmological paradigm, known as the ΛCDM model, combining a cosmological constant and cold dark matter, explains most of the characteristics of our universe. It has demonstrated remarkable agreement with a variety of cosmological observations. However, recently, a few mismatches have occurred between the model's predictions and empirical measurements of selected observables. Among the mismatches that have commanded substantial attention over the past decade, determining the Universe's expansion rate remains a subject of enormous discussion. Noteworthy in this context are the most recent evaluations of the Cosmic Microwave Background (CMB) undertaken by the Planck satellite. These evaluations, within the purview of the ΛCDM framework, yield a derived value for the Hubble parameter denoted as $H_0 = 67.36 \pm 0.54\,\mathrm{km/s/Mpc}$ Aghanim

[1] This chapter is based on two publications Gogoi *et al.* (2021); Sharma *et al.* (2023)

et al. (2018c). Extending beyond the ambit of Planck, observations calibrated with information predating recombination, such as BAO Abbott *et al.* (2018b) and BBN Cooke *et al.* (2016), collectively tend to align with a lower value of the Hubble constant as inferred from the CMB.

Conversely, the SH_0ES team has embarked on a measurement of the Hubble parameter, giving an estimate of $H_0 = 73.04 \pm 1.04\,\mathrm{km/s/Mpc}$. This determination derived from an intricate construction of a distance ladder predicated on type 1a supernovae (SN1a) Riess *et al.* (2019, 2020, 2022). While numerous other local and direct measurements tend to corroborate a higher Hubble parameter value, it is essential to acknowledge that the tension level experienced by these measurements is not as pronounced as that encountered in the SH_0ES findings (for an in-depth synthesis, refer to Ref. Abdalla *et al.* (2022)).

As experimental precision of cosmological observations continues to scale new heights and access to more and more data, the Hubble tension got greater significance, thereby drawing more interest and scrutiny from the cosmological research community Schöneberg *et al.* (2021); Di Valentino *et al.* (2021b,a).

A relatively milder discrepancy is also evident in the determination of the local growth parameter, denoted by $S_8 = \sigma_8\sqrt{\frac{\Omega_M}{0.3}}$, wherein Ω_M represents the current total matter density and σ_8 signifies the rms of matter fluctuations at the scale of 8 Mpc/h.

The Planck 2018 CMB measurements, using the ΛCDM framework, estimate $S_8 = 0.832 \pm 0.013$. In contrast, estimations garnered from the study of galaxies via the technique of weak lensing, as undertaken by the CFHTLenS collaboration, intimate a ΛCDM model forecast for S_8 that ostensibly surpasses the direct measurement by a statistically meaningful margin at the 2σ confidence level Heymans *et al.* (2013); MacCrann *et al.* (2015).

This tension has also got enhanced importance due to the amalgamation of various datasets, such as those from the KiDS/Viking initiative Hildebrandt *et al.* (2020); Joudaki *et al.* (2020) and the DES endeavor Abbott *et al.* (2018a, 2022). Of late, the synergy between KiDS/Viking and SDSS datasets has accentuated the tension to a 3σ significance level, manifesting as $S_8 = 0.766^{+0.02}_{-0.014}$ Heymans *et al.* (2020). It is to acknowledge, however, that the amalgamation of KiDS and DES data points to a slightly lower significance of this tension Abbott *et al.* (2023).

No investigations have thus far reported inaccuracies or systematic issues within the data that could account for the Hubble constant (H_0) tension. This has propelled the notion of novel physics into the limelight, prompting substantial interest. Recent studies Knox and Millea (2019); Schöneberg *et al.* (2021) showed the epoch preceding recombination appears to be the likeliest candidate for harboring concealed new physics, capable of relaxing the Hubble tension by lowering the cosmic microwave background (CMB) sound horizon.

The concept of early dark energy (EDE), initially introduced in references such as Karwal and Kamionkowski (2016); Poulin *et al.* (2019); Lin *et al.* (2019), introduces a scalar field that remains inert until the equilibrium between matter and radiation is achieved, at which point it undergoes a sudden transition to dynamism and dilutes at a faster pace than radiation. While EDE exhibits the potential to alleviate the H_0 tension significantly, it grapples with several formidable challenges (expounded upon in discussions found in references like Kamionkowski and Riess (2022); Poulin *et al.* (2023)). Primarily, akin to models aiming to rectify the Hubble tension by reshaping the pre-recombination era, EDE cosmology introduces an augmentation in the power spectra of matter on smaller scales, inadvertently exacerbating the tension related to S_8 Hill *et al.* (2020); Vagnozzi (2021). Secondarily, the EDE model confronts the predicament of coincidence, necessitating a transition of EDE's dynamism at a specific juncture—namely, the juncture of

matter-radiation equality—which, in turn, raises queries about the need for fine-tuning within the model (as expounded upon in studies like Gogoi *et al.* (2021); Niedermann and Sloth (2022); Lin *et al.* (2023)).

Simultaneously, the persistence of present-day dark energy remains an enigma, plagued by its own fine-tuning challenge. Within this context, dynamical dark energy emerges as one of the most extensively scrutinized alternatives to the cosmological constant for grappling with the fine-tuning quandary.

Several physical models have emerged wherein early dark energy seems to naturally manifest around the period of matter-radiation equality Gogoi *et al.* (2021); Carrillo González *et al.* (2023); Lin *et al.* (2023). In select physical frameworks, the prospect arises to facilitate a dynamic evolution for early dark energy before its rapid dilution. An illustrative example, presented in Ref. Gogoi *et al.* (2021), revolves around a scenario involving an interaction between a neutrino-like particle and a scalar field. Depending on the form of the scalar field's potential, the equation of state of early dark energy can undergo modifications, as demonstrated by the ϕ^2 potential case, where the *initial* equation of state is $w_i = -\frac{1}{3}$.

Drawing inspiration from this premise, our present study explores whether a dynamic early dark energy model could hold advantages over a purely static (akin to cosmological constant) behavior. Should early dark energy indeed possess dynamical attributes, the notion could suggest that a unifying mechanism underlies the activation of dark energy at various cosmic epochs—whether it be inflation, early dark energy, or present-day dark energy. Our investigations uncover intriguing tendencies, indicating that contemporary cosmological datasets might favor an equation of state $w_i \neq -1$.

This chapter is arranged as follows: In section 6.2, we present the physical model. In Section 6.3, we introduce our phenomenological modeling for the early dark

energy component, encompassing both the background and perturbations levels. Section 6.3.1 delves into the influence of the initial equation of state (before fluid dilution) on observables. Transitioning to Section 6.4.1, we present our core analysis setup and methodology, with the ensuing results outlined in Section 6.5. Finally, our findings culminate in concluding remarks offered in Section 6.6.

6.2 Neutrino scalar interaction

An eV mass fermion ψ interacts with a scalar field ϕ in this scenario. The equation of motion of this interacting field is governed by effective potential $V_{eff}(\phi)$, not just $V(\phi)$. The field adiabatically stays at a minimum of potential $V_{eff}(\phi)$. This interaction acts as early dark energy. The Lagrangian of this interacting field is given by Fardon *et al.* (2004)

$$\mathcal{L} \supset m_D \psi_1 \psi_2 + f(\Phi)\psi_2\psi_2 + V(\Phi) + \text{H.c.}, \tag{6.1}$$

The coupled Euler and continuity equations are as follows :

$$\dot{\rho_\nu} + 3H(\rho_\nu + P_\nu) = -\frac{d\ln(m)_\nu(\phi)}{d\phi}(\rho_\nu - 3P_\nu) \tag{6.2}$$

$$\dot{\rho_\phi} + 3H(\rho_\phi + P_\phi) = -\frac{d\ln(m)_\nu(\phi)}{d\phi}(\rho_\nu - 3P_\nu) \tag{6.3}$$

The idea is that when the neutrinos were extremely relativistic, the right-hand side term of the equation 6.2, 6.3 vanishes. So effectively, "no interaction". But slowly, as the neutrino becomes semi-relativistic, the interaction term on the right-hand side becomes relativistic and hence the interaction takes place. During this time, the field feels the effective potential of interaction, not just the scalar field interaction. The equation of state of this effective fluid is negative, and this acts as early dark energy. Finally, when the neutrinos become extremely non-relativistic,

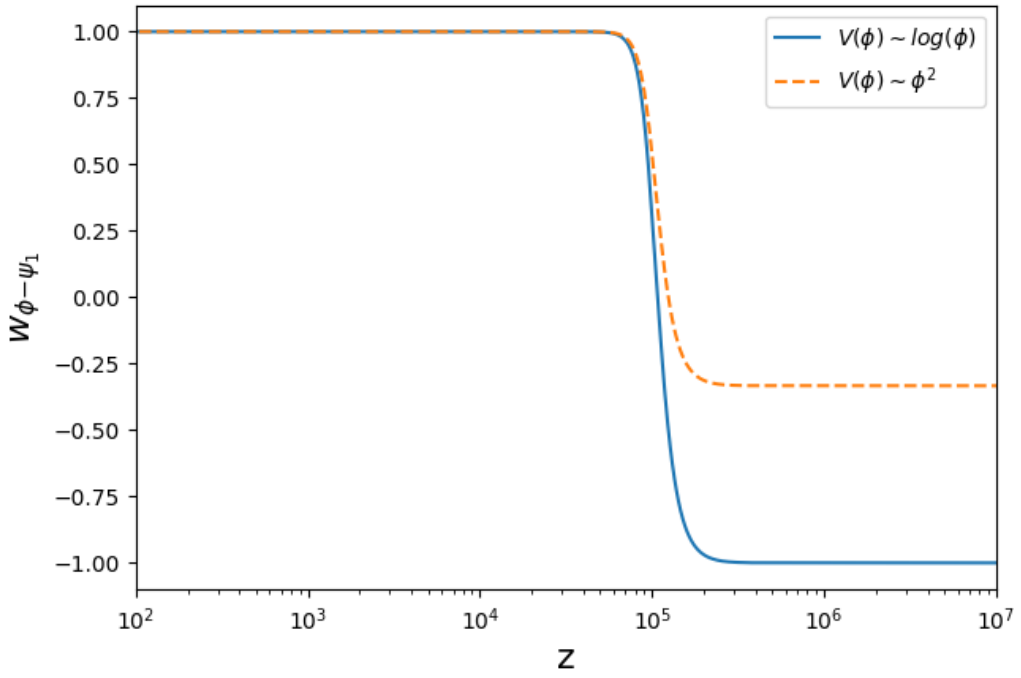

FIGURE 6.1: The equation of state of the interacting neutrino fluid for quadratic potentials and logarithmic potentials of scalar field

the interaction stops, and neutrinos clump down to form nuggets and contribute to the dark matter, and the scalar fields roll away. Thus, this model is where the early dark energy component arrives naturally around matter radiation equality, unlike the conventional EDE models, which are tuned to appear at that epoch.

Equation of state: When the scalar field is in interaction with fermions (neutrinos), the equation of motion is not governed just by $\mathrm{V_{scalar}}(\phi)$ but the effective potential given as $\mathrm{V_{eff}}(\phi) = \mathrm{V_{int}} + \mathrm{V_{scalar}}(\phi)$. The interaction potential is $V_{in} \propto \frac{1}{a^3\phi}$ Gogoi *et al.* (2021); Fardon *et al.* (2004). The equation of state of this interacting fluid is also demonstrated in figure 6.1 as follows:

$$\mathrm{w}_{\phi\psi} = \begin{cases} -\frac{1}{3} & V_{scalar}(\phi) = m_\phi^2\phi^2 \\ -1 & V_{scalar}(\phi) = \log(\phi) \end{cases} \tag{6.4}$$

6.3 Dynamical early dark energy

We are examining a uniform, isotropic, and flat universe, as the FLRW metric describes. This universe is filled with the standard components found in the ΛCDM model, including photons, baryons, neutrinos, cold dark matter, and dark energy. To introduce Early Dark Energy (EDE), we incorporate an additional component using a generalized fluid description. This necessitates specifying its equation of state (w), sound speed (c_s^2), and, if applicable, its anisotropic stress. We assume the anisotropic stress is zero for this scalar field, as discussed in Ref. Sabla and Caldwell (2022).

The equation of state is parameterized as:

$$w_{\rm EDE}(a) = \frac{w_f - w_i}{\left[1 + \left(\frac{a_c}{a}\right)^{3\times(w_f - w_i)}\right]} - w_i \tag{6.5}$$

Here, w_f and w_i represent the final and initial parameters of the equation of state, respectively, and a_c denotes the scale factor at the time of transition. The parameter p controls the width of the transition. The background energy density of the early dark energy component evolves according to:

$$\rho_{\rm EDE}(a) = \rho_{\rm EDE}(1) \times \exp\left(3\int_1^a (1 + w_{\rm EDE}(a))\, da\right) \tag{6.6}$$

To describe perturbations in the fluid, we apply the generalized dark matter formalism Hu (1998). The perturbation equations (Euler and Continuity) in the synchronous gauge are expressed as:

$$\begin{aligned}\frac{d}{d\eta}\left(\frac{\delta_{\rm EDE}}{1+w_{\rm EDE}}\right) &= -\left(\theta_{\rm EDE} + h'\right) \\ &\quad -3H(c_s^2 - c_a^2)\left(\frac{\delta_{\rm EDE}}{1+w_{\rm EDE}} + 3H\frac{\theta_{\rm EDE}}{k^2}\right),\end{aligned}$$

$$\frac{d}{d\eta}\left(\theta_{\rm EDE}\right) = -H\left(1-3c_s^2\right)\theta_{\rm EDE} + c_s^2 k^2 \frac{\delta_{\rm EDE}}{1+w_{\rm EDE}}\,. \tag{6.7}$$

Here, $\delta_{\rm EDE}$ represents the density perturbation, while $\theta_{\rm EDE}$ represents the velocity divergence of the EDE fluid. The sound speed of the EDE fluid governs the relationship between density and pressure perturbations, defined as $c_s^2 = \frac{\delta P}{\delta \rho}$. Here, k denotes the comoving wave-number, H refers to the conformal Hubble parameter, and c_a^2 is the adiabatic sound speed, defined as:

$$c_a^2 = w_{\rm EDE} - \frac{1}{3}\frac{dw_{\rm EDE}/d\ln\left(a\right)}{1+w_{\rm EDE}} \tag{6.8}$$

By employing equation (6.5), we determine that:

$$c_a^2 = \begin{cases} w_i & a \ll a_c\,, \\ w_f & a \gg a_c\,. \end{cases} \tag{6.9}$$

The sound speed c_s^2 is established as follows:

$$c_s^2 = \begin{cases} 1 & a < a_c\,, \\ w_f & a \geq a_c\,, \end{cases} \tag{6.10}$$

However, we observe that the outcomes are not notably influenced by the manner in which we parameterize c_s^2 when we enforce $c_s^2 = w_f$ in the decaying phase.

To establish the initial conditions, we assume that the system initiates in the radiation-dominated era, thus $H = \frac{1}{\eta}$. If the energy density of early dark energy is negligible at the initially, the solution for the metric perturbation h remains unchanged and is given by $h = \frac{(k\eta)^2}{2}$. For super-Hubble modes where $k\eta \ll 1$, equations (6.7) and (6.7) simplify to:

$$\frac{d}{d\eta}\left(\frac{\delta_{\rm EDE}}{1+w_{\rm EDE}}\right) = \frac{k^2\eta}{2} - 3\frac{1}{\eta}(c_s^2 - c_a^2)\left(\frac{\delta_{\rm EDE}}{1+w_{\rm EDE}} + 3\frac{1}{\eta}\frac{\theta_{\rm EDE}}{k^2}\right) \tag{6.11}$$

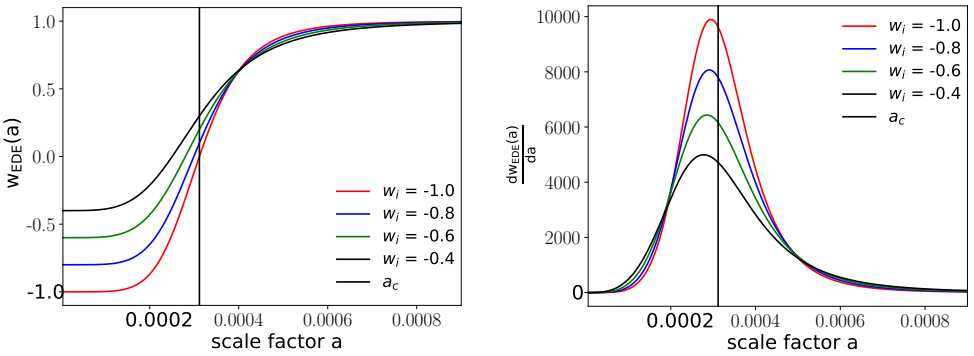

FIGURE 6.2: (a) Effect of varying w_i on the equation of state. (b) Effect of varying w_i on the slope.

$$\frac{d}{d\eta}\left(\theta_{\rm EDE}\right) = -\frac{1}{\eta}\left(1-3c_s^2\right)\theta_{\rm EDE} + c_s^2k^2\frac{\delta_{\rm EDE}}{1+w_{\rm EDE}} \tag{6.12}$$

These can be solved in powers of $(k\eta)^2$, yielding the initial conditions:

$$\frac{\delta_{\rm EDE}}{1+w_{\rm EDE}} = -\frac{(4-3c_s^2)/2}{8+6c_s^2-12c_a^2}(k\eta)^2 \tag{6.13}$$

$$\theta_{\rm EDE} = -\frac{c_s^2/2}{8+6c_s^2-12c_a^2}k(k\eta)^3 \tag{6.14}$$

These equations, along with the initial conditions, have been incorporated into an adapted version of the Boltzmann code CLASS Lesgourgues (2011); Blas *et al.* (2011).

6.3.1 Influence on Background and Perturbation Dynamics

To examine the impact of altering background and perturbation effects, we vary the parameter w_i over a range of values, specifically $w_i = -1, -0.8, -0.6, -0.4$. The effect of this variation on $w_{\rm EDE}(a)$ and $\frac{dw_{\rm EDE}(a)}{da}$ is depicted in Figure 6.2.

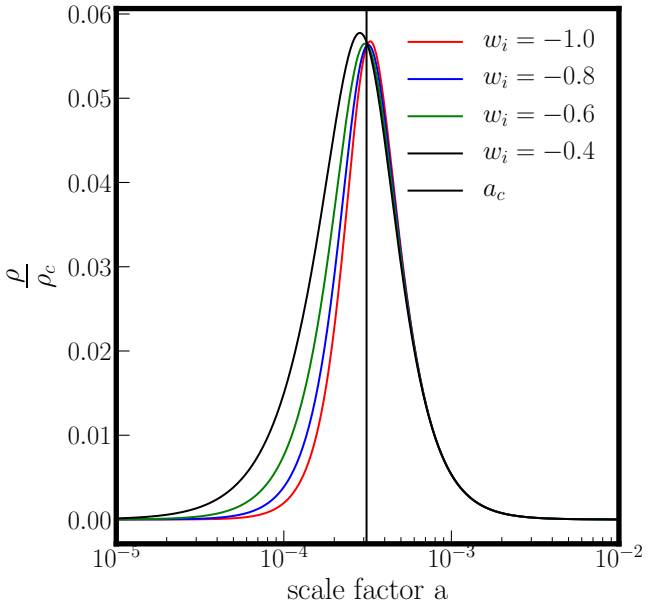

FIGURE 6.3: Effect of varying w_i on the evolution of EDE density fraction.

Effect of w_i ***on EDE Background Evolution***: Initially, we explore the influence on the evolution of the early dark energy's background energy density. This is presented in Figure 6.3. It is readily apparent that as w_i increases, the energy density spreads out over time. The transition becomes more gradual, resulting in the EDE component persisting for longer and influencing the expansion rate from earlier redshifts. Consequently, this leads to a diminished sound horizon value and an increased Hubble parameter value at the present epoch.

We will now explain in detail the impact of w_i on the perturbations of early dark energy and its influence on the matter component.

Effect of w_i ***on EDE Density Perturbations***:

In Figure 6.4, we present a graphical representation of the influence of varying w_i on the density fluctuations of early dark energy, considering modes with $k = 0.01, 0.06, 0.3$ Mpc^{-1}. These modes correspond to those entering the horizon after, around, and before a_c, respectively. Additionally, we indicate the points of horizon

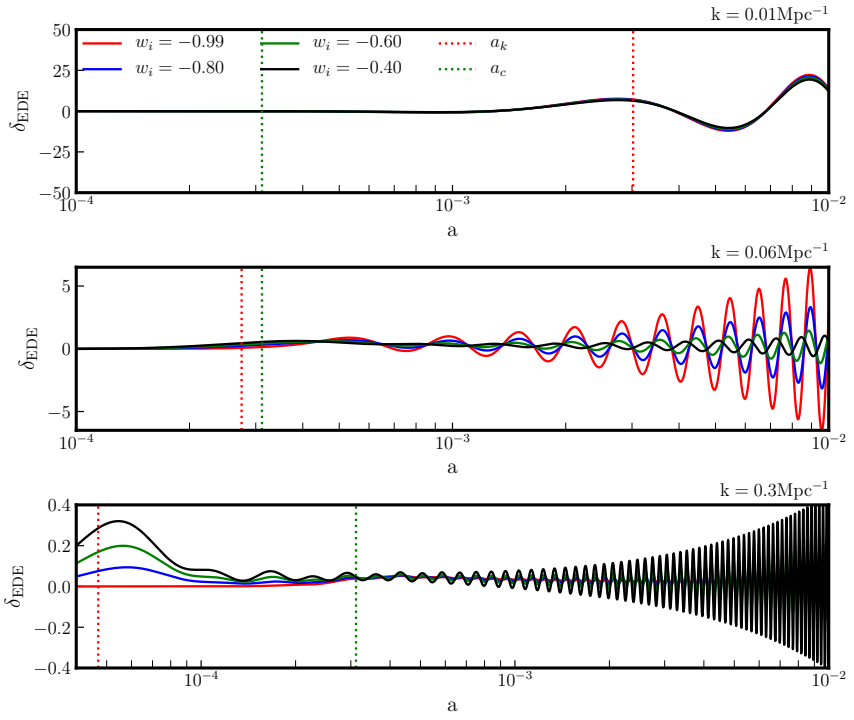

FIGURE 6.4: Effect of varying w_i on the evolution of EDE density fluctuations for three modes $k = 0.01, 0.06, 0.3\text{Mpc}^{-1}$.

crossing for each mode, defined as $k\tau(a_k) \equiv 2\pi$, and denote the values of a_c with red and green dotted vertical lines.

The equation governing early dark energy (EDE) perturbations can be derived by simplifying Equations 6.7 and 6.7 into a second-order differential equation:

$$\begin{aligned} \frac{d^2}{d\eta^2}\left(\frac{\delta_{\rm EDE}}{1+w_{\rm EDE}}\right) &+ k^2 c_s^2 \frac{\delta_{\rm EDE}}{1+w_{\rm EDE}} \\ &+ (1-3c_a^2)\frac{a'}{a}\frac{d}{d\eta}\left(\frac{\delta_{\rm EDE}}{1+w_{\rm EDE}}\right) = 0\,. \end{aligned}$$

This equation bears a resemblance to that of a damped simple harmonic oscillator.

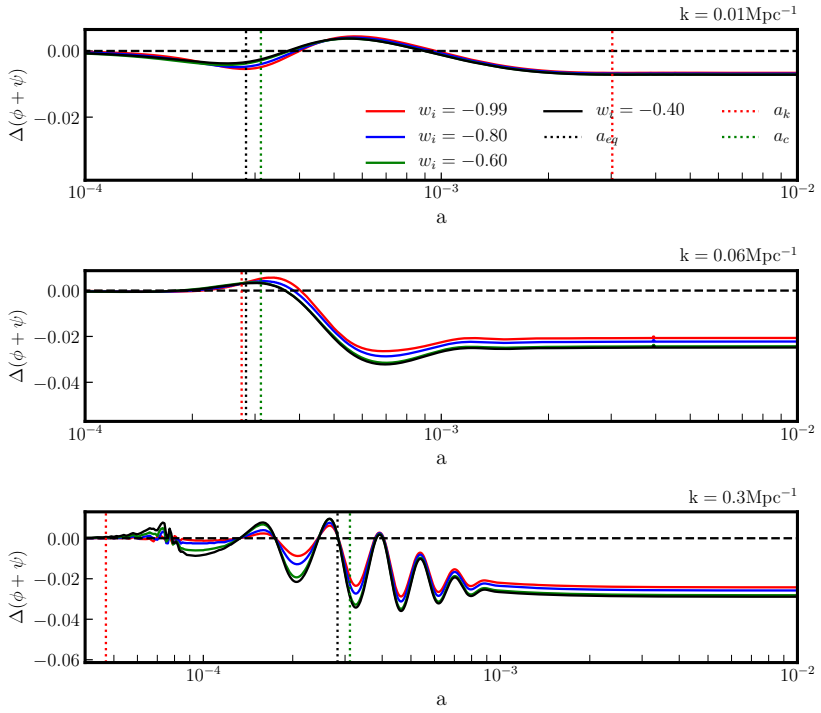

FIGURE 6.5: Effect of varying w_i on the evolution of Weyl potential. We show the difference relative to the ΛCDM model with identical cosmological parameters.

Its solution oscillates, with the amplitude either decreasing or increasing, contingent on the sign of the damping terms. The oscillation frequency is determined by $k^2c_s^2$, while the term $1-3c_a^2$ can be either negative or positive, acting as either a driving force or a friction term, assuming $w_i < -\frac{1}{3}$:

$$1-3c_a^2 = \begin{cases} 1-3w_i > 0 & a \ll a_c \\ 1-3w_f < 0 & a \gg a_c\,. \end{cases} \tag{6.15}$$

The impact of w_i on the growth of EDE density fluctuations for various k modes can be comprehended as follows:

- For modes that enter the horizon well before a_c (i.e., $a_k \ll a_c$): Prior to horizon crossing, the growth of $\delta_{\rm EDE}$ follows the initial condition [Eq. (6.13)], showing a growth proportional to $(k\tau)^2$ and $1+w_{\rm EDE}$. Consequently, models

with higher w_i exhibit faster growth, particularly evident for the mode with $k = 0.3$ Mpc^{-1}, which crosses the horizon earlier. In the $a_k < a < a_c$ region, where $w_i < 0$, the solution of $\delta_{\rm EDE}$ is oscillatory but with a decreasing amplitude (see Equation 6.15). At a_c, models with high w_i exhibit a higher amplitude. Finally, in the $a > a_c$ region, the solution remains oscillatory, but the damping factor changes sign, acting as a driving force and resulting in oscillations with a larger amplitude for modes that had a higher amplitude at a_c, i.e., modes with higher w_i.

- For modes that enter the horizon well after a_c (i.e., $a_k \gg a_c$): In this scenario, all modes have a similar evolution since they are essentially frozen ($(k\tau)^2 \ll 1$) when the fields become dynamic. Around horizon crossing, all modes grow proportionally to $1 + w_{\rm ede}$ as dictated by [Eq. (6.13)], while after horizon crossing, they oscillate with increasing amplitude, similar to larger modes.

- For modes that enter the horizon around a_c (i.e., $a_k \sim a_c$): Before and around horizon crossing, the growth of $\delta_{\rm EDE}$ is still determined by the initial condition [Eq. (6.13)]. After horizon crossing, modes oscillate with increasing amplitude. However, $w_{\rm EDE}$ evolves with time as the modes enter the horizon, and can even become positive around a_k. This introduces a non-trivial time-evolution to the damping term, such that modes with higher amplitude at a_k now have a *smaller* amplitude of oscillations at $a > a_k$. For instance, the model with $w_i = -0.4$ displays a much lower amplitude of oscillations than the model with $w_i = -0.99$ at this scale, whereas it exhibits a significantly larger oscillation amplitude at larger k. It is important to emphasize that this is a specific consequence of our chosen parameterization of $w_{\rm EDE}(a)$, rather than an effect solely attributable to w_i.

Influence on the Weyl Potential Evolution:

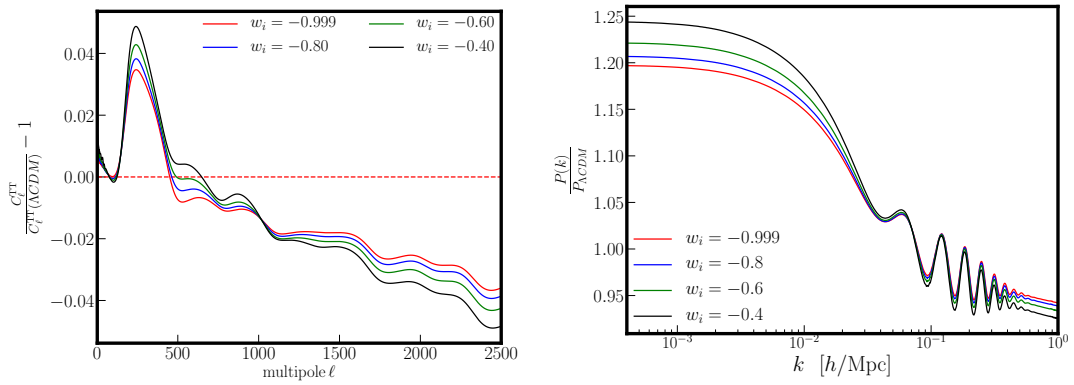

FIGURE 6.6: Effect of varying w_i on matter power spectra (right panel) and CMB TT power spectra (left panel).

To grasp the effect of w_i on the CMB power spectra, it is insightful to visualize the quantity $-(\Psi + \Phi)$, commonly referred to as the Weyl potential. This is determined as Poulin *et al.* (2023):

$$\Phi = -\frac{3}{4k^2}\left(\frac{a'}{a}\right)^2\left(2\delta + \sum_i [1+w_i]\left[\frac{6(a'/a)\theta_i}{k^2} + 3\sigma_i\right]\right) . \tag{6.16}$$

In Figure 6.5, we present the influence of w_i on the evolution of the Weyl potential for various k modes (consistent with the previous figure), normalized to the standard ΛCDM scenario. As discussed earlier, the impact on the Weyl potential can be elucidated through a combination of background and perturbation effects.

- For $a \gg a_c$, the Weyl potential experiences suppression because of the presence of EDE, which contributes to the Hubble rate but doesn't exhibit clustering behavior. In the case of modes that come within the horizon prior to a_c, a higher w_i leads to a more prolonged EDE phase, resulting in greater suppression of the Weyl potential. For modes entering the horizon much later, the degree of suppression remains consistent since EDE primarily influences these modes after a_c, when all models converge.

- At $a \approx a_c$, residual oscillations with diminishing amplitude become evident, attributed to EDE perturbations. The frequency of these oscillations is higher for larger k modes, as the EDE oscillations are characterized by $(kc_s)^2$. For modes entering the horizon before a_c ($k = 0.3$ Mpc^{-1}), a higher w_i leads to a greater amplitude of $\delta_{\rm EDE}$, consequently enhancing the contribution to the Weyl potential around a_c. For the mode entering the horizon around a_c ($k = 0.06$ Mpc^{-1}), a noteworthy non-uniform behavior is observed. Here, the model with a smaller w_i exhibits a more pronounced initial oscillation. As previously discussed, this discrepancy arises from the evolving nature of w, influencing the damping term. Finally, for modes entering the horizon very late ($k = 0.001$ Mpc^{-1}), EDE perturbations are essentially negligible, and the Weyl potential experiences suppression around a_c due to the presence of non-clustering EDE. Minor distinctions arise from slight variations in the time evolution of $w_{\rm EDE}$.

6.3.2 Influence of w_i on the CMB and Matter Power Spectra

In the left panel of Figure 6.6, we present the residuals of the CMB temperature anisotropy power spectra (TT) when w_i is varied while keeping other parameters constant, using ΛCDM as the reference. The primary impact of EDE is comprehensively detailed in Ref. Poulin *et al.* (2023). Here, we concentrate on elucidating the influence of varying w_i. The most prominent effect of w_i on the CMB TT power spectra arises from the following contributions:

- Diffusion Damping: Increasing w_i augments the impact of EDE on the background expansion. Since we maintain θ_s as a constant, and the effects of EDE

on the sound horizon and damping scales differ, adjusting the angular diameter distance D_A through the increase in H_0 cannot simultaneously leave the angular diffusion damping scale $\theta_d = \frac{r_d}{D_A}$ unaffected. Consequently, θ_d increases, resulting in a more pronounced suppression of CMB TT power spectra at high ℓ, a suppression that is more pronounced for larger w_i.

- Sachs-Wolfs Contribution: The alterations to the Weyl potential stemming from the escalation of w_i (and the prolonged EDE phase) significantly impact the Sachs-Wolfs contribution around $\ell \sim 500$. The larger the w_i, the greater the contribution to the Sachs-Wolfs effect at intermediate ℓ's, thereby enhancing the amplitudes of the first acoustic peaks.

In the right panel of Figure 6.6, we illustrate the effect of increasing w_i on the total matter power spectra. Increasing w_i results in a suppression of matter power at smaller scales compared to the case with $w_i = -1$, attributable to the extended period of EDE (which suppresses the Weyl potential). Consequently, we observe a reduced σ_8 for higher w_i, indicating that allowing w_i to vary might help in removing discrepancies with weak lensing surveys. The enhancement in power at larger scales arises from the fact that $\omega_\Lambda = 1 - \Omega_{\rm m}$ is smaller in models with larger w_i, a consequence of the increased h value that has elevated $\Omega_{\rm m} = \omega_{\rm m} h^2$ while keeping $\omega_{\rm m}$ constant.

6.4 Details of Analysis

6.4.1 Data sets

- The Planck 2018 observations encompass a range of measurements, including the low-ℓ Cosmic Microwave Background (CMB) TT, EE power spectra,

and the high-ℓ TT, TE, EE power spectra. These observations also involve reconstructing the gravitational lensing potential, as detailed in Planck Collaboration and Aghanim (2020).

- Baryon Acoustic Oscillation (BAO) measurements originate from diverse sources. Specifically, data from the 6-degree Field Galaxy Survey (6dFGS) at a redshift of $z = 0.106$ Beutler *et al.* (2011), the Sloan Digital Sky Survey Data Release 7 (SDSS DR7) at $z = 0.15$ Ross *et al.* (2015), and the Baryon Oscillation Spectroscopic Survey Data Release 12 (BOSS DR12) at multiple redshifts ($z = 0.38, 0.51, 0.61$) Alam *et al.* (2017a) have been employed. Additionally, the combined limits from the extended Baryon Oscillation Spectroscopic Survey Data Release 14 (eBOSS DR14), involving Ly-α auto-correlation at $z = 2.34$ and cross-correlation at $z = 2.35$, have been integrated de Sainte Agathe *et al.* (2019), Blomqvist *et al.* (2019).

- The growth function $f\sigma_8(z)$ (FS) was determined by CMASS and BOSS DR12 (LOWZ galaxy samples) at redshifts ($z = 0.38, 0.51, 0.61$) Alam *et al.* (2017a).

- The Pantheon catalog of Type Ia supernovae covers a range of redshifts ($0.01 < z < 2.3$) Scolnic *et al.* (2018b).

- The SH0ES collaboration's result was modeled with a Gaussian likelihood, centered on a value of $H_0 = 73.2 \pm 1.3$ km/s/Mpc Riess *et al.* (2020).

- Weak lensing data from KIDS1000+BOSS+2dfLenS was condensed into a split-normal likelihood for the parameter S_8, yielding a value of $0.766^{+0.02}_{-0.014}$ Heymans *et al.* (2020).

6.4.2 Methodology

Our base cosmological framework encompasses the six fundamental ΛCDM parameters, namely $\{\omega_b, \omega_{\rm cdm}, 100\times\theta_s, n_s, \ln(10^{10}A_s), \tau_{\rm reio}\}$, coupled with four additional EDE parameters, as detailed in Section 6.3: w_i, w_f, $z_{\rm c}$, $f_{\rm EDE}$.

To scrutinize the EDE model, we conduct MCMC analyses using various combinations of CMB, BAO, and supernovae datasets (elaborated in Section 7.3.1). We employ the Metropolis-Hasting algorithm integrated into the MontePython-v3 Brinckmann and Lesgourgues (2018) code, interfaced with our modified CLASS version. The reported $\chi^2_{\rm min}$ values are derived using the iMinuit Python package James and Roos (1975). To effectively handle a large number of nuisance parameters, we implement a Choleski decomposition Lewis *et al.* (2000) and consider chains to have converged if they satisfy the Gelman-Rubin convergence criterion with $R-1<0.05$ Gelman and Rubin (1992).

We conduct analyses for three distinct variations of the EDE model: i) a two-parameter fluid model of EDE, exclusively varying ($f_{\rm EDE}$, z_c), while holding the equation of state parameters fixed at ($w_i=-1$, $w_f=1$), denoted as 2pEDE; ii) a three-parameter model (w_f, $f_{\rm EDE}$, z_c), referred to as 3pEDE; iii) a four-parameter model (w_i, w_f, $f_{\rm EDE}$, z_c), termed 4pEDE. We conduct three sets of runs for each model, starting from the baseline Planck+BAO+Pantheon, then incorporating the SH_0ES prior, and finally the S_8 prior. We also perform the same sets of runs with ΛCDM for the sake of comparison. We apply broad flat priors for all ΛCDM parameters. The prior ranges for Early Dark Energy parameters are imposed as follows:

It's important to note that we allow w_i to exceed $-1/3$, ensuring that EDE doesn't strictly correspond to a Dark Energy-like component in certain regions of the

Parameter name	prior range
w_i	[-1,0]
w_f	[0,1]
$f_{\rm EDE}$	[0,0.3]
$\log_{10}(z_c)$	[2,5]

Parameters ↓	ΛCDM	2 param EDE	3 param EDE	4 param EDE
100 θ_s	$1.042066(1.04198)^{+0.00029}_{-0.00028}$	$1.04158(1.04159)^{+0.00034}_{-0.00035}$	$1.04160(1.04156)^{+0.00033}_{-0.00038}$	$1.04124(1.04094)^{+0.0006}_{-0.00053}$
100 ω_b	$2.253(2.249)^{+0.013}_{-0.014}$	$2.284(2.283)^{+0.022}_{-0.023}$	$2.283(2.278)^{+0.022}_{-0.025}$	$2.285(2.271)^{+0.023}_{-0.024}$
$\omega_{\rm cdm}$	$0.1184(0.1183)^{+0.00089}_{-0.00088}$	$0.1258(0.1247)^{+0.0035}_{-0.0031}$	$0.1274(0.1267)^{+0.0034}_{-0.0032}$	$0.128(0.1326)^{+0.0044}_{-0.0041}$
$\log 10^{10} A_s$	$3.054(3.056)^{+0.015}_{-0.016}$	$3.063(3.067)^{+0.015}_{-0.015}$	$3.065(3.072)^{+0.015}_{-0.017}$	$3.063(3.066)^{+0.015}_{-0.016}$
n_s	$0.9697(0.9701)^{+0.0037}_{-0.0037}$	$0.9803(0.9819)^{+0.0062}_{-0.0062}$	$0.9841(0.9849)^{+0.0066}_{-0.0068}$	$0.983(0.9922)^{+0.0078}_{-0.007}$
$\tau_{\rm reio}$	$0.0602(0.0617)^{+0.0073}_{-0.0082}$	$0.0569(0.0600)^{+0.007}_{-0.0076}$	$0.0573(0.0616)^{+0.0073}_{-0.0078}$	$0.0578(0.0554)^{+0.0071}_{-0.0081}$
$f_{\rm EDE}$	–	$0.112(0.105)^{+0.047}_{-0.036}$	$0.118(0.121)^{+0.044}_{-0.034}$	$0.112(0.160)^{+0.054}_{-0.04}$
$\log_{10}(z_c)$	–	$3.53(3.51)^{+0.09}_{-0.12}$	$3.67(3.61)^{+0.091}_{-0.15}$	$3.82(3.81)^{+0.15}_{-0.23}$
w_i	–	–	–	$-0.651(-0.783)^{+0.086}_{-0.35}$
w_f	–	–	$0.74(0.79)^{+0.12}_{-0.13}$	$0.61(0.60)^{+0.1}_{-0.13}$
σ_8	$0.8097(0.8108)^{+0.006}_{-0.0064}$	$0.831(0.8305)^{+0.011}_{-0.011}$	$0.834(0.836)^{+0.011}_{-0.011}$	$0.830(0.841)^{+0.012}_{-0.011}$
H_0 [km/s/Mpc]	$68.18(68.12)^{+0.39}_{-0.41}$	$70.03(70.09)^{+0.91}_{-0.85}$	$70.46(70.52)^{+0.9}_{-0.91}$	$70.68(71.59)^{+1.2}_{-1.1}$
$\chi^2_{\rm min}$	3826.58	3816.46	3814.53	3812.16
$\Delta\chi^2_{\rm min}$	0	-10.12	-12.05	-14.5

TABLE 6.1: The table of various cosmological parameters outcome of MCMC analysis from the lensing-marginalized Planck+BAO+SN1a data with H0 prior. The reported values are in the format of "mean (best-fit) $\pm1\sigma$ error".

parameter space. However, it's worth emphasizing that this doesn't lead to any mathematical inconsistencies in the equations. For an examination of the $w_i > 0$ region of the parameter space, please refer to section 6.5.3.

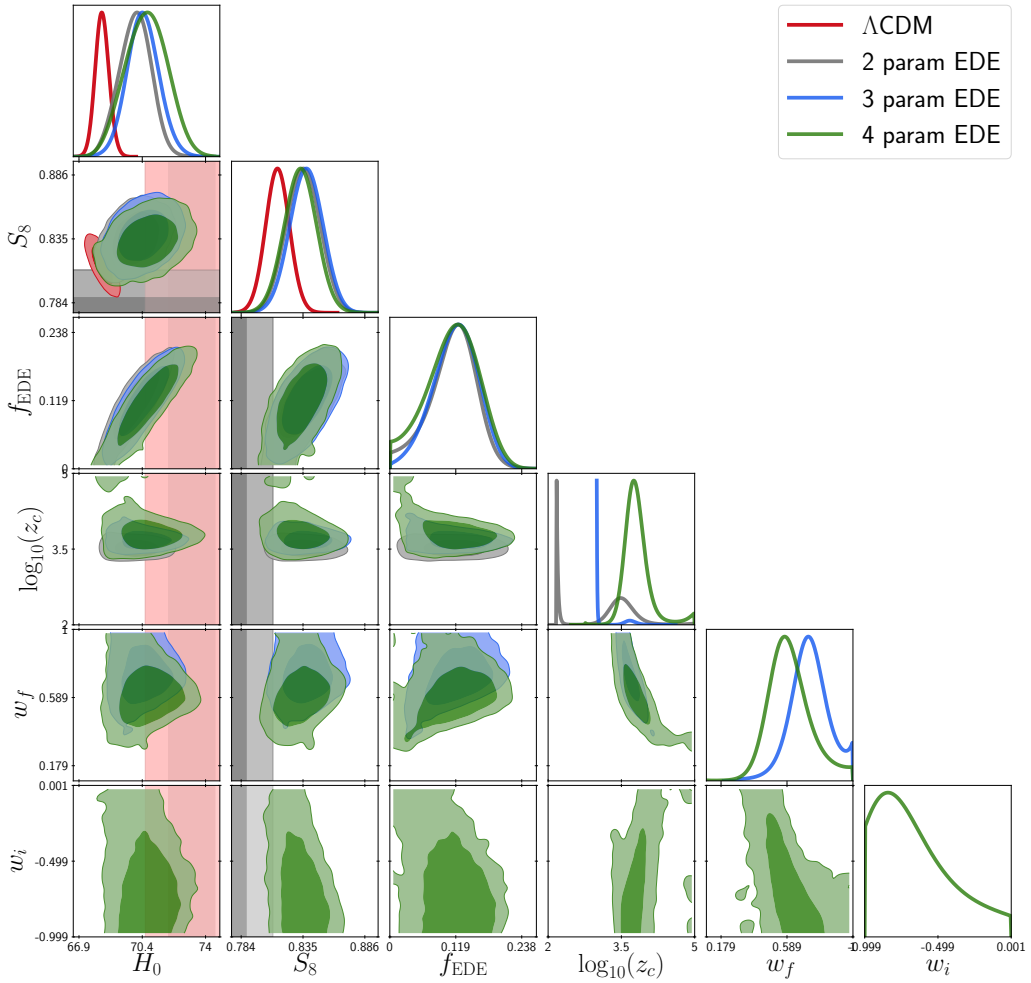

FIGURE 6.7: Posterior distributions in the ΛCDM and EDE models reconstructed from Planck+BAO+Pantheon+H_0

6.5 Results

6.5.1 Results including H0 prior

Let's begin by assessing the effectiveness of various models in addressing the Hubble tension. For this, we primarily focus on the Planck+BAO+Pantheon+SH_0ES analyses.

Table 6.1 provides the reconstructed mean and best-fit values of parameters. In

Appendix 6.6, we present the minimum χ^2 values for the ΛCDM, 2pEDE, 3pEDE, and 4pEDE models, both without SH_0ES (Table 6.4) and with SH_0ES (Table 6.5).

Figure 6.7 displays the 1D and 2D posterior distributions of the EDE parameters, along with H_0 and S_8, comparing ΛCDM to the three different EDE models.

Upon analysis, it's clear that the Hubble parameter value is higher for the 4pEDE model ($H_0 = 70.68^{+1.2}_{-1.1}$) in comparison to the 3pEDE model ($H_0 = 70.46^{+0.9}_{-0.91}$) and the 2pEDE model ($H_0 = 70.03^{+0.91}_{-0.85}$). Notably, the overall $\chi^2_{\rm min}$ also sees an improvement of 2.4 in the 4pEDE model relative to the 3pEDE model, which is a more substantial enhancement than the transition from 2pEDE to 3pEDE.

However, it's worth noting that the value of w_i is only weakly constrained, with only an upper limit at the 1σ level ($w_i < -0.565$), but it remains compatible with 0 at the 2σ level. In section 6.5.3, we establish that the sole stringent limit on w_i is $w_i < 1/3$, stemming from the requirement that EDE doesn't dominate the energy density at early times.

Most significantly, while the H_0 value experiences a slight increase, the σ_8 value undergoes a marginal decrease, approximately 0.4σ lower. This suggests that w_i might contribute to the S_8 tension. Consequently, our attention now shifts towards incorporating S_8 measurements into the analysis.

6.5.2 Results of S8 prior

The mean and best-fit values for various parameters can be found in Table 6.2, and the same parameters are plotted in Figure 6.8. All the minimum χ^2 values are provided in Table 6.6.

Parameters ↓	ΛCDM	3 param EDE	4 param EDE
100 θ_s	$1.04210(1.04214)^{+0.00028}_{-0.00028}$	$1.04185(1.04178)^{+0.00034}_{-0.00042}$	$1.04143(1.04163)^{+0.00072}_{-0.00051}$
100 ω_b	$2.258(2.268)^{+0.013}_{-0.013}$	$2.277(2.271)^{+0.02}_{-0.023}$	$2.281(2.271)^{+0.021}_{-0.024}$
$\omega_{\rm cdm}$	$0.1177(0.1179)^{+0.00085}_{-0.00081}$	$0.1227(0.1225)^{+0.0029}_{-0.0035}$	$0.1238(0.1228)^{+0.0034}_{-0.0044}$
$\log 10^{10} A_s$	$3.048(3.037)^{+0.014}_{-0.015}$	$3.053(3.050)^{+0.015}_{-0.015}$	$3.053(3.044)^{+0.015}_{-0.015}$
n_s	$0.9708(0.9712)^{+0.0036}_{-0.0037}$	$0.9797(0.9814)^{+0.0072}_{-0.0074}$	$0.9795(0.9802)^{+0.0071}_{-0.0074}$
$\tau_{\rm reio}$	$0.0580(0.0520)^{+0.007}_{-0.0078}$	$0.0562(0.0544)^{+0.0072}_{-0.0074}$	$0.0569(0.0526)^{+0.0071}_{-0.0077}$
$f_{\rm EDE}$	–	$0.069(0.068)^{+0.036}_{-0.048}$	$0.075(0.054)^{+0.041}_{-0.048}$
$\log_{10}(z_c)$	–	$3.79(3.72)^{+0.14}_{-0.32}$	$3.89(4.02)^{+0.22}_{-0.33}$
w_i	–	–	unconstrained (-0.34)
w_f	–	unconstrained(0.65)	$0.58(0.45)^{+0.1}_{-0.16}$
σ_8	$0.8051(0.8015)^{+0.0057}_{-0.006}$	$0.817(0.817)^{+0.01}_{-0.011}$	$0.8161(0.8109)^{+0.0095}_{-0.0096}$
H_0 [km/s/Mpc]	$68.48(68.50)^{+0.38}_{-0.38}$	$69.94(69.92)^{+0.92}_{-1}$	$70.25(69.93)^{+1.1}_{-1.2}$
$\chi^2_{\rm min}$	3832.41	3823.99	3823.79
$\Delta\chi^2_{\rm min}$	0	-8.42	-8.62

TABLE 6.2: The table of various cosmological parameters outcome of MCMC analysis from Planck+BAO+SN1a data with H_0 + S_8 priors. The reported values are in format of "mean (best-fit) $\pm 1\sigma$ error"

The primary impact of introducing the S_8 prior is a reduction in the preference for non-zero EDE, along with a decrease in the value of H_0 and a lowering of σ_8. Additionally, the $\Delta\chi^2$ in comparison to ΛCDM sees a significant reduction when compared to the case without the S_8 prior. Moreover, the fit of the 4pEDE model is only marginally superior to that of the 3pEDE model, and w_i is now unconstrained.

In conclusion, while the inclusion of w_i does lead to a slight reduction in the S_8 parameter, it doesn't solve both the H_0 and S_8 tensions simultaneously within the EDE model.

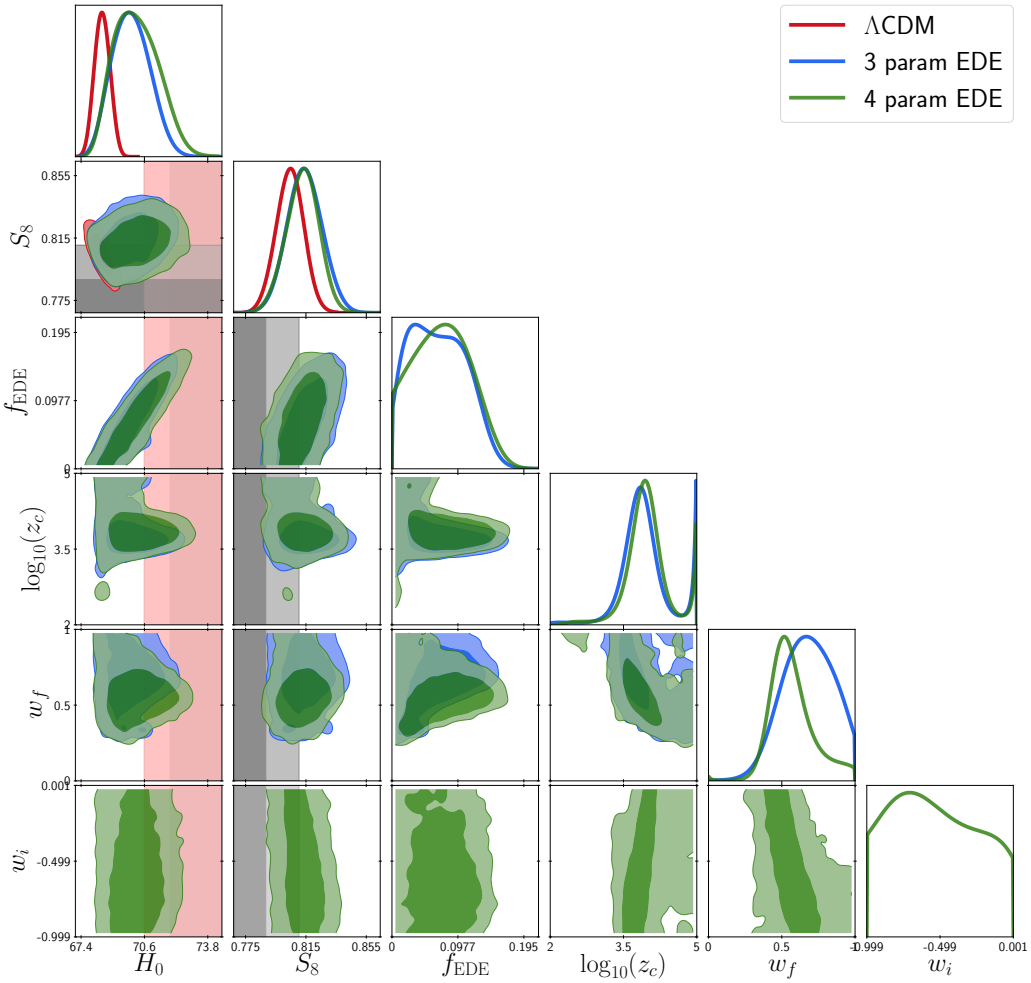

FIGURE 6.8: Same as Fig. 6.7, now also include the S_8 prior.

6.5.3 Impact of Prior Changes on w_i

In the previous sections, we investigated the potential of modifying the initial equation of state parameter, w_i, within the range of $[-1, 0]$. Now, we extend this inquiry beyond Dark Energy, considering w_i in the range of $[-0.33, 1]$. The remaining parameters are adjusted as detailed in the main body of the paper. The primary results are presented in Figure 6.9, comparing the outcomes of $w_i \in [-0.33, 1]$ with the standard prior outlined in the previous section, using Planck+BAO+Pantheon+H_0+S_8 data. Additionally, Table 6.3 provides the reconstructed parameters when including either only the H_0 prior or both the H_0 and S_8 priors.

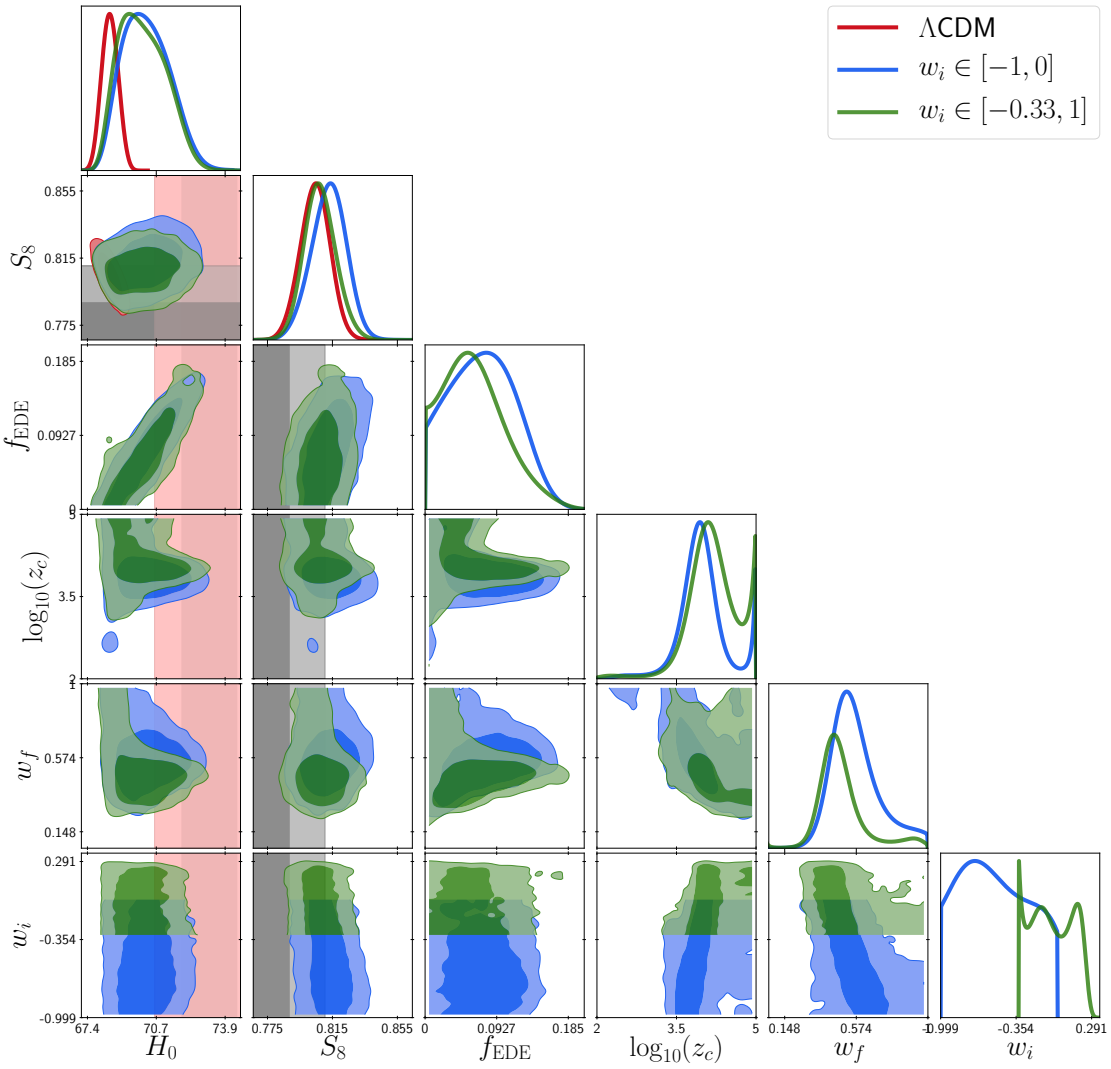

FIGURE 6.9: Effect of changing prior on w_i

Initially, the posterior distribution of w_i exhibits a strict upper bound around 0.3. This arises from the fact that fluid with a higher w_i would dominate the expansion rate in the early universe, leading to discrepancies with observational data. Additionally, it can be observed that the posterior distribution of S_8 precisely matches that of ΛCDM, while H_0 shows a significantly higher value. Essentially, a model featuring an "Early Dark Energy" (EDE) with $w_i > -0.33$ can yield results comparable to the standard EDE model in alleviating tension without exacerbating the S_8 tension.

Parameters ↓	H_0 prior	H_0+S_8 prior
100 θ_s	$1.04143(1.04036)^{+0.0011}_{-0.00095}$	$1.04108(1.04026)^{+0.0013}_{-0.00065}$
100 ω_b	$2.278(2.285)^{+0.02}_{-0.024}$	$2.279(2.272)^{+0.019}_{-0.023}$
$\omega_{\rm cdm}$	$0.126(0.1298)^{+0.0042}_{-0.0042}$	$0.1233(1.268)^{+0.0027}_{-0.0051}$
$\log 10^{10} A_s$	$3.059(3.060)^{+0.015}_{-0.015}$	$3.051(3.062)^{+0.014}_{-0.016}$
n_s	$0.979(0.9826)^{+0.007}_{-0.0067}$	$0.977(0.9810)^{+0.0061}_{-0.0075}$
$\tau_{\rm reio}$	$0.0590(0.0576)^{+0.0073}_{-0.0078}$	$0.0577(0.0605)^{+0.0069}_{-0.0079}$
$f_{\rm EDE}$	$0.081(0.120)^{+0.041}_{-0.045}$	$0.065(0.094)^{+0.028}_{-0.055}$
$\log_{10}(z_c)$	$4.11(3.96)^{+0.12}_{-0.28}$	$4.134(4.038)^{+0.31}_{-0.5}$
w_i	$< 0.33(-0.20)$	$< 0.33(0.0978)$
w_f	$0.461(0.483)^{+0.082}_{-0.089}$	$0.486(0.409)^{+0.057}_{-0.15}$
σ_8	$0.8195(0.8252)^{+0.0085}_{-0.0087}$	$0.8109(0.8172)^{+0.0074}_{-0.0088}$
H_0 [km/s/Mpc]	$70.23(70.97)^{+1.1}_{-1.1}$	$70.08(70.78)^{+0.99}_{-1.3}$
$\chi^2_{\rm min}$	3813.32	3822.69
$\Delta\chi^2_{\rm min}$	-13.26	-9.72

TABLE 6.3: The table of cosmological parameter outcome of MCMC analysis from Planck+BAO+SN1a data with H0 and S_8 when $w_i \in [-0.333, 1]$. The reported values are in format as" mean(bestfit) $\pm 1\sigma$"

In terms of the χ^2 value, the EDE model with $w_i \in [-1, 0]$ performs slightly better (by -1.2) when the H_0 prior is excluded from the analysis. However, the model with $w_i \in [-1/3, 0]$ performs better when S_8 is included, as the EDE effect persists for an extended period, further reducing the growth of cosmic structures.

6.6 Conclusions

This study delves into the cosmological implications of early dark energy (EDE) beyond the slow-roll approximation, specifically by altering the initial equation of state w_i typically set to -1. Here are the key findings:

- Elevating w_i while keeping $f_{\rm EDE}$ and z_c constant extends the contribution of EDE to the expansion rate before recombination. This leads to a diminished sound horizon of the Cosmic Microwave Background (CMB) and consequently an augmented H_0.

- The background effect suppresses the Weyl potential due to the larger contribution of non-clustering EDE to the total energy density. This leads to a relatively lower power at small scales and thus a diminished σ_8. Additionally, we observe additional perturbative effects attributable to w_i for modes entering the horizon around or before z_c, though these effects on observables are relatively minor compared to the primary background effect.

- We subjected three variants of the EDE model to a combination of Planck18+BAO+Pantheon+SH_0ES, a two-parameter EDE model with fixed w_i and w_f, a three-parameter EDE model with a free w_f, and a four-parameter EDE model with both w_i and w_f free. We found that the overall minimum χ^2 improved by -2.4, at the cost of introducing one more parameter (w_i) compared to the three-parameter model and by -4.4 compared to the two-parameter model. However, w_i was not conclusively detected in this analysis, and we derived only a weak upper limit at the 1σ level ($w_i < -0.565$).

- Notably, the model with w_i left free yielded a slightly higher H_0 and a S_8 value reduced by approximately 0.4σ. Nevertheless, incorporating S_8 data diminished the preference for non-zero EDE, resulting in a degradation of the minimum χ^2.

While the findings from this study suggest that a non-cold dark energy (non-cc) EDE might not be able to simultaneously address both the H_0 and S_8 tensions, it is hoped that this work will inspire further investigations to mitigate the surge in small-scale power induced by the EDE cosmology. This is crucial not just for

Experiments/Data	ΛCDM	2-param EDE	3-param EDE	4-param EDE
Planck high$-\ell$ TT,TE,EE	2347.90	2348.99	2346.49	2346.95
Planck low$-\ell$ EE	396.60	396.03	396.65	396.63
Planck low$-\ell$ TT	22.97	22.22	21.89	22.19
Planck lensing	8.76	9.016	9.04	9.16
Pantheon	1025.92	1025.99	1025.81	1026.02
BOSS DR12 (BAO/FS)	6.61	7.23	6.68	7.38
BOSS low$-z$	1.19	1.10	1.30	1.06
total	3809.99	3810.59	3807.90	3809.44

TABLE 6.4: Minimum of χ^2 for each experiment (also total) when no prior was included.

EDE, but also for models that need to compensate for the effects of both an enlarged H_0 (as measured by SH_0ES) and a well-constrained Ω_m (as gauged by Pantheon and BAO data), leading to earlier matter domination and an amplified σ_8. Consequently, it remains an open avenue to explore how one might build upon these results, either within an EDE cosmology or other cosmological frameworks, to ultimately resolve cosmic tensions simultaneously McDonough *et al.* (2022); Joseph *et al.* (2023); Schöneberg *et al.* (2023).

Tables of χ^2

Experiments/Data	ΛCDM	2-param EDE	3-param EDE	4-param EDE	4-param $w_i \in [-0.333, 1]$
Planck high$-\ell$ TT,TE,EE	2348.49	2349.17	2347.96	2349.86	2349.51
Planck low$-\ell$ EE	397.97	397.16	397.77	396.09	396.63
Planck low$-\ell$ TT	22.67	21.57	21.33	20.69	21.37
Planck lensing	8.95	8.96	9.16	9.81	9.24
Pantheon set	1025.69	1025.64	1025.64	1025.70	1025.68
BOSS DR12(BAO/FS)	5.93	6.42	6.61	6.99	6.42
BOSS low$-z$	1.61	1.82	1.79	1.47	1.51
SH_0ES	15.23	5.68	4.23	1.52	2.92
total	3826.58	3816.46	3814.53	3812.16	3813.32

TABLE 6.5: Minimum of χ^2 for each experiment (also total) when the SH_0ES prior is included.

Experiments/Data	ΛCDM	3-param EDE	4-param EDE	4-param $w_i \in [-0.333, 1]$
Planck high$-\ell$ TT,TE,EE	2353.87	2350.49	2351.38	2350.96
Planck low$-\ell$ EE	395.68	395.89	395.75	397.42
Planck low$-\ell$ TT	22.30	21.29	21.32	21.56
Planck lensing	10.63	10.02	10.46	9.40
Pantheon	1025.63	1025.62	1025.63	1025.62
BOSS DR12 (BAO/FS)	5.87	6.29	6.10	6.14
BOSS low$-z$	1.92	2.154	2.069	1.90
SH_0ES	13.06	6.36	6.29	3.40
S_8(KIDS1000)	3.41	5.84	4.74	6.25
total	3832.41	3823.99	3823.79	3822.69

TABLE 6.6: Minimum of χ^2 for each experiment (also total) when SH_0ES+S_8 prior is included.

Chapter 7

Extended dark energy models and neutrino mass [1]

7.1 Introduction

From the observations of type Ia supernovae, we know that the Universe is accelerating. This accelerated expansion of the Universe just can not be explained through the presence of known components such as ordinary matter, dark matter, or radiation. There must be a hidden entity that has negative pressure and dominates the total energy density of the Universe. We call this hidden entity the Dark Energy. The most successful candidate for dark energy is the vacuum or cosmological constant. Although the cosmological constant is the most fit candidate for cosmological observations, It still faces a few problems. The first of them is "From the theoretical point of view, its understanding is not clear see Sahni (2002).". There is a big mismatch between the observed dark energy density and theoretically calculated vacuum energy density through the quantum field theory

[1] This chapter is based on publication Sharma *et al.* (2022)

description. The other problems are fine-tuning and coincidence problems. There have been some alternatives that can replace the cosmological constant description of dark energy. Some of them are modified gravity, phantom dark energy scalar fields such as quintessence field Ballardini *et al.* (2016); Nojiri *et al.* (2017); Farhang and Khosravi (2021); Braglia *et al.* (2021). These alternatives are still active areas of research, as no cosmological observations have strictly ruled out such possibilities. Dynamical dark energy is one such promising model. In this type of model, the equation of the state of dark energy differs from '-1'. Current and future precision cosmological observations will definitely shed light on this mysterious component of the Universe.

Apart from these, the cosmological constant and Cold Dark Matter model (dubbed as ΛCDM model) face a few cosmological tensions, such as Hubble tension and S_8 tension. There is a mismatch between values of the Universe's expansion rate (Hubble parameter H_0) from direct measurements such as Type 1a supernovas and early universe observations such as Cosmic Microwave background. This mismatch is called Hubble tension. The SH0ES (Supernovae H0 for Equation of State) team uses the distance ladder method and gets the value $H_0 = 73.2 \pm 1.3$ km/s/Mpc Riess *et al.* (2019, 2020). On the other hand, The measurement of CMB infers the value $H_0 = 67.36 \pm 0.54$ km/s/Mpc using ΛCDM model Planck Collaboration and Aghanim (2020). So, there is a 4 to 5 σ mismatch between SH0ES and CMB. More details about the tension are already discussed in the introduction. There also exists a tension in the measurement of the S_8 parameter, which tells about the growth of structures. $S_8 = \sigma_8\sqrt{\frac{\Omega_M}{0.3}}$ where σ_8 root mean square of matter density fluctuations on 8 Mpc/h scale, Ω_M is total matter budget of the Universe. Initially, observations of weak lensing of galaxies by the CFHTLenS collaboration indicated a discrepancy between the ΛCDM model's prediction of the S_8 value and the direct measurement at a significance level of 2σ Heymans *et al.* (2013); MacCrann *et al.* (2015). This tension has subsequently been reaffirmed within the KiDS/Viking dataset Hildebrandt *et al.* (2020); Joudaki *et al.* (2020), albeit

to a lesser degree in the DES data Abbott *et al.* (2018a). Nevertheless, a fresh analysis of the DES data, included with KiDS/Viking observations, has yielded a determination of S_8 that significantly deviates from Planck's estimation, reaching a significance level of 3σ, with a value of $S_8 = 0.755^{+0.019}_{-0.021}$ Joudaki *et al.* (2020). More recently, the synthesis of KiDS/Viking and SDSS data has established a value of $S_8 = 0.766^{+0.02}_{-0.014}$ Heymans *et al.* (2020). The details of this tension are also discussed in the Introduction.

A plethora of proposed solutions has emerged to address these cosmological tensions, necessitating modifications in the early Universe—specifically the pre-recombination era—as well as in the late Universe. Nonetheless, no single model has managed to entirely resolve both the H_0 and S_8 tensions in tandem. A category of solutions involving adjustments in the dynamics of dark energy during the late Universe has gotten substantial attention in recent times. These solutions inherently leave the sound horizon at drag unaffected. To reconcile the elevated value of H_0," a strategy involves diminishing $\Omega_{\rm DE}$ or Ω_m at redshifts below z_{rec} in such a manner that $\rm d_A(z)$ remains unaltered. This objective is attainable, for instance, by introducing variations in the equation of state for dark energy Poulin *et al.* (2018); Bhattacharyya *et al.* (2019); Poulin *et al.* (2018); Di Valentino *et al.* (2017, 2016a, 2015); Poulin *et al.* (2019); Gogoi *et al.* (2021); Visinelli *et al.* (2019); Vagnozzi (2020), through changing primordial spectra Hazra *et al.* (2022), or through decaying dark matter Pandey *et al.* (2020), Poulin *et al.* (2016), Abellán *et al.* (2021b), or non-thermal dark matter Das *et al.* (2022), with varying degrees of success.

The exploration of the dynamic behavior of dark energy often involves examining its equation of state, denoted as $w(z) = \frac{P(z)}{\rho(z)}$, which is capable of changing as a function of redshift. The equation of state $w = -1$ corresponds to the cosmological constant.

Recent studies have unveiled instances where the resolution of the H_0 and S_8 tensions necessitates the condition $w(z) < -1$ at certain redshifts $z > 0$, implying a time-varying dark energy equation of state that crosses the phantom barrier Heisenberg *et al.* (2022). Furthermore, studies have indicated that a substantial range of quintessence models ($w > -1$), including those emerging from the string swampland conjecture, tend to lower the H_0 parameter, exacerbating the H_0 tension Banerjee *et al.* (2021). However, there is hope in the form of interacting dark energy models, such as those described in Das *et al.* (2006), where the evolution of $w(z)$ initiates at higher redshifts, potentially mitigating the perplexing H_0 anomaly.

The present observational data has preferred the equations of state at the present time to align closely with the value of approximately $w \approx -1$. Nonetheless, the restrictions on the equation of state at higher redshifts tend to be less stringent. Various endeavors have already been undertaken to parameterize the equation of state governing dark energy. Recent contributions in this vein are documented in references such as Durrive *et al.* (2018); Martins and Colomer (2018); Marcondes and Pan (2017); Yang *et al.* (2021b); Colgáin *et al.* (2021); Chevallier and Polarski (2001); Linder (2003); Jassal *et al.* (2005); Efstathiou (1999); Barboza and Alcaniz (2008); Li and Shafieloo (2019); Yang *et al.* (2021a); Jaber and de la Macorra (2018); Roy *et al.* (2022); Heisenberg *et al.* (2022); Theodoropoulos and Perivolaropoulos (2021); Mawas *et al.* (2021); Anchordoqui *et al.* (2021); Bamba *et al.* (2012).

We thoroughly investigate the potential of a dynamic dark energy (DE) scenario through a broader and model-independent approach, extending beyond the constraints of the Chevalier-Polarski and Linder (CPL) parameterization Linder (2003); Chevallier and Polarski (2001). This parameterization characterizes the evolution of the dark energy equation of state w in a linear fashion with the expansion factor a.

To be more precise, our study deals with a non-linearly evolving equation of state in this research paper. Recent works, such as the one proposed by Colgáin *et al.* (2021), within the dynamic dark energy framework have indicated that the CPL parameterization's sensitivity is limited at lower redshifts. This insight acts as a catalyst for our pursuit of a parameterization that transcends the limitations of CPL, encouraging us to explore a more comprehensive approach.

Recently, it was emphasized that if modifications are introduced to late-time cosmology via a time-varying equation of state of dark energy w, utilizing a prior on the M_B (direct measurement of the absolute magnitude of supernovae), becomes more appropriate than relying on the H_0 prior Efstathiou (2021); Benevento *et al.* (2020); Camarena and Marra (2021); Lemos *et al.* (2019). This study marks the pioneering effort to present an in-depth study of the extended dynamical dark energy model in which the equation of state is smoothened by four parameters.

Regarding this, we employ a comprehensive 4-parameter model for the time-dependent equation of state of dark energy (w), initially discussed in Corasaniti and Copeland (2003), and aim it to test against the Planck-18, BAO, and Pantheon data. In contrast to the CPL model, this particular model incorporates two additional parameters to accommodate the smooth and nonlinear evolution of the dark energy equation of state over time. The focal point of this parameterization lies in its capacity to capture potential transitions in dark energy, the equation of state during its evolutionary phase as various phantom dark energy models and quintessence/K-essence suggest Corasaniti and Copeland (2003).

Several previous investigations found that the neutrino mass (Σm_ν) has degeneracy with several cosmological parameters—such as Ω_m (represents the total matter density)and the H_0 (expansion rate of the Universe) when relying on the CMB observations alone. Furthermore, the constraints stemming from CMB observations are effectively associated with a single parameter, namely the effective dark

energy equation of state parameter $w_{\rm eff}$ (Jassal *et al.* 2010). By incorporating measurements from low redshift data, for example, the observations of BAO and supernovae (SNe), such degeneracies can be effectively broken (Sutherland 2018; Di Valentino *et al.* 2016b), thereby enhancing the precision of constraints on both Σm_ν and the parameters related to dark energy (DE).

Within the scope of this study, we confirmed that the complete constraint of all four parameters pertaining to the equation of state is not feasible using existing observational data. Notably, the Planck 2018 data alone exhibits limited efficacy in constraining dark energy parameters. However, upon the inclusion of data from BAO and Pantheon, the precision of constraints improves significantly. Consequently, the Hubble tension is attenuated to a 2.5σ discrepancy from the direct measurement by SH0ES, while the S_8 tension is reduced to a 1.5σ discordance from the KIDS1000/Viking measurements.

This study's pivotal focus is establishing constraints on neutrino mass within the context of the 4pDE model. The standard neutrinos (massive) significantly influence the Universe's evolution, leaving imprints on the structure formation and the cosmic microwave background observations at various stages of the cosmic timeline. Exploiting these effects enables the establishment of an upper limit on neutrino mass. During specific cosmic epochs, the impacts of dark energy and standard massive neutrinos coincide, rendering the nature of dark energy pivotal in refining constraints on neutrino mass. Previous literature has explored these connections extensively, as observed in references such as Hannestad (2005), Lorenz *et al.* (2017), Calabrese *et al.* (2011), Di Valentino and Melchiorri (2021), Poulin *et al.* (2018), Vagnozzi *et al.* (2018), Vagnozzi *et al.* (2017), Abellán *et al.* (2021a).

In our results, we got a nonzero mass of standard neutrinos at the 1σ confidence level ($\Sigma m_\nu \sim 0.2 \pm 0.1$ eV), yet neutrino mass meets with zero at the 2σ confidence

level. This contrasts with a prior study Poulin *et al.* (2018), which included the old Planck data (2015) and reported a nonzero mass of neutrinos Σm_ν at a significance exceeding 2σ.

7.2 Background and Perturbations

To study the impact of an equation of state that evolves nonlinearly, we use a model-independent approach with a time-varying dark energy equation of state denoted as $w_{\rm de}(a)$, as proposed by Corasaniti and Copeland (2003):

$$w_{\rm de}(a) = w_0 + (w_m - w_0) \times \Gamma(a) \tag{7.1}$$

Here, w_m and w_0 represent the final value and initial value of the equation of state for dark energy, defined as $w_m = w_{\rm de}(a \ll 1)$ and $w_0 = w_{\rm de}(a = 1)$. The function $\Gamma(a)$ incorporates additional parameters governing the evolution of $w_{\rm de}(a)$, given by:

$$\Gamma(a) = \frac{1 - \exp\left(-\frac{a-1}{\Delta_{\rm de}}\right)}{1 - \exp\left(\frac{1}{\Delta_{\rm de}}\right)} \times \frac{1 + \exp\left(\frac{a_{\rm t}}{\Delta_{\rm de}}\right)}{1 + \exp\left(-\frac{a-a_{\rm t}}{\Delta_{\rm de}}\right)} \tag{7.2}$$

Here, $a_{\rm t}$ is the scale factor at the transition of the equation of state initial value to final value occurs, $\Delta_{\rm de}$ governs the sharpness of this transition.

Figure 7.1 provides a visual representation of the evolution of $w_{\rm de}$ for various combinations of $a_{\rm t}$ and $\Delta_{\rm de}$, while keeping w_0 and w_m fixed at -0.8 and -1.2 respectively. The parameter $(\Delta_{\rm de})$ in Equation 7.1 dictates the trajectory of $(w_{\rm de}(a))$. As shown in Figure 7.1, this plot illustrates the behavior of the parameters $\Delta_{\rm de}$ and $a_{\rm t}$. It can be demonstrated that in the limits such that $(\Delta_{\rm de} \to \infty$ and $\Delta_{\rm de} \to 0)$, Equation 7.1 reduces to:

$$\lim_{\Delta_{\rm de} \to \infty} w_{\rm de}(a) = w_0 + (w_m - w_0) \times (1 - a) \tag{7.3}$$

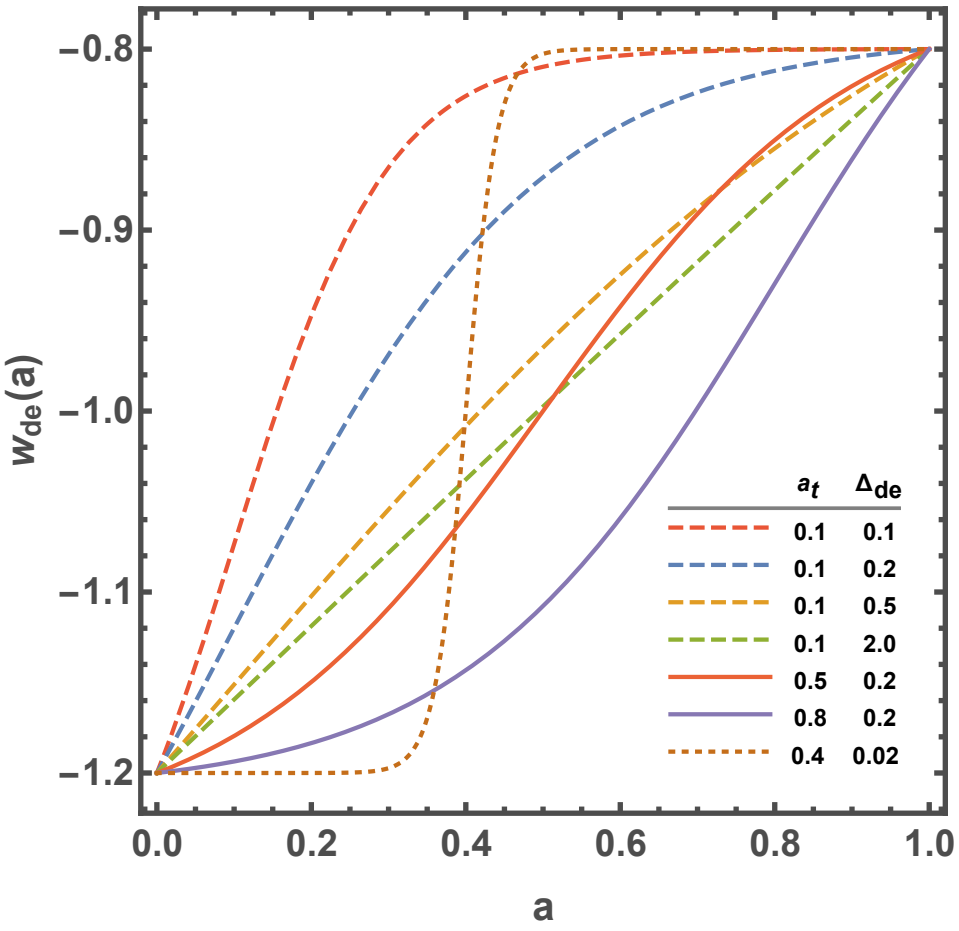

FIGURE 7.1: Visual representation of the evolution of $w_{\rm de}$ for various combinations of $a_{\rm t}$ and $\Delta_{\rm de}$, while keeping w_0 and w_m fixed at -0.8 and -1.2 respectively.

and

$$\lim_{\Delta_{\rm de}\to 0} w_{\rm de}(a) = w_0 + \Theta(a_{\rm t} - a) \times (w_m - w_0) \tag{7.4}$$

respectively. In the extreme limit of $(\Delta_{\rm de})$, the function becomes linear and Heaviside (another case) as demonstrated in figure 7.1.

It's important to note that our parameterization applies specifically to a certain class of models dynamical dark energy, assuming $c^{\rm eff}_{s,{\rm de}} = 1$, also the equation of state should have monotonic evolution.

For our analysis, we assumed the background to be isotropic and homogenous, as described by the FLRW metric. The Friedmann equation with matter (Ω_M),

Parameter	Prior
w_0	[-5,-0.5]
w_m	[-5,-0.5]
$\log(at_{\rm de})$	[-3,0]
$\log(\Delta_{\rm de})$	[-1,0]
Σm_ν	[0,5]

TABLE 7.1: The priors range for the model parameters. Priors for the rest base parameters such as $\{\omega_{\rm cdm}, \omega_b, 100\times\theta_s, n_s, \ln(10^{10}A_s), \tau_{\rm reio}\}$ are kept same as the default set into the MontePython-code (Brinckmann and Lesgourgues 2018) code.

radiation (Ω_M), and dark energy $\Omega_{\rm DE}$ components of the universe given as

$$\frac{H^2}{H_0^2} = \Omega_M/a^3 + \Omega_R/a^3 + \Omega_{\rm DE}\exp\left(3\times\int_1^a \frac{1+w_{\rm de}(a')}{a'}da'\right) \tag{7.5}$$

For a flat universe, $\Omega_{\rm DE}+\Omega_M+\Omega_R = 1$.

7.3 Details of Analysis

7.3.1 Observational Data

As we already explained about Cosmic Microwave background data, BAO data, and Pantheon data in the section, here just briefly name the data sets used in this chapter

- The Planck 2018 observations encompass a range of measurements, including the low-ℓ Cosmic Microwave Background (CMB) TT, EE power spectra, and the high-ℓ TT, TE, EE power spectra. These observations also involve

	ν4pDE			
Data-set ↓	I	II	III	IV
Planck high$-\ell$ TT,TE,EE	2345.70	2347.49	2347.84	2349.06
Planck low$-\ell$ EE	396.31	395.78	396.16	396.90
Planck low$-\ell$ TT	23.56	22.87	22.86	22.76
Planck lensing	8.84	8.95	8.70	9.37
Pantheon	1026.90	1027.22	1027.89	1027.93
BAO FS BOSS DR12	7.15	7.18	8.52	9.96
BAO BOSS low$-z$	1.63	2.68	3.245	3.47
absolute M	–	13.05	10.43	–
SHOES	–	–	–	9.865
S8	–	–	4.717	2.15
Total	3810.13	3825.18	3830.39	3831.50

TABLE 7.2: Minimum of χ^2 for each dataset in the ν4pDE model. The columns correspond to I)Planck+BA0+SN1a, II) Planck+BA0+SN1a+MB, III) Planck+BA0+SN1a+MB+S8, IV) Planck+BA0+SN1a+H0+S8

reconstructing the gravitational lensing potential, as detailed in Planck Collaboration and Aghanim (2020).

- Baryon Acoustic Oscillation (BAO) measurements originate from diverse sources. Specifically, data from the 6-degree Field Galaxy Survey (6dFGS) at a redshift of $z = 0.106$ Beutler *et al.* (2011), the Sloan Digital Sky Survey Data Release 7 (SDSS DR7) at $z = 0.15$ Ross *et al.* (2015), and the Baryon Oscillation Spectroscopic Survey Data Release 12 (BOSS DR12) at multiple redshifts ($z = 0.38, 0.51, 0.61$) Alam *et al.* (2017a) have been employed. Additionally, the combined limits from the extended Baryon Oscillation Spectroscopic Survey Data Release 14 (eBOSS DR14), involving Ly-α auto-correlation at $z = 2.34$ and cross-correlation at $z = 2.35$, have been integrated de Sainte Agathe *et al.* (2019), Blomqvist *et al.* (2019).

	ν4pDE			
Parameter	Planck+Ext	Planck+Ext+M_B	Planck+Ext+M_B+S_8	Planck+Ext+H_0+S_8
$100\ \omega_b$	$2.231(2.235)^{+0.01423}_{-0.01359}$	$2.235(2.247)^{+0.01554}_{-0.01479}$	$2.239(2.249)^{0.0155}_{-0.0148}$	$2.238(2.239)^{+0.015}_{-0.015}$
$\omega_{\rm cdm}$	$0.1202(0.1202)^{+0.00108}_{-0.0010613}$	$0.1200(0.1185)^{+0.0010481}_{-0.0010872}$	$0.1193(0.1191)^{0.00105}_{-0.00109}$	$0.1194(0.1192)^{+0.0011}_{-0.001}$
$100 * \theta_s$	$1.0418(1.0417)^{+0.00028}_{-0.0003067}$	$1.0419(1.0419)^{+0.0003093}_{-0.0002733}$	$1.0419(1.0419)^{0.000309}_{-0.00273}$	$1.042(1.04198)^{+0.00029}_{-0.00028}$
n_s	$0.9631(0.9642)^{0.0038948}_{-0.004134}$	$0.9636(0.9679)^{0.004.000}_{-0.0042631}$	$0.9647(0.9652)^{0.004}_{-0.00426}$	$0.9645(0.9644)^{+0.0042}_{-0.0042}$
$\ln(10^{10}A_s)$	$3.043(3.047)^{+0.0150}_{-0.0147}$	$3.042(3.037)^{+0.01488}_{-0.014812}$	$3.042(3.040)^{0.0149}_{-0.0148}$	$3.042(3.0469)^{+0.015}_{-0.016}$
$\tau_{\rm reio}$	$0.0537(0.0555)^{+0.007626}_{-0.007351}$	$0.05357(0.05308)^{+0.0072268}_{-0.007737}$	$0.05436(0.05511)^{+0.00723}_{-0.00754}$	$0.054(0.0577)^{+0.0076}_{-0.0079}$
Σm_ν [eV]	$0.1129(0.038)^{0.0276}_{-0.1129}$	$0.1069(0.0094)^{0.0697}_{-0.1069}$	$0.1847(0.1043)^{0.0698}_{-0.165}$	$0.1857(0.2748)^{+0.091}_{-0.13}$
w_0	$-0.9856(-1.038)^{+0.053}_{-0.065}$	$-0.9886(-1.011)^{+0.053}_{-0.073}$	$-0.9901(-1.029)^{0.0561}_{-0.0766}$	$-1.04(-0.9446)^{+0.049}_{-0.062}$
w_m	$-2.285(-1.040)^{+1.5}_{-0.59}$	$-2.715(-1.611)^{+1.6}_{-0.91}$	unconstrained	$-2.45(-3.1)^{+1.4}_{-0.78}$
$\log_{10}(a_{\rm t})$	unconstrained	unconstrained	unconstrained	unconstrained
$\log_{10}(\Delta_{\rm de})$	$-0.6752(-0.7649)^{+0.066}_{-0.32}$	$-0.6687(-0.9264)^{+0.065}_{-0.33}$	$-0.6313(-0.8739)^{0.0809}_{-0.368}$	$-0.6936(-0.4452)^{+0.068}_{-0.31}$
M_B	$-19.40(-19.40)^{+0.01887}_{-0.01962}$	$-19.37(-19.37)^{+0.01629}_{-0.01655}$	$-19.369(-19.359)^{+0.01580}_{-0.01615}$	$-19.37(-19.36)^{+0.017}_{-0.015}$
σ_8	$0.8135(0.8279)^{+0.01685}_{-0.01203}$	$0.8225(0.8216)^{+0.01658}_{-0.01303}$	$0.8073(0.8206)^{+0.01763}_{-0.01462}$	$0.8093(0.7966)^{+0.017}_{-0.014}$
Ω_m	$0.3064(0.3038)^{+0.00779}_{-0.00810}$	$0.2973(0.2954)^{+0.0069}_{-0.0074}$	$0.294(0.2893)^{0.00637}_{-0.00654}$	$0.2919(0.2955)^{+0.006}_{-0.0064}$
S_8	$0.822(0.832)^{+0.0170}_{-0.0117}$	$0.8188(0.81)^{+0.016}_{-0.013}$	$0.799(0.8051)^{0.0163}_{-0.0134}$	$0.7982(0.8043)^{+0.014}_{-0.013}$
H_0 [km/s/Mpc]	$68.21(68.53)^{+0.846}_{-0.823}$	$69.22(69.14)^{+0.843}_{-0.791}$	$69.44(69.87)^{0.697}_{-0.724}$	$69.71(69.58)^{+0.7}_{-0.7}$
$\chi^2_{\rm min}$	3810.13	3825.18	3830.34	3831.50
$\Delta\chi^2_{\rm min}$	-1.4	-6.53	-5.5	-4.3

TABLE 7.3: The table for the various cosmological parameters outcome of MCMC analysis from the lensing-marginalized Planck+BAO+SN1a data and combinations of M_B and S_8 priors for ν4pDE model in the format as follows "mean (best-fit) $\pm1\sigma$ error". We also report the corresponding $\Delta\chi^2_{\rm min}$ values.

- The growth function $f\sigma_8(z)$ (FS) was determined by CMASS and BOSS DR12 (LOWZ galaxy samples) at redshifts ($z = 0.38, 0.51, 0.61$) Alam *et al.* (2017a).

- The Pantheon catalog of Type Ia supernovae covers a range of redshifts ($0.01 < z < 2.3$) Scolnic *et al.* (2018b).

- The SH0ES collaboration's result was modeled with a Gaussian likelihood, centered on a value of $H_0 = 73.2 \pm 1.3$ km/s/Mpc Riess *et al.* (2020).

- Weak lensing data from KIDS1000+BOSS+2dfLenS was condensed into a split-normal likelihood for the parameter S_8, yielding a value of $0.766^{+0.02}_{-0.014}$ Heymans *et al.* (2020).

	νCPL		
Parameter	Planck+Ext	Planck+Ext+M_B	Planck+Ext+S_8+M_B
$100\ \omega_b$	$2.2334(2.23425)^{+0.01460}_{-0.01418}$	$2.2364(2.2461)^{+0.01429}_{-0.01442}$	$2.239(2.2291)^{+0.015}_{-0.015}$
$\omega_{\rm cdm}$	$0.12016(0.1197)^{+0.001131}_{-0.001073}$	$0.1201(0.1196)^{+0.0011}_{-0.0011}$	$0.1194(0.1189)^{+0.0011}_{-0.001}$
$100 * \theta_s$	$1.0419(1.197716)^{+0.0002927}_{-0.0003023}$	$1.042(1.04173)^{+0.0003}_{-0.00028}$	$1.042(1.0418)^{+0.00028}_{-0.00031}$
$\ln(10^{10}A_s)$	$3.0448(1.197716)^{+0.01478}_{-0.01570}$	$3.043(3.0378)^{+0.015}_{-0.015}$	$3.041(3.0268)^{+0.015}_{-0.015}$
n_s	$0.96397(0.9657)^{+0.00416}_{-0.00394}$	$0.9641(0.9657)^{+0.0041}_{-0.0041}$	$0.9645(0.9669)^{+0.0041}_{-0.0042}$
$\tau_{\rm reio}$	$0.05446(0.05415)^{+0.00752}_{-0.00801}$	$0.05375(0.05149)^{+0.0074}_{-0.0077}$	$0.05388(0.04686)^{+0.0073}_{-0.0074}$
Σm_ν [eV]	$0.1092(0.04848)^{+0.0255}_{0.100}$	$0.09942(0.00578)^{+0.025}_{-0.099}$	$0.1877(0.074)^{+0.094}_{-0.14}$
w_0	$-0.9690(-0.99195)^{+0.0787}_{-0.0830}$	$-0.9541(-0.9558)^{+0.076}_{-0.094}$	$-0.9393(-1.08)^{+0.09}_{-0.095}$
w_a	$-0.2915(-0.1680)^{+0.409}_{-0.292}$	$-0.5008(-0.3023)^{+0.49}_{-0.28}$	$-0.6716(0.0303)^{+0.55}_{-0.39}$
M_B	$-19.40(-19.3923)^{+0.0191}_{-0.0179}$	$-19.37(-19.374)^{+0.016}_{-0.016}$	$-19.37(-19.376)^{+0.016}_{-0.017}$
σ_8	$0.8134(0.8237)^{+0.0155}_{-0.0120}$	$0.8237(-0.8306)^{+0.016}_{-0.012}$	$0.8061(0.8172)^{+0.018}_{-0.015}$
Ω_m	$0.3074(0.3017)^{+0.00723}_{-0.00808}$	$0.2974(0.2977)^{+0.00664}_{-0.00718}$	$0.2948(0.2860)^{+0.00673}_{-0.00703}$
S_8	$0.8233(0.827)^{+0.0156}_{-0.0124}$	$0.820(0.825)^{+0.0152}_{-0.0125}$	$0.798(0.802)^{+0.0157}_{-0.0127}$
H_0 [km/s/Mpc]	$68.09(68.62)^{+0.824}_{-0.768}$	$69.23(69.10)^{+0.740}_{-0.742}$	$69.36(69.71)^{+0.720}_{-0.772}$
$\chi^2_{\rm min}$	3809.86	3824.43	3833.08
$\Delta\chi^2_{\rm min}$	-1.67	-7.23	-2.76

TABLE 7.4: The table for the various cosmological parameters outcome of MCMC analysis when Planck+BAO+SN1a data and combinations of M_B and S_8 priors used for νCPL model. The reported values are in the following format: "mean (best-fit) $\pm 1\sigma$ error". The corresponding $\Delta\chi^2_{\rm min}$ values are in the table's last row.

- A Gaussian prior on the absolute magnitude M_B was established as $M_B = -19.244 \pm 0.037$ mag, based on Supernova measurements from the SH0ES project Camarena and Marra (2021).

7.3.2 Methodology

Our foundational cosmological model encompasses a fusion of six ΛCDM parameters: $\{\omega_{\rm cdm}, \omega_b, 100 \times \theta_s, \ln(10^{10}A_s), n_s, \tau_{\rm reio}\}$. Additionally, we incorporate four free-parameters governing the dark energy equation of state, as explained in Section 7.2, denoted as $\rm w_m$, $\rm w_0$, a_t, $\Delta_{\rm de}$, along with the neutrino mass Σm_ν. This model is named ν4pDE. We performed a detailed MCMC analysis for this

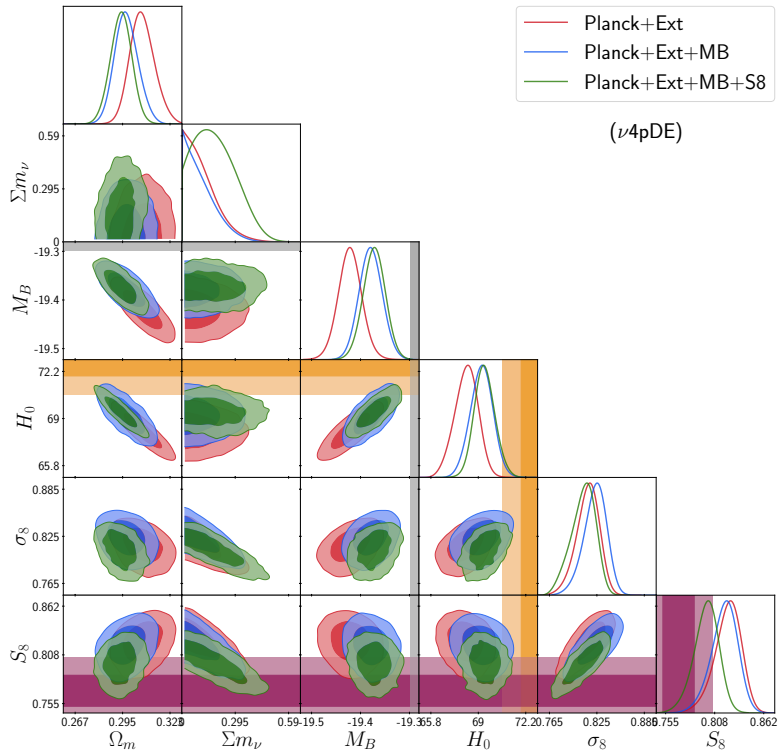

FIGURE 7.2: Triangle plot showing 2D and 1D posterior distributions of parameters (S_8,σ_8, H_0, M_B, Σm_ν,Ω_m) for ν4pDE model with "Planck+BAO+Pantheon" data and prior combination of S_8 and H_0. We have also added 1σ (dark) and 2σ (light) bands(orange) corresponding to direct measurement of H_0 from SH0ES and similarly 1σ (dark) and 2σ (light) bands (purple) corresponding to S_8 measurement from "KIDS1000+BOSS+2dfLenS".

ν4pDE model using a variety of Cosmic Microwave Backgrounds, Baryon Acoustic Oscillations, and supernovae observations, as detailed in Section 7.3.1. This analysis is performed using the Metropolis-Hastings algorithm, which exists in the MontePython-v3 code (Brinckmann and Lesgourgues 2018), which interfaces with a code CLASS (modified for our model). We fixed the priors as shown in Table 7.1. while priors used for the rest standard cosmological parameters $\{\omega_\mathrm{cdm}, \omega_b, 100\times\theta_s, \ln(10^{10}A_s), n_s, \tau_\mathrm{reio}\}$ remain consistent with the default settings in the MontePython-v3 code (Brinckmann and Lesgourgues 2018).

The reported values of χ^2_min are computed using the Python package named iMinuit James and Roos (1975). To effectively manage the substantial number of nuisance parameters, we employ a Choleski decomposition Lewis *et al.* (2000).

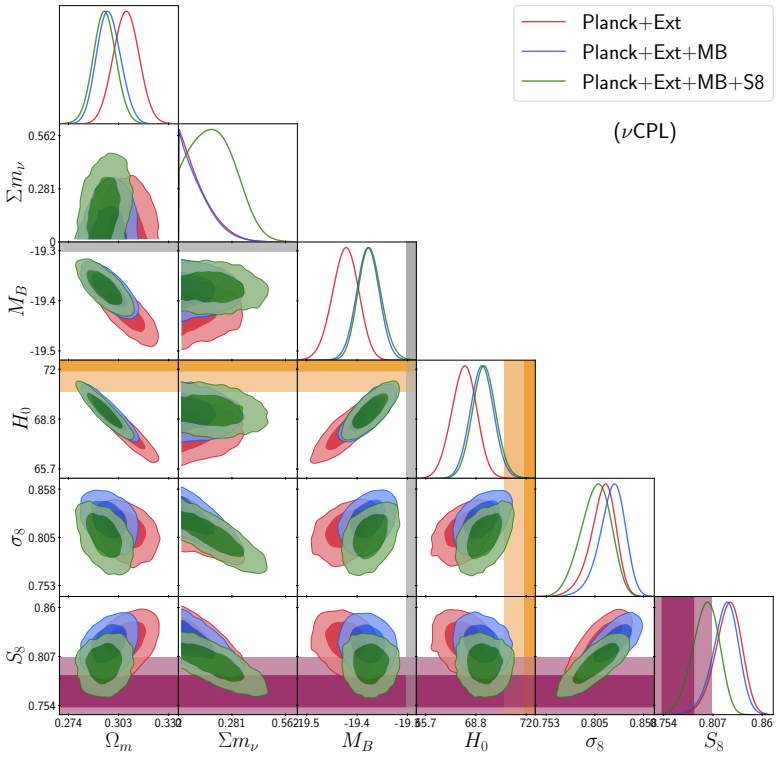

FIGURE 7.3: Triangle plot showing 2D and 1D posterior distributions of parameters (S_8,σ_8, H_0, M_B, Σm_ν,Ω_m) for ν4pDE model with "Planck+BAO+Pantheon" data and prior combinations of S_8 and H_0. We have also added 1σ (dark) and 2σ (light) bands(orange) corresponding to direct measurement of H_0 from SH0ES and similarly 1σ (dark) and 2σ (light) bands (purple) corresponding to S_8 measurement from "KIDS1000+BOSS+2dfLenS".

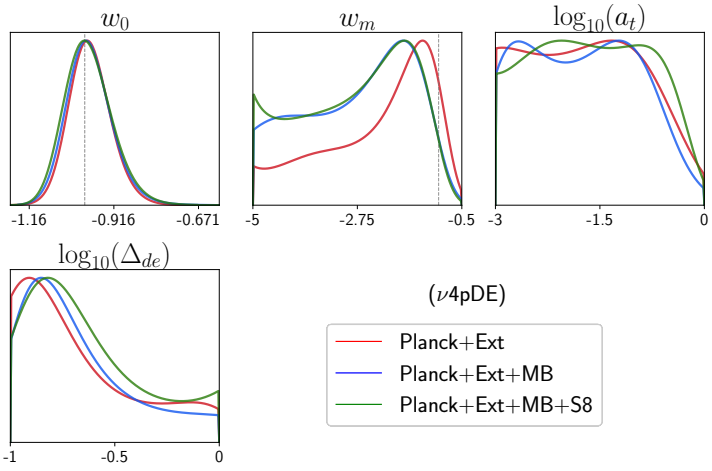

FIGURE 7.4: One-dimensional posterior distributions of dark energy equation of state parameters $\{w_m,\ w_0,\ \log_{10}(a_\mathrm{t}),\ \log_{10}(\Delta_\mathrm{de})\}$ for ν4pDE model with Planck+BAO+Pantheon data and prior combinations of S_8 and H_0.

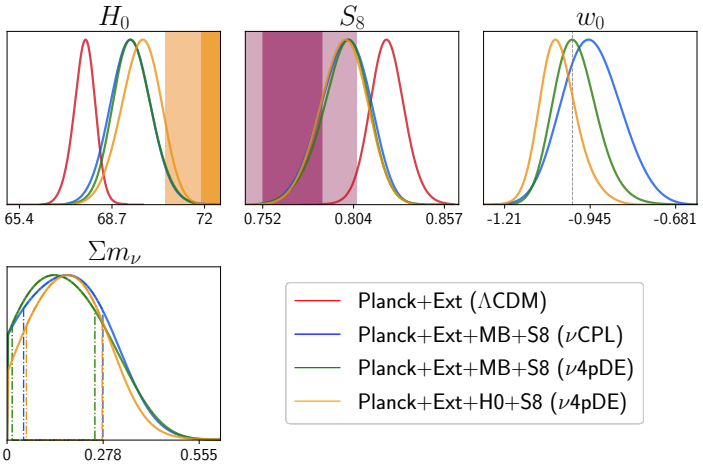

FIGURE 7.5: One dimensional posterior distributions of (H_0, S_8, w_0, $\sum m_\nu$) for different models and combinations of priors . The dot-dashed vertical lines in the Σm_ν panel correspond to respective 1 σ level.

Convergence of chains is assessed using the Gelman-Rubin criterion (see Gelman and Rubin (1992)) with the threshold $R - 1 \leq 0.05$. Additionally, we perform MCMC runs for the CPL model with neutrino mass (νCPL) and the standard ΛCDM model using a variety of datasets and priors for comparative analysis.

7.4 Results

First, we ran the vanilla "ΛCDM Model." Then we ran νCPL,ν4pDE models, which are dynamic dark energy models. We also performed the runs for the equivalent CPL and 4pDE models, fixing the mass of standard neutrinos to the accepted value of $\Sigma m_\nu = 0.06$ eV. We confront each model to combinations of the data from Planck TT, EE, TE+Planck Lensing (see Section 7.3.1), BAO+Pantheon (see Section 7.3.1), collectively referred to as "Ext," and the priors M_B, H_0, and S_8 (see Section 7.3.1), each of which is referred to as "MB" "H0" and "S8". For computing $\Delta\chi 2$ values, we employ the vanilla ΛCDM model as our basis model.

We report the results for the ν4pDE model in Table 7.3 for various data sets. The

triangle plots, including 1D and 2D posterior distributions of the equation of state parameters for dark energy, are shown in Figure 7.4, and the 1D posterior distributions of the Σm_ν, M_B, H_0 and S_8 are presented in Figure 7.2. Table 7.2" reports the $\chi^2_{\rm min}$" values for this model for various datasets/prior combinations. We found that w_0 is consistent with the cosmological constant (CC) and is well-constrained for each dataset combination. The other three DE parameters, however, are less restricted or unrestricted. We don't find the lower bound, particularly for the parameter $\log_{10}(a_t)$. This makes sense as the given cosmological observations do not favor very steep transitions, i.e., very small values for $\Delta_{\rm de}$; this is not surprising. Also, In this scenario(for smooth transition), the parameter a_t is of less significance (see Equations "7.3" and "7.4"), that's why parameter a_t is poorly constrained. Still, the H_0 tension at $\sim 3.2\sigma$ level and the S_8 tension at $\sim 2.5\sigma$ level are sustained even with this model, but the overall $\Delta\chi^2_{\rm min}$ is -1.7 with respect to our base ΛCDM model.

The equation of state parameters is not significantly affected by the M_B prior, with the exception of a tiny shift in the values of w_m towards the negative. With SH0ES results, the model in this instance has H_0 tension at $\sim 2.6\sigma$. Comparing the $\chi^2_{\rm min}$ model to the ΛCDM model, the overall shift is -6.5.

We observe that H_0 attains high value and there is a drop in S_8 value in the scenario where M_B and S_8 priors are applied concurrently, i.e., we detect a negative correlation in posteriors of parameter H_0 and S_8 in this case (see Figure 7.2). This model reduces the S_8 discrepancy to less than 1.5 σ and the H_0 tension to less than 2.5 σ. In this instance, we also see a peak in the neutrino mass's posterior region (see Figure 7.2).

7.4.1 Comparing the results for the ν4pDE model with results for νCPL Model

With the same data combinations, we also performed MCMC analysis for the νCPL model. Results of these runs are provided in Table 7.4 and Figure 7.3, respectively. For the νCPL model, both the w_0 and w_a parameters are tightly limited. We discover that this model's posterior distribution of the base cosmological parameters, ($\omega_{\rm cdm}$,ω_b, $100 \times \theta_s$, $\ln(10^10\mathrm{A_s})n_s$, and $\tau_{\rm rei}$), matches corresponding values of the ν4pDE model. However, there are obvious differences in the model parameters of the CPL model (w_m and w_0).

The 1d posteriors of the parameters S_8, H_0, w_0, and $\sum m_\nu$, Corresponding to ΛCDM, νCPL,ν4pDE are shown in Figure7.5. Compared to the νCPL model, the ν4pDE model places greater restrictions on the parameter w_0. In the case, where none of the priors are used, we don't see a big difference either in H_0 or S_8 compared to the ΛCDM model. However, the amount of H_0 tension decreases when we apply M_B prior and is within the bounds of the SH0ES measurement's 2.5σ level. Similar to how adding S_8 earlier causes a small decrease in the S_8 parameter.

7.4.2 Comparing the results for M_B prior with results for H_0 prior

The parameters w_0 and H_0 have the greatest influence on results when the prior on H_0 is used instead of M_B. Compared to the M_B prior example, the parameter H_0 reaches a little higher value, while the w_0 value changes downward. In Figure 7.5," the outcomes are contrasted. The νCPL model also yields the same conclusion. Additionally, we observe that the H_0 prior supports a non-zero neutrino mass more

Data →	Planck+Ext+MB		Planck+Ext+MB+S8	
Model ↓	$\Delta\chi^2_{\rm min}$	ΔAIC	$\Delta\chi^2_{\rm min}$	ΔAIC
ΛCDM	0	0	0	0
νCPL	-7.23	-1.23	-2.76	$+3.24$
ν4pDE	-6.53	$+3.47$	-5.50	$+4.50$

TABLE 7.5: Comparison of $\Delta\chi^2_{\rm min}$ and ΔAIC for ν4pDE and νCPL models.

strongly than the M_B prior. In conclusion, we state that the use of the H_0 prior has a bigger effect on the w_0, Σm_ν, and obviously the H_0 than the use of the M_B prior.

7.5 Discussion and Conclusion

We have explored a versatile model involving the non-linear evolution of dynamical dark energy characterized by the equation of state w while incorporating massive neutrinos (referred to as the ν4pDE model). This investigation was conducted using the latest data from Planck, Supernovae, and Baryon Acoustic Oscillations (BAO), as well as up-to-date measurements of H_0 and S_8. Our analysis delved into the impact of this parameterization on both the background and derived cosmological parameters.

Our findings align with earlier studies that considered a linear evolution of $w_{\rm de}$ (akin to the CPL model) Poulin *et al.* (2018); Di Valentino *et al.* (2017, 2016a, 2015) and various other parameterizations of dynamical dark energy Zhao *et al.* (2017); Zhang *et al.* (2017); Bhattacharyya *et al.* (2019). We did not observe strong constraints on the additional parameters $a_{\rm t}$ and $\Delta_{\rm de}$ beyond the $\gtrsim 1\sigma$ level. The constraints on w_0 are in good accordance with the νCPL parameterization.

However, when tested against a combination of Planck and external data (Pantheon+BAO), we obtained more tightly constrained and slightly different values for w_0. The inclusion of external priors on M_B and S_8 further emphasizes the difference between the ν4pDE and νCPL parameterizations. The ν4pDE model relaxes the H_0 tension to approximately a 2.5σ (from direct measurement of SH0ES) level and reduces the S_8 tension to around a 1.5σ (with KIDS/Viking) level when tested against Planck18+BAO+Pantheon data collectively. Significantly, we identified a slight negative correlation between the posteriors of parameters H_0 and S_8 within the ν4pDE model, which is of particular interest for such studies.

Both the models (νCPL and ν4pDE) lead to an improvement in $\Delta\chi^2_{\rm min}$ for the "Planck+Ext" dataset and latest measurements of H_0 and S_8 compared to the ΛCDM model. However, this reduction in $\chi^2_{\rm min}$ comes at the cost of including additional model parameters. Consequently, if we employ the ΔAIC criteria, we find that the level of preference of these models diminishes, as none of them exhibit a significantly improved ΔAIC value over the standard ΛCDM model. Upon examining Table 7.5, it becomes clear that when considering Planck+BAO+Pantheon+MB, the νCPL model remains the preferred choice. However, when including Planck+BAO+Pantheon+MB+S8, all models (ν4pDE,νCPL,4pDE, CPL) perform less favorably compared to the standard ΛCDM model.

Incorporating the S_8 prior, we observe that the ν4pDE model prefers a non-zero value for the mass of standard neutrinos ($\Sigma m_\nu \approx 0.2 \pm 0.1$ eV). This finding aligns with prior research employing the νCPL model (Poulin *et al.* 2018). However, it's noteworthy that we do not find a lower bound on the Σm_ν beyond the $\gtrsim 1\sigma$ level. In previous studies, such as that of Poulin *et al.* (2018) utilizing the old Planck data (2015), a non-zero value for Σm_ν was detected even at $\gtrsim 2\sigma$. Similarly, a recent study by Di Valentino and Melchiorri (2021) reports a non-zero value for the mass of standard neutrinos when using WMAP data in conjunction with SPT-3G and ACT-DR4 data. However, their results on Σm_ν are consistent with

ours when recent Planck and BAO data are employed. It's worth noting that the widely recognized lensing anomaly in the Planck data ($A_{\rm lens} \neq 1$) may potentially be a contributing factor, warranting further investigation in greater detail.

Chapter 8

Conclusion and Summary

The main focus of the thesis was to investigate the role of neutrinos in cosmological tensions, namely the "Hubble tension" and the "S8 tension". I investigated the signatures of sterile neutrinos or neutrino-like particles on the early Universe observational data sets such as CMB and BAO and the late-time structure formation data sets. Let me summarize my findings in chronological order here:

In Chapter 1, we studied the nonthermal neutrino-like species that impact Cosmological observations, such as CMB and BAO. It can be easily distinguished from the standard neutrinos. Also, these species are exempted from the strong bounds on N_{eff} from CMB and BBN data. Because of the nonthermal nature of their momentum distribution, they minimally contribute to ΔN_{eff}. We have also seen the presence of nonthermal neutrino-like species, and the S_8 tension has significantly come down (below 2σ). At the linear level, the different nonthermal neutrino species are indistinguishable from each other given their contribution to ΔN_{eff} and M_s^{eff} are the same.

In Chapter 2, In the Next part, I performed the N-body simulation of Nonthermal LiMRs since they impact the nonlinear scales in a unique way. I showed that nonlinear matter power differs from its linear predictions. I also showed the impact of

LiMRs on the mean concentration of massive halo, the impact of mass function, and the weak lensing signal. In all of the signals, the LiMRs have significantly Unique signatures than the Standard ΛCDM. Photometric surveys may trace all those signals discussed above. Moreover, for the nonthermal models which were indistinguishable at the linear level, we can easily distinguish them using nonlinear signatures.

In the third chapter, we further explore that nonthermal production through moduli decay can be a generic mechanism for a candidate of Warm Dark Matter. We obtained the constraints on nonthermal WDM from the satellite population and strong lensing. We found out that a 107 keV nonthermal WDM particle is allowed while in the case of thermal relics, this limit was 9.7 keV.

In the fourth chapter, We proposed an early dark energy candidate which is dynamical in nature. We did a detailed analysis of such ede fluid and found out the present data preferred a non-cosmological constant nature. This also solved the Hubble tension in a better way and did not worsen the S_8 tension if compared to conventional EDE models. This model is also free from the fine-tuning problem of EDE. However, the EDE model is not able to solve both H_0 and S_8 tensions simultaneously.

In chapter five, we studied an extended dark energy impact on cosmological tensions and neutrino mass. We got detection of nonzero neutrino mass when using the S8 prior. The cosmological tension also came down partially. However, the 4 parameters of the equation of state were not well constrained using present Planck CMB, BAO, and Pantheon data. It will interesting to use more low z observational probes to test these models against neutrino mass.

In the future, The neutrino models can be explored with upcoming precision data such as CMB-S4 and weak lensing data from LSST(VRO), and Lyman alpha data. We might be able to detect or constrain such models using precision data sets. The work related to nonthermal neutrino-like species can be explored in light of short baseline anomalies.

Bibliography

Abazajian, Kevork and Koushiappas, Savvas M., 2006, "Constraints on Sterile Neutrino Dark Matter", *Phys. Rev. D*, **74**, 023 527. [DOI], [arXiv:astro-ph/0605271]

Abbott, T. *et al.* [DES], 2005, "The Dark Energy Survey". [arXiv:astro-ph/0510346]

Abbott, T. M. C., Aguena, M., Alarcon, A., Allam, S., Allen, S., Annis, J., Avila, S., Bacon, D., Bechtol, K., Bermeo, A., Bernstein, G. M., Bertin, E., Bhargava, S., Bocquet, S., Brooks, D., Brout and DES Collaboration, 2020, "Dark Energy Survey Year 1 Results: Cosmological constraints from cluster abundances and weak lensing", , **102**(2), 023509. [DOI], [ADS], [arXiv:2002.11124 [astro-ph.CO]]

Abbott, T. M. C. *et al.* [DES], 2018a, "Dark Energy Survey year 1 results: Cosmological constraints from galaxy clustering and weak lensing", *Phys. Rev.*, **D98**(4), 043 526. [DOI], [arXiv:1708.01530 [astro-ph.CO]]

Abbott, T. M. C. *et al.* [DES], 2018b, "Dark Energy Survey Year 1 Results: A Precise H0 Estimate from DES Y1, BAO, and D/H Data", *Mon. Not. Roy. Astron. Soc.*, **480**(3), 3879–3888. [DOI], [arXiv:1711.00403 [astro-ph.CO]]

Abbott, T. M. C. *et al.* [DES], 2022, "Dark Energy Survey Year 3 results: Cosmological constraints from galaxy clustering and weak lensing", *Phys. Rev. D*, **105**(2), 023 520. [DOI], [arXiv:2105.13549 [astro-ph.CO]]

Abbott, T. M. C. *et al.* [Kilo-Degree Survey, DES], 2023, "DES Y3 + KiDS-1000: Consistent cosmology combining cosmic shear surveys". [arXiv:2305.17173 [astro-ph.CO]]

Abdalla, Elcio *et al.*, 2022, "Cosmology Intertwined: A Review of the Particle Physics, Astrophysics, and Cosmology Associated with the Cosmological Tensions and Anomalies", [arXiv:2203.06142 [astro-ph.CO]]

Abel, S. A., Goodsell, M. D., Jaeckel, J., Khoze, V. V. and Ringwald, A., 2008, "Kinetic mixing of the photon with hidden U(1)s in string phenomenology", *Journal of High Energy Physics*, **2008**(7), 124. [DOI], [ADS], [arXiv:0803.1449 [hep-ph]]

Abellan, Guillermo F., Murgia, Riccardo, Poulin, Vivian and Lavalle, Julien, 2020. [2008.09615]

Abellán, Guillermo F., Chacko, Zackaria, Dev, Abhish, Du, Peizhi, Poulin, Vivian and Tsai, Yuhsin, 2021a, "Improved cosmological constraints on the neutrino mass and lifetime". [arXiv:2112.13862 [hep-ph]]

Abellán, Guillermo F., Murgia, Riccardo and Poulin, Vivian, 2021b, "Linear cosmological constraints on 2-body decaying dark matter scenarios and robustness of the resolution to the S_8 tension". [arXiv:2102.12498 [astro-ph.CO]]

Abratenko, P. *et al.* [MicroBooNE], 2021, "Search for an anomalous excess of charged-current quasi-elastic ν_e interactions with the MicroBooNE experiment using Deep-Learning-based reconstruction". [arXiv:2110.14080 [hep-ex]]

Acero, Mario A. and Lesgourgues, Julien, 2009a, "Cosmological constraints on a light non-thermal sterile neutrino", *Phys. Rev. D*, **79**, 045 026. [DOI], [arXiv:0812.2249 [astro-ph]]

Acero, Mario A. and Lesgourgues, Julien, 2009b, "Cosmological constraints on a light non-thermal sterile neutrino", *Phys. Rev. D*, **79**, 045 026. [DOI], [arXiv:0812.2249 [astro-ph]]

Acharya, Bobby S., Dhuria, Mansi, Ghosh, Diptimoy, Maharana, Anshuman and Muia, Francesco, 2019, "Cosmology in the presence of multiple light moduli", *JCAP*, **11**, 035. [DOI], [arXiv:1906.03025 [hep-th]]

Adams, Corey *et al.* [LBNE], 2013, "The Long-Baseline Neutrino Experiment: Exploring Fundamental Symmetries of the Universe", [arXiv:1307.7335 [hep-ex]]

Ade, P. A. R. *et al.* [BICEP2, Keck Array], 2016, "Improved Constraints on Cosmology and Foregrounds from BICEP2 and Keck Array Cosmic Microwave Background Data with Inclusion of 95 GHz Band", *Phys. Rev. Lett.*, **116**, 031 302. [DOI], [arXiv:1510.09217 [astro-ph.CO]]

Ade, P. A. R. *et al.* [BICEP2, Keck Array], 2018, "BICEP2 / Keck Array x: Constraints on Primordial Gravitational Waves using Planck, WMAP, and New BICEP2/Keck Observations through the 2015 Season", *Phys. Rev. Lett.*, **121**, 221 301. [DOI], [arXiv:1810.05216 [astro-ph.CO]]

Aghamousa, Amir *et al.* [DESI], 2016, "The DESI Experiment Part I: Science,Targeting, and Survey Design". [arXiv:1611.00036 [astro-ph.IM]]

Aghanim, N. *et al.* [Planck], 2018a, "Planck 2018 results. VI. Cosmological parameters". [arXiv:1807.06209 [astro-ph.CO]]

Aghanim, N. *et al.* [Planck], 2018b. [1807.06209]

Aghanim, N. *et al.* [Planck], 2018c, "Planck 2018 results. VI. Cosmological parameters". [arXiv:1807.06209 [astro-ph.CO]]

Aghanim, N. *et al.* [Planck], 2020a, "Planck 2018 results. I. Overview and the cosmological legacy of Planck", *Astron. Astrophys.*, **641**, A1. [DOI], [arXiv:1807.06205 [astro-ph.CO]]

Aghanim, N. *et al.* [Planck], 2020b, "Planck 2018 results. VI. Cosmological parameters", *Astron. Astrophys.*, **641**, A6. [DOI], [arXiv:1807.06209 [astro-ph.CO]]. [Erratum: Astron.Astrophys. 652, C4 (2021)]

Aguilar-Arevalo, A. *et al.* [LSND], 2001, "Evidence for neutrino oscillations from the observation of $\bar{\nu}_e$ appearance in a $\bar{\nu}_\mu$ beam", *Phys. Rev. D*, **64**, 112 007. [DOI], [arXiv:hep-ex/0104049]

Aguilar-Arevalo, A. A. *et al.* [MiniBooNE], 2013, "Improved Search for $\bar{\nu}_\mu \to \bar{\nu}_e$ Oscillations in the MiniBooNE Experiment", *Phys. Rev. Lett.*, **110**, 161 801. [DOI], [arXiv:1303.2588 [hep-ex]]

Aiola, Simone *et al.* [ACT], 2020, "The Atacama Cosmology Telescope: DR4 Maps and Cosmological Parameters". [arXiv:2007.07288 [astro-ph.CO]]

Alam, Shadab *et al.* [BOSS], 2017a, "The clustering of galaxies in the completed SDSS-III Baryon Oscillation Spectroscopic Survey: cosmological analysis of the DR12 galaxy sample", *Mon. Not. Roy. Astron. Soc.*, **470**(3), 2617–2652. [DOI], [arXiv:1607.03155 [astro-ph.CO]]

Alam, Shadab *et al.* [BOSS], 2017b, "The clustering of galaxies in the completed SDSS-III Baryon Oscillation Spectroscopic Survey: cosmological analysis of the DR12 galaxy sample", *Mon. Not. Roy. Astron. Soc.*, **470**(3), 2617–2652. [DOI], [arXiv:1607.03155 [astro-ph.CO]]

Ali-Haïmoud, Yacine and Bird, Simeon, 2013, "An efficient implementation of massive neutrinos in non-linear structure formation simulations", , **428**(4), 3375–3389. [DOI], [ADS], [arXiv:1209.0461 [astro-ph.CO]]

Allahverdi, Rouzbeh, Brandenberger, Robert, Cyr-Racine, Francis-Yan and Mazumdar, Anupam, 2010, "Reheating in Inflationary Cosmology: Theory and Applications", *Ann. Rev. Nucl. Part. Sci.*, **60**, 27–51. [DOI], [arXiv:1001.2600 [hep-th]]

Alonso, David *et al.* [LSST Dark Energy Science], 2018, "The LSST Dark Energy Science Collaboration (DESC) Science Requirements Document". [arXiv:1809.01669 [astro-ph.CO]]

Amendola, Luca *et al.*, 2018, "Cosmology and fundamental physics with the Euclid satellite", *Living Rev. Rel.*, **21**(1), 2. [DOI], [arXiv:1606.00180 [astro-ph.CO]]

An, Rui, Gluscevic, Vera, Nadler, Ethan O. and Zhang, Yue, 2023, "Can Neutrino Self-interactions Save Sterile Neutrino Dark Matter?". [arXiv:2301.08299 [astro-ph.CO]]

Anchordoqui, Luis A., Di Valentino, Eleonora, Pan, Supriya and Yang, Weiqiang, 2021, "Dissecting the H0 and S8 tensions with Planck + BAO + supernova type Ia in multi-parameter cosmologies", *JHEAp*, **32**, 121. [DOI], [arXiv:2107.13932 [astro-ph.CO]]

Anderhalden, Donnino, Schneider, Aurel, Macciò, Andrea V., Diemand, Juerg and Bertone, Gianfranco, 2013, "Hints on the nature of dark matter from the properties of Milky Way satellites", , **2013**(3), 014. [DOI], [ADS], [arXiv:1212.2967 [astro-ph.CO]]

Angulo, Raul E., Hahn, Oliver and Abel, Tom, 2013, "The warm dark matter halo mass function below the cut-off scale", , **434**(4), 3337–3347. [DOI], [ADS], [arXiv:1304.2406 [astro-ph.CO]]

Archidiacono, Maria, Fornengo, Nicolao, Giunti, Carlo, Hannestad, Steen and Melchiorri, Alessandro, 2013, "Sterile neutrinos: Cosmology versus short-baseline experiments", *Phys. Rev. D*, **87**(12), 125 034. [DOI], [arXiv:1302.6720 [astro-ph.CO]]

Archidiacono, Maria, Gariazzo, Stefano, Giunti, Carlo, Hannestad, Steen, Hansen, Rasmus, Laveder, Marco and Tram, Thomas, 2016, "Pseudoscalar—sterile neutrino interactions: reconciling the cosmos with neutrino oscillations", *JCAP*, **08**, 067. [DOI], [arXiv:1606.07673 [astro-ph.CO]]

Archidiacono, Maria, Hooper, Deanna C., Murgia, Riccardo, Bohr, Sebastian, Lesgourgues, Julien and Viel, Matteo, 2019, "Constraining Dark Matter-Dark Radiation interactions with CMB, BAO, and Lyman-α", *JCAP*, **10**, 055. [DOI], [arXiv:1907.01496 [astro-ph.CO]]

Archidiacono, Maria, Gariazzo, Stefano, Giunti, Carlo, Hannestad, Steen and Tram, Thomas, 2020, "Sterile neutrino self-interactions: H_0 tension and short-baseline anomalies", *JCAP*, **12**, 029. [DOI], [arXiv:2006.12885 [astro-ph.CO]]

Argüelles, C. A., Esteban, I., Hostert, M., Kelly, Kevin J., Kopp, J., Machado, P. A. N., Martinez-Soler, I. and Perez-Gonzalez, Y. F., 2021, "MicroBooNE and the ν_e Interpretation of the MiniBooNE Low-Energy Excess". [arXiv:2111.10359 [hep-ph]]

Arkani-Hamed, Nima and Weiner, Neal, 2008, "LHC signals for a SuperUnified theory of Dark Matter", *Journal of High Energy Physics*, **2008**(12), 104. [DOI], [ADS], [arXiv:0810.0714 [hep-ph]]

Arkani-Hamed, Nima, Cohen, Timothy, D'Agnolo, Raffaele Tito, Hook, Anson, Kim, Hyung Do and Pinner, David, 2016, "Solving the Hierarchy Problem at Reheating with a Large Number of Degrees of Freedom", , **117**(25), 251801. [DOI], [ADS], [arXiv:1607.06821 [hep-ph]]

Arvanitaki, Asimina, Dimopoulos, Savas, Dubovsky, Sergei, Kaloper, Nemanja and March-Russell, John, 2010, "String axiverse", , **81**(12), 123530. [DOI], [ADS], [arXiv:0905.4720 [hep-th]]

Bagla, Jasjeet S., 2002, "A TreePM code for cosmological N-body simulations", *J. Astrophys. Astron.*, **23**, 185–196. [DOI], [arXiv:astro-ph/9911025]

Balkenhol, L. *et al.* [SPT], 2021, "Constraints on ΛCDM Extensions from the SPT-3G 2018 EE and TE Power Spectra". [arXiv:2103.13618 [astro-ph.CO]]

Ballardini, M., Finelli, F., Umiltà, C. and Paoletti, D., 2016, "Cosmological constraints on induced gravity dark energy models", , **5**, 067. [DOI], [ADS], [arXiv:1601.03387]

Ballesteros, Guillermo, Garcia, Marcos A. G. and Pierre, Mathias, 2021, "How warm are non-thermal relics? Lyman-α bounds on out-of-equilibrium dark matter", *JCAP*, **03**, 101. [DOI], [arXiv:2011.13458 [hep-ph]]

Bamba, Kazuharu, Capozziello, Salvatore, Nojiri, Shin'ichi and Odintsov, Sergei D., 2012, "Dark energy cosmology: the equivalent description via different theoretical models and cosmography tests", , **342**(1), 155–228. [DOI], [ADS], [arXiv:1205.3421 [gr-qc]]

Banerjee, A., Cai, H., Heisenberg, L., Colgáin, E. Ó., Sheikh-Jabbari, M. M. and Yang, T., 2021, "Hubble sinks in the low-redshift swampland", , **103**(8), L081305. [DOI], [ADS], [arXiv:2006.00244 [astro-ph.CO]]

Banerjee, Arka and Dalal, Neal, 2016, "Simulating nonlinear cosmological structure formation with massive neutrinos", , **2016**(11), 015. [DOI], [ADS], [arXiv:1606.06167 [astro-ph.CO]]

Banerjee, Arka, Jain, Bhuvnesh, Dalal, Neal and Shelton, Jessie, 2018a, "Tests of neutrino and dark radiation models from galaxy and CMB surveys", , **2018**(1), 022. [DOI], [ADS], [arXiv:1612.07126 [astro-ph.CO]]

Banerjee, Arka, Powell, Devon, Abel, Tom and Villaescusa-Navarro, Francisco, 2018b, "Reducing noise in cosmological N-body simulations with neutrinos", , **2018**(9), 028. [DOI], [ADS], [arXiv:1801.03906 [astro-ph.CO]]

Banerjee, Arka, Adhikari, Susmita, Dalal, Neal, More, Surhud and Kravtsov, Andrey, 2020a, "Signatures of self-interacting dark matter on cluster density profile and subhalo distributions", , **2020**(2), 024. [DOI], [ADS], [arXiv:1906.12026 [astro-ph.CO]]

Banerjee, Arka, Castorina, Emanuele, Villaescusa-Navarro, Francisco, Court, Travis and Viel, Matteo, 2020b, "Weighing neutrinos with the halo environment", , **2020**(6), 032. [DOI], [ADS], [arXiv:1907.06598 [astro-ph.CO]]

Banerjee, Arka, Das, Subinoy, Maharana, Anshuman and Kumar Sharma, Ravi, 2022, "Signatures of Light Massive Relics on non-linear structure formation", *Mon. Not. Roy. Astron. Soc.*, **516**(2), 2038–2049. [DOI], [arXiv:2202.09840 [astro-ph.CO]]

Banerjee, Arka, Das, Subinoy, Maharana, Anshuman, Nadler, Ethan O. and Sharma, Ravi Kumar, 2023, "Nonthermal warm dark matter limits from small-scale structure", *Phys. Rev. D*, **108**(4), 043 518. [DOI], [arXiv:2305.15736 [astro-ph.CO]]

Banks, Tom, Kaplan, David B. and Nelson, Ann E., 1994, "Cosmological implications of dynamical supersymmetry breaking", *Phys. Rev. D*, **49**, 779–787. [DOI], [arXiv:hep-ph/9308292]

Barboza, Jr., E. M. and Alcaniz, J. S., 2008, "A parametric model for dark energy", *Phys. Lett. B*, **666**, 415–419. [DOI], [arXiv:0805.1713 [astro-ph]]

Barkana, Rennan and Loeb, Abraham, 2001, "In the beginning: The First sources of light and the reionization of the Universe", *Phys. Rept.*, **349**, 125–238. [DOI], [arXiv:astro-ph/0010468]

Barnes, Josh and Hut, Piet, 1986, "A Hierarchical 0 Nlogn Force Calculation Algorithm", *Nature*, **324**, 446–449. [DOI]

Baumann, Daniel, Green, Daniel, Meyers, Joel and Wallisch, Benjamin, 2016, "Phases of new physics in the CMB", , **2016**(1), 007. [DOI], [ADS], [arXiv:1508.06342 [astro-ph.CO]]

Baur, Julien, Palanque-Delabrouille, Nathalie, Yeche, Christophe, Boyarsky, Alexey, Ruchayskiy, Oleg, Armengaud, Éric and Lesgourgues, Julien, 2017, "Constraints from Ly-α forests on non-thermal dark matter including resonantly-produced sterile neutrinos", *JCAP*, **12**, 013. [DOI], [arXiv:1706.03118 [astro-ph.CO]]

Bayer, Adrian E., Banerjee, Arka and Feng, Yu, 2021, "A fast particle-mesh simulation of non-linear cosmological structure formation with massive neutrinos", , **2021**(1), 016. [DOI], [ADS], [arXiv:2007.13394 [astro-ph.CO]]

Bayer, Adrian E., Banerjee, Arka and Seljak, Uroš, 2022, "Beware of fake ν 's: The effect of massive neutrinos on the nonlinear evolution of cosmic structure", , **105**(12), 123510. [DOI], [ADS], [arXiv:2108.04215 [astro-ph.CO]]

Becker, Niklas, Hooper, Deanna C., Kahlhoefer, Felix, Lesgourgues, Julien and Schöneberg, Nils, 2021, "Cosmological constraints on multi-interacting dark matter", *JCAP*, **02**, 019. [DOI], [arXiv:2010.04074 [astro-ph.CO]]

Behroozi, Peter S., Wechsler, Risa H. and Wu, Hao-Yi, 2013, "The ROCKSTAR Phase-space Temporal Halo Finder and the Velocity Offsets of Cluster Cores", , **762**(2), 109. [DOI], [ADS], [arXiv:1110.4372 [astro-ph.CO]]

Benevento, Giampaolo, Hu, Wayne and Raveri, Marco, 2020, "Can late dark energy transitions raise the Hubble constant?", , **101**(10), 103517. [DOI], [ADS], [arXiv:2002.11707 [astro-ph.CO]]

Benisty, David, 2021, "Quantifying the S_8 tension with the Redshift Space Distortion data set", *Phys. Dark Univ.*, **31**, 100 766. [DOI], [arXiv:2005.03751 [astro-ph.CO]]

Beranek, T., Merkel, H. and Vanderhaeghen, M., 2013, "Theoretical framework to analyze searches for hidden light gauge bosons in electron scattering fixed target experiments", , **88**(1), 015032. [DOI], [ADS], [arXiv:1303.2540 [hep-ph]]

Berlin, Asher, Hooper, Dan and Krnjaic, Gordan, 2016, "Thermal Dark Matter From A Highly Decoupled Sector", *Phys. Rev. D*, **94**(9), 095 019. [DOI], [arXiv:1609.02555 [hep-ph]]

Berlin, Asher, Blinov, Nikita and Li, Shirley Weishi, 2019, "Dark Sector Equilibration During Nucleosynthesis", *Phys. Rev. D*, **100**(1), 015 038. [DOI], [arXiv:1904.04256 [hep-ph]]

Beutler, Florian, Blake, Chris, Colless, Matthew, Jones, D. Heath, Staveley-Smith, Lister, Campbell, Lachlan, Parker, Quentin, Saunders, Will and Watson, Fred,

2011, "The 6dF Galaxy Survey: Baryon Acoustic Oscillations and the Local Hubble Constant", *Mon. Not. Roy. Astron. Soc.*, **416**, 3017–3032. [DOI], [arXiv:1106.3366 [astro-ph.CO]]

Bhattacharya, Sukannya, Das, Subinoy, Dutta, Koushik, Gangopadhyay, Mayukh Raj, Mahanta, Ratul and Maharana, Anshuman, 2020, "Non-thermal Hot Dark Matter from Inflaton/Moduli Decay: The Momentum Distribution and Relaxing the Cosmological Mass Bound". [arXiv:2009.05987 [astro-ph.CO]]

Bhattacharya, Sukannya, Das, Subinoy, Dutta, Koushik, Gangopadhyay, Mayukh Raj, Mahanta, Ratul and Maharana, Anshuman, 2021a, "Nonthermal hot dark matter from inflaton or moduli decay: Momentum distribution and relaxation of the cosmological mass bound", *Phys. Rev. D*, **103**(6), 063 503. [DOI], [arXiv:2009.05987 [astro-ph.CO]]

Bhattacharya, Sukannya, Das, Subinoy, Dutta, Koushik, Gangopadhyay, Mayukh Raj, Mahanta, Ratul and Maharana, Anshuman, 2021b, "Nonthermal hot dark matter from inflaton or moduli decay: Momentum distribution and relaxation of the cosmological mass bound", *Phys. Rev. D*, **103**(6), 063 503. [DOI], [arXiv:2009.05987 [astro-ph.CO]]

Bhattacharyya, Archita, Alam, Ujjaini, Lal Pandey, Kanhaiya, Das, Subinoy and Pal, Supratik, 2019, "Are H $_0$ and σ $_8$ Tensions Generic to Present Cosmological Data?", , **876**(2), 143. [DOI], [ADS], [arXiv:1805.04716 [astro-ph.CO]]

Bird, Simeon, Ali-Haïmoud, Yacine, Feng, Yu and Liu, Jia, 2018, "An efficient and accurate hybrid method for simulating non-linear neutrino structure", , **481**(2), 1486–1500. [DOI], [ADS], [arXiv:1803.09854 [astro-ph.CO]]

Bjaelde, Ole Eggers and Das, Subinoy, 2010, "Dark Matter Decaying into a Fermi Sea of Neutrinos", *Phys. Rev. D*, **82**, 043 504. [DOI], [arXiv:1002.1306 [astro-ph.CO]]

Blas, Diego, Lesgourgues, Julien and Tram, Thomas, 2011, "The Cosmic Linear Anisotropy Solving System (CLASS). Part II: Approximation schemes", , **2011**(7), 034. [DOI], [ADS], [arXiv:1104.2933 [astro-ph.CO]]

Blas, Diego, Lesgourgues, Julien and Tram, Thomas, 2011, "The Cosmic Linear Anisotropy Solving System (CLASS) II: Approximation schemes", *JCAP*, **1107**, 034. [DOI], [arXiv:1104.2933 [astro-ph.CO]]

Blomqvist, Michael *et al.*, 2019, "Baryon acoustic oscillations from the cross-correlation of Lyα absorption and quasars in eBOSS DR14", *Astron. Astrophys.*, **629**, A86. [DOI], [arXiv:1904.03430 [astro-ph.CO]]

Bocquet, S., Dietrich, J. P., Schrabback, T., Bleem, L. E. and Klein, et. al, 2019, "Cluster Cosmology Constraints from the 2500 deg^2 SPT-SZ Survey: Inclusion of Weak Gravitational Lensing Data from Magellan and the Hubble Space Telescope", , **878**(1), 55. [DOI], [ADS], [arXiv:1812.01679 [astro-ph.CO]]

Bode, Paul, Ostriker, Jeremiah P. and Turok, Neil, 2001, "Halo formation in warm dark matter models", *Astrophys. J.*, **556**, 93–107. [DOI], [arXiv:astro-ph/0010389]

Bogorad, Zachary and Toro, Natalia, 2021, "Ultralight Millicharged Dark Matter via Misalignment". [arXiv:2112.11476 [hep-ph]]

Bond, J. R. and Szalay, A. S., 1983, "The Collisionless Damping of Density Fluctuations in an Expanding Universe", *Astrophys. J.*, **274**, 443–468. [DOI]

Boyarsky, Alexey, Lesgourgues, Julien, Ruchayskiy, Oleg and Viel, Matteo, 2009, "Lyman-α constraints on warm and on warm-plus-cold dark matter models", , **2009**(5), 012. [DOI], [ADS], [arXiv:0812.0010 [astro-ph]]

Boyarsky, Alexey, Ovchynnikov, Maksym, Sabti, Nashwan and Syvolap, Vsevolod, 2021, "When FIMPs Decay into Neutrinos: The $N_{\rm eff}$ Story". [arXiv:2103.09831 [hep-ph]]

Boylan-Kolchin, Michael, Bullock, James S. and Kaplinghat, Manoj, 2011, , **415**(1), L40–L44. [DOI], [ADS], [1103.0007]

Braglia, Matteo, Ballardini, Mario, Finelli, Fabio and Koyama, Kazuya, 2021, "Early modified gravity in light of the H_0 tension and LSS data", , **103**(4), 043528. [DOI], [ADS], [arXiv:2011.12934 [astro-ph.CO]]

Brandbyge, Jacob and Hannestad, Steen, 2017, "Cosmological N-body simulations with generic hot dark matter", , **2017**(10), 015. [DOI], [ADS], [arXiv:1706.00025 [astro-ph.CO]]

Brandbyge, Jacob, Hannestad, Steen, Haugbølle, Troels and Thomsen, Bjarne, 2008, "The effect of thermal neutrino motion on the non-linear cosmological matter power spectrum", , **2008**(8), 020. [DOI], [ADS], [arXiv:0802.3700 [astro-ph]]

Brinckmann, Thejs and Lesgourgues, Julien, 2018, "MontePython 3: boosted MCMC sampler and other features". [arXiv:1804.07261 [astro-ph.CO]]

Brust, Christopher, Kaplan, David E. and Walters, Matthew T., 2013, "New Light Species and the CMB", *JHEP*, **12**, 058. [DOI], [arXiv:1303.5379 [hep-ph]]

Bullock, J. S., Kolatt, T. S., Sigad, Y., Somerville, R. S., Kravtsov, A. V., Klypin, A. A., Primack, J. R. and Dekel, A., 2001, "Profiles of dark haloes: evolution, scatter and environment", , **321**(3), 559–575. [DOI], [ADS], [arXiv:astro-ph/9908159 [astro-ph]]

Bullock, James S. and Boylan-Kolchin, Michael, 2017, "Small-Scale Challenges to the ΛCDM Paradigm", *Ann. Rev. Astron. Astrophys.*, **55**, 343–387. [DOI], [arXiv:1707.04256 [astro-ph.CO]]

Burenin, R. A. and Vikhlinin, A. A., 2012, "Cosmological parameters constraints from galaxy cluster mass function measurements in combination with other cosmological data", *Astronomy Letters*, **38**(6), 347–363. [DOI], [ADS], [arXiv:1202.2889 [astro-ph.CO]]

Burgess, C. P., Conlon, J. P., Hung, L-Y., Kom, C. H., Maharana, Anshuman and Quevedo, F., 2008, "Continuous Global Symmetries and Hyperweak Interactions in String Compactifications", *JHEP*, **07**, 073. [DOI], [arXiv:0805.4037 [hep-th]]

Calabrese, Erminia, Huterer, Dragan, Linder, Eric V., Melchiorri, Alessandro and Pagano, Luca, 2011, "Limits on dark radiation, early dark energy, and relativistic degrees of freedom", *Phys. Rev. D*, **83**, 123 504. [DOI]URL: https://link.aps.org/doi/10.1103/PhysRevD.83.123504

Camarena, David and Marra, Valerio, 2021, "On the use of the local prior on the absolute magnitude of Type Ia supernovae in cosmological inference", *Mon. Not. Roy. Astron. Soc.*, **504**, 5164–5171. [DOI], [arXiv:2101.08641 [astro-ph.CO]]

Carrillo González, Mariana, Liang, Qiuyue, Sakstein, Jeremy and Trodden, Mark, 2023, "Neutrino-Assisted Early Dark Energy is a Natural Resolution of the Hubble Tension". [arXiv:2302.09091 [astro-ph.CO]]

Carroll, Sean M., 2019, *Spacetime and Geometry: An Introduction to General Relativity*, Cambridge University Press. [DOI]

Carroll, Sean M., Press, William H. and Turner, Edwin L., 1992, "The cosmological constant.", , **30**, 499–542. [DOI], [ADS]

Cataneo, Matteo, Rapetti, David, Schmidt, Fabian, Mantz, Adam B., Allen, Steven W., Applegate, Douglas E., Kelly, Patrick L., von der Linden, Anja and Morris, R. Glenn, 2015, "New constraints on f(R) gravity from clusters of galaxies", , **92**(4), 044009. [DOI], [ADS], [arXiv:1412.0133 [astro-ph.CO]]

Chacko, Zackaria, Cui, Yanou, Hong, Sungwoo and Okui, Takemichi, 2015, "Hidden dark matter sector, dark radiation, and the CMB", , **92**(5), 055033. [DOI], [ADS], [arXiv:1505.04192 [hep-ph]]

Chambers, K. C. *et al.*, 2016, "The Pan-STARRS1 Surveys". [arXiv:1612.05560 [astro-ph.IM]]

Chang, C., Baxter, et .al and DES Collaboration, 2018, "The Splashback Feature around DES Galaxy Clusters: Galaxy Density and Weak Lensing Profiles", , **864**(1), 83. [DOI], [ADS], [arXiv:1710.06808 [astro-ph.CO]]

Cheung, Kingman and Yuan, Tzu-Chiang, 2007, "Hidden fermion as milli-charged dark matter in Stueckelberg Z' model", *Journal of High Energy Physics*, **2007**(3), 120. [DOI], [ADS], [arXiv:hep-ph/0701107 [hep-ph]]

Chevallier, M. and Polarski, D., 2001, "Accelerating Universes with Scaling Dark Matter", *International Journal of Modern Physics D*, **10**, 213–223. [DOI], [ADS], [gr-qc/0009008]

Chevallier, Michel and Polarski, David, 2001, "Accelerating universes with scaling dark matter", *Int. J. Mod. Phys. D*, **10**, 213–224. [DOI], [arXiv:gr-qc/0009008]

Chu, Xiaoyong, Dasgupta, Basudeb and Kopp, Joachim, 2015, "Sterile neutrinos with secret interactions—lasting friendship with cosmology", *JCAP*, **10**, 011. [DOI], [arXiv:1505.02795 [hep-ph]]

Cicoli, Michele, Dutta, Koushik, Maharana, Anshuman and Quevedo, Fernando, 2016, "Moduli Vacuum Misalignment and Precise Predictions in String Inflation", *JCAP*, **08**, 006. [DOI], [arXiv:1604.08512 [hep-th]]

Cicoli, Michele, Conlon, Joseph P, Maharana, Anshuman, Parameswaran, Susha, Quevedo, Fernando and Zavala, Ivonne, 2023, "String Cosmology: from the Early Universe to Today", *arXiv:2303.04819 [hep-th]*

Clark, Steven J., Vattis, Kyriakos and Koushiappas, Savvas M., 2020. [2006.03678]

Colgáin, Eoin Ó., Sheikh-Jabbari, M. M. and Yin, Lu, 2021, "Can dark energy be dynamical?", *Phys. Rev. D*, **104**(2), 023 510. [DOI], [arXiv:2104.01930 [astro-ph.CO]]

Comerford, Julia M. and Natarajan, Priyamvada, 2007, "The observed concentration-mass relation for galaxy clusters", , **379**(1), 190–200. [DOI], [ADS], [arXiv:astro-ph/0703126 [astro-ph]]

Conlon, Joseph P. and Marsh, M. C. David, 2013a, "The Cosmophenomenology of Axionic Dark Radiation", *JHEP*, **10**, 214. [DOI], [arXiv:1304.1804 [hep-ph]]

Conlon, Joseph P. and Marsh, M. C. David, 2013b, "The Cosmophenomenology of Axionic Dark Radiation", *JHEP*, **10**, 214. [DOI], [arXiv:1304.1804 [hep-ph]]

Cooke, Ryan J., Pettini, Max, Nollett, Kenneth M. and Jorgenson, Regina, 2016, "The primordial deuterium abundance of the most metal-poor damped Lyα system", *Astrophys. J.*, **830**(2), 148. [DOI], [arXiv:1607.03900 [astro-ph.CO]]

Corasaniti, P. S. and Copeland, E. J., 2003, "Model independent approach to the dark energy equation of state", , **67**, 063521. [DOI], [ADS], [arXiv:astro-ph/0205544 [astro-ph]]

Coughlan, G. D., Fischler, W., Kolb, Edward W., Raby, S. and Ross, Graham G., 1983, "Cosmological Problems for the Polonyi Potential", *Phys. Lett. B*, **131**, 59–64. [DOI]

Covone, Giovanni, Sereno, Mauro, Kilbinger, Martin and Cardone, Vincenzo F., 2014, "Measurement of the Halo Bias from Stacked Shear Profiles of Galaxy Clusters", , **784**(2), L25. [DOI], [ADS], [arXiv:1402.4815 [astro-ph.CO]]

Cuoco, Alessandro, Lesgourgues, Julien, Mangano, Gianpiero and Pastor, Sergio, 2005, "Do observations prove that cosmological neutrinos are thermally distributed?", *Phys. Rev. D*, **71**, 123 501. [DOI], [arXiv:astro-ph/0502465]

Cyr-Racine, Francis-Yan, de Putter, Roland, Raccanelli, Alvise and Sigurdson, Kris, 2014, "Constraints on Large-Scale Dark Acoustic Oscillations from Cosmology", *Phys. Rev. D*, **89**(6), 063 517. [DOI], [arXiv:1310.3278 [astro-ph.CO]]

D'Amico, Guido, Gleyzes, Jérôme, Kokron, Nickolas, Markovic, Katarina, Senatore, Leonardo, Zhang, Pierre, Beutler, Florian and Gil-Marín, Héctor, 2020, "The cosmological analysis of the SDSS/BOSS data from the Effective Field Theory of Large-Scale Structure", , **2020**(5), 005. [DOI], [ADS], [arXiv:1909.05271 [astro-ph.CO]]

Das, Subinoy and Nadler, Ethan O., 2020, "Constraints on the Epoch of Dark Matter Formation from Milky Way Satellites". [arXiv:2010.01137 [astro-ph.CO]]

Das, Subinoy and Nadler, Ethan O., 2021, "Constraints on the epoch of dark matter formation from Milky Way satellites", , **103**(4), 043517. [DOI], [ADS], [arXiv:2010.01137 [astro-ph.CO]]

Das, Subinoy and Sigurdson, Kris, 2012, "Cosmological Limits on Hidden Sector Dark Matter", *Phys. Rev. D*, **85**, 063 510. [DOI], [arXiv:1012.4458 [astro-ph.CO]]

Das, Subinoy and Weiner, Neal, 2011, "Late Forming Dark Matter in Theories of Neutrino Dark Energy", *Phys. Rev. D*, **84**, 123 511. [DOI], [arXiv:astro-ph/0611353]

Das, Subinoy, Corasaniti, Pier Stefano and Khoury, Justin, 2006, "Super-acceleration as signature of dark sector interaction", *Phys. Rev. D*, **73**, 083 509. [DOI], [arXiv:astro-ph/0510628]

Das, Subinoy, Mondal, Rajesh, Rentala, Vikram and Suresh, Srikanth, 2018, "On dark matter - dark radiation interaction and cosmic reionization", *JCAP*, **08**, 045. [DOI], [arXiv:1712.03976 [astro-ph.CO]]

Das, Subinoy, Maharana, Anshuman, Poulin, Vivian and Sharma, Ravi Kumar, 2022, "Nonthermal neutrino-like hot dark matter in light of the S_8 tension", , **105**(10), 103503. [DOI], [ADS], [arXiv:2104.03329 [astro-ph.CO]]

Davis, Jr., Raymond, Harmer, Don S. and Hoffman, Kenneth C., 1968, "Search for neutrinos from the sun", *Phys. Rev. Lett.*, **20**, 1205–1209. [DOI]

de Carlos, B., Casas, J. A., Quevedo, F. and Roulet, E., 1993, "Model independent properties and cosmological implications of the dilaton and moduli sectors of 4-d strings", *Phys. Lett. B*, **318**, 447–456. [DOI], [arXiv:hep-ph/9308325]

de Gouvea, Andre, 2004, "TASI lectures on neutrino physics", in *Theoretical Advanced Study Institute in Elementary Particle Physics: Physics in $D \geqq 4$*, [arXiv:hep-ph/0411274]

De Gouvêa, André, Sen, Manibrata, Tangarife, Walter and Zhang, Yue, 2020, "Dodelson-Widrow Mechanism in the Presence of Self-Interacting Neutrinos", *Phys. Rev. Lett.*, **124**(8), 081 802. [DOI], [arXiv:1910.04901 [hep-ph]]

de Sainte Agathe, Victoria *et al.*, 2019, "Baryon acoustic oscillations at z = 2.34 from the correlations of Lyα absorption in eBOSS DR14", *Astron. Astrophys.*, **629**, A85. [DOI], [arXiv:1904.03400 [astro-ph.CO]]

de Salas, P. F., Lattanzi, M., Mangano, G., Miele, G., Pastor, S. and Pisanti, O., 2015, "Bounds on very low reheating scenarios after Planck", *Phys. Rev. D*, **92**(12), 123 534. [DOI], [arXiv:1511.00672 [astro-ph.CO]]

Decant, Quentin, Heisig, Jan, Hooper, Deanna C. and Lopez-Honorez, Laura, 2022, "Lyman-α constraints on freeze-in and superWIMPs", *JCAP*, **03**, 041. [DOI], [arXiv:2111.09321 [astro-ph.CO]]

Dentler, Mona, Hernández-Cabezudo, Álvaro, Kopp, Joachim, Machado, Pedro A. N., Maltoni, Michele, Martinez-Soler, Ivan and Schwetz, Thomas, 2018, "Updated Global Analysis of Neutrino Oscillations in the Presence of eV-Scale Sterile Neutrinos", *JHEP*, **08**, 010. [DOI], [arXiv:1803.10661 [hep-ph]]

Denton, Peter B., 2021, "Sterile Neutrino Searches with MicroBooNE: Electron Neutrino Disappearance". [arXiv:2111.05793 [hep-ph]]

DePorzio, Nicholas, Xu, Weishuang Linda, Muñoz, Julian B. and Dvorkin, Cora, 2021, "Finding eV-scale light relics with cosmological observables", , **103**(2), 023504. [DOI], [ADS], [arXiv:2006.09380 [astro-ph.CO]]

DES Collaboration, Abbott, T. M. C. and Aguena, et. al, 2021, "Dark Energy Survey Year 3 Results: Cosmological Constraints from Galaxy Clustering and Weak Lensing", *arXiv e-prints*, arXiv:2105.13549. [ADS], [arXiv:2105.13549 [astro-ph.CO]]

Di Valentino, E., Melchiorri, A. and Silk, J., 2015, "Beyond six parameters: Extending Λ CDM", , **92**(12), 121302. [DOI], [ADS], [arXiv:1507.06646]

Di Valentino, E., Melchiorri, A. and Silk, J., 2016a, "Reconciling Planck with the local value of H_0 in extended parameter space", *Physics Letters B*, **761**, 242–246. [DOI], [ADS], [arXiv:1606.00634]

Di Valentino, E., Melchiorri, A., Linder, E. V. and Silk, J., 2017, "Constraining dark energy dynamics in extended parameter space", , **96**(2), 023523. [DOI], [ADS], [arXiv:1704.00762]

Di Valentino, Eleonora and Melchiorri, Alessandro, 2021, "Neutrino Mass Bounds in the era of Tension Cosmology", *arXiv e-prints*, arXiv:2112.02993. [ADS], [arXiv:2112.02993 [astro-ph.CO]]

Di Valentino, Eleonora and Melchiorri, Alessandro, 2021, "Neutrino Mass Bounds in the era of Tension Cosmology". [arXiv:2112.02993 [astro-ph.CO]]

Di Valentino, Eleonora, Giusarma, Elena, Mena, Olga, Melchiorri, Alessandro and Silk, Joseph, 2016b, "Cosmological limits on neutrino unknowns versus low redshift priors", , **93**(8), 083527. [DOI], [ADS], [arXiv:1511.00975 [astro-ph.CO]]

Di Valentino, Eleonora, Mena, Olga, Pan, Supriya, Visinelli, Luca, Yang, Weiqiang, Melchiorri, Alessandro, Mota, David F., Riess, Adam G. and Silk, Joseph, 2021a, "In the Realm of the Hubble tension − a Review of Solutions". [arXiv:2103.01183 [astro-ph.CO]]

Di Valentino, Eleonora *et al.*, 2020. [2008.11285]

Di Valentino, Eleonora *et al.*, 2021b, "Snowmass2021 - Letter of interest cosmology intertwined II: The hubble constant tension", *Astropart. Phys.*, **131**, 102 605. [DOI], [arXiv:2008.11284 [astro-ph.CO]]

Dike, Veronica, Gilman, Daniel and Treu, Tommaso, 2023, "Strong lensing constraints on primordial black holes as a dark matter candidate", *Mon. Not. Roy. Astron. Soc.*, **522**(4), 5434–5441. [DOI], [arXiv:2210.09493 [astro-ph.CO]]

Dodelson, Scott and Widrow, Lawrence M., 1994a, "Sterile neutrinos as dark matter", *Physical Review Letters*, **72**(1), 17–20. [DOI]URL: https://doi.org/10.1103/physrevlett.72.17

Dodelson, Scott and Widrow, Lawrence M., 1994b, "Sterile neutrinos as dark matter", *Phys. Rev. Lett.*, **72**, 17–20. [DOI]URL: https://link.aps.org/doi/10.1103/PhysRevLett.72.17

Drlica-Wagner, Alex *et al.* [LSST Dark Matter Group], 2019, "Probing the Fundamental Nature of Dark Matter with the Large Synoptic Survey Telescope". [arXiv:1902.01055 [astro-ph.CO]]

Du, Wei, Fan, Zuhui, Shan, Huanyuan, Zhao, Gong-uro, Covone, Giovanni, Fu, Liping and Kneib, Jean-Paul, 2015, "Mass-Concentration Relation of Clusters of Galaxies from CFHTLenS", , **814**(2), 120. [DOI], [ADS], [arXiv:1510.08193 [astro-ph.CO]]

Durrive, Jean-Baptiste, Ooba, Junpei, Ichiki, Kiyotomo and Sugiyama, Naoshi, 2018, "Updated observational constraints on quintessence dark energy models", *Phys. Rev. D*, **97**, 043 503. [DOI]URL: https://link.aps.org/doi/10.1103/PhysRevD.97.043503

Efstathiou, G., 1999, "Constraining the equation of state of the universe from distant type Ia supernovae and cosmic microwave background anisotropies", *Mon. Not. Roy. Astron. Soc.*, **310**, 842–850. [DOI], [arXiv:astro-ph/9904356]

Efstathiou, George, 2021, "To H_0 or not to H_0?", , **505**(3), 3866–3872. [DOI], [ADS], [arXiv:2103.08723 [astro-ph.CO]]

Einstein, Albert, 1916, "The foundation of the general theory of relativity.", *Annalen Phys.*, **49**(7), 769–822. [DOI]

Elbers, Willem, Frenk, Carlos S., Jenkins, Adrian, Li, Baojiu and Pascoli, Silvia, 2021, "An optimal non-linear method for simulating relic neutrinos", , **507**(2), 2614–2631. [DOI], [ADS], [arXiv:2010.07321 [astro-ph.CO]]

Englert, F. and Brout, R., 1964, "Broken Symmetry and the Mass of Gauge Vector Mesons", *Phys. Rev. Lett.*, **13**, 321–323. [DOI]

Enqvist, Kari, Nadathur, Seshadri, Sekiguchi, Toyokazu and Takahashi, Tomo, 2015, *JCAP*, **09**, 067. [DOI], [1505.05511]

Enzi, Wolfgang *et al.*, 2020. [2010.13802]

Essig, Rouven, Schuster, Philip and Toro, Natalia, 2009, "Probing dark forces and light hidden sectors at low-energy e^+e^- colliders", , **80**(1), 015003. [DOI], [ADS], [arXiv:0903.3941 [hep-ph]]

Esteban, Ivan, Gonzalez-Garcia, M. C., Maltoni, Michele, Schwetz, Thomas and Zhou, Albert, 2020, "The fate of hints: updated global analysis of three-flavor neutrino oscillations", *JHEP*, **09**, 178. [DOI], [arXiv:2007.14792 [hep-ph]]

Fardon, Rob, Nelson, Ann E and Weiner, Neal, 2004, "Dark energy from mass varying neutrinos", *Journal of Cosmology and Astroparticle Physics*, **2004**(10), 005. [DOI]URL: https://dx.doi.org/10.1088/1475-7516/2004/10/005

Farhang, Marzieh and Khosravi, Nima, 2021, "Phenomenological gravitational phase transition: Reconciliation between the late and early Universe", , **103**(8), 083523. [DOI], [ADS], [arXiv:2011.08050 [astro-ph.CO]]

Feldman, Daniel, Liu, Zuowei and Nath, Pran, 2007, "Stueckelberg $Z^{'}$ extension with kinetic mixing and millicharged dark matter from the hidden sector", , **75**(11), 115001. [DOI], [ADS], [arXiv:hep-ph/0702123 [hep-ph]]

Feng, Jonathan L., Tu, Huitzu and Yu, Hai-Bo, 2008, "Thermal Relics in Hidden Sectors", *JCAP*, **10**, 043. [DOI], [arXiv:0808.2318 [hep-ph]]

Fields, Brian and Sarkar, Subir, 2006, "Big-Bang nucleosynthesis (2006 Particle Data Group mini-review)". [arXiv:astro-ph/0601514]

Flores, Ricardo A. and Primack, Joel R., 1994, "Observational and theoretical constraints on singular dark matter halos", *Astrophys. J. Lett.*, **427**, L1–4. [DOI], [arXiv:astro-ph/9402004]

Foot, R., 2014, "Mirror dark matter: Cosmology, galaxy structure and direct detection", *Int. J. Mod. Phys. A*, **29**, 1430 013. [DOI], [arXiv:1401.3965 [astro-ph.CO]]

Fran$\chi_b$ca, *Urbano*, *Lineros*, *Roberto A.*, *Palacio*, *JoaquimandPastor*, *Sergio*, 2013, "*Probinginte*

Freedman, Wendy L., Madore, Barry F., Hoyt, Taylor, Jang, In Sung, Beaton, Rachael, Lee, Myung Gyoon, Monson, Andrew, Neeley, Jill and Rich, Jeffrey, 2020, "Calibration of the Tip of the Red Giant Branch (TRGB)". [arXiv:2002.01550 [astro-ph.GA]]

Frey, Andrew R., Danos, Rebecca J. and Cline, James M., 2009, "Warped Kaluza-Klein Dark Matter", *JHEP*, **11**, 102. [DOI], [arXiv:0908.1387 [hep-th]]

Friedmann, A., 1924, "On the Possibility of a world with constant negative curvature of space", *Z. Phys.*, **21**, 326–332. [DOI]

Gariazzo, S., Giunti, C. and Laveder, M., 2013, "Light Sterile Neutrinos in Cosmology and Short-Baseline Oscillation Experiments", *JHEP*, **11**, 211. [DOI], [arXiv:1309.3192 [hep-ph]]

Gell-Mann, Murray, Ramond, Pierre and Slansky, Richard, 1979, "Complex Spinors and Unified Theories", *Conf. Proc. C*, **790927**, 315–321. [arXiv:1306.4669 [hep-th]]

Gelman, Andrew and Rubin, Donald B., 1992, "Inference from Iterative Simulation Using Multiple Sequences", *Statist. Sci.*, **7**, 457–472. [DOI]

Gelmini, Graciela, Palomares-Ruiz, Sergio and Pascoli, Silvia, 2004, "Low reheating temperature and the visible sterile neutrino", *Phys. Rev. Lett.*, **93**, 081 302. [DOI], [arXiv:astro-ph/0403323]

Gelmini, Graciela, Osoba, Efunwande, Palomares-Ruiz, Sergio and Pascoli, Silvia, 2008, "MeV sterile neutrinos in low reheating temperature cosmological scenarios", *JCAP*, **10**, 029. [DOI], [arXiv:0803.2735 [astro-ph]]

Gezari, Suvi *et al.*, 2022, "R2-D2: Roman and Rubin – From Data to Discovery". [arXiv:2202.12311 [astro-ph.IM]]

Gilman, Daniel, Du, Xiaolong, Benson, Andrew, Birrer, Simon, Nierenberg, Anna and Treu, Tommaso, 2020, "Constraints on the mass–concentration relation of cold dark matter haloes with 11 strong gravitational lenses", *Mon. Not. Roy. Astron. Soc.*, **492**(1), L12–L16. [DOI], [arXiv:1909.02573 [astro-ph.CO]]

Gilman, Daniel, Benson, Andrew, Bovy, Jo, Birrer, Simon, Treu, Tommaso and Nierenberg, Anna, 2022, "The primordial matter power spectrum on sub-galactic scales", *Mon. Not. Roy. Astron. Soc.*, **512**(3), 3163–3188. [DOI], [arXiv:2112.03293 [astro-ph.CO]]

Gilman, Daniel, Zhong, Yi-Ming and Bovy, Jo, 2023, "Constraining resonant dark matter self-interactions with strong gravitational lenses", *Phys. Rev. D*, **107**(10), 103 008. [DOI], [arXiv:2207.13111 [astro-ph.CO]]

Gogoi, Antareep, Sharma, Ravi Kumar, Chanda, Prolay and Das, Subinoy, 2021, "Early Mass-varying Neutrino Dark Energy: Nugget Formation and Hubble Anomaly", *Astrophys. J.*, **915**(2), 132. [DOI], [arXiv:2005.11889 [astro-ph.CO]]

Gross, D. J. and Wilczek, Frank, 1973, "Asymptotically Free Gauge Theories - I", *Phys. Rev. D*, **8**, 3633–3652. [DOI]

Guralnik, G. S., Hagen, C. R. and Kibble, T. W. B., 1964, "Global Conservation Laws and Massless Particles", *Phys. Rev. Lett.*, **13**, 585–587. [DOI]

Halverson, James and Langacker, Paul, 2018, "TASI Lectures on Remnants from the String Landscape", *PoS*, **TASI2017**, 019. [DOI], [arXiv:1801.03503 [hep-th]]

Hamann, Jan, Hannestad, Steen, Raffelt, Georg G. and Wong, Yvonne Y. Y., 2011, "Sterile neutrinos with eV masses in cosmology: How disfavoured exactly?", *JCAP*, **09**, 034. [DOI], [arXiv:1108.4136 [astro-ph.CO]]

Hannestad, Steen, 2005, "Neutrino Masses and the Dark Energy Equation of State:Relaxing the Cosmological Neutrino Mass Bound", *Phys. Rev. Lett.*, **95**, 221 301. [DOI]URL: https://link.aps.org/doi/10.1103/PhysRevLett.95.221301

Hannestad, Steen and Madsen, Jes, 1995, "Neutrino decoupling in the early universe", *Phys. Rev. D*, **52**, 1764–1769. [DOI], [arXiv:astro-ph/9506015]

Haridasu, Balakrishna S. and Viel, Matteo, 2020. [2004.07709]

Hasenkamp, Jasper and Kersten, Jörn, 2013a, "Dark radiation from particle decay: cosmological constraints and opportunities", *JCAP*, **08**, 024. [DOI], [arXiv:1212.4160 [hep-ph]]

Hasenkamp, Jasper and Kersten, Jörn, 2013b, "Dark radiation from particle decay: cosmological constraints and opportunities", *JCAP*, **08**, 024. [DOI], [arXiv:1212.4160 [hep-ph]]

Hastings, W. K., 1970, "Monte Carlo sampling methods using Markov chains and their applications", *Biometrika*, **57**(1), 97–109. [DOI], [https://academic.oup.com/biomet/article-pdf/57/1/97/23940249/57-1-97.pdf]URL: https://doi.org/10.1093/biomet/57.1.97

Hazra, Dhiraj Kumar, Antony, Akhil and Shafieloo, Arman, 2022, "One spectrum to cure them all: Signature from early Universe solves major anomalies and tensions in cosmology". [arXiv:2201.12000 [astro-ph.CO]]

Heavens, Alan, 2009, "Statistical techniques in cosmology", *arXiv e-prints*, arXiv:0906.0664. [DOI], [ADS], [arXiv:0906.0664 [astro-ph.CO]]

Heisenberg, Lavinia, Villarrubia-Rojo, Hector and Zosso, Jann, 2022, "Can late-time extensions solve the H_0 and σ_8 tensions?", *arXiv e-prints*, arXiv:2202.01202. [ADS], [arXiv:2202.01202 [astro-ph.CO]]

Heisenberg, Lavinia, Villarrubia-Rojo, Hector and Zosso, Jann, 2022, "Simultaneously solving the H_0 and σ_8 tensions with late dark energy". [arXiv:2201.11623 [astro-ph.CO]]

Heymans, Catherine *et al.*, 2013, "CFHTLenS tomographic weak lensing cosmological parameter constraints: Mitigating the impact of intrinsic galaxy alignments", *Mon. Not. Roy. Astron. Soc.*, **432**, 2433. [DOI], [arXiv:1303.1808 [astro-ph.CO]]

Heymans, Catherine *et al.*, 2020, [arXiv:2007.15632 [astro-ph.CO]]

Higgs, Peter W., 1964, "Broken symmetries, massless particles and gauge fields", *Phys. Lett.*, **12**, 132–133. [DOI]

Hikage, Chiaki, Oguri, Masamune, Hamana, Takashi, More, Surhud, Mandelbaum, Rachel, Takada, Masahiro, Köhlinger, Fabian, Miyatake, Hironao, Nishizawa, Atsushi J., Aihara, Hiroaki, Armstrong, Robert, Bosch, James, Coupon, Jean, Ducout, Anne, Ho, Paul, Hsieh, Bau-Ching, Komiyama, Yutaka, Lanusse, Franχ_b*cois*, *Leauthaud*, *Alexie*, *Lupton*, *Robert H.*, *Medezinski*, *Elinor*, *Mineo*, *Sogo*, *Miyama*, *Shoken*, *Yuand Yamada*, *Yoshihiko*, 2019, "*Cosmology from cosmic shear power spectra with Subaru Hyper Supri*

Hildebrandt, H. *et al.*, 2020, "KiDS+VIKING-450: Cosmic shear tomography with optical+infrared data", *Astron. Astrophys.*, **633**, A69. [DOI], [arXiv:1812.06076 [astro-ph.CO]]

Hill, J. Colin, McDonough, Evan, Toomey, Michael W. and Alexander, Stephon, 2020, "Early Dark Energy Does Not Restore Cosmological Concordance", *Phys. Rev. D*, **102**(4), 043 507. [DOI], [arXiv:2003.07355 [astro-ph.CO]]

Hockney, R. W. and Eastwood, J. W., 1981, *Computer Simulation Using Particles*. [ADS]

Holder, Gilbert, Haiman, Zoltán and Mohr, Joseph J., 2001, "Constraints on Ω_m, Ω_Λ, and σ_8 from Galaxy Cluster Redshift Distributions", , **560**(2), L111–L114. [DOI], [ADS], [arXiv:astro-ph/0105396 [astro-ph]]

Hou, Zhen, Keisler, Ryan, Knox, Lloyd, Millea, Marius and Reichardt, Christian, 2013, "How Massless Neutrinos Affect the Cosmic Microwave Background Damping Tail", *Phys. Rev. D*, **87**, 083 008. [DOI], [arXiv:1104.2333 [astro-ph.CO]]

Hu, Wayne, 1998, "Structure formation with generalized dark matter", *Astrophys. J.*, **506**, 485–494. [DOI], [arXiv:astro-ph/9801234 [astro-ph]]

Iršič, Vid, Viel, Matteo, Haehnelt, Martin G., Bolton, James S. and Becker, George D., 2017a, "First Constraints on Fuzzy Dark Matter from Lyman-α Forest Data and Hydrodynamical Simulations", , **119**(3), 031302. [DOI], [ADS], [arXiv:1703.04683 [astro-ph.CO]]

Iršič, Vid, Viel, Matteo, Haehnelt, Martin G., Bolton, James S., Cristiani, Stefano, Becker, George D., D'Odorico, Valentina, Cupani, Guido, Kim, Tae-Sun, Berg, Trystyn A. M., López, Sebastian, Ellison, Sara, Christensen, Lise, Denney, Kelly D. and Worseck, Gábor, 2017b, "New constraints on the free-streaming of warm dark matter from intermediate and small scale Lyman-α forest data", , **96**(2), 023522. [DOI], [ADS], [arXiv:1702.01764 [astro-ph.CO]]

Ivanov, Mikhail M., Simonović, Marko and Zaldarriaga, Matias, 2020, "Cosmological parameters from the BOSS galaxy power spectrum", , **2020**(5), 042. [DOI], [ADS], [arXiv:1909.05277 [astro-ph.CO]]

Ivezić, Željko *et al.* [LSST], 2019, "LSST: from Science Drivers to Reference Design and Anticipated Data Products", *Astrophys. J.*, **873**(2), 111. [DOI], [arXiv:0805.2366 [astro-ph]]

Jaber, Mariana and de la Macorra, Axel, 2018, "Probing a Steep EoS for Dark Energy with latest observations", *Astropart. Phys.*, **97**, 130–135. [DOI], [arXiv:1708.08529 [astro-ph.CO]]

James, F. and Roos, M., 1975, "Minuit – a system for function minimization and analysis of the parameter errors and correlations", *Computer Physics Communications*, **10**, 343–367. [DOI], [ADS]

Jassal, H. K., Bagla, J. S. and Padmanabhan, T., 2010, "Understanding the origin of CMB constraints on dark energy", , **405**(4), 2639–2650. [DOI], [ADS], [arXiv:astro-ph/0601389 [astro-ph]]

Jassal, Harvinder Kaur, Bagla, J. S. and Padmanabhan, T., 2005, "Observational constraints on low redshift evolution of dark energy: How consistent are different observations?", *Phys. Rev. D*, **72**, 103 503. [DOI], [arXiv:astro-ph/0506748]

Joseph, Melissa, Aloni, Daniel, Schmaltz, Martin, Sivarajan, Eashwar N. and Weiner, Neal, 2023, "A Step in understanding the S8 tension", *Phys. Rev. D*, **108**(2), 023 520. [DOI], [arXiv:2207.03500 [astro-ph.CO]]

Joudaki, S. *et al.*, 2020, "KiDS+VIKING-450 and DES-Y1 combined: Cosmology with cosmic shear", *Astron. Astrophys.*, **638**, L1. [DOI], [arXiv:1906.09262 [astro-ph.CO]]

Kajita, Takaaki, 2012, "Atmospheric neutrinos", *Adv. High Energy Phys.*, **2012**, 504 715. [DOI]

Kajita, Takaaki, 2016, "Nobel Lecture: Discovery of atmospheric neutrino oscillations", *Rev. Mod. Phys.*, **88**(3), 030 501. [DOI]

Kamionkowski, Marc and Riess, Adam G., 2022, "The Hubble Tension and Early Dark Energy". [arXiv:2211.04492 [astro-ph.CO]]

Kane, Gordon, Sinha, Kuver and Watson, Scott, 2015, "Cosmological Moduli and the Post-Inflationary Universe: A Critical Review", *Int. J. Mod. Phys. D*, **24**(08), 1530 022. [DOI], [arXiv:1502.07746 [hep-th]]

Karwal, Tanvi and Kamionkowski, Marc, 2016, "Dark energy at early times, the Hubble parameter, and the string axiverse", *Phys. Rev. D*, **94**(10), 103 523. [DOI], [arXiv:1608.01309 [astro-ph.CO]]

Klypin, A. A. and Shandarin, S. F., 1983, "Three-dimensional numerical model of the formation of large-scale structure in the Universe.", , **204**, 891–907. [DOI], [ADS]

Klypin, Anatoly and Holtzman, Jon, 1997, "Particle mesh code for cosmological simulations". [arXiv:astro-ph/9712217]

Klypin, Anatoly A., Kravtsov, Andrey V., Valenzuela, Octavio and Prada, Francisco, 1999, *Astrophys. J.*, **522**, 82–92. [DOI], [astro-ph/9901240]

Knox, Lloyd and Millea, Marius, 2019, "The Hubble Hunter's Guide". [arXiv:1908.03663 [astro-ph.CO]]

Ko, P., Nagata, Natsumi and Tang, Yong, 2017, "Hidden Charged Dark Matter and Chiral Dark Radiation", *Phys. Lett. B*, **773**, 513–520. [DOI], [arXiv:1706.05605 [hep-ph]]

Kofman, Lev, Linde, Andrei D. and Starobinsky, Alexei A., 1997, "Towards the theory of reheating after inflation", *Phys. Rev. D*, **56**, 3258–3295. [DOI], [arXiv:hep-ph/9704452]

Kogut, A. *et al.* [WMAP], 2003, "Wilkinson Microwave Anisotropy Probe (WMAP) first year observations: TE polarization", *Astrophys. J. Suppl.*, **148**, 161. [DOI], [arXiv:astro-ph/0302213]

Kreisch, Christina D., Cyr-Racine, Francis-Yan and Doré, Olivier, 2019, "The Neutrino Puzzle: Anomalies, Interactions, and Cosmological Tensions". [arXiv:1902.00534 [astro-ph.CO]]

Krolewski, Alex, Ferraro, Simone and White, Martin, 2021, "Cosmological constraints from unWISE and Planck CMB lensing tomography", , **2021**(12), 028. [DOI], [ADS], [arXiv:2105.03421 [astro-ph.CO]]

Kumar, Suresh and Nunes, Rafael C., 2016, *Phys. Rev.*, **D94**(12), 123 511. [DOI], [1608.02454]

Laroche, Alexander, Gilman, Daniel, Li, Xinyu, Bovy, Jo and Du, Xiaolong, 2022, "Quantum fluctuations masquerade as halos: Bounds on ultra-light dark matter from quadruply-imaged quasars", *Mon. Not. Roy. Astron. Soc.*, **517**(2), 1867–1883. [DOI], [arXiv:2206.11269 [astro-ph.CO]]

Lemaître, Abbé G., 1931, "A Homogeneous Universe of Constant Mass and Increasing Radius accounting for the Radial Velocity of Extra-galactic Nebulæ", *Monthly Notices of the Royal Astronomical Society*, **91**(5), 483–490. [DOI], [https://academic.oup.com/mnras/article-pdf/91/5/483/3079971/mnras91-0483.pdf]URL: https://doi.org/10.1093/mnras/91.5.483

Lemos, Pablo, Lee, Elizabeth, Efstathiou, George and Gratton, Steven, 2019, "Model independent H(z) reconstruction using the cosmic inverse distance ladder", , **483**(4), 4803–4810. [DOI], [ADS], [arXiv:1806.06781 [astro-ph.CO]]

Lesgourgues, Julien, 2011, "The Cosmic Linear Anisotropy Solving System (CLASS) I: Overview". [arXiv:1104.2932 [astro-ph.IM]]

Lesgourgues, Julien, 2011, "The Cosmic Linear Anisotropy Solving System (CLASS) I: Overview", *arXiv e-prints*, arXiv:1104.2932. [ADS], [arXiv:1104.2932 [astro-ph.IM]]

Lesgourgues, Julien and Pastor, Sergio, 2006, "Massive neutrinos and cosmology", *Phys. Rept.*, **429**, 307–379. [DOI], [astro-ph/0603494]

Lesgourgues, Julien and Tram, Thomas, 2011, "The Cosmic Linear Anisotropy Solving System (CLASS) IV: efficient implementation of non-cold relics", *JCAP*, **2011**(9), 032. [DOI], [ADS], [arXiv:1104.2935 [astro-ph.CO]]

Lesgourgues, Julien, Mangano, Gianpiero, Miele, Gennaro and Pastor, Sergio, 2013, *Neutrino Cosmology*, Cambridge University Press

Lewis, Antony, Challinor, Anthony and Lasenby, Anthony, 2000, "Efficient computation of CMB anisotropies in closed FRW models", , **538**, 473–476. [DOI], [arXiv:astro-ph/9911177 [astro-ph]]

Li, Xiaolei and Shafieloo, Arman, 2019, "A Simple Phenomenological Emergent Dark Energy Model can Resolve the Hubble Tension", *Astrophys. J. Lett.*, **883**(1), L3. [DOI], [arXiv:1906.08275 [astro-ph.CO]]

Lin, Meng-Xiang, Benevento, Giampaolo, Hu, Wayne and Raveri, Marco, 2019, "Acoustic Dark Energy: Potential Conversion of the Hubble Tension", *Phys. Rev.*, **D100**(6), 063 542. [DOI], [arXiv:1905.12618 [astro-ph.CO]]

Lin, Meng-Xiang, McDonough, Evan, Hill, J. Colin and Hu, Wayne, 2023, "Dark matter trigger for early dark energy coincidence", *Phys. Rev. D*, **107**(10), 103 523. [DOI], [arXiv:2212.08098 [astro-ph.CO]]

Linder, E. V., 2003, "Exploring the Expansion History of the Universe", *Physical Review Letters*, **90**(9), 091301. [DOI], [ADS], [astro-ph/0208512]

Linder, Eric V., 2003, "Exploring the expansion history of the universe", *Phys. Rev. Lett.*, **90**, 091 301. [DOI], [arXiv:astro-ph/0208512]

Liu, Jia, Bird, Simeon, Zorrilla Matilla, José Manuel, Hill, J. Colin, Haiman, Zoltán, Madhavacheril, Mathew S., Petri, Andrea and Spergel, David N., 2018, "MassiveNuS: cosmological massive neutrino simulations", , **2018**(3), 049. [DOI], [ADS], [arXiv:1711.10524 [astro-ph.CO]]

Lorenz, Christiane S., Calabrese, Erminia and Alonso, David, 2017, "Distinguishing between neutrinos and time-varying dark energy through cosmic time", *Phys. Rev. D*, **96**, 043 510. [DOI]URL: https://link.aps.org/doi/10.1103/PhysRevD.96.043510

Ludlow, Aaron D., Bose, Sownak, Angulo, Raúl E., Wang, Lan, Hellwing, Wojciech A., Navarro, Julio F., Cole, Shaun and Frenk, Carlos S., 2016, "The mass-concentration-redshift relation of cold and warm dark matter haloes", , **460**(2), 1214–1232. [DOI], [ADS], [arXiv:1601.02624 [astro-ph.CO]]

Maamari, Karime, Gluscevic, Vera, Boddy, Kimberly K., Nadler, Ethan O. and Wechsler, Risa H., 2021, "Bounds on velocity-dependent dark matter-proton scattering from Milky Way satellite abundance", *Astrophys. J. Lett.*, **907**(2), L46. [DOI], [arXiv:2010.02936 [astro-ph.CO]]

Macciò, Andrea V., Ruchayskiy, Oleg, Boyarsky, Alexey and Muñoz-Cuartas, Juan C., 2013, "The inner structure of haloes in cold+warm dark matter models", , **428**(1), 882–890. [DOI], [ADS], [arXiv:1202.2858 [astro-ph.CO]]

MacCrann, Niall, Zuntz, Joe, Bridle, Sarah, Jain, Bhuvnesh and Becker, Matthew R., 2015, "Cosmic Discordance: Are Planck CMB and CFHTLenS weak lensing measurements out of tune?", *Mon. Not. Roy. Astron. Soc.*, **451**(3), 2877–2888. [DOI], [arXiv:1408.4742 [astro-ph.CO]]

Maki, Ziro, Nakagawa, Masami and Sakata, Shoichi, 1962, "Remarks on the Unified Model of Elementary Particles", *Progress of Theoretical Physics*, **28**(5), 870–880. [DOI], [https://academic.oup.com/ptp/article-pdf/28/5/870/5258750/28-5-870.pdf]URL:
https://doi.org/10.1143/PTP.28.870

Mandelbaum, Rachel, Seljak, Uroš and Hirata, Christopher M., 2008, "A halo mass—concentration relation from weak lensing", , **2008**(8), 006. [DOI], [ADS], [arXiv:0805.2552 [astro-ph]]

Mangano, Gianpiero, Miele, Gennaro, Pastor, Sergio, Pinto, Teguayco, Pisanti, Ofelia and Serpico, Pasquale D., 2005, "Relic neutrino decoupling including flavor oscillations", *Nucl. Phys. B*, **729**, 221–234. [DOI], [arXiv:hep-ph/0506164]

Mantz, Adam B., von der Linden, Anja, Allen, Steven W., Applegate, Douglas E., Kelly, Patrick L., Morris, R. Glenn, Rapetti, David A., Schmidt, Robert W., Adhikari, Saroj, Allen, Mark T., Burchat, Patricia R., Burke, David L., Cataneo, Matteo, Donovan, David, Ebeling, Harald, Shandera, Sarah and Wright, Adam, 2015, "Weighing the giants - IV. Cosmology and neutrino mass", , **446**(3), 2205–2225. [DOI], [ADS], [arXiv:1407.4516 [astro-ph.CO]]

Marcondes, Rafael J. F. and Pan, Supriya, 2017, "Cosmic chronometers constraints on some fast-varying dark energy equations of state". [arXiv:1711.06157 [astro-ph.CO]]

Martins, C. J. A. P. and Colomer, M. Prat, 2018, "Constraining late-time transitions in the dark energy equation of state", *Astron. Astrophys.*, **616**, A32. [DOI], [arXiv:1806.07653 [astro-ph.CO]]

Mau, S. *et al.* [DES], 2022, "Milky Way Satellite Census. IV. Constraints on Decaying Dark Matter from Observations of Milky Way Satellite Galaxies", *Astrophys. J.*, **932**(2), 128. [DOI], [arXiv:2201.11740 [astro-ph.CO]]

Mawas, Ennis, Street, Lauren, Gass, Richard and Wijewardhana, L. C. R., 2021, "Interacting dark energy axions in light of the Hubble tension". [arXiv:2108.13317 [astro-ph.CO]]

McClintock, Thomas, Rozo, Eduardo, Becker, Matthew R., DeRose, Joseph, Mao, Yao-Yuan, McLaughlin, Sean, Tinker, Jeremy L., Wechsler, Risa H. and Zhai, Zhongxu, 2019, "The Aemulus Project. II. Emulating the Halo Mass Function", , **872**(1), 53. [DOI], [ADS], [arXiv:1804.05866 [astro-ph.CO]]

McDonough, Evan, Lin, Meng-Xiang, Hill, J. Colin, Hu, Wayne and Zhou, Shengjia, 2022, "Early dark sector, the Hubble tension, and the swampland", *Phys. Rev. D*, **106**(4), 043 525. [DOI], [arXiv:2112.09128 [astro-ph.CO]]

Merten, J., Meneghetti, M., Postman, M., Umetsu, K., Zitrin, A., Medezinski, E., Nonino, M., Koekemoer, A., Melchior, P., Gruen, D., Moustakas, L. A., Bartelmann, M., Host, O., Donahue, M., Coe, D., Molino, A., Jouvel, S., Monna, A.,

Seitz, S., Czakon, N., Lemze, D., Sayers, J., Balestra, I., Rosati, P., Benítez, N., Biviano, A., Bouwens, R., Bradley, L., Broadhurst, T., Carrasco, M., Ford, H., Grillo, C., Infante, L., Kelson, D., Lahav, O., Massey, R., Moustakas, J., Rasia, E., Rhodes, J., Vega, J. and Zheng, W., 2015, "CLASH: The Concentration-Mass Relation of Galaxy Clusters", , **806**(1), 4. [DOI], [ADS], [arXiv:1404.1376 [astro-ph.CO]]

Metropolis, Nicholas, Rosenbluth, Arianna W., Rosenbluth, Marshall N., Teller, Augusta H. and Teller, Edward, 2004, "Equation of State Calculations by Fast Computing Machines", *The Journal of Chemical Physics*, **21**(6), 1087–1092. [DOI], [https://pubs.aip.org/aip/jcp/article-pdf/21/6/1087/8115285/1087_1_online.pdf]URL: https://doi.org/10.1063/1.1699114

Miller, Carisa, Erickcek, Adrienne L. and Murgia, Riccardo, 2019a, "Constraining nonthermal dark matter's impact on the matter power spectrum", *Phys. Rev. D*, **100**(12), 123 520. [DOI], [arXiv:1908.10369 [astro-ph.CO]]

Miller, Carisa, Erickcek, Adrienne L. and Murgia, Riccardo, 2019b, "Constraining nonthermal dark matter's impact on the matter power spectrum", *Phys. Rev. D*, **100**(12), 123 520. [DOI], [arXiv:1908.10369 [astro-ph.CO]]

Miralda-Escude, Jordi, 2003, "The dark age of the universe", *Science*, **300**, 1904–1909. [DOI], [arXiv:astro-ph/0307396]

Miyatake, Hironao, More, Surhud, Takada, Masahiro, Spergel, David N., Mandelbaum, Rachel, Rykoff, Eli S. and Rozo, Eduardo, 2016, "Evidence of Halo Assembly Bias in Massive Clusters", , **116**(4), 041301. [DOI], [ADS], [arXiv:1506.06135 [astro-ph.CO]]

Moore, B., 1994, "Evidence against dissipationless dark matter from observations of galaxy haloes", *Nature*, **370**, 629. [DOI]

Moore, B., Ghigna, S., Governato, F., Lake, G., Quinn, Thomas R., Stadel, J. and Tozzi, P., 1999, "Dark matter substructure within galactic halos", *Astrophys. J. Lett.*, **524**, L19–L22. [DOI], [arXiv:astro-ph/9907411]

Murgia, Riccardo, Gariazzo, Stefano and Fornengo, Nicolao, 2016, *JCAP*, **04**, 014. [DOI]

Murgia, Riccardo, Merle, Alexander, Viel, Matteo, Totzauer, Maximilian and Schneider, Aurel, 2017, ""Non-cold" dark matter at small scales: a general approach", *JCAP*, **11**, 046. [DOI], [arXiv:1704.07838 [astro-ph.CO]]

Murgia, Riccardo, Irsic, Vid and Viel, Matteo, 2018, "Novel constraints on noncold, nonthermal dark matter from Lyman- α forest data", *Phys. Rev. D*, **98**(8), 083 540. [DOI], [arXiv:1806.08371 [astro-ph.CO]]

Nadler, E. O., Drlica-Wagneret. al and DES Collaboration, 2021, "Constraints on Dark Matter Properties from Observations of Milky Way Satellite Galaxies", , **126**(9), 091101. [DOI], [ADS], [arXiv:2008.00022 [astro-ph.CO]]

Nadler, E. O. *et al.* [DES], 2020, "Milky Way Satellite Census – II. Galaxy-Halo Connection Constraints Including the Impact of the Large Magellanic Cloud", *Astrophys. J.*, **893**, 48. [DOI], [arXiv:1912.03303 [astro-ph.GA]]

Nadler, E. O. *et al.* [DES], 2021a, "Milky Way Satellite Census. III. Constraints on Dark Matter Properties from Observations of Milky Way Satellite Galaxies", *Phys. Rev. Lett.*, **126**, 091 101. [DOI], [arXiv:2008.00022 [astro-ph.CO]]

Nadler, Ethan O., Gluscevic, Vera, Boddy, Kimberly K. and Wechsler, Risa H., 2019, "Constraints on Dark Matter Microphysics from the Milky Way Satellite Population", , **878**(2), L32. [DOI], [ADS], [arXiv:1904.10000 [astro-ph.CO]]

Nadler, Ethan O., Gluscevic, Vera, Boddy, Kimberly K. and Wechsler, Risa H., 2019, "Constraints on Dark Matter Microphysics from the Milky Way Satellite Population", *Astrophys. J. Lett.*, **878**(2), 32. [DOI], [arXiv:1904.10000 [astro-ph.CO]]. [Erratum: Astrophys.J.Lett. 897, L46 (2020), Erratum: Astrophys.J. 897, L46 (2020)]

Nadler, Ethan O., Birrer, Simon, Gilman, Daniel, Wechsler, Risa H., Du, Xiaolong, Benson, Andrew, Nierenberg, Anna M. and Treu, Tommaso, 2021b, "Dark Matter

Constraints from a Unified Analysis of Strong Gravitational Lenses and Milky Way Satellite Galaxies", *Astrophys. J.*, **917**(1), 7. [DOI], [arXiv:2101.07810 [astro-ph.CO]]

Natarajan, Aravind and Yoshida, Naoki, 2014, "The Dark Ages of the Universe and Hydrogen Reionization", *PTEP*, **2014**(6), 06B112. [DOI], [arXiv:1404.7146 [astro-ph.CO]]

Navarro, Julio F., Frenk, Carlos S. and White, Simon D. M., 1996, "The Structure of Cold Dark Matter Halos", , **462**, 563. [DOI], [ADS], [arXiv:astro-ph/9508025 [astro-ph]]

Nguyen, David V., Sarnaaik, Dimple, Boddy, Kimberly K., Nadler, Ethan O. and Gluscevic, Vera, 2021, "Observational constraints on dark matter scattering with electrons", *Phys. Rev. D*, **104**(10), 103 521. [DOI], [arXiv:2107.12380 [astro-ph.CO]]

Niedermann, Florian and Sloth, Martin S., 2022, "Hot new early dark energy: Towards a unified dark sector of neutrinos, dark energy and dark matter", *Phys. Lett. B*, **835**, 137 555. [DOI], [arXiv:2112.00759 [hep-ph]]

Nojiri, S., Odintsov, S. D. and Oikonomou, V. K., 2017, "Modified Gravity Theories on a Nutshell: Inflation, Bounce and Late-time Evolution", *Phys. Rept.*, **692**, 1–104. [DOI], [arXiv:1705.11098 [gr-qc]]

Oguri, Masamune and Marshall, Philip J., 2010, "Gravitationally lensed quasars and supernovae in future wide-field optical imaging surveys", *Mon. Not. Roy. Astron. Soc.*, **405**, 2579–2593. [DOI], [arXiv:1001.2037 [astro-ph.CO]]

Orebi Gann, G. D., 2015, "Everything Under the Sun: A Review of Solar Neutrinos". [arXiv:1504.02154 [nucl-ex]]

Palanque-Delabrouille, Nathalie, Yèche, Christophe, Schöneberg, Nils, Lesgourgues, Julien, Walther, Michael, Chabanier, Solène and Armengaud, Eric, 2020, "Hints, neutrino bounds and WDM constraints from SDSS DR14 Lyman-α and Planck full-survey data", *JCAP*, **04**, 038. [DOI], [arXiv:1911.09073 [astro-ph.CO]]

Pandey, Kanhaiya L., Karwal, Tanvi and Das, Subinoy, 2020, "Alleviating the H_0 and σ_8 anomalies with a decaying dark matter model", , **2020**(7), 026. [DOI], [ADS], [arXiv:1902.10636 [astro-ph.CO]]

Pandey, Kanhaiya L., Karwal, Tanvi and Das, Subinoy, 2020, "Alleviating the H_0 and σ_8 anomalies with a decaying dark matter model", *JCAP*, **07**, 026. [DOI], [arXiv:1902.10636 [astro-ph.CO]]

Pardo, Kris and Doré, Olivier, 2021, "Detecting dark matter subhalos with the Nancy Grace Roman Space Telescope", *Phys. Rev. D*, **104**(10), 103 531. [DOI], [arXiv:2108.10886 [astro-ph.CO]]

Parimbelli, G., Scelfo, G., Giri, S. K., Schneider, A., Archidiacono, M., Camera, S. and Viel, M., 2021, "Mixed dark matter: matter power spectrum and halo mass function", , **2021**(12), 044. [DOI], [ADS], [arXiv:2106.04588 [astro-ph.CO]]

Penzias, A. A. and Wilson, R. W., 1965, "A Measurement of Excess Antenna Temperature at 4080 Mc/s.", , **142**, 419–421. [DOI], [ADS]

Planck Collaboration and Aghanim, N. et.al, 2020, "Planck 2018 results. VI. Cosmological parameters", , **641**, A6. [DOI], [ADS], [arXiv:1807.06209 [astro-ph.CO]]

Pontecorvo, B., 1957a, "Mesonium and anti-mesonium", *Sov. Phys. JETP*, **6**, 429

Pontecorvo, B., 1957b, "Inverse beta processes and nonconservation of lepton charge", *Zh. Eksp. Teor. Fiz.*, **34**, 247

Pontecorvo, B., 1967, "Neutrino Experiments and the Problem of Conservation of Leptonic Charge", *Zh. Eksp. Teor. Fiz.*, **53**, 1717–1725

Poulin, Vivian, Serpico, Pasquale D. and Lesgourgues, Julien, 2016, *JCAP*, **1608**(08), 036. [DOI], [1606.02073]

Poulin, Vivian, Boddy, Kimberly K., Bird, Simeon and Kamionkowski, Marc, 2018, "Implications of an extended dark energy cosmology with massive neutrinos for cosmological tensions", , **97**, 123504. [DOI], [ADS], [arXiv:1803.02474 [astro-ph.CO]]

Poulin, Vivian, Boddy, Kimberly K., Bird, Simeon and Kamionkowski, Marc, 2018, "Implications of an extended dark energy cosmology with massive neutrinos for cosmological tensions", *Phys. Rev.*, **D97**(12), 123 504. [DOI], [arXiv:1803.02474 [astro-ph.CO]]

Poulin, Vivian, Smith, Tristan L., Karwal, Tanvi and Kamionkowski, Marc, 2018, "Early Dark Energy Can Resolve The Hubble Tension", *arXiv e-prints*, arXiv:1811.04083. [ADS], [arXiv:1811.04083 [astro-ph.CO]]

Poulin, Vivian, Smith, Tristan L., Karwal, Tanvi and Kamionkowski, Marc, 2019, "Early Dark Energy Can Resolve The Hubble Tension", *Phys. Rev. Lett.*, **122**(22), 221 301. [DOI], [arXiv:1811.04083 [astro-ph.CO]]

Poulin, Vivian, Smith, Tristan L. and Karwal, Tanvi, 2023, "The Ups and Downs of Early Dark Energy solutions to the Hubble tension: a review of models, hints and constraints circa 2023". [arXiv:2302.09032 [astro-ph.CO]]

Randall, Lisa and Thomas, Scott D., 1995, "Solving the cosmological moduli problem with weak scale inflation", *Nucl. Phys. B*, **449**, 229–247. [DOI], [arXiv:hep-ph/9407248]

Reece, Matthew and Roxlo, Thomas, 2016, "Nonthermal production of dark radiation and dark matter", *JHEP*, **09**, 096. [DOI], [arXiv:1511.06768 [hep-ph]]

Riess, Adam G., Casertano, Stefano, Yuan, Wenlong, Macri, Lucas M. and Scolnic, Dan, 2019, "Large Magellanic Cloud Cepheid Standards Provide a 1% Foundation for the Determination of the Hubble Constant and Stronger Evidence for Physics beyond ΛCDM", *Astrophys. J.*, **876**(1), 85. [DOI], [arXiv:1903.07603 [astro-ph.CO]]

Riess, Adam G., Casertano, Stefano, Yuan, Wenlong, Bowers, J. Bradley, Macri, Lucas, Zinn, Joel C. and Scolnic, Dan, 2020. [2012.08534]

Riess, Adam G. *et al.*, 2022, "A Comprehensive Measurement of the Local Value of the Hubble Constant with 1 km s^1 Mpc^1 Uncertainty from the Hubble

Space Telescope and the SH0ES Team", *Astrophys. J. Lett.*, **934**(1), L7. [DOI], [arXiv:2112.04510 [astro-ph.CO]]

Riotto, Antonio, 1998, "Theories of baryogenesis", in *ICTP Summer School in High-Energy Physics and Cosmology*, [arXiv:hep-ph/9807454]

Robertson, H. P., 1935, "Kinematics and World-Structure", *Astrophys. J.*, **82**, 284–301. [DOI]

Rogers, Keir K. and Peiris, Hiranya V., 2021, "Strong Bound on Canonical Ultralight Axion Dark Matter from the Lyman-Alpha Forest", , **126**(7), 071302. [DOI], [ADS], [arXiv:2007.12705 [astro-ph.CO]]

Ross, Ashley J., Samushia, Lado, Howlett, Cullan, Percival, Will J., Burden, Angela and Manera, Marc, 2015, "The clustering of the SDSS DR7 main Galaxy sample – I. A 4 per cent distance measure at $z = 0.15$", *Mon. Not. Roy. Astron. Soc.*, **449**(1), 835–847. [DOI], [arXiv:1409.3242 [astro-ph.CO]]

Roy, Nandan, Goswami, Sangita and Das, Sudipta, 2022, "Quintessence or Phantom: Study of scalar field dark energy models through a general parametrization of the Hubble parameter". [arXiv:2201.09306 [astro-ph.CO]]

Roy Choudhury, Shouvik and Choubey, Sandhya, 2019a, "Constraining light sterile neutrino mass with the BICEP2/Keck Array 2014 B-mode polarization data", *Eur. Phys. J. C*, **79**(7), 557. [DOI], [arXiv:1807.10294 [astro-ph.CO]]

Roy Choudhury, Shouvik and Choubey, Sandhya, 2019b, "Constraining light sterile neutrino mass with the BICEP2/Keck Array 2014 B-mode polarization data", *Eur. Phys. J. C*, **79**(7), 557. [DOI], [arXiv:1807.10294 [astro-ph.CO]]

Roy Choudhury, Shouvik and Hannestad, Steen, 2020, "Updated results on neutrino mass and mass hierarchy from cosmology with Planck 2018 likelihoods", *JCAP*, **07**, 037. [DOI], [arXiv:1907.12598 [astro-ph.CO]]

Rykoff, E. S., Rozo, et. al and DES Collaboration, 2016, "The RedMaPPer Galaxy Cluster Catalog From DES Science Verification Data", , **224**(1), 1. [DOI], [ADS], [arXiv:1601.00621 [astro-ph.CO]]

Sabla, Vivian I. and Caldwell, Robert R., 2022, "Microphysics of early dark energy", *Phys. Rev. D*, **106**(6), 063 526. [DOI], [arXiv:2202.08291 [astro-ph.CO]]

Sahni, Varun, 2002, "The Cosmological constant problem and quintessence", *Class. Quant. Grav.*, **19**, 3435–3448. [DOI], [arXiv:astro-ph/0202076]

Sakharov, A. D., 1967, "Violation of CP Invariance, C asymmetry, and baryon asymmetry of the universe", *Pisma Zh. Eksp. Teor. Fiz.*, **5**, 32–35. [DOI]

Sales, Laura V., Wetzel, Andrew and Fattahi, Azadeh, 2022, "Baryonic solutions and challenges for cosmological models of dwarf galaxies", *Nature Astron.*, **6**(8), 897–910. [DOI], [arXiv:2206.05295 [astro-ph.GA]]

Scherrer, Robert J. and Turner, Michael S., 1988, "Primordial Nucleosynthesis with Decaying Particles. 1. Entropy Producing Decays. 2. Inert Decays", *Astrophys. J.*, **331**, 19–32. [DOI]

Schneider, Aurel, Smith, Robert E., Macciò, Andrea V. and Moore, Ben, 2012, "Nonlinear evolution of cosmological structures in warm dark matter models", , **424**(1), 684–698. [DOI], [ADS], [arXiv:1112.0330 [astro-ph.CO]]

Schneider, Aurel, Smith, Robert E., Maccio, Andrea V. and Moore, Ben, 2012, "Nonlinear Evolution of Cosmological Structures in Warm Dark Matter Models", *Mon. Not. Roy. Astron. Soc.*, **424**, 684. [DOI], [arXiv:1112.0330 [astro-ph.CO]]

Schöneberg, Nils, Franco Abellán, Guillermo, Pérez Sánchez, Andrea, Witte, Samuel J., Poulin, Vivian and Lesgourgues, Julien, 2021, "The H_0 Olympics: A fair ranking of proposed models". [arXiv:2107.10291 [astro-ph.CO]]

Schöneberg, Nils, Franco Abellán, Guillermo, Simon, Théo, Bartlett, Alexa, Patel, Yashvi and Smith, Tristan L., 2023, "The weak, the strong and the ugly –

A comparative analysis of interacting stepped dark radiation". [arXiv:2306.12469 [astro-ph.CO]]

Scolnic, D. M. *et al.* [Pan-STARRS1], 2018a, "The Complete Light-curve Sample of Spectroscopically Confirmed SNe Ia from Pan-STARRS1 and Cosmological Constraints from the Combined Pantheon Sample", *Astrophys. J.*, **859**(2), 101. [DOI], [arXiv:1710.00845 [astro-ph.CO]]

Scolnic, D. M. *et al.*, 2018b, "The Complete Light-curve Sample of Spectroscopically Confirmed SNe Ia from Pan-STARRS1 and Cosmological Constraints from the Combined Pantheon Sample", *Astrophys. J.*, **859**(2), 101. [DOI], [arXiv:1710.00845 [astro-ph.CO]]

Sharma, Ravi Kumar, Pandey, Kanhaiya Lal and Das, Subinoy, 2022, "Implications of an Extended Dark Energy Model with Massive Neutrinos", *Astrophys. J.*, **934**(2), 113. [DOI], [arXiv:2202.01749 [astro-ph.CO]]

Sharma, Ravi Kumar, Das, Subinoy and Poulin, Vivian, 2023, "Early Dark Energy beyond slow-roll: implications for cosmic tensions". [arXiv:2309.00401 [astro-ph.CO]]

Shi, Xiang-Dong and Fuller, George M., 1999, "A New dark matter candidate: Non-thermal sterile neutrinos", *Phys. Rev. Lett.*, **82**, 2832–2835. [DOI], [arXiv:astro-ph/9810076]

Shin, T., Jain, B. and Adhikari, et. al., 2021, "The mass and galaxy distribution around SZ-selected clusters", , **507**(4), 5758–5779. [DOI], [ADS], [arXiv:2105.05914 [astro-ph.CO]]

Smoot, G. F., Bennett, C. L., Kogut, A., Wright, E. L., Aymon, J., Boggess, N. W., Cheng, E. S., de Amici, G., Gulkis, S., Hauser, M. G., Hinshaw, G., Jackson, P. D., Janssen, M., Kaita, E., Kelsall, T., Keegstra, P., Lineweaver, C., Loewenstein, K., Lubin, P., Mather, J., Meyer, S. S., Moseley, S. H., Murdock, T., Rokke, L., Silverberg, R. F., Tenorio, L., Weiss, R. and Wilkinson, D. T., 1992, "Structure in the COBE Differential Microwave Radiometer First-Year Maps", , **396**, L1. [DOI], [ADS]

Spergel, D. *et al.*, 2015, "Wide-Field InfrarRed Survey Telescope-Astrophysics Focused Telescope Assets WFIRST-AFTA 2015 Report". [arXiv:1503.03757 [astro-ph.IM]]

Springel, Volker, 2005, "The cosmological simulation code GADGET-2", , **364**(4), 1105–1134. [DOI], [ADS], [arXiv:astro-ph/0505010 [astro-ph]]

Sutherland, Will, 2018, "The CMB neutrino mass/vacuum energy degeneracy: a simple derivation of the degeneracy slopes", , **477**(2), 1913–1920. [DOI], [ADS], [arXiv:1803.02298 [astro-ph.CO]]

Tenkanen, Tommi and Vaskonen, Ville, 2016, "Reheating the Standard Model from a hidden sector", *Phys. Rev. D*, **94**(8), 083 516. [DOI], [arXiv:1606.00192 [astro-ph.CO]]

Theodoropoulos, Anastasios and Perivolaropoulos, Leandros, 2021, "The Hubble Tension, the M Crisis of Late Time H(z) Deformation Models and the Reconstruction of Quintessence Lagrangians", *Universe*, **7**(8), 300. [DOI], [arXiv:2109.06256 [astro-ph.CO]]

Tinker, Jeremy, Kravtsov, Andrey V., Klypin, Anatoly, Abazajian, Kevork, Warren, Michael, Yepes, Gustavo, Gottlöber, Stefan and Holz, Daniel E., 2008, "Toward a Halo Mass Function for Precision Cosmology: The Limits of Universality", , **688**(2), 709–728. [DOI], [ADS], [arXiv:0803.2706 [astro-ph]]

To, C., Krause, et. al. and DES Collaboration, 2021, "Dark Energy Survey Year 1 Results: Cosmological Constraints from Cluster Abundances, Weak Lensing, and Galaxy Correlations", , **126**(14), 141301. [DOI], [ADS], [arXiv:2010.01138 [astro-ph.CO]]

Trodden, Mark, 1999, "Electroweak baryogenesis", *Rev. Mod. Phys.*, **71**, 1463–1500. [DOI], [arXiv:hep-ph/9803479]

Tröster, Tilman, Asgari, Marika, Blake, Chris, Cataneo, Matteo, Heymans, Catherine, Hildebrandt, Hendrik, Joachimi, Benjamin, Lin, Chieh-An, Sánchez, Ariel G.,

Wright, Angus H., Bilicki, Maciej, Bose, Benjamin, Crocce, Martin, Dvornik, Andrej, Erben, Thomas, Giblin, Benjamin, Glazebrook, Karl, Hoekstra, Henk, Joudaki, Shahab, Kannawadi, Arun, Köhlinger, Fabian, Kuijken, Konrad, Lidman, Chris, Lombriser, Lucas, Mead, Alexander, Parkinson, David, Shan, HuanYuan, Wolf, Christian and Xia, Qianli, 2021, "KiDS-1000 Cosmology: Constraints beyond flat ΛCDM", , **649**, A88. [DOI], [ADS], [arXiv:2010.16416 [astro-ph.CO]]

Trotta, Roberto, 2008, "Bayes in the sky: Bayesian inference and model selection in cosmology", *Contemp. Phys.*, **49**, 71–104. [DOI], [arXiv:0803.4089 [astro-ph]]

Tytler, David, O'Meara, John M., Suzuki, Nao and Lubin, Dan, 2000, "Review of Big Bang nucleosynthesis and primordial abundances", *Phys. Scripta T*, **85**, 12. [DOI], [arXiv:astro-ph/0001318]

Umetsu, Keiichi, Medezinski, Elinor, Nonino, Mario, Merten, Julian, Postman, Marc, Meneghetti, Massimo, Donahue, Megan, Czakon, Nicole, Molino, Alberto, Seitz, Stella, Gruen, Daniel, Lemze, Doron, Balestra, Italo, Benítez, Narciso, Biviano, Andrea, Broadhurst, Tom, Ford, Holland, Grillo, Claudio, Koekemoer, Anton, Melchior, Peter, Mercurio, Amata, Moustakas, John, Rosati, Piero and Zitrin, Adi, 2014, "CLASH: Weak-lensing Shear-and-magnification Analysis of 20 Galaxy Clusters", , **795**(2), 163. [DOI], [ADS], [arXiv:1404.1375 [astro-ph.CO]]

Umetsu, Keiichi, Zitrin, Adi, Gruen, Daniel, Merten, Julian, Donahue, Megan and Postman, Marc, 2016, "CLASH: Joint Analysis of Strong-lensing, Weak-lensing Shear, and Magnification Data for 20 Galaxy Clusters", , **821**(2), 116. [DOI], [ADS], [arXiv:1507.04385 [astro-ph.CO]]

Vagnozzi, Sunny, 2020, "New physics in light of the H_0 tension: An alternative view", *Phys. Rev. D*, **102**(2), 023 518. [DOI], [arXiv:1907.07569 [astro-ph.CO]]

Vagnozzi, Sunny, 2021, "Consistency tests of ΛCDM from the early integrated Sachs-Wolfe effect: Implications for early-time new physics and the Hubble tension", *Phys. Rev. D*, **104**(6), 063 524. [DOI], [arXiv:2105.10425 [astro-ph.CO]]

Vagnozzi, Sunny, Giusarma, Elena, Mena, Olga, Freese, Katherine, Gerbino, Martina, Ho, Shirley and Lattanzi, Massimiliano, 2017, "Unveiling ν secrets with cosmological data: neutrino masses and mass hierarchy", *Phys. Rev. D*, **96**(12), 123 503. [DOI], [arXiv:1701.08172 [astro-ph.CO]]

Vagnozzi, Sunny, Dhawan, Suhail, Gerbino, Martina, Freese, Katherine, Goobar, Ariel and Mena, Olga, 2018, "Constraints on the sum of the neutrino masses in dynamical dark energy models with $w(z) \geq -1$ are tighter than those obtained in ΛCDM", *Phys. Rev. D*, **98**(8), 083 501. [DOI], [arXiv:1801.08553 [astro-ph.CO]]

Van Uitert, Edo, Gilbank, David G., Hoekstra, Henk, Semboloni, Elisabetta, Gladders, Michael D. and Yee, Howard K. C., 2016, "Weak-lensing-inferred scaling relations of galaxy clusters in the RCS2: mass-richness, mass-concentration, mass-bias, and more", , **586**, A43. [DOI], [ADS], [arXiv:1506.03817 [astro-ph.CO]]

Vattis, Kyriakos, Koushiappas, Savvas M. and Loeb, Abraham, 2019, *Phys. Rev.*, **D99**(12), 121 302. [DOI], [1903.06220]

Verde, Licia, 2007, "A practical guide to Basic Statistical Techniques for Data Analysis in Cosmology". [arXiv:0712.3028 [astro-ph]]

Viel, Matteo, Lesgourgues, Julien, Haehnelt, Martin G., Matarrese, Sabino and Riotto, Antonio, 2005, "Constraining warm dark matter candidates including sterile neutrinos and light gravitinos with WMAP and the Lyman-alpha forest", *Phys. Rev. D*, **71**, 063 534. [DOI], [arXiv:astro-ph/0501562]

Viel, Matteo, Haehnelt, Martin G. and Springel, Volker, 2010, "The effect of neutrinos on the matter distribution as probed by the intergalactic medium", , **2010**(6), 015. [DOI], [ADS], [arXiv:1003.2422 [astro-ph.CO]]

Viel, Matteo, Becker, George D., Bolton, James S. and Haehnelt, Martin G., 2013, "Warm dark matter as a solution to the small scale crisis: New constraints from high redshift Lyman-α forest data", , **88**(4), 043502. [DOI], [ADS], [arXiv:1306.2314 [astro-ph.CO]]

Villaescusa-Navarro, Francisco, Marulli, Federico, Viel, Matteo, Branchini, Enzo, Castorina, Emanuele, Sefusatti, Emiliano and Saito, Shun, 2014, "Cosmology with massive neutrinos I: towards a realistic modeling of the relation between matter, haloes and galaxies", , **2014**(3), 011. [DOI], [ADS], [arXiv:1311.0866 [astro-ph.CO]]

Villaescusa-Navarro, Francisco, Hahn, ChangHoon, Massara, Elena, Banerjee, Arka, Delgado, Ana Maria, Ramanah, Doogesh Kodi, Charnock, Tom, Giusarma, Elena, Li, Yin, Allys, Erwan, Brochard, Antoine, Uhlemann, Cora, Chiang, Chi-Ting, He, Siyu, Pisani, Alice, Obuljen, Andrej, Feng, Yu, Castorina, Emanuele, Contardo, Gabriella, Kreisch, Christina D., Nicola, Andrina, Alsing, Justin, Scoccimarro, Roman, Verde, Licia, Viel, Matteo, Ho, Shirley, Mallat, Stephane, Wandelt, Benjamin and Spergel, David N., 2020, "The Quijote Simulations", , **250**(1), 2. [DOI], [ADS], [arXiv:1909.05273 [astro-ph.CO]]

Visinelli, Luca, Vagnozzi, Sunny and Danielsson, Ulf, 2019, "Revisiting a negative cosmological constant from low-redshift data", *Symmetry*, **11**(8), 1035. [DOI], [arXiv:1907.07953 [astro-ph.CO]]

Vogel, Cannon M. and Abazajian, Kevork N., 2022, "Entering the Era of Measuring Sub-Galactic Dark Matter Structure: Accurate Transfer Functions for Axino, Gravitino & Sterile Neutrino Thermal Warm Dark Matter". [arXiv:2210.10753 [hep-ph]]

Walker, A. G., 1937, "On Milne's Theory of World-Structure", *Proceedings of the London Mathematical Society*, **42**, 90–127. [DOI], [ADS]

Wang, Mei-Yu, Croft, Rupert A. C., Peter, Annika H. G., Zentner, Andrew R. and Purcell, Chris W., 2013, *Phys. Rev. D*, **88**(12), 123 515. [DOI], [1309.7354]

Wang, Yunchong, Nadler, Ethan O., Mao, Yao-Yuan, Adhikari, Susmita, Wechsler, Risa H. and Behroozi, Peter, 2021, "UniverseMachine: Predicting Galaxy Star Formation over Seven Decades of Halo Mass with Zoom-in Simulations", , **915**(2), 116. [DOI], [ADS], [arXiv:2102.11876 [astro-ph.GA]]

Weiner, Charles, Serjeant, Stephen and Sedgwick, Chris, 2020, "Predictions for Strong-lens Detections with the Nancy Grace Roman Space Telescope", *Research Notes of the American Astronomical Society*, **4**(10), 190. [DOI], [ADS], [arXiv:2010.15173 [astro-ph.GA]]

Weller, Jochen, Battye, Richard A. and Kneissl, Rüdiger, 2002, "Constraining Dark Energy with Sunyaev-Zel'dovich Cluster Surveys", *Phys. Rev. Lett.*, **88**, 231 301. [DOI]URL: https://link.aps.org/doi/10.1103/PhysRevLett.88.231301

Wong, Yvonne Y. Y., 2011, "Neutrino mass in cosmology: status and prospects", *Ann. Rev. Nucl. Part. Sci.*, **61**, 69–98. [DOI], [arXiv:1111.1436 [astro-ph.CO]]

Xu, Guohong, 1995, "A New Parallel N-Body Gravity Solver: TPM", , **98**, 355. [DOI], [ADS], [arXiv:astro-ph/9409021 [astro-ph]]

Xu, Weishuang Linda, Muñoz, Julian B. and Dvorkin, Cora, 2021, "Cosmological Constraints on Light (but Massive) Relics", *arXiv e-prints*, arXiv:2107.09664. [ADS], [arXiv:2107.09664 [astro-ph.CO]]

Yang, Weiqiang, Di Valentino, Eleonora, Pan, Supriya, Shafieloo, Arman and Li, Xiaolei, 2021a, "Generalized emergent dark energy model and the Hubble constant tension", *Phys. Rev. D*, **104**(6), 063 521. [DOI], [arXiv:2103.03815 [astro-ph.CO]]

Yang, Weiqiang, Di Valentino, Eleonora, Pan, Supriya, Wu, Yabo and Lu, Jianbo, 2021b, "Dynamical dark energy after Planck CMB final release and H_0 tension", *Mon. Not. Roy. Astron. Soc.*, **501**(4), 5845–5858. [DOI], [arXiv:2101.02168 [astro-ph.CO]]

Zaroubi, Saleem, 2013, "The Epoch of Reionization", in *The First Galaxies*, (Eds.) Wiklind, Tommy, Mobasher, Bahram, Bromm, Volker, Astrophysics and Space Science Library, 396, [DOI], [ADS], [arXiv:1206.0267 [astro-ph.CO]]

Zel'Dovich, Y. B., 1970, "Reprint of 1970A&A.....5...84Z. Gravitational instability: an approximate theory for large density perturbations.", , **500**, 13–18. [ADS]

Zelko, Ioana A., Treu, Tommaso, Abazajian, Kevork N., Gilman, Daniel, Benson, Andrew J., Birrer, Simon, Nierenberg, Anna M. and Kusenko, Alexander, 2022, "Constraints on Sterile Neutrino Models from Strong Gravitational Lensing, Milky Way Satellites, and the Lyman-α Forest", *Phys. Rev. Lett.*, **129**(19), 191 301. [DOI], [arXiv:2205.09777 [hep-ph]]

Zennaro, M., Bel, J., Villaescusa-Navarro, F., Carbone, C., Sefusatti, E. and Guzzo, L., 2017, "Initial conditions for accurate N-body simulations of massive neutrino cosmologies", , **466**(3), 3244–3258. [DOI], [ADS], [arXiv:1605.05283 [astro-ph.CO]]

Zhang, Y.-C., Zhang, H.-Y., Wang, D.-D., Qi, Y.-H., Wang, Y.-T. and Zhao, G.-B., 2017, "Probing dynamics of dark energy with latest observations", *Research in Astronomy and Astrophysics*, **17**, 050. [DOI], [ADS], [arXiv:1703.08293]

Zhao, G.-B., Raveri, M., Pogosian, L., Wang, Y., Crittenden, R. G., Handley, W. J., Percival, W. J., Beutler, F., Brinkmann, J., Chuang, C.-H., Cuesta, A. J., Eisenstein, D. J., Kitaura, F.-S., Koyama, K., L'Huillier, B., Nichol, R. C., Pieri, M. M., Rodriguez-Torres, S., Ross, A. J., Rossi, G., Sánchez, A. G., Shafieloo, A., Tinker, J. L., Tojeiro, R., Vazquez, J. A. and Zhang, H., 2017, "Dynamical dark energy in light of the latest observations", *Nature Astronomy*, **1**, 627–632. [DOI], [ADS], [arXiv:1701.08165]